Computational homogenization of confined granular media

vom Fachbereich Maschinenbau und Verfahrenstechnik
der Technischen Universität Kaiserslautern
zur Verleihung des akademischen Grades
Doktor–Ingenieur (Dr.–Ing.)
genehmigte Dissertation

von Dipl.–Ing. Holger Andreas Meier
aus Essen

Hauptreferent:	Prof. Dr.–Ing. P. Steinmann
Korreferenten:	Prof. Dr.–Ing. E. Kuhl
	Prof. Dr.–Ing. T. I. Zohdi
	Prof. Dr.–Ing. R. Müller
Vorsitzender:	JP Dr.–Ing. J. Mergheim
Dekan:	Prof. Dr.–Ing. S. Ripperger

Tag der Einreichung:	22.04.2009
Tag der mündl. Prüfung:	12.06.2009

Kaiserslautern, Juni 2009

D 386

Preface

The present work originated during the years 2005–2009 as research associate at the Chair of Applied Mechanics, University of Kaiserslautern, Germany.

First and foremost I would like to express my deepest gratitude to Professor P. Steinmann for both his scientific and kind support throughout all phases of this project. His expertise and guidance combined with consistent inspiration allowed the development of this research work.

I also would like to express profound recognition to Professor E. Kuhl for her extended willingness to support and provide assistance. Her inspiring knowledge and reinforcement proved to be extremely beneficial. Furthermore, I would like to acknowledge Professor T. I. Zohdi for his hospitality during my time of research in his laboratory at the University of California, Berkeley. Our fruitful discussions as well as his research experience essentially contributed to this work. Moreover, I would like to express my appreciation to Professor R. Müller for kindly providing a review of this work and for the useful conversations and plentiful discussions at the Chair of Applied Mechanics. For taking over the chair of the Ph.D. defense as well as for our useful discussions and continued encouragement, I would like to give thanks to JP J. Mergheim.

I would like to acknowledge my colleges at the Chair of Applied Mechanics, in particular P. Jäger, as well as former colleges S. Bargmann, P. Fischer, G. Albers, G. Possart and P. Schmitt for always creating an enjoyable work and social environment.

Last but not least, I would like to thank my father Bernd, wife Nicole as well as our children Anabela and Andreas for their continuous love and support.

Kaiserslautern, Juni 2009 Holger Meier

Zusammenfassung

Die Zielsetzung der vorliegenden Arbeit ist die Entwicklung, Implementierung und Analyse einer innovativen numerischen Homogenisierungsmethode für granulare Medien. Granulare Medien definieren eine Ansammlung von Objekten unterschiedlicher Form und Größe, wobei jedes einzelne Objekt den Gesetzen der klassischen Mechanik unterliegt. Obwohl jedes Objekt einen Festkörper darstellt, können granulare Medien auf Grund ihres randbedingungsspezifischen Gesamtverhaltens weder als klassischer Festkörper noch als klassisches Fluid bezeichnet werden. Dieses einzigartige Verhalten führt zu zwei weitverbreiteten Beschreibungsansätzen.

Der auf der Kontinuumsmechanik beruhende Ansatz geht von einem Festkörper aus. Das eigentliche Gesamtverhalten wird durch ein phänomenologisch basiertes Materialmodell beschrieben. Die Form und Größe der einzelnen Objekte sowie deren topologische Anordnung werden somit nicht explizit berücksichtigt. Auszeichnende granulartypische Effekte wie das Entstehen und Brechen von Kontakten können daher nicht explizit modelliert oder berücksichtigt werden. Stattdessen muß jede durch die granulare Mikrostruktur hervorgerufene Verhaltensweise in das makroskopisch phänomenologisch basierte Materialmodell eingearbeitet werden. Dieses geschieht im allgemeinen durch ein sogenanntes elasto-pastisches Materialmodell. Im Hinblick auf die numerische Umsetzung hat sich die Methode der finiten Elemente bewährt. Diese stellt ein robustes und leistungsfähiges Simulationsverfahren dar.

Im Gegensatz zur kontinuumsbasierten Beschreibungsweise, welche nur an der makroskopischen Gesamtantwort interessiert ist, richtet die diskrete Beschreibungsweise ihr Hauptaugenmerk auf die granulare Mikrostruktur. Besonderes Interesse gilt den individuellen diskreten Objekten und deren Bewegung. Die diskrete Grundstruktur ermöglicht die Beschreibung granulartypischer Effekte auf natürliche Weise. Somit erlaubt sie neben der Modellierung von granularen Festkörpern auch die Simulation von Fluiden. Desweiteren befähigt der individueller Charakter die explizite Einbettung vorhandener Sieblinien sowie die Modellierung spezifischer Objektanordnungen. Nachteilig wirkt sich die diskrete Betrachtungsweise auf die Rechenzeit aus, wodurch sogenannte Diskrete Elemente Methoden nur für granulare Medien kleiner oder moderater Größe verwendet werden.

Zu der in dieser Arbeit vorgeschlagenen innovativen numerischen Simulation granularer Medien werden die erwähnten Ansätze unter Verwendung einer numerischen Homogenisierungsmethode kombiniert. In diesem Zusammenhang wird zwischen einer kontinuierlichen Makroskala und einer diskreten Mikroskala unterschieden. Auf der Makroskala wird eine finite Elemente Methode angewandt. Auf der Mikroskala wird das Verhalten des granularen Mediums mit Hilfe einer diskreten Elemente Methode beschreiben. Das im klassischen Fall benutzte makroskopisch phänomenologische

Materialmodell wird durch die homogenisierte mikroskopische Antwort ersetzt. Die eigentliche Kopplung der individuellen Skalen erfolgt über das Konzept eines repräsentativen Volumenelements und unterliegt der sogenannten Skalentrennung. Diesbezüglich stellt ein repräsentatives Volumenelement die kleinste, jedoch immer noch charakteristische Materialprobe dar. Für den vorliegenden Fall bedeutet dieses unter Anderem die Berücksichtigung einer vorgeschriebenen Korngrößenverteilung sowie die willkürliche Anordnung der einzelnen Partikel. Der Hauptvorteil der vorgeschlagenen Skalenverknüpfung liegt in dem ausdrücklich Abhanden sein eines makroskopisch phänomenologisch basierten Materialmodells. Stattdessen wird das makroskopische Materialverhalten ausschließlich durch die mikroskopische Antwort beschrieben. Für die vorliegende Arbeit bedeutet dies, daß alle makroskopisch kontinuierlichen Materialgrößen aus mikroskopisch diskreten Größen hergeleitet werden. Weiterhin nutzt die beschriebene Kombination die jeweiligen Vorteile der Methoden aus.

Die vorliegende Arbeit ist in sieben Kapitel unterteilt. Nach einer kurzen Einführung werden relevante Grundgleichungen und Größen der Kontinuumsmechanik vorgestellt, siehe **Kapitel** 2. Insbesondere beschränkt sich diese Einführung auf den makroskopischen Deformationsgradienten, im Folgenden verwendete makroskopische Spannungsmaße, makroskopische Gleichgewichtsaussagen für Kontinua und den für die Numerik benötigten Tangentenoperator. Die Generierung geeigneter diskreter Mikrostrukturen ist in **Kapitel** 3 beschrieben. Wie bereits erwähnt, muß die verwendete Mikrostruktur gewissen Anforderungen genügen, um eine hinreichend genaue Abbildung des zu modellierenden Materials sicherzustellen. Der hierfür vorgeschlagene Generierungsalgorithmus ist aus dem Bereich der Molekulardynamik entnommen und erlaubt eine effiziente sowie anforderungsgerechte Herstellung granularer Volumenelemente. In Bezug auf die weitere Verwendung der generierten diskreten Mikrostrukturen ist ein, unter numerischen Gesichtspunkten, periodischer Rand von großer Bedeutung. Diese in der Natur nicht vorkommende Einschränkung erlaubt die Anwendung von periodischen Randbedingungen. Unter diesen Randbedingungen bleiben übliche Randeffekte unberücksichtigt, was einer unendlichen Erweiterung des untersuchten Gebiets gleichwertig ist. Zur weiteren Berechnung der generierten diskreten Mikrostruktur wird eine diskrete Elemente Methode herangezogen, vergleiche **Kapitel** 4. Die Verwendung dieser Methode erlaubt eine weitgehend realistische Simulation der einzelnen granularen Partikel. Wesentlicher Bestandteil ist die Lösung der NEWTONschen Bewegungsgleichung durch ein explizites Lösungsverfahren. Der hier verwendete diskrete Elemente Algorithmus basiert auf einem vorgeschriebenen konstitutiven Potenzial, welches den Kontakt zwischen zwei Partikeln beschreibt. Alle weiteren benötigten Größen sind von diesem Potenzial abgeleitet. Mikroskopisch erforderliche Randbedingungen werden durch den makroskopischen Deformationsgradienten vorgeschrieben. Im einzelnen werden die Annahme von TAYLOR, die reduzierte Annahme von TAYLOR als auch periodische Randbedingungen beschrieben und verwendet. Die eigentliche Homogenisierung der diskreten granularen Mikrostruktur wird in **Kapitel** 5 erläutert. Hauptaugenmerk gilt der Identität zwischen der mikroskopischen Gesamtenergie des zugrundegelegten Volumenelements und der makroskopischen Energiedichte an einem makroskopisch materiellen Punkt. Die Kopplung zwischen den beiden Skalen erfolgt über ein standard volumenbasiertes Mittelwertverfahren.

Nach den Regeln der klassischen Kontinuumsmechanik wird die generalisierte Form eines makroskopischen Spannungsmaßes abgeleitet werden. Hierbei stellt das Bestehen der makroskopischen Energiedichte eine wichtige Voraussetzung dar. Kann eine Funktion für die makroskopischen Energiedichte nicht aufgestellt werden, so erlaubt die sogenannte HILL-MANDEL-Bedingung eine eindeutige Definition generalisierter makroskopischer Spannungsmaße. Einbringen der zuvor erwähnten Randbedingungen liefert explizite Formulierungen von makroskopischen Spannungsmaßen unter klar definierten, mikroskopischen Randbedingungen. Die Einbindung in ein Finite Elemente Programsystem bedarf der Bekanntheit des makroskopischen Tangentenoperators. Dessen generalisierte sowie randbedingungsspezifische Herleitung wird in **Kapitel** 6 beschrieben. Das abermalige Ausnutzen der makroskopischen Energiedichte erlaubt eine eindeutige Herleitung des makroskopischen Tangentenoperators. Wie bei den zuvor bestimmten Spannungen ergibt sich der makroskopische Tangentenoperator aus einer Volumenmittlung über diskrete granulare Größen der Mikroskala. Reibung zwischen den einzelnen Partikeln wird in **Kapitel** 7 studiert. Die benötigten Reibkräfte werden aus einer inkrementellen Variationsformulierung hergeleitet, welche auf einem vorgeschlagenen reduzierten inkrementellen Potenzial beruht. Die vorliegende Arbeit schließt mit einer Diskussion der erhaltenen Ergebnisse und zeigt mögliche Perspektiven zur Erweiterung auf.

Contents

1. Introduction **1**

2. The big picture **5**
2.1. Continuum mechanics 5
2.1.1. Deformation measure 5
2.1.2. Stress measures 6
2.1.3. Equilibrium equations 7
2.1.4. Incremental tangent modulus 9
2.2. Computational homogenization 9

3. Representative volume element generation **11**
3.1. Introduction 11
3.2. Generation of representative volume elements 12
3.2.1. Event-driven time step calculation 12
3.2.2. Event handling 14
3.2.3. Event-driven generation of the rve 14
3.3. Concept of periodicity 15
3.4. Representative numerical examples 16
3.4.1. Grain size distributions - number of grains 18
3.4.2. Grain size distribution of quartz sand 20
3.4.3. Grain size distribution of concrete aggregates 23
3.5. Basic particle sets 28

4. Soft particle contact methods **31**
4.1. Introduction 31
4.2. A discrete element method 33
4.2.1. Contact normal potential 33
4.2.2. Contact normal force 36
4.2.3. Aggregate normal stiffness 37
4.3. Boundary conditions 38
4.3.1. The overall continuous case 38
4.3.2. Assumption of Taylor 40
4.3.3. Restricted Taylor assumption 43
4.3.4. Periodic boundary conditions 44
4.3.5. On the regularity of the global aggregate stiffness 47
4.4. The dynamic relaxation method 49
4.4.1. Explicit vector iteration 49
4.4.2. Iteration parameters 51

4.5. Representative numerical examples . . . 53
4.5.1. Microscopic investigations - uni-axial compression . . . 54
4.5.2. Microscopic investigations - simple shear . . . 61

5. Discrete homogenization 67
5.1. Introduction . . . 67
5.2. General macroscopic stress . . . 68
5.2.1. Macroscopic potential energy density . . . 68
5.2.2. General macroscopic stress - energy approach . . . 69
5.3. Boundary specific macroscopic stress . . . 72
5.3.1. Macroscopic stress - Taylor assumption . . . 72
5.3.2. Macroscopic stress - restricted Taylor assumption . . . 73
5.3.3. Macroscopic stress - periodic boundary conditions . . . 74
5.4. Representative numerical examples . . . 77
5.4.1. Macroscopic investigations - uni-axial compression . . . 77
5.4.2. Macroscopic investigations - simple shear . . . 82
5.4.3. Macroscopic investigations - cyclic loading . . . 87

6. Fem - dem coupling 89
6.1. Introduction . . . 89
6.2. General macroscopic tangent operator . . . 90
6.3. Boundary specific macroscopic tangent . . . 91
6.3.1. Macroscopic tangent - Taylor assumption . . . 91
6.3.2. Macroscopic tangent - restricted Taylor assumption . . . 93
6.3.3. Macroscopic tangent - periodic boundary conditions . . . 94
6.4. Representative numerical examples . . . 95
6.4.1. Rectangular block. . . . 95
6.4.2. Bi-axial compression test . . . 101
6.4.3. Slope stability problem . . . 104

7. Interparticle friction 107
7.1. Introduction . . . 107
7.2. Frictional extension . . . 108
7.2.1. Inter-particle kinematics . . . 108
7.2.2. Reduced incremental potential . . . 110
7.2.3. Contact tangential force . . . 112
7.3. Representative numerical examples . . . 115
7.3.1. Macroscopic investigations - uni-axial compression . . . 115
7.3.2. Macroscopic investigations - simple shear . . . 117
7.3.3. Macroscopic investigations - cyclic loading . . . 118

8. Closure 121
8.1. Discussion and conclusion . . . 121
8.2. Future work . . . 124

A. Tensor operations and derivatives 125

A.1. Tensor operations 125
A.2. Frequently used tensor derivatives 125
A.2.1. Derivatives with respect to the microscopic branch vector 126
A.2.2. Derivatives with respect to the macroscopic deformation gradient 126
A.2.3. Derivatives with respect to the microscopic material fluctuation . 126
A.3. The non-trivial derivative 127

. **Bibliography** **129**

. **List of figures** **141**

. **List of tables** **143**

. **Index** **145**

1. Introduction

Sand, a typical representative of granular matter is known to all of us - either from "sandbox experiments" in childhood or everyday life. We have to acknowledge our frequent contact with granular material, be it the cereal in the morning or today's fine particulate air pollution. General granular matter is defined as an accumulation of individual objects of arbitrary size and shape. Each object is subjected to the laws of classical mechanics, whereby the communication between the individual grains is restricted by a complex contact network. Particulate media as a whole take a special position in terms of its behavior, i.e., its general behavior cannot be accounted as solid nor fluid-like. Prominent examples include a standard package of coffee. Vacuum-packed, the collection of coffee beans are regarded as solid-like, however, breaking the confining pressure yields a liquid-like behavior and allows the pouring into various shaped objects. Interestingly, natural and modified particulates are one of the most commonly used materials in industry [120]. Examples of natural particulates include pebbles and sand, whereas modified materials comprise powders and victuals. Thus, its range of application spans pharmaceutical, food and numerous engineering disciplines, amongst others. The research interest in granular matter has a long history starting with the observations of COULOMB [24] and REYNOLDS [118, 119], however, the phenomena as well as characteristics of particulates are still inspiring to today's researchers and pose multiple queries. Naturally, the great adaptiveness of particulates permits a board field of application and research. We restrict the current research to the statics of confined dry granular matter, i.e., we disregard the ability of particulate flow as well as the influence of inter-particle liquid bridges.

In the context of the mechanics of confined dry granular matter, one has to differentiate between physical and computational investigations. Physical investigations rely on well prepared specimens, whereby their undistorted fabrication poses a non-trivial task. These specimens are often restricted in size and therefore introduce boundary effects which are not apparent in nature. One of the main drawbacks of physical investigations of natural particulates, e.g., soil, associates to the dissimilarities between the individual specimens: The arbitrary and random structure of granular media does not allow to obtain multiple exactly matching results. Experiments make the investigators dependent on boundary measures, consisting of stresses and strains. The precise microscopic behavior, i.e., the interaction between the individual grains, cannot be monitored during the experiments in a trivial manner. To circumvent these problems, JENKINS [62], ROWE [125], SCHNEEBELI [127] and others base their experiments on metal disks. These disks allow the tracking of positions as well as the observation of boundary quantities. Deeper insight in regards to the inter-particle contact forces as well as their distribution is not achieved. These queries are tackled by BREWSTER [15], DANTU [31], DE JOSSELIN DE JONG & VERRIJT [32], DRESCHER & DE JOSSELIN DE JONG [37] and WAKABAYASHI [150]. Founded on the establishment of BREWSTER, i.e.,

the phenomenon of polarization by reflection, DANTU and WAKABAYASHI suggest the use of optical sensitive material in the context of experimental granular mechanics. The proposed material is used by DE JOSSELIN DE JONG & VERRIJY and DRESCHER & DE JOSSELIN DE JONG to simulate the behavior of two dimensional disks. *Inter alia*, their experiments are performed on an apparatus, originally introduced by SCHNEEBELI. The use of photo elastic material, viewed in polarized light, uncovers the stresses inside the individual disks. These stresses relate to the inter-particle contact forces. DRESCHER & DE JOSSELIN DE JONG average the obtained contact forces over an internal area, yielding an area specific stress tensor. Even though novel techniques like X-ray micro-tomography in combination with image processing [45, 121] and index matching liquid images [116] are presently used to access the grain-level information, the effort is considered to be enormous.

Tending to the computational modeling and simulation of particulate arrangements, one has to differentiate between continuous and dis-continuous approaches. The field of continuum mechanics presents a large variety of possible modeling approaches. Classical continuum elasto-plasticity of particulate matter describes one attempt, see for example DRUCKER, GIBSON & HENKEL [38], GOODMAN & COWIN [48], GUDEHUS [50], NOVA [103], RETTIG [117] or ROSCOE, SCHOFIELD & WROTH [123], whereby the theory itself is founded on the theory of metal plasticity. More advanced modeling techniques include the so-called gradient plasticity models, see for example AIFANTIS, or micropolar continua like the COSSERAT theory, compare COSSERAT. Without a detailed examination of the individual approaches, it is obvious that the microscopic level is not fully considered. In particular, grain size distributions, topological placements of the individual grains, the related contact network as well as its changes, particle interaction as well as the dislocation of individual grains are left aside. Thus, granular media distinguishing features are not *a priori* included. Instead, similar to the experimental approach, the material response is identified by stresses and strains as well as additional internal variables. The main uncertainty is related to the formulation of the evolution equations of the internal variables.

A more realistic and intuitive approach consists of the discrete description of particulate matter. Dis-continuum approaches consist of a finite number of discrete unbonded objects and permit to capture the behavior of granular matter in a natural way. Their fundamental idea is based on solving NEWTON's equation of motion in an explicit manner. The required driving forces are derived of inter-particle contact laws, in general depending on the infinitesimal inter-particle overlap. In contrast to continuum-based simulations, discrete particle methods allow the individual grains to form clusters and break contacts. This behavior is distinguishing for particulate media and is directly related to their failure characteristics. The most prominent algorithm that traces the behavior of particle collections is with no doubt the discrete element method (dem) by CUNDALL & STRACK [27–29]. Various modifications of the original algorithm exist, mainly divided in the application of different particle shapes, see D'ADDETTA ET AL. [30] JOHNSON & WILLIAMS [63] LILIE [73], and the modification of particle interaction, compare VU-QUOC & ZHANG [146,147], VU-QUOC, ZHANG & LESBURG [148], VU-QUOC, ZHANG & WALTON [149], ZOHDI [164, 165]. The drawbacks of discrete simulation techniques mainly relate to the limited number of grains, their idealization,

as well as the computational expensive contact search, restricting their environments to large clusters. Nevertheless, the increase of computational power, the decline in price of computer memory as well as ongoing research for efficient implementation techniques allow the handling of moderate discrete assemblies on today's standard personal computers.

This manuscript approaches the modeling of particulate matter by applying a computational homogenization method. Mainly due to the increase of computational power, the past decades are characterized by the rise of these modeling strategies, compare: D'ADDETTA ET AL. [30], DETTMAR [33], EHLERS ET AL. [41], GRYTZ & MESCHKE [49], HIRSCHBERGER [59], KOUZNETSOVA, GEERS & BREKELMANS [68, 69], LARRSON & RUNESSON [71], MEIER, STEINMANN & KUHL [88], MIEHE [89,90], MIEHE ET AL. [91–96] MISRA & CHANG [98], NEMAT-NASSER [101], SCHRÖDER [128], SUNYK [134], TEMIZER & ZOHDI [138], TADMOR ET AL. [135], TANG ET AL. [136], WELLMANN, LILLIE & WRIGGERS [154],ZOHDI [163] or ZOHDI ET AL. [166–170]. The overall concept of computational homogenization goes back to the works of HILL [40, 58] and finds its main attention in describing the effective properties of heterogeneous media. This technique allows for the local incorporation of well defined microstructures into the standard continuum model. The resulting problem may be regarded as a nested boundary value problem, typically containing a macroscale and a microscale level. The major advantage of such schemes is linked to the absence of explicitly formulated macroscopic material models. Instead, the required constitutive information is solely provided by the locally attached microscopic boundary value problem which is essentially driven by macroscopic quantities. The attached microscopic volume element needs to be known *a priori* and is required to reflect the natural microscopic properties of the investigated material. Assuming that the attached microstructure is capable of reproducing the overall material behavior, the volume element may be considered as representative, see for example GITMAN, GITMAN & ASKES [46], KANIT ET AL. [65] or MEIER, STEINMANN & KUHL [84], STROEVEN, ASKES & SLUYS [132]. The existence of a representative volume element (rve) enables to restrict the computational effort to the smallest, still representative, material sample. We extend the common theory of continuum homogenization to particulate aggregates, by a two-scale approach. The macroscale defines a continuum with a locally attached discrete microstructure. Thus, this research restricts to the so-called first-order computational homogenization. A discrete element approach provides an optimal choice to model the particulate behavior. The dis-continuous nature of the applied approach allows for the natural incorporation of particulate matter distinguishing features. Based on the well known mechanics of a single grain, the microscopic algorithm itself may be considered to be trivial. Nevertheless, the resulting averaged material response allows for the modeling of complicated macroscopic behaviors, i.e., it reflects the nature of the underlying material. The used rves are randomly composed by disk-like particles and incorporate a prescribed grain size distribution as well as a geometric periodic boundary. Of course one is not able to find a geometric periodic granular assembly in nature, however, the assumption of geometric periodicity allows the application of periodic boundary conditions. These boundary conditions leave the usual boundary effects unconsidered.

The present manuscript divides in 7 chapters. **Chapter** 2 briefly introduces the reader

to the elementary measures of classical continuum mechanics and thus allows to familiarize with the employed notation. Furthermore, deeper insight of the proposed first-order computational homogenization strategy is presented. Based on the need for a discrete rve, **Chapter** 3 focuses on a proper rve generation algorithm. Therein, the algorithm itself is described in detail. Additionally, we introduce the concept of periodicity. This chapter finalizes by granting multiple representative examples. A potential based soft particle contact method, used for the computations on the microscale level, is defined in **Chapter** 4. Included are a description of the used discrete element method (dem) as well as the applied macroscopically driven DIRICHLET boundary conditions. The chapter closes with the proposition of a proper solution algorithm as well as illustrative representative examples. Homogenization of the discrete microscopic quantities is discussed in **Chapter** 5. Therein, the focus is on the upscaling of the aggregate energy as well as on the derivation of related macroscopic stress measures. Necessary quantities for coupling between a standard finite element method and the proposed discrete microscale are presented in **Chapter** 6. Therein, we tend to the derivation of the macroscopic tangent, necessary for the inclusion into the standard finite element programs. **Chapter** 7 focuses on the incorporation of inter-particle friction. We select to derive a variational based formulation of inter-particle friction forces, founded on a proposed reduced incremental potential. This contribution is closed by providing a discussion as well as an outlook.

2. The big picture

2.1. Continuum mechanics

This section provides the reader with selected quantities of classical continuum mechanics and is not intended to be exhaustive. For a complete overview as well as further details, the interested reader is encouraged to review the books of BETTEN [11], GURTIN [51], HOLZAPFEL [60], MALVERN [78], OGDEN [109], PODIO-GUIDUGLI [115], SPENCER [131] or WILLNER [157]. Our main focal points are the macroscopic continuum quantities which are used on or defined by the microscopic grain-scale level. This selection includes a macroscopic deformation measure, macroscopic stress measures, macroscopic equilibrium statements, and macroscopic tangent operators. With respect to the used tensor operations as well as related derivatives, the reader is referred to Appendix A.

2.1.1. Deformation measure

Summarizing the supplicated notation, we initially devote attention to the definition of the kinematics of the continuum model. Throughout the whole manuscript, vector and tensor quantities are denoted by bold letters. Upper case letters refer to quantities of the material (undeformed) configuration, while lower case letters are employed to define spatial (deformed) quantities. Variables related to the macroscopic level identify by a superimposed bar. In the three dimensional space we define the reference configuration of a homogeneous and continuous macroscopic body $\overline{\mathcal{B}}^0$. The body itself relates to a collection of material points. Each material point is uniquely described by a position vector $\overline{\boldsymbol{X}}$. The body deforms via $\overline{\boldsymbol{\varphi}}$, a non-linear spatial motion map, see Figure 2.1. This procedure carries the material body to the so called spatial configuration, i.e., $\overline{\boldsymbol{\varphi}} : \overline{\mathcal{B}}^0 \rightarrow \overline{\mathcal{B}}^t$. Hence, each point $\overline{\boldsymbol{X}}$ in $\overline{\mathcal{B}}^0$ is associated to a point $\overline{\boldsymbol{x}}$ in $\overline{\mathcal{B}}^t$ by

$$\overline{\boldsymbol{x}} = \overline{\boldsymbol{\varphi}}\left(\overline{\boldsymbol{X}}\right). \tag{2.1}$$

We demand $\overline{\boldsymbol{\varphi}}$ to be one-to-one, such that an inverse map from the spatial to the material configuration exists. The displacement field $\overline{\boldsymbol{u}}$ specifies as the difference between the points in the two configurations,

$$\overline{\boldsymbol{u}} = \overline{\boldsymbol{x}} - \overline{\boldsymbol{X}}. \tag{2.2}$$

Local deformation is described by the deformation gradient tensor $\overline{\boldsymbol{F}}$, compare Figure 2.1. The deformation gradient defines as a quantity, mapping an infinitesimal ma-

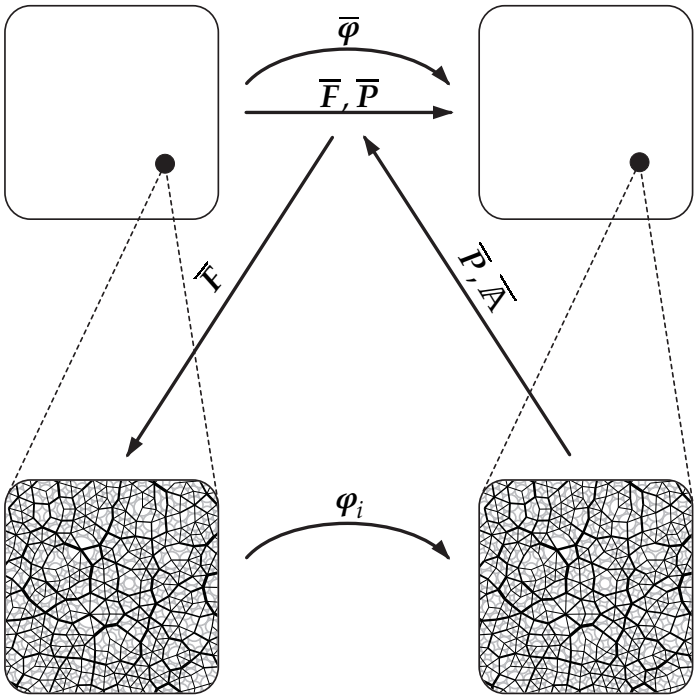

Figure 2.1.: Homogenization concept

terial line element $\mathrm{d}\overline{X}$ to an infinitesimal spatial line element $\mathrm{d}\overline{x}$. In terms of the spatial motion map, an expression of the deformation gradient is gained by linearization with respect to the material position,

$$\overline{F} = \frac{\partial \overline{\varphi}}{\partial \overline{X}}. \tag{2.3}$$

With respect to the theory of classical continuum mechanics, the deformation gradient represents a key-quantity. The entire deformation is included in this single two-point second order tensor. In particular, the determinant of $\overline{F}$, denoted by $\overline{J}$, defines the transformation between volumes, while the co-factor, $\mathrm{cof}\left(\overline{F}\right) = \overline{J}\overline{F}^{-t}$, relates between area elements. Related to the previous demand of an injective deformation map, the determinant of the deformation gradient is demanded to be non-zero. To eliminate unphysical self penetrations, we enhance this demand and require $\overline{J} = \det\left(\overline{F}\right) > 0$.

2.1.2. Stress measures

We postulate a traction vector $\overline{t}$ in the spatial configuration, which defines as a force per unit area. Tractions are solely located on surfaces, either on the boundary surface $\partial\overline{\mathcal{B}}^t$ or on a cross section of an arbitrary cut through the body $\overline{\mathcal{B}}^t$. In case of intersection related tractions, equilibrium requirements demand the traction vectors on the opposite cross sections to be equal in magnitude and reversed with respect to the di-

rections. These demands are commonly known as CAUCHY lemma. Each surface in the deformed configuration may be uniquely identified by an outward surface normal, denoted by $\overline{\boldsymbol{n}}$. We introduce the CAUCHY stress tensor $\overline{\boldsymbol{\sigma}}$ as the unique map between the spatial tractions acting on a surface and the surface orientation itself.

$$\overline{\boldsymbol{t}} = \overline{\boldsymbol{\sigma}} \bullet \overline{\boldsymbol{n}} \tag{2.4}$$

This unique relation is commonly known as CAUCHY's theorem and defines a linear relation between the spatial traction vectors and related spatial surface orientations. We remark that the stress inside a body is considered as counter part to the subjected loading. Without proof, we require the CAUCHY stress tensor to be symmetric. The present manuscript requires the introduction of another stress measure, the so-called PIOLA stress $\overline{\boldsymbol{P}}$, see Figure 2.1. The PIOLA stress

$$\overline{\boldsymbol{P}} = \overline{J}\overline{\boldsymbol{\sigma}} \bullet \overline{\boldsymbol{F}}^{-t}, \tag{2.5}$$

defines as a linear mapping between the material surface direction and the related material traction vector, $\overline{\boldsymbol{T}} = \overline{\boldsymbol{P}} \bullet \overline{\boldsymbol{N}}$. Therein, $\overline{\boldsymbol{N}}$ defines the outward surface normal in the reference configuration. Note that the CAUCHY stress is symmetric, while the PIOLA stress is not. Related to the CLAUSIUS-PLANCK inequality, the PIOLA stress is thermodynamically work conjugated to the deformation gradient. Under the existence of an energy storage function $\overline{\Phi}$ and the arbitrariness of the deformation gradient as well as its temporal derivative, we may define:

$$\overline{\boldsymbol{P}} = \frac{\mathrm{d}\overline{\Phi}}{\mathrm{d}\overline{\boldsymbol{F}}}. \tag{2.6}$$

2.1.3. Equilibrium equations

Let us now tend to the equilibrium equations for continuous systems. Assuming the existence of an energy storage function, we may derive the desired equilibrium equations by means of the principle of minimum total potential energy. Thereby, the supplicated principle relates to a natural process, i.e., the endeavor of a body to find a state of minimum potential energy. This specific state expresses a status of equilibrium for prescribed boundary conditions. Yet, the reader is advised that equivalent equilibrium statements may be obtained by considering the balance of linear momentum or by inspecting the equilibrium of an infinitesimal volume element. For the considered approach, we define a strain energy $\overline{\mathsf{U}}$ of the body $\overline{\boldsymbol{\mathcal{B}}}^0$ by integrating over the point-wise defined energy storage function $\overline{\Phi}$,

$$\overline{\mathsf{U}} = \int_{\overline{\boldsymbol{\mathcal{B}}}^0} \overline{\Phi}\, \mathrm{d}V. \tag{2.7}$$

As external contribution we define a potential energy function $\overline{\mathsf{V}}$, considering prescribed material boundary tractions $\overline{\boldsymbol{T}}^p$, as well as material body forces $\overline{\boldsymbol{B}}$. Thereby, boundary tractions are related to the undeformed boundary surface $\partial\overline{\mathcal{B}}^0_t$, whereas body forces define per unit volume of $\overline{\mathcal{B}}^0$.

$$\overline{\mathsf{V}} = -\int_{\overline{\mathcal{B}}^0} \overline{\boldsymbol{\varphi}} \cdot \overline{\boldsymbol{B}} \mathrm{d}V - \int_{\partial\overline{\mathcal{B}}^0_t} \overline{\boldsymbol{\varphi}} \cdot \overline{\boldsymbol{T}}^p \mathrm{d}A. \tag{2.8}$$

We remark that the total surface of the body $\overline{\mathcal{B}}^0$ is divided into two non-intersecting boundary surfaces, $\partial\overline{\mathcal{B}}^0_t$ and $\partial\overline{\mathcal{B}}^0_u$, with $\partial\overline{\mathcal{B}}^0 = \partial\overline{\mathcal{B}}^0_t \cup \partial\overline{\mathcal{B}}^0_u$ and $\partial\overline{\mathcal{B}}^0_t \cap \partial\overline{\mathcal{B}}^0_u = \emptyset$. While tractions are prescribed on $\partial\overline{\mathcal{B}}^0_t$, displacements are prescribed on $\partial\overline{\mathcal{B}}^0_u$. Additively combining (2.7) and (2.8) yields the total potential energy of the undeformed body $\overline{\mathcal{B}}^0$. The requirement of a minimum of the total potential energy identifies with a stationary state where a variation in position does not produce a change in energy, i.e.,

$$\delta\left[\overline{\mathsf{U}} + \overline{\mathsf{V}}\right] = 0. \tag{2.9}$$

Having defined the total potential energy in the material configuration allows switching between the order of integration and variation. As final result we obtain an equation, known as the weak form of equilibrium, having $\delta\overline{\boldsymbol{\varphi}}$ as a so-called test function or virtual displacement.

$$\int_{\overline{\mathcal{B}}^0} \overline{\boldsymbol{P}} : \delta\overline{\boldsymbol{F}} \mathrm{d}V - \int_{\overline{\mathcal{B}}^0} \delta\overline{\boldsymbol{\varphi}} \cdot \overline{\boldsymbol{B}} \mathrm{d}V - \int_{\partial\overline{\mathcal{B}}^0_t} \delta\overline{\boldsymbol{\varphi}} \cdot \overline{\boldsymbol{T}}^p \mathrm{d}A = 0. \tag{2.10}$$

The reader is advised that the virtual displacement field is not related to the introduced real displacement field, see (2.2). Instead, we require this particular field to be arbitrary as well as to vanish on boundaries of prescribed real displacements. For the sake of completeness, we provide the so-called EULER-LAGRANGE equations, arising from (2.10) by demanding the arbitrariness of the test functions. These equations state the local form of equilibrium, also known as CAUCHY's equation of motion for the quasi-static case, as well as the NEUMANN-type boundary conditions,

$$\begin{array}{lll} \mathrm{DIV}\overline{\boldsymbol{P}} + \overline{\boldsymbol{B}} = \boldsymbol{0} & \text{in} & \overline{\mathcal{B}}^0 \\ \overline{\boldsymbol{P}} \cdot \overline{\boldsymbol{N}} = \overline{\boldsymbol{T}}^p & \text{on} & \partial\overline{\mathcal{B}}^0_t \end{array}, \tag{2.11}$$

In addition, the weak form of equilibrium defines the foundation of the well-established finite element method (fem). Without further details in regards to the fem, we direct the interested reader to the works of BELYTSCHKO, LIU & MORAN [8], WRIGGERS [160], as well as ZIENKIEWICZ & TAYLOR [162] for further insight.

2.1.4. Incremental tangent modulus

With respect to the solution of (2.10), e.g., by means of a NEWTON-RAPHSON type solution strategy, linearization of (2.6) is required. The linearization of (2.6) defines an incremental tangent modulus which links the increment in stress to the increment in deformation,

$$\Delta\overline{\boldsymbol{P}} = \frac{\mathrm{d}\overline{\boldsymbol{P}}}{\mathrm{d}\overline{\boldsymbol{F}}} : \Delta\overline{\boldsymbol{F}} = \overline{\mathbb{A}} : \Delta\overline{\boldsymbol{F}}. \tag{2.12}$$

For the present case, the particular tangent modulus denoted by $\overline{\mathbb{A}}$ connects the change in the PIOLA stress to the change of the deformation gradient. The fourth order tensor $\overline{\mathbb{A}}$ generally incorporates 81 independent components. Under the existence of an energy storage function, a major symmetry is observed, i.e., with respect to the components, $\overline{\mathbb{A}}_{\alpha\beta\gamma\delta} = \overline{\mathbb{A}}_{\gamma\delta\alpha\beta}$. Thus, the number of independent components reduces to a number of 36. Considering (2.6), i.e., assuming the existence of and energy storage function, allows to define the incremental tangent modulus by the second derivative of the potential with respect to the deformation gradient,

$$\overline{\mathbb{A}} = \frac{\mathrm{d}^2\overline{\Phi}}{\mathrm{d}\overline{\boldsymbol{F}} \otimes \mathrm{d}\overline{\boldsymbol{F}}}. \tag{2.13}$$

Standard continuum formulations define the incremental tangent modulus by means of continuum quantities of the same scale. Applying the concept of computational homogenization, the macroscopic incremental tangent modulus is exclusively defined by microscopic quantities.

2.2. Computational homogenization

Having introduced the necessary macroscopic quantities, including the deformation gradient, an energy conjugated stress measure, a tangent modulus which describes the incremental relation in between as well as the weak form of quasi-static equilibrium, we tend to the actual computational homogenization process. Computational homogenization is defined as a process which delivers macroscopically required quantities by solving a microscopic boundary value problem, see Figure 2.1. For the present consideration, i.e., leaving microscopic NEUMANN boundary conditions unconsidered, the microscopic rve is subjected to the macroscopic deformation gradient tensor. This tensorial quantity is understood as the main driving measure on the microscale level, whereby the procedure itself defines a macro-micro transition between the scales. Assuming a DIRICHLET boundary value problem on the microscale level, the latter is solved by employing an appropriate solution strategy. Having obtained a quasi-static equilibrium in the deformed state, we presume that each discrete grain i was mapped by an individual non-linear deformation, denoted by $\boldsymbol{\varphi}_i$. Under the assumption of quasi-static equilibrium on the microscale level, apparent macroscopic variables, i.e., the PIOLA stress as well as the related tangent operator $\overline{\mathbb{A}}$ are exclusively defined

by microscopic quantities. As mentioned, the present case defines a continuum on the macroscopic scale, while the microscopic scale is modeled by a dis-continuum approach. Thus, the required macroscopic constitutive law of the continuum is expressed by discrete quantities of the grain-scale level. Therefore, each material point on the macroscopic level is assigned to a discrete microscopic collection of grains. Returning the apparent measures to the macroscale, i.e., performing a micro-macro transition, allows the solution of the macroscopic boundary value problem.
Naturally, computational multiscale calculations lead to high computational costs. These expenses are produced by solving the locally attached microscopic boundary value problems. Besides the option of adaptivity, i.e., selecting only specific macroscopic points which incorporate an attached microscale, parallel computation of the individual microscopic boundary value problems defines an attractive solution to save computation time. The absence of information exchange between the individual, locally attached microstructures allows for a trivial but efficient parallelization of the outlined computational homogenization method. Computationally speaking, multiscale methods allow for a straight forward implementation of the "embarrassingly parallel" type, usually implemented by using standard message passing interface (mpi) libraries.

3. Representative volume element generation

3.1. Introduction

This chapter approaches one of the oldest problems known to mankind, the packing of objects into a predefined area or volume, see BERNAL [9]. While ordered close packings, see for example the KEPLER conjecture (recently proven by HALES [52–57]), aim to pack identical spheres in tight arrangements, we focus on the construction of irregular, densely populated particle arrangements. We note that the KEPLER conjecture is only valid if the aggregate has more than 57 identical spheres. For less than 57 spheres, the so-called Wurstvermutung of TÓTH [141], i.e., the centers of the contacting spheres are assumed to lay on a strait line, represents the most densely packed arrangement. Further comments in regards to the Wurstvermutung in small dimensions are given by BETKE & GRITZMANN [10]. Although theoretically well understood, the efficient construction of an rve, having a high volume fraction and at the same time being irregular regarding the particle setup, is part of intensive research. In general, when considering packing strategies, one needs to differentiate between static and dynamic packing techniques. The simplest static packing procedure consists of arranging the single grains on a given pattern, e.g., a predefined equidistant grid. Naturally, this algorithm is capable of producing ordered dense packings in a minimum amount of time. Despite this advantage, the resulting assemblies are far from packings found in granular materials. Granular matter is highly heterogeneous and exhibits an unstructured particle distribution. Furthermore, ordered assemblies tend to directional dependent properties, see BAGI [4], i.e., these packings are highly anisotropic. While this manuscript does not focus on the anisotropy in granular media in detail, this relevant topic is discussed in CAMBOU, DUBUJET & NOUGUIER-LEHON [16]. A more elaborate static packing technique was introduced by BAGI [5], the so-called inwards packing method. This method allows the generation of random periodic packings, leading to results with initial isotropic properties. While the algorithm itself allows to use data from a prescribed grains size distribution, the resulting assembly is not guaranteed to reproduce the entered distribution exactly. Furthermore, the inward packing method is restricted to the generation of two dimensional rves. In contrast to the previously mentioned static packing algorithms, which are based on simple geometric properties, dynamic packing methods develop the assembly of particles over time. Based on the time dependence, most dynamic procedures are computationally more expensive, when compared to the static procedures. The most popular dynamic algorithms include gravitation and expansion techniques.
We would like to draw the reader's attention to a class of dynamic particle packing methods developed in the context of computational chemistry. These packing methods are extremely efficient and their outcome is congruent with the expectations of

an irregular highly packed geometrically periodic rve used in geo-mechanical multiscale methods, see LUBACHEVSKY [74] and LUBACHEVSKY ET AL. [75, 76] for the original algorithm and MEIER, KUHL & STEINMANN [84, 86] for additional information. In contrast to the vast majority of the static and dynamic rve generation schemes, the LUBACHEVSKY-STILLINGER algorithm is capable of incorporating geometric periodic boundaries in a natural way, allows to obtain a prescribed grain size distribution and is not restricted to a specific dimension. In the following, we will demonstrate how prescribed grain size distributions can be incorporated directly in the classical LUBACHEVSKY-STILLINGER approach. Note, we do not aim to reach the highest possible packing density, rather than, we like to produce a packing of particles, possessing geometric periodic boundaries, suitable in a multiscale approach, see BORJA & WREN [13], DETTMAR [33], KANEKO ET AL. [64], MEIER, KUHL & STEINMANN [83], MIEHE & DETTMAR [91], WREN & BORJA [159] as well as Chapter 5 within this manuscript. With respect to high packing densities, we refer the interested reader to BARAM [6] and references therein. In summary, the algorithm presented is used as a preprocessor generating geometrically periodic rves. Embedding, as well as further computation of the generated rves is the focal point of Chapter 4 within the publication.

3.2. Generation of representative volume elements

Within the LUBACHEVSKY-STILLINGER algorithm, the generation of an rve is accomplished by employing an event-driven scheme, advancing from one event to another, see LUBACHEVSKY [74] and LUBACHEVSKY ET AL. [75,76]. Here, an event is considered to be the discrete collision between two particles. Each event is considered individually and in serial, postulating that only one discrete event is taking place at one discrete time. This allows to handle each event individually. The basic steps of finding and handling an event are specified in the Subsections 3.2.1 and 3.2.2, whereas the algorithm used to produce the rves, is described in Subsection 3.2.3.

3.2.1. Event-driven time step calculation

In an event-driven scheme, the particles evolve independently at all times, except for discrete asynchronous instances of pairwise interactions. The time step size is thus governed by the sequence of events. To calculate the time step Δt, needed to advance the particle system from time t^n (Figure 3.1, left) to time t^{n+1} (Figure. 3.1, right), the event, collision between two particles, has to be observed. During the rve generation we use a hard contact model. Thus, we do not allow for particle overlap. Entering at time t^n, we assume that the positions of the particle centers $\boldsymbol{x}_i^n$, the particle radii r_i^n as well as the particle velocities $\boldsymbol{v}_i^n$ are known. The key idea of the present rve generation scheme is that the initial individual particle radii are set to zero, such that, *ab initio* the particles are not in contact. The particle radii r_i are then assumed to increase as

$$\dot{r}_i = g_i \quad \forall \quad i \in \mathscr{P}, \quad r_i, g_i \in \mathbb{R}^+, \tag{3.1}$$

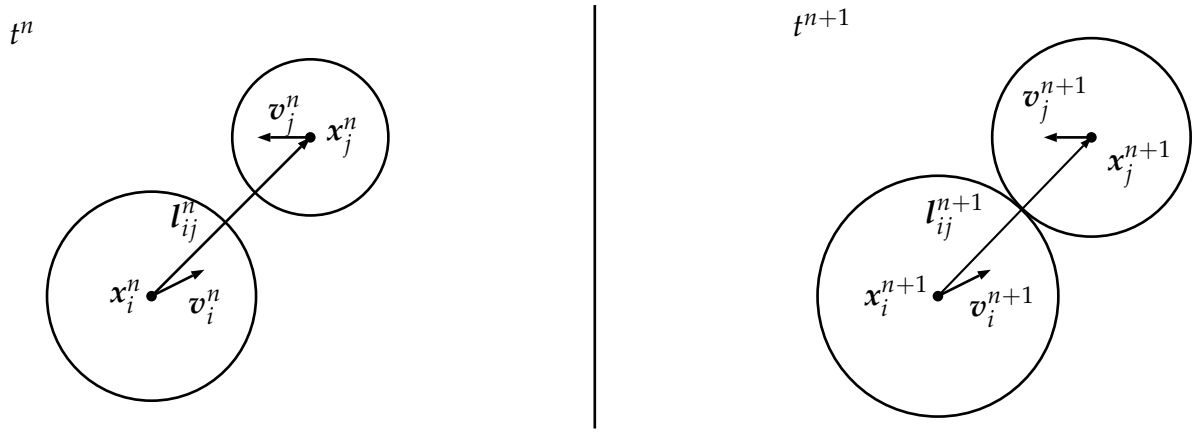

Figure 3.1.: Hard particle contact. *Left*: Configuration of particle i and j at time t^n prior to contact. *Right*: Particle configuration at t^{n+1}, defining the time step size Δt due to the event "particles in contact".

whereby set $\mathscr{P}$ defines the set of all particles. The volume fraction ϕ, i.e., the volume occupied by the particles per volume of the periodic boundary box is controlled by the growth rate g_i, $\phi = \phi\left(g_i\right)$. If g_i is equal for all particles i, a monodisperse packing is constructed. Different growth rates g_i generate a polydisperse packing, see KANSAL, TORQUATO & STILLINGER [66]. The discrete counterpart of (3.1) can be constructed, e.g., with the help of a finite difference scheme, i.e., $\dot{r}_i \approx \left[r_i^{n+1} - r_i^n\right] / \Delta t$. The discrete update equation of the particle radii at time t^{n+1} yields:

$$r_i^{n+1} = r_i^n + g_i \Delta t \quad \forall \quad i \in \mathscr{P}. \tag{3.2}$$

Postulating a constant velocity between the time nodes, the position of particle i at time t^{n+1} is calculated by using the well-known forward EULER formula.

$$\boldsymbol{x}_i^{n+1} = \boldsymbol{x}_i^n + \Delta t\, \boldsymbol{v}_i^n \quad \forall \quad i \in \mathscr{P}, \quad \boldsymbol{x}_i, \boldsymbol{v}_i \in \mathbb{R}^{\mathsf{dim}}. \tag{3.3}$$

The branch vector $\boldsymbol{l}_{ij}^{n+1}$, connecting the centers of the particles i and j, is calculated by subtracting the position vectors of the particles.

$$\boldsymbol{l}_{ij}^{n+1} = \boldsymbol{x}_j^{n+1} - \boldsymbol{x}_i^{n+1} \quad \forall \quad i \neq j, \qquad i, j \in \mathscr{P}. \tag{3.4}$$

Its direction is indicated by the order of the indices. For the sum of the particle radii being equal to the length of the branch vector, $\left|\left|\boldsymbol{l}_{ij}^{n+1}\right|\right| = r_i^{n+1} + r_j^{n+1}$, particle i and j are in contact, see Figure 3.1 (right). Using (3.2) and (3.3), we can define the relevant time step size for the event-driven scheme Δt,

$$\Delta t = \min_{\Delta t > 0} \left\{ \frac{\left[-\mathsf{u} \pm \sqrt{\mathsf{u}^2 - \mathsf{vw}}\right]}{\mathsf{v}} \right\} \tag{3.5}$$

with,

$$\mathsf{u} = \boldsymbol{l}_{ij}^{n} \bullet \left[\boldsymbol{v}_j^n - \boldsymbol{v}_i^n\right] - \left[r_i^n + r_j^n\right]\left[g_i + g_j\right], \tag{3.6}$$

$$\mathsf{v} = \left[\boldsymbol{v}_j^n - \boldsymbol{v}_i^n\right]^2 - \left[g_i + g_j\right]^2, \tag{3.7}$$

$$\mathsf{w} = \boldsymbol{l}_{ij}^{n\,2} - \left[r_i^n + r_j^n\right]^2. \tag{3.8}$$

The minimum of the two possible solutions for all possible particle contacts of the system defines the first contact and thus the time needed to advance to the next event.

3.2.2. Event handling

Being able to advance to the next event, the event itself has to be handled. Contact between two particles is treated as a purely elastic impact between two bodies of equal mass, see for example GOLDSMITH [47] or STRONGE [133]. Taking into account the additional increase in size of the two colliding particles, the relation between the particle normal velocities directly before and right after the collision can be formulated as

$$v_{\mathsf{n}_i}^{\overset{+}{n+1}} = \mathsf{min}\left\{v_{\mathsf{n}_i}^{\overset{-}{n+1}}, v_{\mathsf{n}_j}^{\overset{-}{n+1}}\right\} - g_i, \quad v_{\mathsf{n}_j}^{\overset{+}{n+1}} = \mathsf{max}\left\{v_{\mathsf{n}_i}^{\overset{-}{n+1}}, v_{\mathsf{n}_j}^{\overset{-}{n+1}}\right\} + g_j \tag{3.9}$$

in terms of the growth rate g_i and the normal contact velocity

$$v_{\mathsf{n}}^{n+1} = \boldsymbol{v}^{n+1} \bullet \boldsymbol{n}_{ij}^{n+1}, \text{with } \boldsymbol{n}_{ij}^{n+1} = \boldsymbol{l}_{ij}^{n+1} / \left|\left|\boldsymbol{l}_{ij}^{n+1}\right|\right|. \tag{3.10}$$

Herein, $\overset{-}{(\bullet)}$ indicates quantities prior and $\overset{+}{(\bullet)}$ posterior to the collision. The assumption of the smoothness of the particles leaves the tangential particle velocities unchanged. We emphasize that the alternation of the normal velocities is exclusively based on geometric aspects.

3.2.3. Event-driven generation of the rve

For simplicity the rve is set to be a square with dimensions $\mathsf{l}_{\mathsf{rve}} \times \mathsf{l}_{\mathsf{rve}}$, however any reasonable shape is possible. The desired number of particles is randomly distributed inside the periodic boundary box, initialized with random particle velocities. The radii of all particles are set to zero. Of interest is the next particle pair collision and its time. The time step calculation outlined in Subsection 3.2.1 is performed for each particle pair being able to collide. Different algorithms for fast collision detection can be found in the literature [99]. We use a parallelized screening contact detection algorithm, the search time is of the order $\mathcal{O}(\mathsf{nop})$. The minimum time step of all possible collisions, calculated by (3.5), is selected to advance the event-driven scheme. Next, all particle positions $\boldsymbol{x}_i^{n+1}$ are updated in terms of a forward EULER scheme (3.3). The post contact velocities of the colliding particle pair are determined according to (3.9), followed by

1. initialization:
   $\text{random}\boldsymbol{x}_i^0, \text{random}\boldsymbol{v}_i^0, r_i^0 = 0, g_i \quad \forall i \in \mathscr{P}$
2. select minimum collision time of all possible collisions
   $$\Delta t = \min_{\Delta t > 0} \left\{ \frac{\left[-\mathsf{u} \pm \sqrt{\mathsf{u}^2 - \mathsf{vw}} \right]}{\mathsf{v}} \right\}$$
3. advance all particle positions regarding the minimum time step
   $\boldsymbol{x}_i^{n+1} = \boldsymbol{x}_i^n + \Delta t \, \boldsymbol{v}_i^n$
4. update velocities of colliding particle pair
   $$v_{\mathsf{n}_i}^{\overset{+}{n+1}} = \min \left\{ v_{\mathsf{n}_i}^{\overset{-}{n+1}}, v_{\mathsf{n}_j}^{\overset{-}{n+1}} \right\} - g_i, \quad v_{\mathsf{n}_j}^{\overset{+}{n+1}} = \max \left\{ v_{\mathsf{n}_i}^{\overset{-}{n+1}}, v_{\mathsf{n}_j}^{\overset{-}{n+1}} \right\} + g_j$$
5. check the increase of volume fraction
   $\texttt{IF}\, \Delta\phi \geq \Delta\phi^{\text{crit}} \texttt{GOTO2}.$

Table 3.1.: Pseudocode of the packing algorithm. Basic algorithm to produce dense particle packings by using a periodic boundary box.

a new search for the next collision. Allowing the algorithm to take its course, the particles float around inside the rve, collide and grow depending on the elapsed time. Postulation of a dropout criterion can be accomplished in many ways. We select the increase of volume fraction,

$$\Delta\phi = \phi^{n+1} - \phi^{n+1-c} \quad \text{with} \quad \phi^{n+1} = \frac{\mathsf{v}_{\mathsf{par}}^{n+1}}{\mathsf{v}_{\mathsf{rve}}} = \frac{\pi}{\mathsf{v}_{\mathsf{rve}}} \sum_{i=1}^{\mathsf{nop}} {r_i^{n+1}}^2, \tag{3.11}$$

to be the variable of interest. With $\Delta\phi$ dropping under a certain threshold over a specified number of events c fulfills our criterion. The complete algorithm is listed in Table 3.1. In virtue of the fact that the particles are prescribed to grow, while the size of the boundary box is held fixed, particles are guaranteed to collide, compare MEIER, KUHL & STEINMANN [86].

3.3. Concept of periodicity

In contrast to most existing rve generation strategies in the literature, our algorithm essentially generates periodic microstructures which can eventually be used for multiscale simulations on the integration point level of large scale finite element simulations, see BORJA & WREN [13], DETTMAR [33], KANEKO ET AL. [64], MIEHE & DETTMAR [91] and WREN & BORJA [159] for typical examples. We thus aim at generating a geometrically periodic rve. Its construction typically starts with the definition of a periodic boundary box, see Figure 3.2. Topologically speaking, the periodic boundary box for two dimensional systems can be thought of as a torus with particles moving on the

torus surface. The torus is set up by connecting the opposite boundary box sides, marked by $\ominus$ and $\oplus$. A particle with its center being inside the boundary box is con-

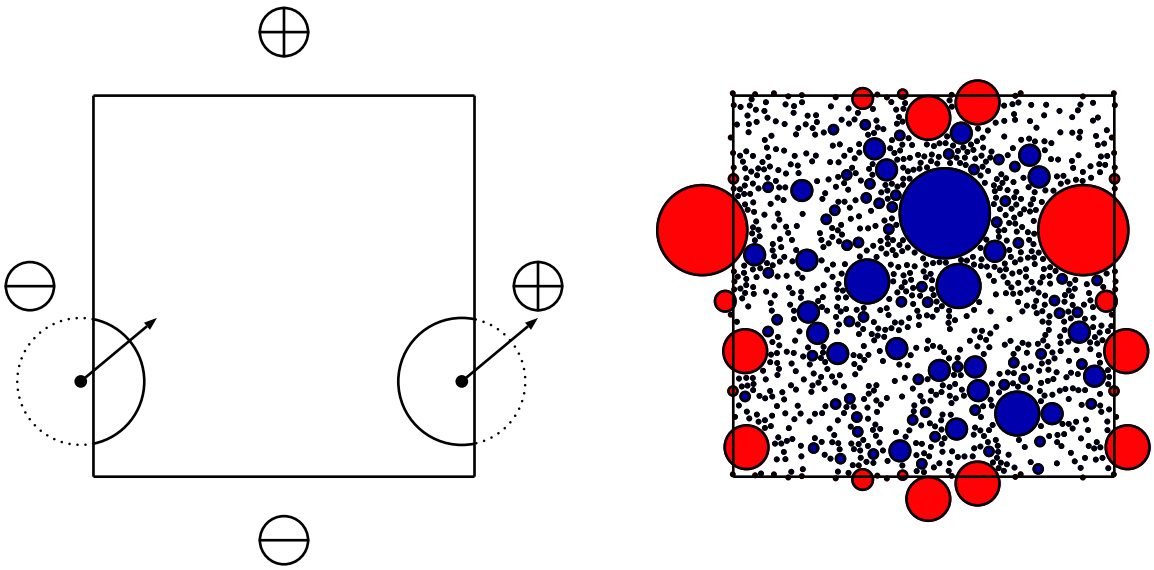

Figure 3.2.: Concept of periodicity, the periodic boundary box. *Left*: Schematic illustration of a periodic boundary box, including one primary particle and its replica. *Right*: Computational realization, including 1000 primary and 34 replica particles with volume fraction $\phi \approx 0.45$.

sidered to be a primary particle. If a primary particle intersects with a boundary of the periodic boundary box, a replica of this particle is positioned on the opposite side. All properties of the primary particle are projected onto the replicated particle. As soon as the center of the primary particle leaves the boundary box, the replicated particle center enters the boundary box and their states change. This leads to a constant number of primary particles inside the periodic boundary box. The periodic boundary box is used as a frame for the geometric periodic rve.

3.4. Representative numerical examples

Finally, the features of the suggested LUBACHEVSKY-STILLINGER algorithm will be illustrated by means of selected representative examples. First we aim to generate a two and three dimensional monodisperse particle arrangement. Since the maximal volume fractions for monodisperse spheres, in two as well as in three dimensions, are mathematically defined and proven, the generation of a monodisperse rve allows the observation of the packing capabilities of the used algorithm. To generate a monodisperse packing, we select an identical growth rate for all particles, i.e., $g_i = g = 1$. The number of primary particles is selected to 1000. These grains are randomly distributed inside the periodic boundary box. Each particle is subjected to a random velocity.

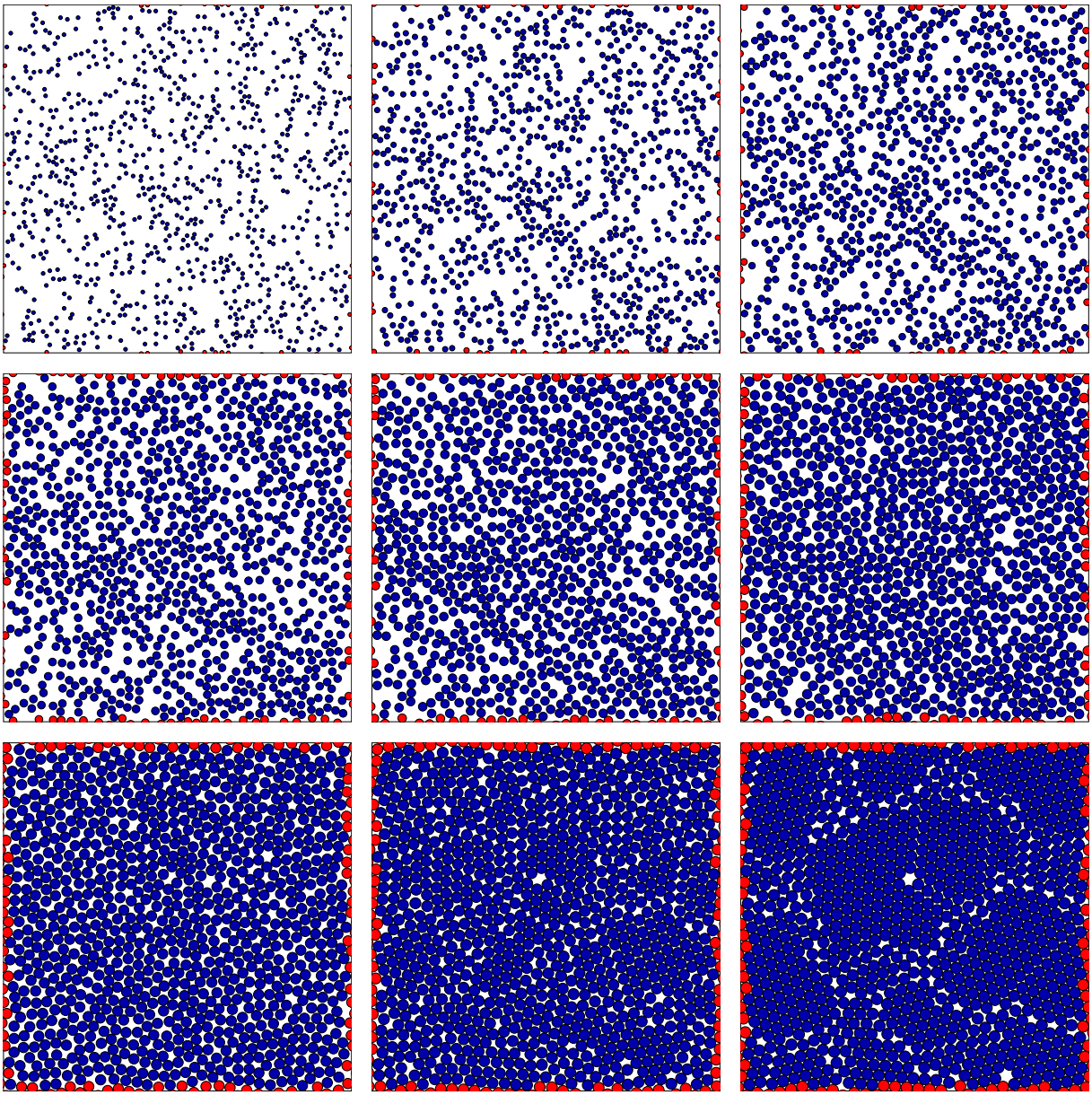

Figure 3.3.: Evolution process of a two dimensional monodisperse rve (1000 primary particles). Particles inside the rve are colored in blue (dark gray), particles intersecting with the periodic boundary box are colored in red (light gray). The periodic boundary box is illustrated by a black frame. The evolution is depicted from the upper left to the lower right image. The corresponding volume fractions start with $\phi = 0.1$, advance with $\Delta\phi = 0.1$ and reach a final $\phi \approx 0.863$ in the lower right image.

While this example is of a rather academic nature, the capacity and the efficiency of the LUBACHEVSKY-STILLINGER algorithm is demonstrated. The evolution process of the two dimensional monodisperse packing is shown in Figure 3.3. Starting at the top left, the assembly of grains has a volume fraction of $\phi = 0.1$, increasing by $\Delta\phi = 0.1$ in each image. The final monodisperse packing reaches a volume density of $\phi \approx 0.863$. The result is depicted in the lower right corner of Figure 3.3. We observe that the final snap shot includes large clusters of ordered particle distributions. Nevertheless, the ordered clusters of the rve are separated by disordered grain arrangements. Com-

paring the final volume density of $\phi \approx 0.863$ to the theoretical possible density for monodisperse packings in two dimensions, $\phi = \pi/\sqrt{12} \approx 0.907$, the LUBACHEVSKY-STILLINGER algorithm indeed produces irregular highly packed particle assemblies and almost converges to the theoretical density of two dimensional packing arrangement. The evolution of a three dimensional monodisperse rve is shown in Figure 3.4. The images in Figure 3.4 are ordered from the top left to the bottom right. The volume fractions increase by $\Delta\phi = 0.1$ between the images. The last snap shot of Figure 3.4 shows the converged rve, having a volume fraction of $\phi \approx 0.636$. Comparing the obtained volume fraction to the theoretical possible volume fraction for three dimensional monodisperse packings, i.e., $\phi = \pi/\sqrt{18} \approx 0.740$, we observe once more the capability and efficiency of the LUBACHEVSKY-STILLINGER algorithm.

3.4.1. Grain size distributions - number of grains

A common means to classify particular granular media is their grain size distribution in the form of sieve curves. Typical sieve curves are depicted in the Figures 3.5 and 3.9. The diagram in Figure 3.5 shows a characteristic grain size distribution of a quartz sand whereas the diagram in Figure 3.9 depicts a concrete aggregate distribution, required to ensure concrete of a particular quality. This curve, taken from German DIN standards [1], depicts the volume percentage of particles passing sieves of particular diameters, plotted over the individual sieve diameters. As such, they have to be converted to provide the appropriate input format for the applied rve generation algorithm. To begin with, the volume percentage of passing particles needs to be extracted for each grain size fraction of Figure 3.5 or 3.9. With the individual volume percentages passing per grain size fraction at hand, the particle percentage per grain size fraction is calculated as follows.

$$\text{particle } \%_i\,(\varnothing_i) = \frac{\dfrac{\text{volume } \%_i}{{\varnothing_i}^2}}{\displaystyle\sum_j \frac{\text{volume } \%_j}{{\varnothing_j}^2}}. \tag{3.12}$$

To select the minimal number of particles, needed to include at least one particle of each grain size fraction, the following equation,

$$\mathscr{P}_{\text{min}} = \left[\min_{\text{particle } \%_i > 0} \{\text{particle } \%_i\,(\varnothing_i)\}\right]^{-1} \bullet 100, \tag{3.13}$$

is evaluated. For a number of particles larger than $\mathscr{P}_{\text{min}}$, the number of particles per grain size fraction follows straightforward by scaling the particle percentage derived by (3.12). The growth rate g_i of each particle i is set to be equivalent to the expected particle diameter itself. This approach guarantees the preservation of a scaled version of the prescribed grain size distribution during the evolution process. Note the importance of keeping the ratios between the growth rates equal to the ratios between the different grain sizes. In what follows, we elaborate the rve generation based on the

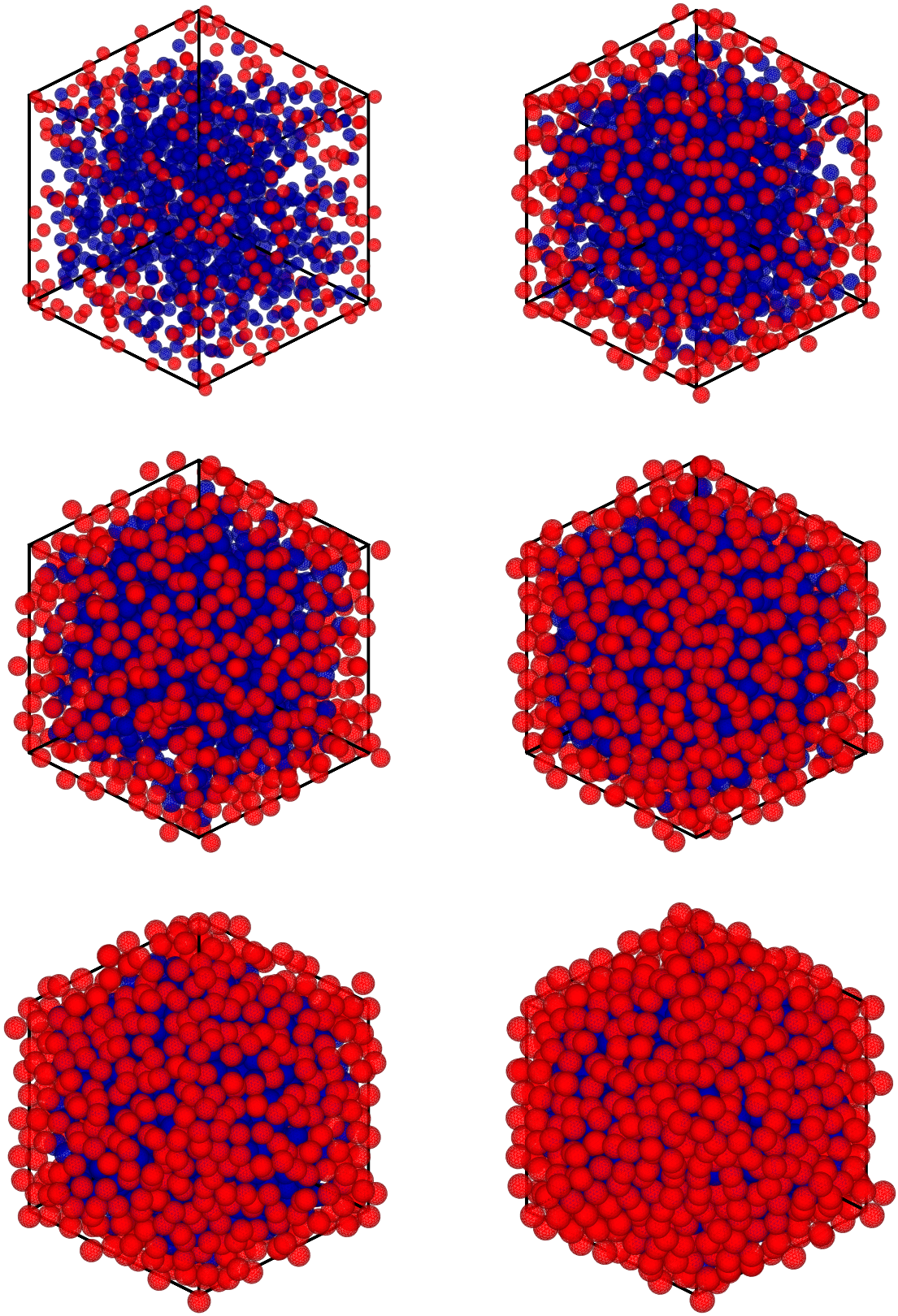

Figure 3.4.: Evolution process of a three dimensional monodisperse rve (1000 primary particles). Particles inside the rve are colored in blue (dark gray), particles intersecting with the periodic boundary box are colored in red (light gray). The periodic boundary box is illustrated by a black frame. The evolution is depicted from the upper left to the lower right image. The corresponding volume fractions start with $\phi = 0.1$, advance with $\Delta\phi = 0.1$ and reach a final $\phi \approx 0.636$ in the lower right image.

two sieve curves, given in the Figures 3.5 and 3.9.

3.4.2. Grain size distribution of quartz sand

The first example is taken from the field of geo-mechanics. In this case we selected a grain size distribution of a quartz sand, provided by the Institute of Foundation Engineering and Soil Mechanics of the Ruhr-University Bochum, see WICHTMANN [156]. The chosen quartz sand is distinguished by a low non-uniformity index of 1.4 and a mean diameter of 0.15 mm. The related sieve curve is illustrated in Figure 3.5. Its eval-

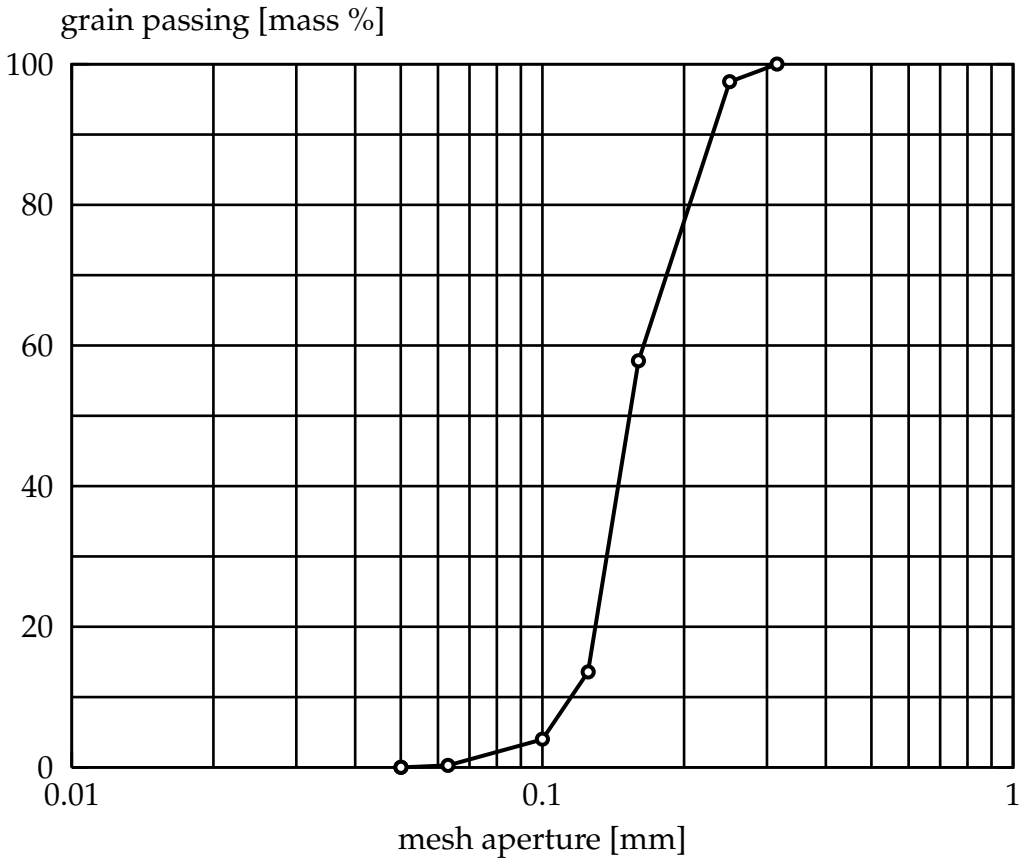

Figure 3.5.: Grain size distributions: quartz sand. Grain passing in mass percent over mesh aperture. The abscissa shows the mesh aperture in [mm], whereas the ordinate reads the grain passing in volume percent.

uation renders the relevant grain diameters and the corresponding mass and volume percentage as columns I, II and III of Table 3.2. The particle percentage summarized in column IV follows straightforwardly from equation (3.12). Its scaling renders the number of particles per grain fraction for a total number of 1000 particles, see column V. We produce a two and a three dimensional rve. A series of different stages of the two

Table 3.2.: Input parameter: Quartz sand example (1000 primary particles).

grain ∅ [mm]	mass % [%]	volume % [%]	particle % [%]	particle [/]
0.315	0.00	0.00	0.0000	0
0.250	2.50	2.50	0.6227	6
0.160	39.72	39.72	24.1531	242
0.125	44.22	44.22	44.0557	441
0.100	9.58	9.58	14.9131	149
0.063	3.70	3.70	14.5119	145
0.050	0.28	0.28	1.7435	17

dimensional rve generation process, based on the initialization of Table 3.2 is shown in Figure 3.6. The series starts in the upper left corner with an overall volume fraction of $\phi = 0.1$, increasing up to $\phi = 0.8$ by $\Delta\phi = 0.1$ from one snapshot to the next. The final distribution in the lower right corner which can be interpreted as a closest packing for the given sieve curve, corresponds to a volume fraction of $\phi = 0.848$. In the early stages of the evolution process particles move freely from collision to collision. At these stages, no oscillations of the particles are noticed. As the particle radii increase, the space available for particles to move becomes limited. This point is distinguished by a high oscillation of particles, resulting in a drastically decreasing time step sizes Δt. These stages roughly correspond to the lower row of snap shots in Figure 3.6, related to overall volume fractions of $\phi > 0.7$. From this point on, the rve generation process is dominated by shifts of patterns and reorganization of larger subunits. Due to the close packing of particles, time between collisions narrows down quickly. Accordingly, the individual particles hardly increase in size and the overall volume fraction tends to saturate. The largest packing density of $\phi = 0.848$ is defined algorithmically in terms of the incremental increase in volume fraction dropping below the critical value of $\Delta\phi^{\text{crit}} = 1.0\text{E}{-}09$. The evolution of the time step size Δt is depicted in Figure 3.7. For each subsequent event, the time step size is indicated by one single dot in the diagram. The abscissa illustrates the number of relevant events, starting from one and increasing up to almost 1.6E+07 from left to right. It is obvious that the time step size decreases drastically during the onset of the rve generation procedure. After approximately 1.6E+07 events, the time step size has converged towards an almost constant value, somewhat below 1.0E−10. Figure 3.7 nicely demonstrates why our definition of algorithmic convergence in terms of the critical value $\Delta\phi^{\text{crit}}$, as introduced in equation (3.11), is indeed a reasonable choice. Generally, one could be tempted to use the readily available time step size as a criterion for convergence. However, the diagram in Figure 3.7 shows that due to the stochastic nature of the contact distribution, the choice of a single absolute convergence criterion might have stopped the simulation long before overall convergence is observed. Accordingly, controlling an integral value, which has been replaced by its discrete counterpart in form of a sum in equation (3.11), seems an excellent choice. In contrast to the result of the monodisperse packings, the polydisperse packing does not allow to identify regions of ordered particle

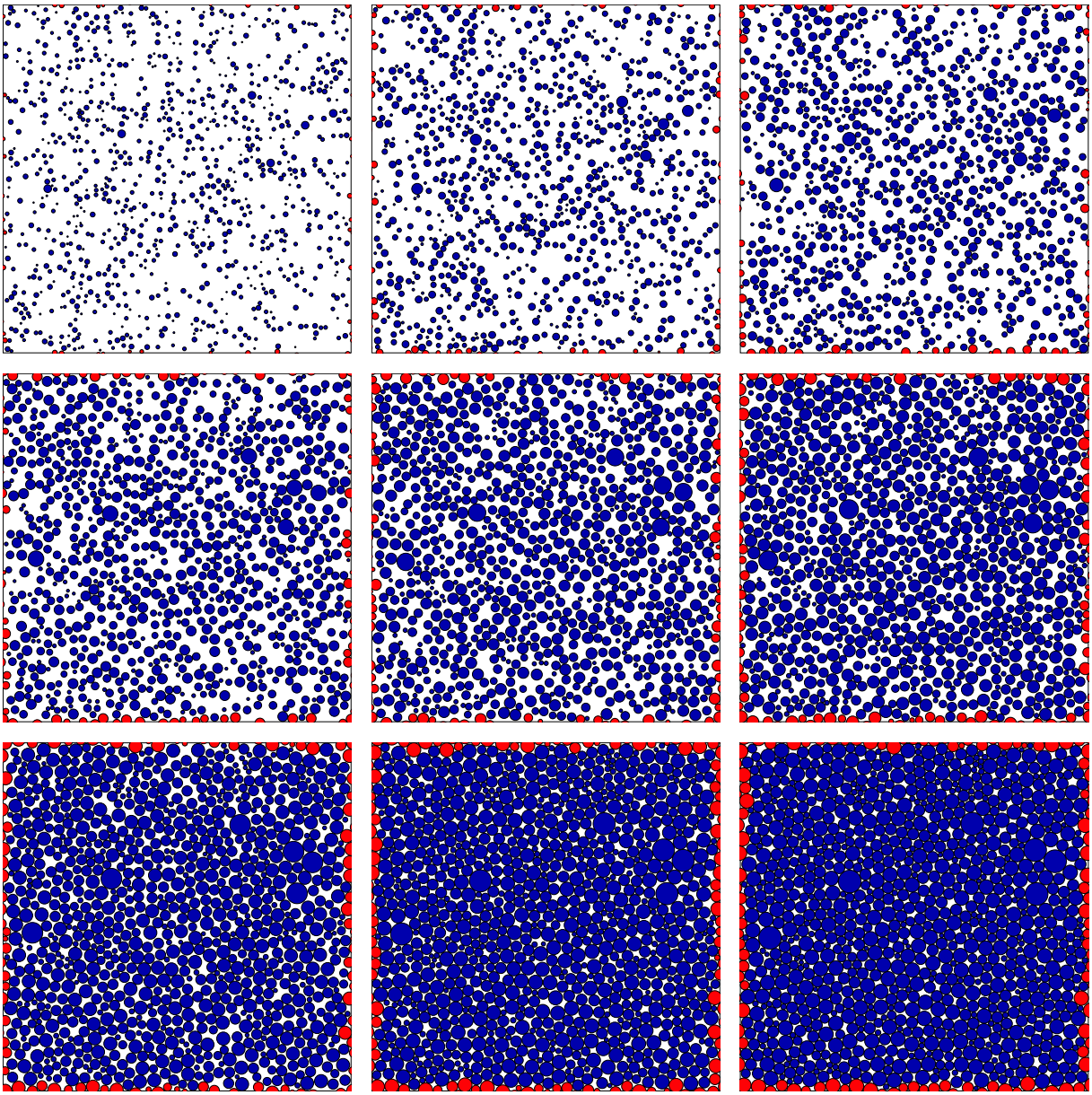

Figure 3.6.: Evolution process of a two dimensional polydisperse rve (1000 primary particles). The evolution process is initiated with values of Table 3.2. Particles inside the rve are colored in blue (dark gray), particles intersecting with the periodic boundary box are colored in red (light gray). The periodic boundary box is illustrated by a black frame. The evolution is depicted from the upper left to the lower right image. The corresponding volume fractions start with $\phi = 0.1$, advance with $\Delta\phi = 0.1$ and reach a final $\phi \approx 0.848$ in the lower right image.

arrangements. Instead, we notice a rather uniform, but irregular, distribution of the single grains, which does not allow to identify any regular patterns. The evolution of the three dimensional rve is depicted in Figure 3.8. Starting from an overall volume fraction $\phi = 0.1$ on the top left, increases in each images by $\Delta\phi = 0.1$. The lower right snap shot shows the rve possessing a volume fraction of $\phi = 0.6$. The finished result having a volume fraction of $\phi = 0.652$ is shown in in Figure 3.12. The observations, regarding the time step size as well as the volume fraction, resemble the behavior of the two dimensional rve generation.

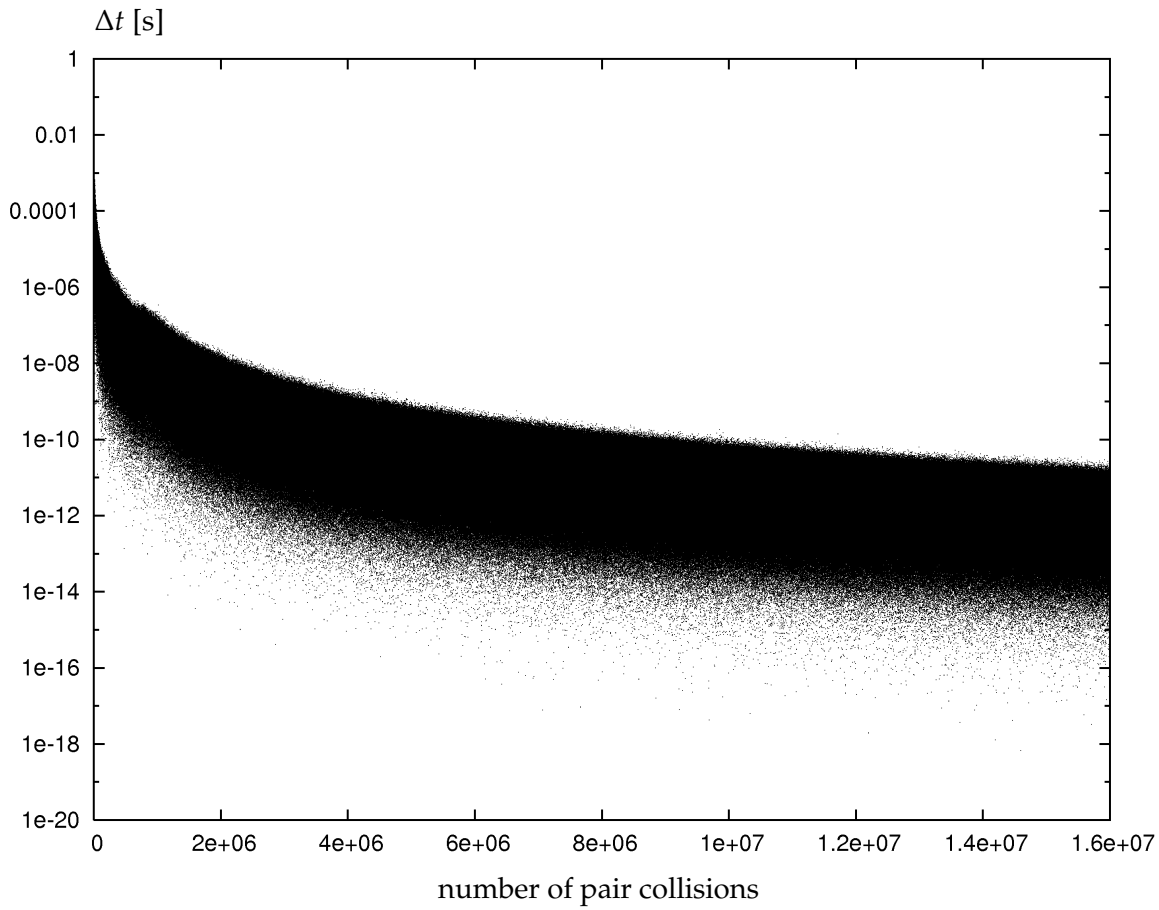

Figure 3.7.: Evolution of the time step size. Time step size over number of particle pair collisions for the two dimensional quartz sand example. Each time step size Δt is represented by a single dot

3.4.3. Grain size distribution of concrete aggregates

The second example of concrete aggregates is maybe more spectacular, since the overall particle size distribution is much more non-uniform than in the previous example. Figure 3.9, represents a concrete aggregate distribution curve taken from the German standard DIN 1045. Here we selected the coarse grained sieve curve A32, with the largest grain having a diameter of 32 mm. For practical reasons, we restricted the finest grain to have a diameter of 1 mm. Columns I and II of Table 3.3 summarize the grain diameters and their corresponding volume percentage. The particle percentage of column III is calculated with the help of equation (3.12). Again, we assume a representative number of 1000 particles and obtain the absolute number of particles for each grain size which is one-to-one related to the individual growth rates g_i, compare column IV. Figure 3.10 illustrates the generation procedure for the two dimensional concrete aggregate rve . The upper left corner corresponds to a volume fraction of $\phi = 0.1$ which increases by $\Delta\phi = 0.1$ from one image to the next. The final snap shot thus corresponds to an overall volume fraction of $\phi = 0.9$. The largest packing density, found algorithmically on the basis of the convergence criterion $\Delta\phi^{\text{crit}} = 1.0\text{E}{-}09$, was found to be slightly larger at $\phi \approx 0.914793$, see Figure 3.12. In contrast to the previous example of a rather uniform quartz sand, the aggregate size distribution in concrete is

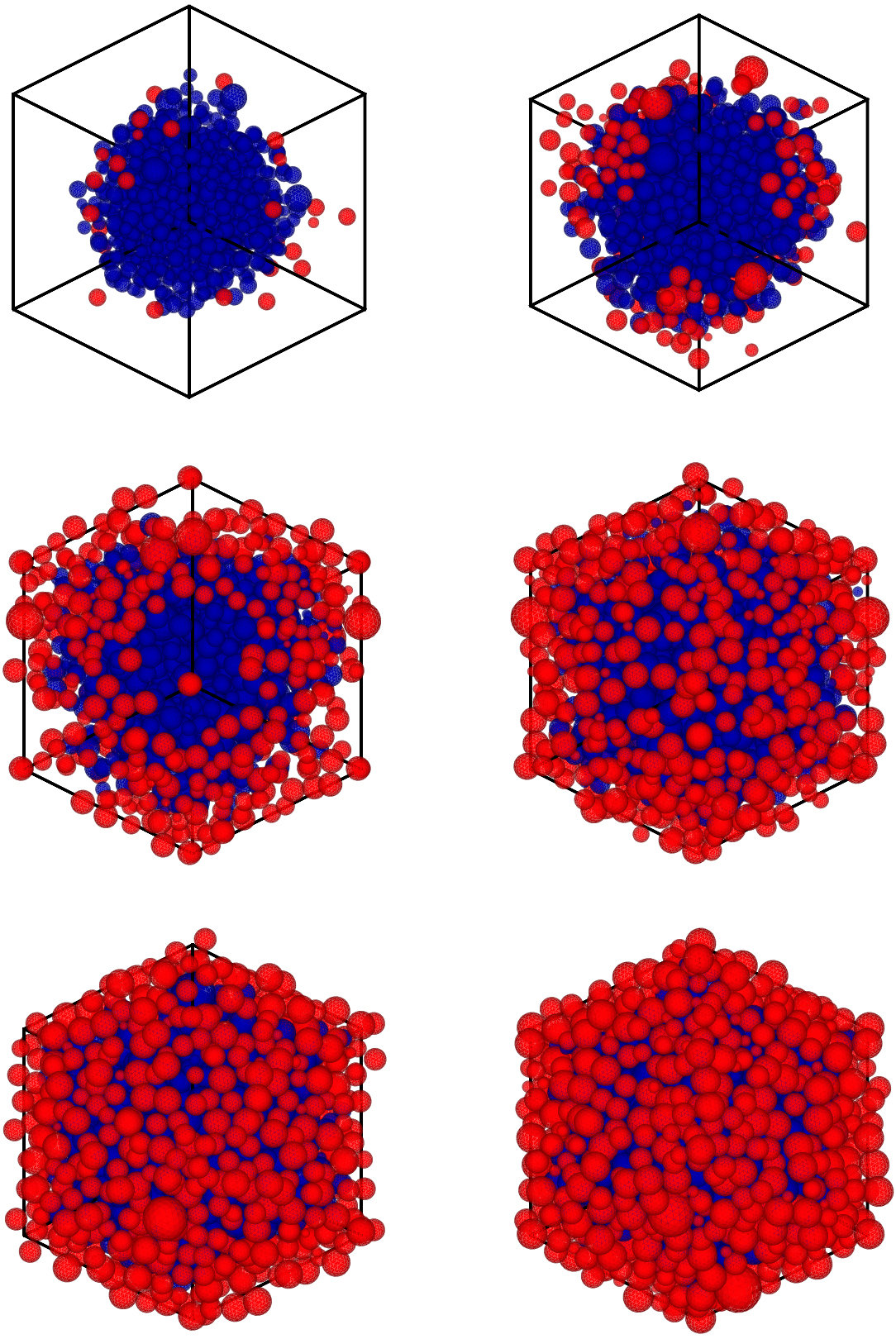

Figure 3.8.: Evolution process of a three dimensional polydisperse rve (1000 primary particles). The evolution process is started with values of Table 3.2. Particles inside the rve are colored in blue (dark gray), particles intersecting with the periodic boundary box are colored in red (light gray). The periodic boundary box is illustrated by a black frame. The evolution is depicted from the upper left to the lower right image. The corresponding volume fractions start with $\phi = 0.1$, advance with $\Delta\phi = 0.1$ and reach $\phi \approx 0.6$ in the lower right image.

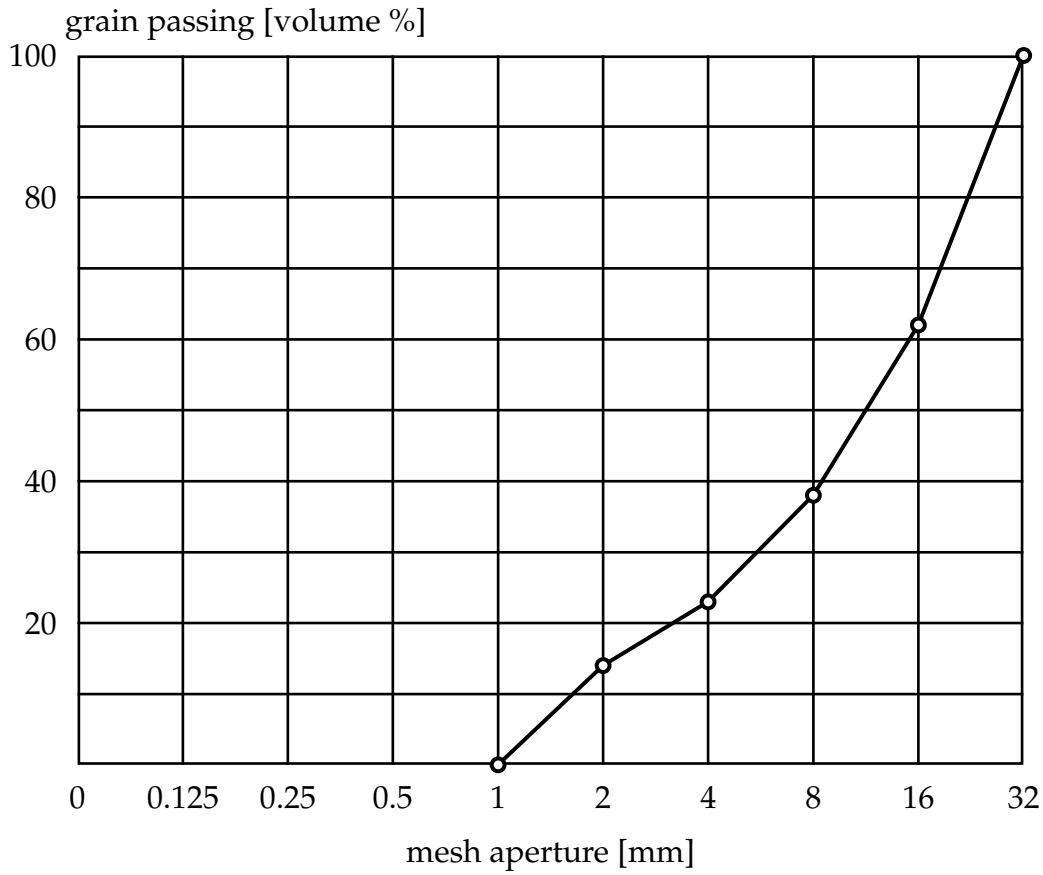

Figure 3.9.: Grain size distribution: Concrete aggregate. Grain size distributions of A32 from German standard DIN 1045. The abscissa shows the mesh aperture in [mm], whereas the ordinate reads the grain passing in volume percent.

Table 3.3.: Input parameter: Concrete aggregate example (1000 primary particles).

grain ∅ $[mm]$	volume % [%]	particle % [%]	particle [/]
32	0	0.0000	0
16	38	0.8381	8
8	24	2.1173	21
4	15	5.2933	53
2	9	12.7040	127
1	14	79.0472	791

extremely heterogeneous. It is quite obvious that this heterogeneity allows for larger packing densities which is, of course, a desired property for high performance concrete. Algorithmically, heterogeneous polydisperse packings are much more challeng-

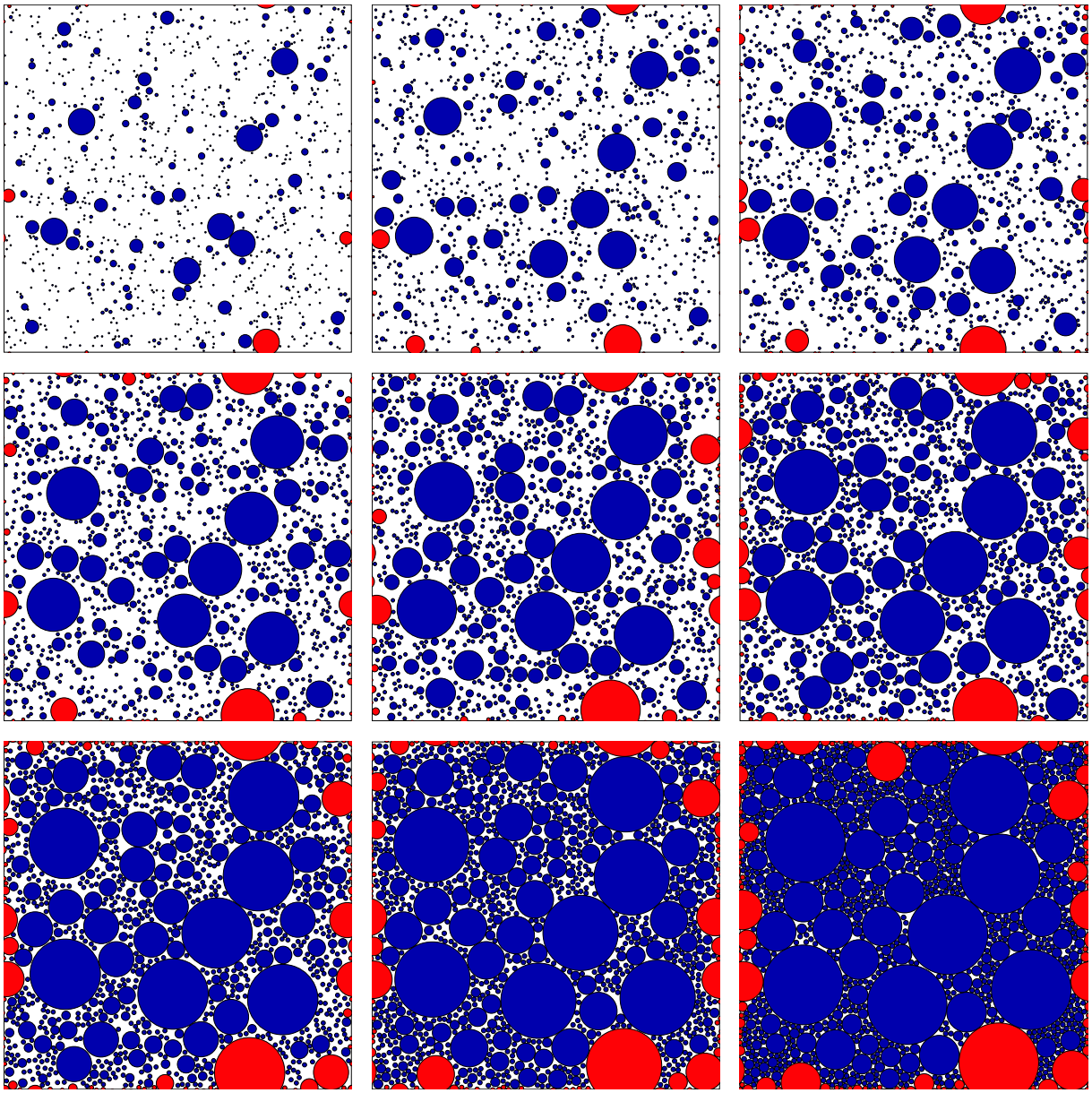

Figure 3.10.: Evolution process of a two dimensional polydisperse rve (1000 primary particles). The procedure is launched with values of Table 3.3. Particles inside the rve are colored in blue (dark gray), particles intersecting with the quadratic periodic boundary box are colored in red (light gray). The periodic boundary box is illustrated by a black frame and has dimensions 100. The evolution is depicted from the upper left to the lower right image. The corresponding volume fractions start with $\phi = 0.1$, advance with $\Delta\phi = 0.1$ and reach $\phi = 0.9$ in the lower right image. All images are cropped at the outline of the quadratic periodic boundary box. The final rve is shown in Figure 3.12 (right).

ing than almost uniform or even entirely monodisperse packings. Particle collisions are more likely to take place at the early stages of the generation process. In general, smaller time steps are needed, even at the early low density stages. Another distinguishing feature of heterogeneous polydisperse packings is their ability to pack very densely. Clustering and formation of subunits are less likely, when compared to uniform or even monodisperse packings. It is quite obvious that the time step size related to the final snap shot of Figure 3.10 at a packing density of $\phi = 0.9$ is extremely small.

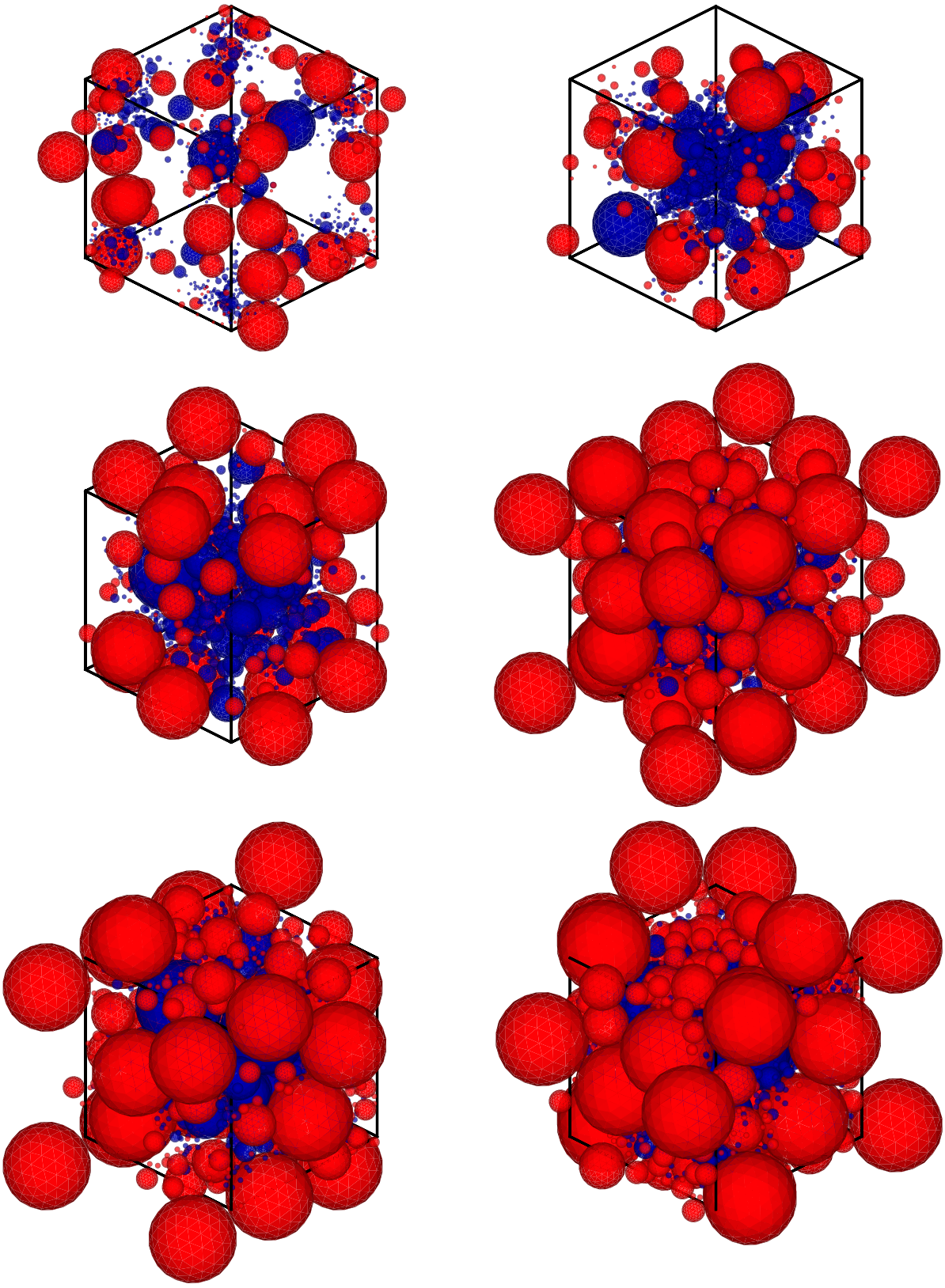

Figure 3.11.: Evolution process of a three dimensional polydisperse rve (1000 primary particles). The procedure is launched with values of Table 3.3. Particles inside the rve are colored in blue (dark gray), particles intersecting with the quadratic periodic boundary box are colored in red (light gray). The periodic boundary box is illustrated by a black frame and has dimensions 100. The evolution is depicted from the upper left to the lower right image. The corresponding volume fractions start with $\phi = 0.1$, advance with $\Delta\phi = 0.1$ and reach $\phi = 0.6$ in the lower right image.

Nevertheless, we should keep in mind that realistic aggregate volume fractions in concrete typically lie within the range of $0.65 \leq \phi \leq 0.85$ corresponding to the first and second snap shot in the lower row of fig 3.10. The final stages of the generation process, which are represented by the final snap shot, are extremely expensive from a computational point of view. The evolution process of the three dimensional concrete aggregate rve is shown in Figure 3.11. Similar to the previous examples, the images are based on a density step of $\Delta\phi = 0.1$. The resulting three dimensional concrete aggregate rve has a volume fraction of $\phi \approx 0.724$, which resembles a realistic aggregate volume fraction of concrete. The overall generation characteristics equal the two dimensional aggregate examples, i.e., collision times are smaller when compared to a more uniform grain size distribution.

3.5. Basic particle sets

To allow for the further use of the generated rves, we introduce two basic particle sets. Recall that the aggregate of all particles is denoted by $\mathscr{P}$. We define the boundary particle set $\mathscr{B}$ to include all particles which intersect with the mentioned periodic boundary box,

$$\mathscr{B} := \left\{ i \in \mathscr{P} : \overline{B}_{R_i}(\boldsymbol{x}_i) \cap \partial \text{rve} \neq \emptyset \right\}. \tag{3.14}$$

Subsequently, $\mathscr{B}$ represents the hull of the rve. The remaining particles in the inside belong to the inner particle set $\mathscr{I}$,

$$\mathscr{I} := \mathscr{P} \setminus \mathscr{B}, \tag{3.15}$$

such that: $\mathscr{I} \cap \mathscr{B} = \emptyset$. We note that all three sets are natural geometric properties of the rve, i.e., none of these sets are dependent on any kind of boundary conditions. The ultimate goal of the rve generation process is to subject the generated substructure to selected mechanical loading scenarios such as simple shear, compression or combinations thereof. The quality of the final rve thus strongly depends on a full boundary set $\mathscr{B}$. Set $\mathscr{B}$ is considered a full set, if the distance between the centers of two neighboring particles is less than the sum of their radii and the smallest particle diameter within the entire rve. The condition of a full set $\mathscr{B}$ ensures that no particles from inside can escape the boundary frame, when subjected to moderate shear or compression. Figure 3.12 depicts the full boundary sets of the final rves of the quartz sand example, left, and of the concrete aggregate example, right. In the case of a non-full boundary set $\mathscr{B}$, see for example the three dimensional packing of concrete aggregate, additional care has to be spent on ensuring that the possible outgoing particle flux is equivalent to its incoming counterpart.

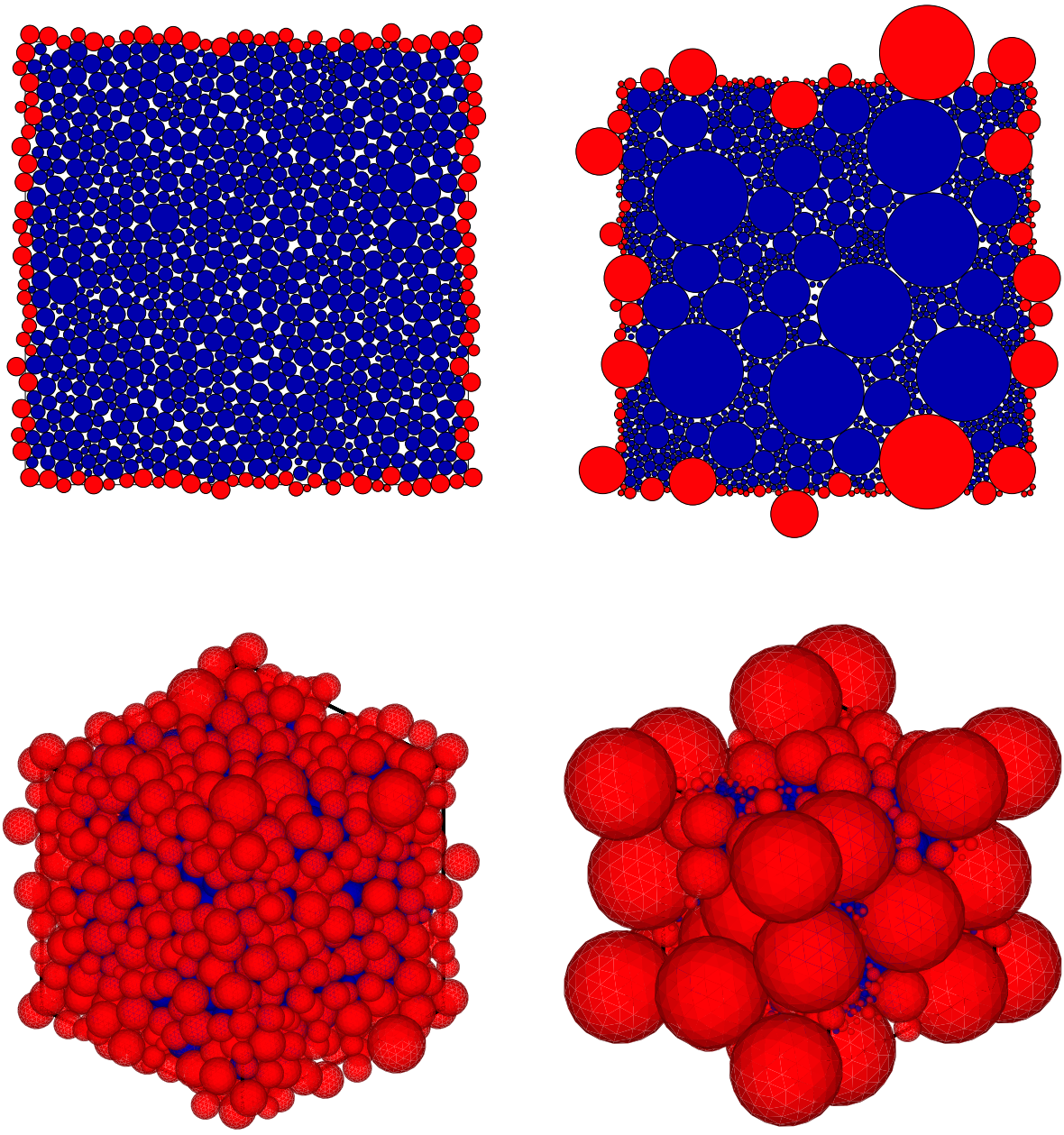

Figure 3.12.: Final rves, including 1000 primary particles. *Left*: Quartz sand. *Right*: Concrete aggregate.

4. Soft particle contact methods

4.1. Introduction

This chapter will focus on a proper description of the microscopic problem. Thereby, the attention is on the formulation of the inter-particle contact forces, the related aggregate stiffness matrix, as well as the different types of applied boundary conditions. Additionally, we provide deeper insight of an appropriate solution strategy. The most prominent tool for investigating the mechanics of granular materials is the discrete element method of CUNDALL & STRACK [27–29]. Dependent on rheological elements, this method was proposed to study the behavior of discrete particle aggregates and traces the displacements of the individual grains to find a state of quasi-static equilibrium. CUNDALL & STRACK validated their postulated numerical method by comparing their results to the experiments of DRESCHER & DE JOSSELIN DE JONG [37], as well as ODA & KONISHI [108]. These experimental analyzes of particulate media are based on metal or photo-elastic disks; a traditional way of investigating the behavior of granular aggregates, see JENKIN [62] or ROWE [125]. Each aggregate sample, used in the context of the proposed numerical treatment, is composed of a large number of individual solid objects which themselves are considered rigid. The transfer of loads between the individual grains is related to the classical interaction of normal and tangential contact forces, solely acting at the contact points. We emphasize that this particular chapter exclusively deals with smooth particles. Hence, we disregard the tangential force component. Based on assuming solely homogeneous circular particles, couples do not appear and the motion of the single grains is restricted to translation.
Next to adhesive-repulsive models for the normal contact, see for example the VAN DER WAALS forces between molecules, as well as the so-called near field forces in ZOHDI [165], solely repulsive contact forces play an important role when modeling dry particulate materials. Apart from the computationally expensive model of HERTZ which allows a very accurate definition of the normal contact forces basic force formulations are of great interest for the present approach. In this context, LUDING [77] pointed out that many microscopic details do not appear to be crucial for the description of macroscopic behaviors. Particular basic contact models define a linear contact normal force which is proportionate to the inter-particle overlap, see for example CUNDALL & STRACK [27–29], DETTMAR [33], MEIER ET AL. [82, 87, 88], MIEHE & DETTMAR [91] as well as WELLMANN, LILLIE & WRIGGERS [154]. More elaborate, but computationally costly, piecewise linear contact normal models are for example used by LUDING, HERRMAN & LÄTZEL [72], whereas non-linear contact models are proposed by VU-QUOC & ZHANG [147] or VU-QUOC, ZHANG & LESBURG [148]. While most approaches are founded on rheology, this contribution sets the focal point on a potential based formulation. In detail, we obtain the normal contact forces and the

related aggregate stiffness matrix by derivation of a postulated potential.
In the classical dem, basic geometric objects are utilized to account for the confinement of the particulate assembly, whereby confinement itself associates with a discrete border or boundary which cannot be crossed. In novel, homogenization related approaches, see, e.g., BORJA & WREN [13], KANEKO ET AL. [64] or MEIER, STEINMANN & KUHL [82, 87, 88], the aggregate is confined by a distinct selection of particles. Postulating such an innovative confinement, the microscopic problem reflects a standard boundary/initial value problem, i.e., the focus is on determining the motion of the single grains, subjected to different types of boundary conditions. While detailed information regarding the topic of boundary value problems are found in the work of EVANS [42], we focus on the proper description of discrete boundary conditions, compare COSTANZO, GRAY & ANDIA [23]. At this point, we emphasize that the accurate description, as well as application of the boundary conditions is essential for the overall homogenization procedure. In general, one can differentiate between two types of boundary conditions, the DIRICHLET and the NEUMANN boundary conditions, see BONET & WOOD [12] or MALVERN [78]. The two types of microscopic boundary conditions differ depending on the enforced macroscopic quantity, see for example MIEHE [90]. Sharing the same opinion as COSTANZO, GRAY & ANDIA, i.e., finding the NEUMANN boundary conditions to be less appealing for the problem under consideration, we restrict this research to DIRICHLET type boundary conditions. Thus, our attention is on enforcing the macroscopic deformation gradient $\overline{\boldsymbol{F}}$ on the microscopic rve. Next to various other DIRICHLET type boundary conditions, we restrict our research to the assumption of TAYLOR [137] and VOIGT [144], the restricted TAYLOR assumption as well as periodic boundary conditions. Exhaustively covered by the literature, see for example COSTANZO, GRAY & ANDIA [23], GRYTZ & MESCHKE [49], KOUZNETSOVA, GEERS & BREKELMANS [69], MIEHE [89, 90] and ZOHDI & WRIGGERS [170], the formulation of microscopic boundary conditions for the continuous case is used to derive the discrete boundary conditions for the discrete rve on the microscale level.
Furthermore, we place emphasis on proper solution algorithms of the non-linear system of equations. In the present case, the non-linear character of the equation system results from the permanent evolving inter-particle contact network, i.e., the continuous breaking and forming of individual inter-particle contacts. Obviously, considering a dis-continuous medium, changes in the contact network may lead to isolation of individual grains or grain clusters, compare BAGI [2]. This behavior as well as highly complex stability issues of the overall aggregate, see for example MIEHE & DETTMAR [91] or SCHRÖDER [128], do not allow the application of standard solving procedures, as e.g., the classical NEWTON-RAPHSON scheme. Nevertheless, there exist static based methods to solve such non-linear equations. One possibility consists of applying complicated solution strategies as proposed by BAGI [2] and KISHINO [67], which are capable of handling topology changes and singularities. While the algorithm of BAGI displaces all grains at the same time, the static algorithm introduced by KISHINO is based on a sequential displacement of individual grains. Hence, a slower convergence is expected. Both algorithms depend on the assembling of stiffness matrices, whereby the algorithm of BAGI uses a global and the algorithm of KISHINO solely local aggregate matrix. Obviously, the computation, assembly as well as the solution of these systems

is computationally expensive, and, in contrast to the standard NEWTON-RAPHSON procedure, do not guarantee a quadratic convergence towards the solution.
Another alternative is found in utilizing explicit vector iteration methods which basically replace the commonly used implicit solution schemes. In general, these methods do not require the inversion of a local or global stiffness matrix. A particular choice is the dynamic relaxation method. This specific method is based on the second-order RICHARDSON scheme, see RICHARDSON [122], which, compare OTTER [112], conforms to the classical shape of simultaneous accelerated relaxation schemes. An excellent review of this method is found in UNDERWOOD [143], while further improvements regarding the adaptive dynamic relaxation scheme are published in PAPADRAKAKIS [114]. Problem specific improvements of the standard dynamic and adaptive dynamic relaxation procedure are found in the contributions of BARDET & PROUBET [7], MUNJIZA, OWEN & CROOK [100], PAN, METZGER & NIEWCZAS [113], ŘEŘICHA [145], as well as in SAUVÉ & METZGER [126]. As presented by OAKLEY & KNIGHT [104–107], the method under consideration is very competitive for large structures and highly non-linear problems, including instabilities. In the case of the dynamic relaxation method, the static system of equations is converted to a dynamic problem including mass proportional damping. While the transient solution is not of interest, the artificial mass and damping terms are adjusted to allow fast convergence towards the desired static solution. The assumption of artificial components is justified by the disappearance of the damping and inertia forces at the point of static equilibrium. Even though explicit integration methods require a small pseudo time step to guarantee the stability of the overall algorithm, their vector character allows to perform a high number of iterations in a minimum amount of time. Recently, by comparing the well-known preconditioned conjugate gradient method to a special central difference time integration scheme for damped dynamic systems, FENG [43] related the conjugate gradient method to the dynamic relaxation method. Thereby, the preconditioning matrix relates to the mass matrix and the search direction is closely related to the velocities. An additional advantage of the general vector iteration method relies on its parallelization potential, see OAKLEY & KNIGHT [106, 107]. In the present case, parallelization was solely applied to the particle force calculation.

4.2. A discrete element method

4.2.1. Contact normal potential

In the following, we dedicate ourselves to a penalty type contact approach. This concept allows the postulation of a contact potential, which is based on the particle overlap. In contrast to the hard contact approach, used for the generation of the microscopic rves, the present dem requires the allowance of a small inter-particle overlap. Thereby, we assume that the overlap itself is small when compared to the particle radii, $\varepsilon_{ij} \ll r_i$, see Figure 4.1. We consider two circular and homogeneous grains i and j, having radii r_i and r_j, see Figure 4.1 (center). The contact specific overlap ε_{ij}, depicted on the right side of Figure 4.1, is defined by subtracting the distance of the particle centers from the

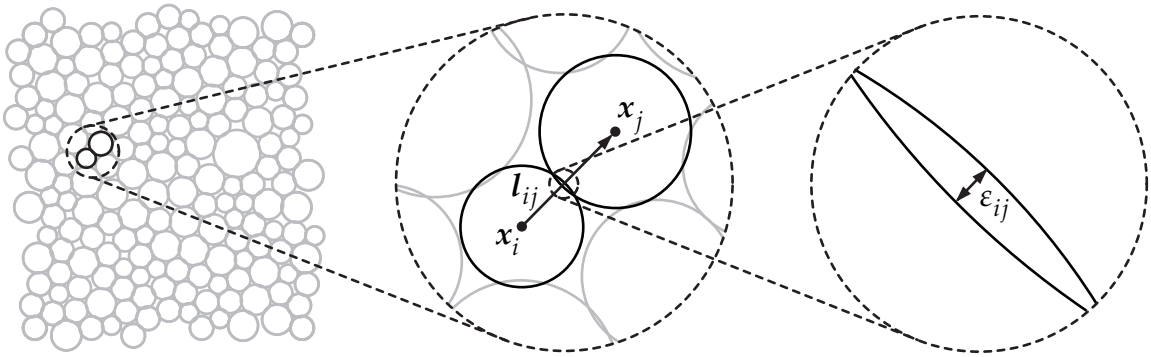

Figure 4.1.: Inter-particle contact. *Left*: Overall particle arrangement. Two grains are selected, marked in black. *Center*: Zoom in on the region of the selected grains. *Right*: Zoom in on the contact region.

sum of the particle radii,

$$\varepsilon_{ij} = r_i + r_j - \left|\left| \boldsymbol{l}_{ij} \right|\right| . \tag{4.1}$$

Therein, the so-called branch vector, defined in (3.4), connects the particle centers, see Figure 4.1 (center). Recall that the index order indicates the direction of the branch vector, i.e., the branch vector in (4.1) points from the center of particle i to the center of particle j. Its length equates the distance between the particle centers. Inspecting (4.1) leads to the observation that the particles i and j are only in contact for $\varepsilon_{ij} \geq 0$. For $\varepsilon_{ij} < 0$ we find the particles separated.

$$\text{particle pair } ij = \begin{cases} \text{separated}, & \text{if} \quad \varepsilon_{ij} < 0 \\ \text{in contact}, & \text{if} \quad \varepsilon_{ij} \geq 0 \end{cases} \tag{4.2}$$

Thus, (4.1) does not solely serve as a measurement of penetration, but also as an implicit contact check, see MIEHE & DETTMAR [91]. As contact potential for the normal direction, we postulate a one-sided harmonic pair potential,

$$\Phi_{\mathrm{n}ij} = \frac{E_{\mathrm{n}ij}}{2} \mathscr{H}\Big(\varepsilon_{ij}\Big) \Big[\varepsilon_{ij}\Big]^2 , \tag{4.3}$$

compare Figure 4.2 (left). However, any reasonable one-sided potential may be appropriate. The potential in (4.3) depends on the previously introduced particle overlap ε_{ij}. The constant $E_{\mathrm{n}ij}$ represents the contact normal stiffness between the contacting grains. The one-sided harmonic nature of (4.3) is based on the inclusion of the HEAVISIDE function, denoted by $\mathscr{H}$. Its insertion allows a comfortable and efficient recognition of forming and breaking of inter-particle contacts. The normal contact potential solely produces an output if the particles i and j are in contact: For ε_{ij} less than zero, i.e., the distance between the grains is larger than the sum of the particle radii, compare (4.2), the HEAVISIDE function causes the potential function to output a value of zero. With an overlap greater than or equal to zero the HEAVISIDE function responds with a value

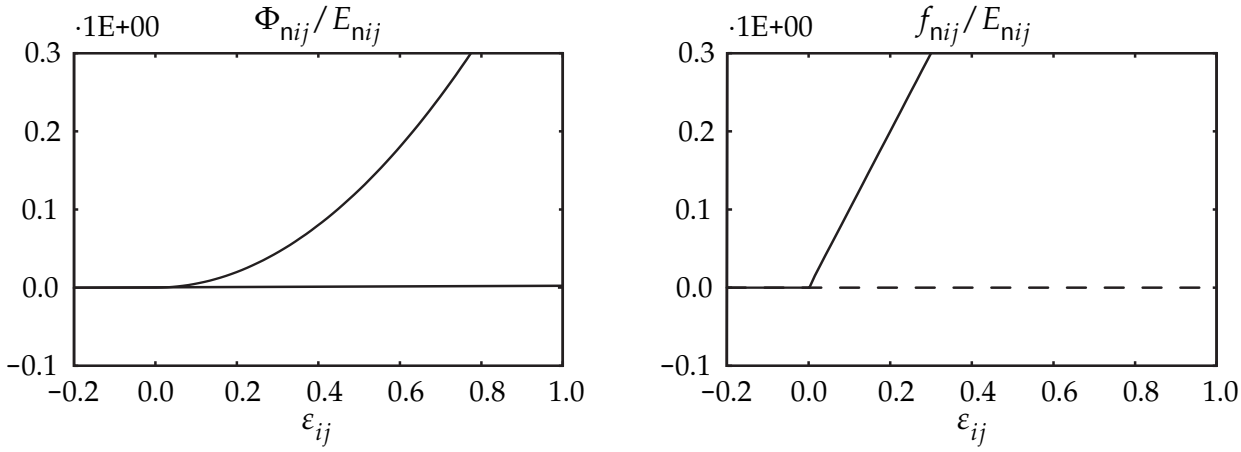

Figure 4.2.: *Left*: One-sided harmonic potential over the particle overlap. *Right*: Inter-particle contact force versus the overlap.

of one. Consequently, the contact potential produces a value greater than or equal to zero.

$$\mathscr{H}\Big(\varepsilon_{ij}\Big) = \begin{cases} 0, & \text{if} \quad \varepsilon_{ij} < 0 \\ 1, & \text{if} \quad \varepsilon_{ij} \geq 0 \end{cases} \tag{4.4}$$

Excluding the HEAVISIDE function, (4.3) transforms to a standard harmonic potential. This modification allows for attraction between the individual grains. The resulting system might be compared to a discrete mass-spring assembly or to a framework structure, see HRENNIKOFF [61]. In the case of a framework structure, the interaction network (connectivity), may be prescribed *ab initio*. Note that in the present case, contact breaking as well as forming are considered to be important features of particulate material, thus are included in our approach. Having introduced the normal contact potential for a single contact, the total normal contact energy of a single grain results from the summation over all particles in the discrete granular system,

$$\Phi_{ni} = \sum_{\substack{j \in \mathscr{P} \\ j \neq i}} \Phi_{nij} = \frac{1}{2} \sum_{\substack{j \in \mathscr{P} \\ j \neq i}} E_{nij} \mathscr{H}\Big(\varepsilon_{ij}\Big) \Big[\varepsilon_{ij}\Big]^2 . \tag{4.5}$$

Repeating the summation over all granules yields the total normal contact energy of the aggregate,

$$\Phi_{n} = \frac{1}{2} \sum_{i \in \mathscr{P}} \Phi_{ni} = \frac{1}{2} \sum_{i \in \mathscr{P}} \sum_{\substack{j \in \mathscr{P} \\ j \neq i}} \Phi_{nij} = \frac{1}{4} \sum_{i \in \mathscr{P}} \sum_{\substack{j \in \mathscr{P} \\ j \neq i}} E_{nij} \mathscr{H}\Big(\varepsilon_{ij}\Big) \Big[\varepsilon_{ij}\Big]^2 . \tag{4.6}$$

Remark 4.1 (Summation range) Based on the repeated summation over all particles in the discrete system, the result in (4.6) includes a multiplication with a factor of one half. This operation takes care of the double consideration of each contact. A possibility to

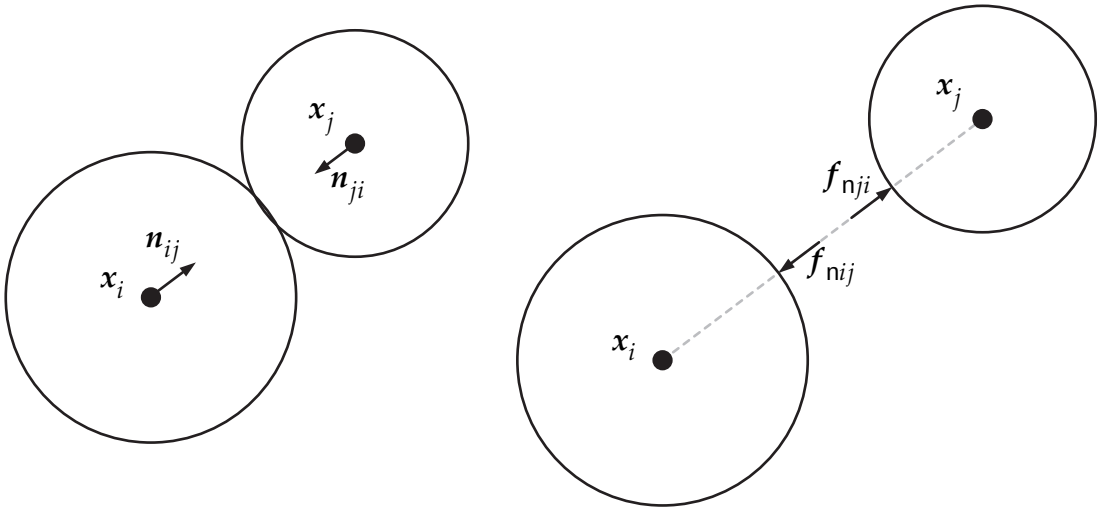

Figure 4.3.: Inter-particle contact force. *Left*: Two grains in contact. *Right*: Depiction of the particle contact forces. The dashed line shows the line of action of the particle contact forces.

circumvent the double consideration of each contact consists of a reformulation of the summation ranges,

$$\Phi_{\mathrm{n}} = \frac{1}{2} \sum_{i=1}^{\#\mathscr{P}-1} \sum_{j=i+1}^{\#\mathscr{P}} E_{\mathrm{n}ij} \mathscr{H}\Big(\varepsilon_{ij}\Big) \Big[\varepsilon_{ij}\Big]^2. \tag{4.7}$$

Nevertheless, due to practical reasons and the legibility, we favor the formulation in (4.6). ■

4.2.2. Contact normal force

The contact normal force, resulting from a single contact between two particles, equals the negative derivative of the normal contact potential with respect to the particle position,

$$\boldsymbol{f}_{\mathrm{n}ij} = -\frac{\partial \Phi_{\mathrm{n}ij}}{\partial \boldsymbol{x}_i} = -E_{\mathrm{n}ij} \mathscr{H}\Big(\varepsilon_{ij}\Big)\, \varepsilon_{ij} \boldsymbol{n}_{ij}. \tag{4.8}$$

A representation of the inter-particle contact force is depicted in Figure 4.3 (right). Obviously, based on the selected one-sided harmonic pair potential, the resulting contact force is linear dependent on the inter-particle overlap. The magnitude of the contact normal force is defined by $f_{\mathrm{n}ij} = E_{\mathrm{n}ij} \mathscr{H}\Big(\varepsilon_{ij}\Big)\, \varepsilon_{ij}$. Its direction is given by the negative contact normal $\boldsymbol{n}_{ji} = -\boldsymbol{n}_{ij} = -\boldsymbol{l}_{ij} / \Big|\Big| \boldsymbol{l}_{ij} \Big|\Big|$, see Figure 4.3 (left). The point of origin is the contact point, see Figure 4.3 (right). However, the rigidity of the grains allows the contact force to translate on its line of action. Based on the restriction to circular and homogeneous particles, the obtained contact normal forces do not enforce particle ro-

tations. N.B. the reciprocal character of the corresponding contact forces, which itself is related to NEWTON's third axiom (compare cover),

$$f_{\mathsf{n}ij} = -f_{\mathsf{n}ji}. \tag{4.9}$$

The total particle force of a single grain trivially defines by summing over all relevant particle contact forces:

$$f_{\mathsf{n}i} = \sum_{\substack{j\in\mathscr{P}\\ j\neq i}} f_{\mathsf{n}ij}. \tag{4.10}$$

The point of origin of the particle force is the center of mass. The particle force is considered to be a quantity of particular importance, being the main driving quantity of the particulate system. We remark that the definition in (4.10) is also obtained by taking the derivative of (4.5) with respect to the current particle position.

4.2.3. Aggregate normal stiffness

The global aggregate matrix $\boldsymbol{K}_{\mathsf{n}}$ concerning the normal contacts is constructed in a straightforward manner. Similar to the standard fem, compare BELYTSCHKO, LIU & MORAN [8] or WRIGGERS [160], the normal aggregate stiffness equals the derivative of the internal forces with respect to the current particle positions. Therefore, with $\partial\Phi/\partial\boldsymbol{x}_i$ representing the internal forces, the global normal aggregate stiffness matrix is constructed by taking the second derivative of the normal potential function, given in (4.6), with respect to the individual current particle positions. Note, each entry of the global aggregate stiffness matrix is computed directly, i.e., no additional assembling procedures are necessary.

$$\boldsymbol{K}_{\mathsf{n}} = \begin{bmatrix} \boldsymbol{k}_{\mathsf{n}11} & \cdots & \boldsymbol{k}_{\mathsf{n}1\#\mathscr{P}} \\ \vdots & \ddots & \vdots \\ \boldsymbol{k}_{\mathsf{n}\#\mathscr{P}1} & \cdots & \boldsymbol{k}_{\mathsf{n}\#\mathscr{P}\#\mathscr{P}} \end{bmatrix} \quad \text{with} \quad \boldsymbol{k}_{\mathsf{n}mn} = \frac{\partial^2\Phi_{\mathsf{n}}}{\partial\boldsymbol{x}_m\otimes\partial\boldsymbol{x}_n}. \tag{4.11}$$

The dimensions of the derived global aggregate stiffness matrix relate to the number of particles in the rve. Hence, for a two dimensional system, the aggregate stiffness matrix is of size $[2\#\mathscr{P}\times 2\#\mathscr{P}]$. The entries of $(4.11)_1$ compute to:

$$\frac{\partial^2\Phi_{\mathsf{n}}}{\partial\boldsymbol{x}_m\otimes\partial\boldsymbol{x}_n} = \begin{cases} \dfrac{E_{\mathsf{n}mn}\mathscr{H}(\varepsilon_{mn})}{||\boldsymbol{l}_{mn}||}\left[\varepsilon_{mn}\mathbf{1} - [r_m+r_n]\,\boldsymbol{n}_{mn}\otimes\boldsymbol{n}_{mn}\right] & \text{if} \quad m\neq n \\ -\displaystyle\sum_{\substack{i\in\mathscr{P}\\ i\neq m}} \dfrac{E_{\mathsf{n}im}\mathscr{H}(\varepsilon_{im})}{||\boldsymbol{l}_{mi}||}\left[\varepsilon_{mi}\mathbf{1} - [r_m+r_i]\,\boldsymbol{n}_{mi}\otimes\boldsymbol{n}_{mi}\right] & \text{if} \quad m=n \end{cases} \tag{4.12}$$

Based on the used tensor operations, one is able to notice that both terms of (4.12) are symmetric. Recognizing that interchanging the indices of the expressions in (4.12)

does not alter their results, yields knowledge of the symmetry of the global aggregate matrix. The operation of interchanging the indices relates to the rule of SCHWARZ, i.e., the interchange of the derivation order,

$$\frac{\partial^2 \Phi_{\mathsf{n}}}{\partial \boldsymbol{x}_m \otimes \partial \boldsymbol{x}_n} = \frac{\partial^2 \Phi_{\mathsf{n}}}{\partial \boldsymbol{x}_n \otimes \partial \boldsymbol{x}_m}. \tag{4.13}$$

We witness that the diagonal terms equal the negative sum over the related off-diagonal terms. Hence, $(4.12)_2$ may be constructed by using $(4.12)_1$, i.e.,

$$\frac{\partial^2 \Phi_{\mathsf{n}}}{\partial \boldsymbol{x}_m \otimes \partial \boldsymbol{x}_m} = - \sum_{\substack{m \in \mathscr{P} \\ i \neq m}} \frac{\partial^2 \Phi_{\mathsf{n}}}{\partial \boldsymbol{x}_m \otimes \partial \boldsymbol{x}_i}. \tag{4.14}$$

This result is of particular importance since it guarantees a zero energy production under a prescribed rigid body motion. Furthermore, considering (4.13) as well as (4.14) reduces the computational costs drastically. Known from the classical structural mechanics, $\boldsymbol{K}_{\mathsf{n}}$ and thus (4.12) can be additively decomposed in a solely material as well as geometric part. The geometric part, denoted by geo, relates to the linearization of the non-linear finite particle kinematics. The material part, denoted by mat, deduces from the linearization of the non-linear constitutive equation. In virtue of the relations between $(4.11)_1$, $(4.11)_2$, $(4.12)_1$ and $(4.12)_2$, it is sufficient to perform the decomposition for the case $m \neq n$.

$$\left\{ \frac{\partial^2 \Phi_{\mathsf{n}}}{\partial \boldsymbol{x}_m \otimes \partial \boldsymbol{x}_n} \right\}_{\mathsf{geo}} = \frac{E_{\mathsf{n}mn} \mathscr{H}(\varepsilon_{mn})}{||\boldsymbol{l}_{mn}||} \varepsilon_{mn} \mathbf{1} \tag{4.15}$$

$$\left\{ \frac{\partial^2 \Phi_{\mathsf{n}}}{\partial \boldsymbol{x}_m \otimes \partial \boldsymbol{x}_n} \right\}_{\mathsf{mat}} = - \frac{E_{\mathsf{n}mn} \mathscr{H}(\varepsilon_{mn})}{||\boldsymbol{l}_{mn}||} \left[r_m + r_n \right] \boldsymbol{n}_{mn} \otimes \boldsymbol{n}_{mn} \tag{4.16}$$

Remark 4.2 (Small deformations) Restricting the focus on small deformations with the presumption of the initial particle overlap being equal to zero, the geometric part of the aggregate stiffness matrix vanishes. Hence, for the geometric linear case, the aggregate stiffness matrix solely relies on (4.16). ■

4.3. Boundary conditions

4.3.1. The overall continuous case

As remarked by KOUZNETSOVA, GEERS & BREKELMANS [69], numerical homogenization schemes rely on the *a priori* assumption of the scale transition, i.e., the PIOLA stress as well as the deformation gradient on the macroscale are assumed to be equivalent to

their volume average microscopic counterparts,

$$\overline{\boldsymbol{F}} = \frac{1}{V_{\mathsf{rve}}} \int_{\Omega} \boldsymbol{F} \mathrm{d}V \qquad \text{and} \qquad \overline{\boldsymbol{P}} = \frac{1}{V_{\mathsf{rve}}} \int_{\Omega} \boldsymbol{P} \mathrm{d}V. \tag{4.17}$$

As pointed out in the latter, our focus is on enforcing $(4.17)_1$ on the microscale level. We devote ourselves to the three most prominent DIRICHLET boundary conditions. These consists of the assumption of TAYLOR [137], the thereof derived restricted TAYLOR assumption, also known as displacement boundary conditions [69], and the periodic boundary condition. In general, each material point on the microscale is assumed to map according to,

$$\boldsymbol{x} = \overline{\boldsymbol{F}} \bullet [\boldsymbol{X} + \boldsymbol{\Xi}]. \tag{4.18}$$

Equation (4.18) includes a homogeneous part as well as a superimposed fluctuational part. The homogeneous share of deformation relates to the linear mapping of the microscopic material position, denoted by $\boldsymbol{X}$. We chose to define the superimposed fluctuations $\boldsymbol{\Xi}$ in the material configuration, guaranteeing an *a priori* invariance in regards to rigid body rotations. Further details are found in COUSINS [25, 26] and MARTIN [79–81]. Please note that the superimposed individual fluctuations themselves depend on the macroscopic deformation gradient as well, i.e., $\boldsymbol{\Xi} = \boldsymbol{\Xi}\left(\overline{\boldsymbol{F}}\right)$. Taking the derivative of (4.18) with respect to the material position $\boldsymbol{X}$, as well as inserting the result in $(4.17)_1$ yields,

$$\overline{\boldsymbol{F}} = \overline{\boldsymbol{F}} + \frac{1}{V_{\mathsf{rve}}} \int_{\Omega} \overline{\boldsymbol{F}} \bullet \frac{\partial \boldsymbol{\Xi}}{\partial \boldsymbol{X}} \mathrm{d}V. \tag{4.19}$$

While the first part of (4.19) fulfills the scale transition, the second part of (4.19) is required to vanish,

$$\int_{\Omega} \frac{\partial \boldsymbol{\Xi}}{\partial \boldsymbol{X}} \mathrm{d}V = \boldsymbol{0}. \tag{4.20}$$

Using the divergence theorem as well as requiring quasi-static equilibrium, (4.20) is rewritten to the boundary of the rve,

$$\int_{\partial\Omega} \boldsymbol{\Xi} \otimes \boldsymbol{N} \mathrm{d}A = \boldsymbol{0}, \tag{4.21}$$

The outward unit normal vector on the boundary of the reference configuration is denoted by $\boldsymbol{N}$. Equation (4.20) as well as (4.21) are considered as necessary conditions to fulfill the proposed scale transition. The demands stated in (4.20) as well as (4.21) are fulfilled by appropriate boundary conditions on the microscale. Next to numerous possible others, see COSTANZO, GRAY & ANDIA [23], we restrict this contribution by focusing on the three previously named boundary conditions.

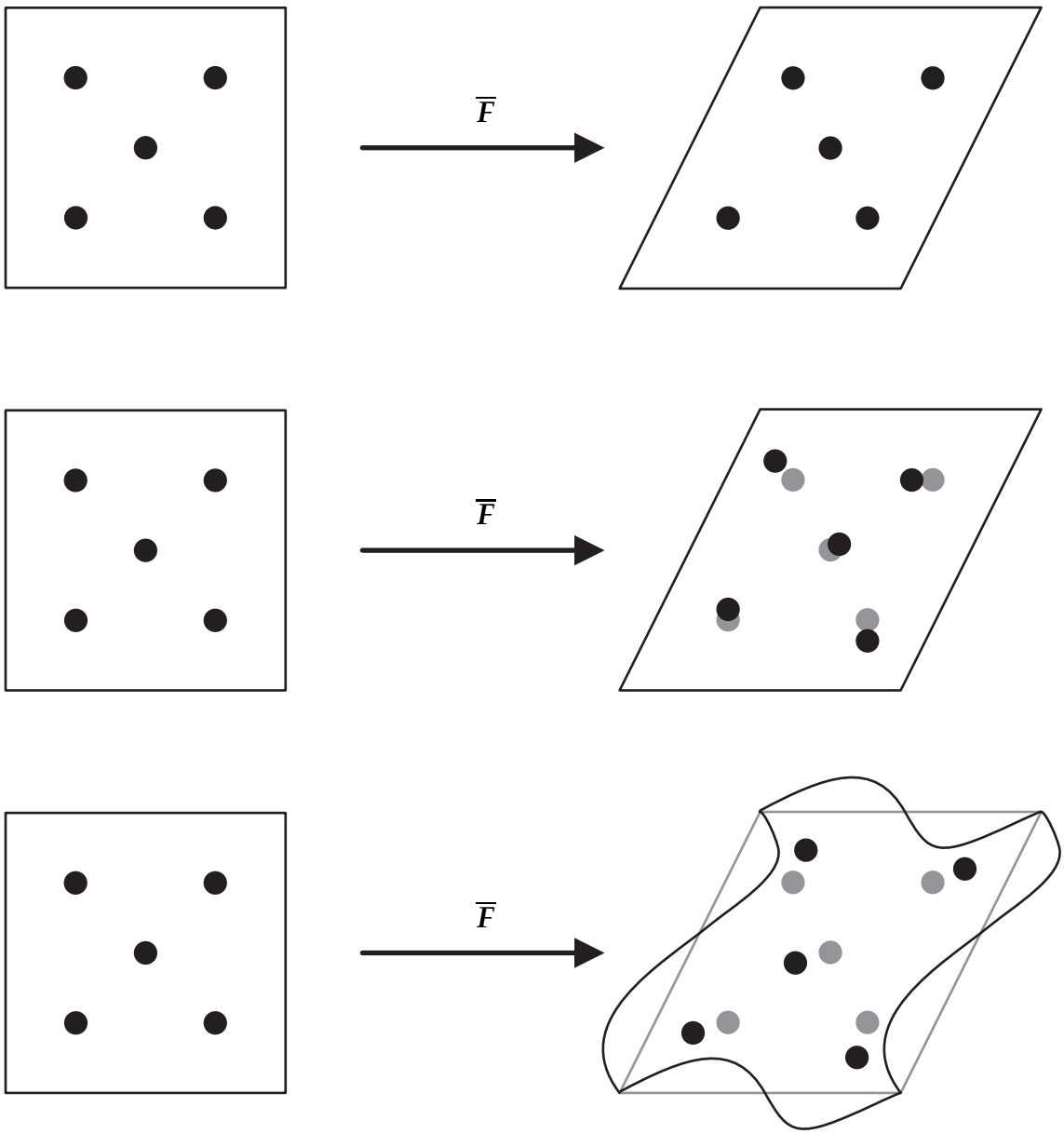

Figure 4.4.: Comparison of different microscopic boundary conditions: Continuous case. *Top*: Assumption of Taylor. Each point in the microscopic rve deforms homogeneously. *Center*: Restricted Taylor assumption. The boundary of the rve deforms homogeneously, while the bulk is free to deform. *Bottom*: Periodic boundary condition. The four corners map homogeneously. The boundary of the rve deforms periodically while the bulk deforms freely.

4.3.2. Assumption of Taylor

TAYLOR [137] and VOIGT [144] assumed that if a point on the macroscopic scale is deformed by a macroscopic deformation gradient $\overline{\boldsymbol{F}}$, the microstructure connected to this material point deforms homogeneously with the same deformation gradient, i.e., we assume $\boldsymbol{F} = \overline{\boldsymbol{F}}$ over the whole microstructure. By inserting this assumption in

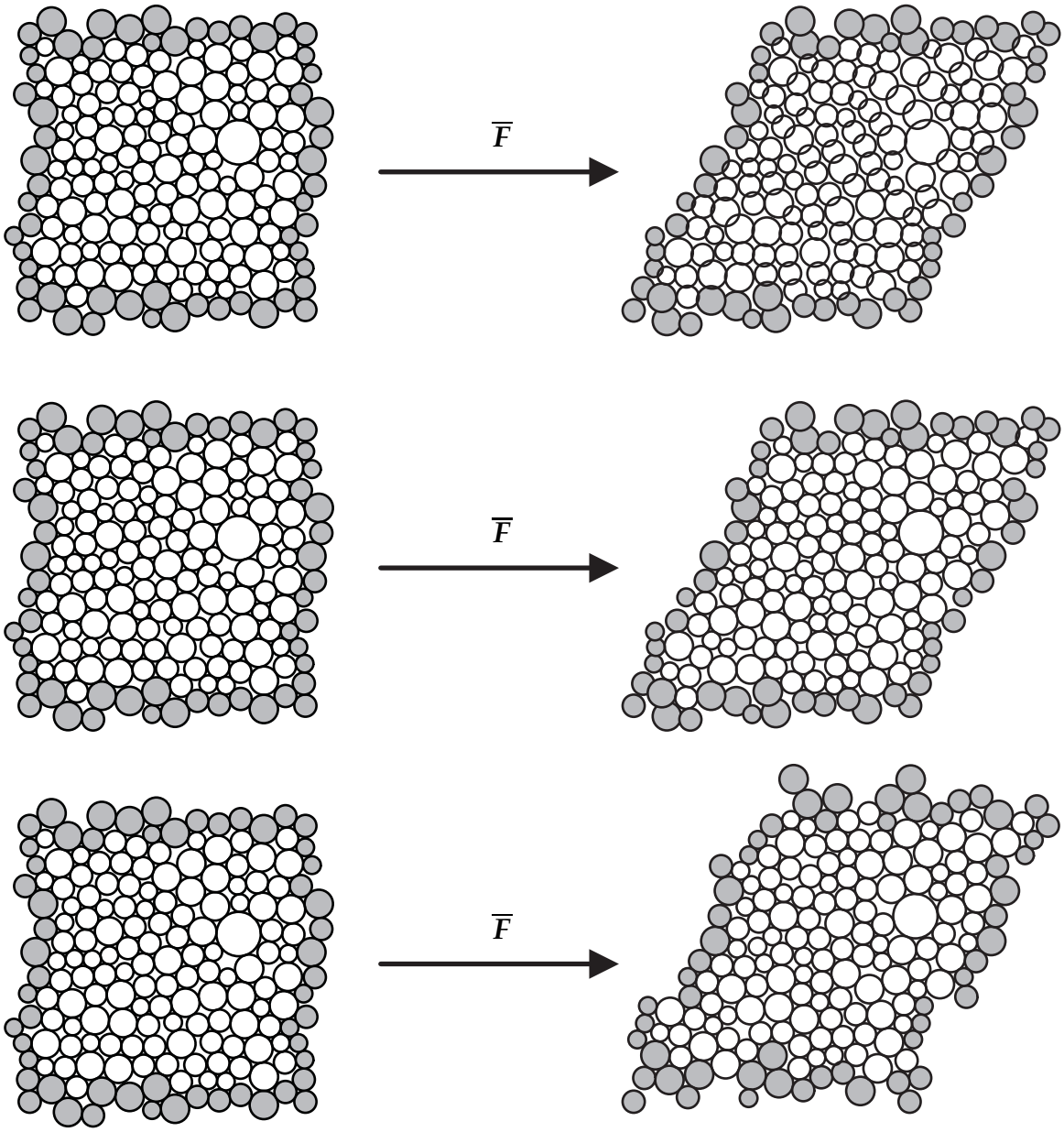

Figure 4.5.: Comparison of different microscopic boundary conditions: Discrete case. *Top*: Assumption of Taylor. Each point in the microscopic rve deforms homogeneously. *Center*: Restricted Taylor assumption. The boundary of the rve deforms homogeneously, while the bulk is free to deform. *Bottom*: Periodic boundary condition. The four corners map homogeneously. The boundary of the rve deforms periodically while the bulk deforms freely.

$(4.17)_1$, the proposed scale transition of the deformation gradient is fulfilled,

$$\overline{\boldsymbol{F}} = \frac{1}{V_{\text{rve}}} \int_{\Omega} \boldsymbol{F} \mathrm{d}V = \frac{1}{V_{\text{rve}}} \int_{\Omega} \overline{\boldsymbol{F}} \mathrm{d}V = \overline{\boldsymbol{F}}. \tag{4.22}$$

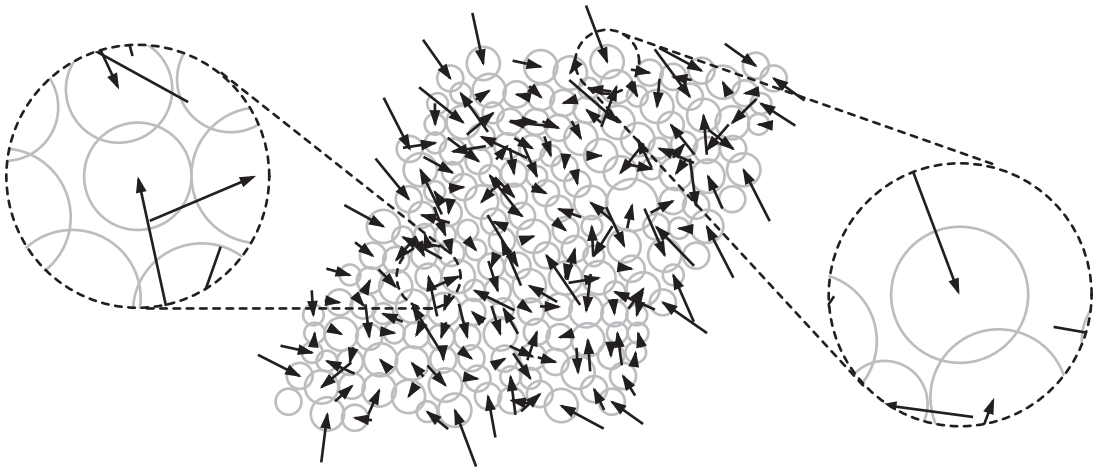

Figure 4.6.: Particle reaction forces: Assumption of TAYLOR. The particle reaction forces are depicted in black. A zoom in on the boundary as well as on the bulk is granted. Please observe the overall presence of particle reaction forces.

Each point in the continuous microstructure deforms linearly, solely dependent on the macroscopic deformation gradient,

$$\boldsymbol{x} = \overline{\boldsymbol{F}} \bullet \boldsymbol{X}, \qquad \forall \boldsymbol{X} \in \Omega. \tag{4.23}$$

Individual microscopic fluctuations stay unconsidered, see Figure 4.4 (top). The assumption of an overall homogeneous deformation field is directly related to the 1st CAUCHY-BORN rule, see BORN [14] and CAUCHY [17,18], used in the context of molecular dynamics. We emphasize that prescribing each spatial position of a general rve is kinematically non-admissible and may lead to an unbalanced force field over the whole rve, see LARSSON & RUNESSON [71]. For the present discrete approach, we adopt the assumption of TAYLOR, letting the macroscopic deformation gradient map each grain in a homogeneous manner,

$$\boldsymbol{x}_i = \overline{\boldsymbol{F}} \bullet \boldsymbol{X}_i, \qquad \forall i \in \mathscr{P}, \tag{4.24}$$

The homogeneous mapping of the grains is depicted in Figure 4.5 (top). Similar as in the continuous case, prescribing the spatial positions for all particles is kinematically non-admissible. The resulting reaction forces, i.e, $\boldsymbol{r}_i = -\boldsymbol{f}_i$, act on the centers of the prescribed grains, see Figure 4.6. One notices the non-zero particle reaction forces on the boundary as well as on the interior particles. However, we remark that the global equilibrium, i.e., $\sum_{i \in \mathscr{P}} \boldsymbol{f}_i = \boldsymbol{0}$ is fulfilled.

Remark 4.3 (Computational implementation of the Taylor assumption) While the numerical implementation of this boundary conditions is straightforward, we note some important facts regarding the storage of microstructural variables. In the case of the TAYLOR assumption, the microstructure itself does not evolve. Deformation states can be reproduced by simply mapping the material particle positions by the appro-

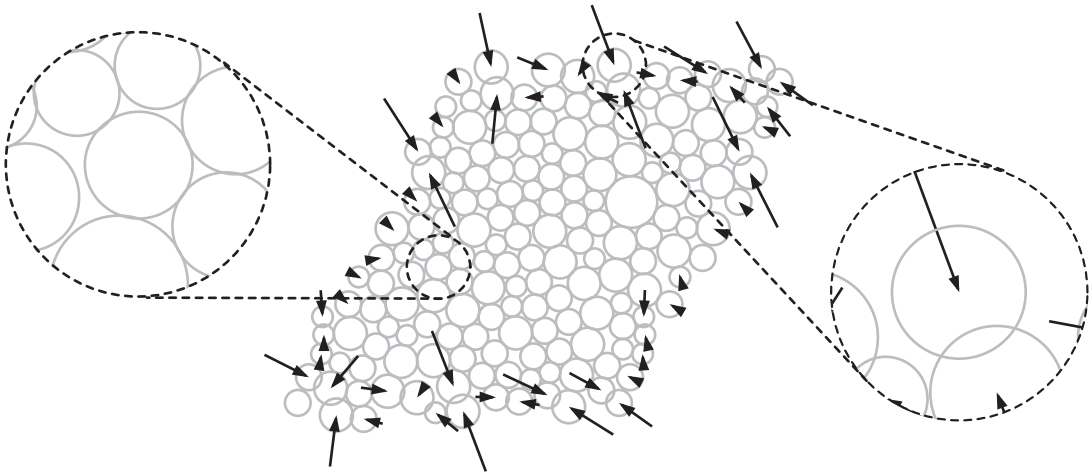

Figure 4.7.: Particle reaction forces: Restricted TAYLOR boundary condition. The particle reaction forces are depicted in black. A zoom in on the boundary as well as on the bulk is granted. Please observe the concentration of particle reaction forces to the boundary of the rve.

priate macroscopic deformation gradient. Therefore, as long as we assume a simple, e.g., history independent, force-overlap relation for the contacting particles, there is no computational or numerical need to store any kind of variables on the microscale. Nevertheless, for post processing reasons it is recommended to store appropriate spatial information. ■

4.3.3. Restricted Taylor assumption

The restricted TAYLOR assumption, also known as displacement boundary condition, see for example KOUZNETSOVA, GEERS & BREKELMANS [69] or MIEHE ET AL. [91,92], limits the assumption of TAYLOR and VOIGT, to the boundary of the rve. Clearly, under this particular assumption, the kinematically non-admissible deformation is solely restricted to the boundary. Each point of the rve is demanded to be in a state of quasi-static equilibrium, see Figure 4.4 (center). Based on the natural disappearance of (4.21), i.e., the microscopic fluctuations are prescribed to be zero on the boundary of the rve, the scale transition of the macroscopic deformation gradient is satisfied. Combined, we adhere the following statements for the restricted TAYLOR assumption,

$$\begin{aligned} \boldsymbol{x} &= \overline{\boldsymbol{F}} \cdot \boldsymbol{X}, && \forall \boldsymbol{X} \in \partial\Omega, \\ \mathrm{DIV}\boldsymbol{P} &= \boldsymbol{0}, && \text{in } \Omega. \end{aligned} \tag{4.25}$$

Based on the previous introduced partitioning of the particles, for details see Section 3.5, we transfer the restricted TAYLOR assumption from the continuous case to the discrete case. According to the continuous case, the spatial positions of the particles belonging to the boundary set $\mathscr{B}$ are prescribed by the macroscopic deformation gradient, see Figure 4.5 (center). Thereby, non-zero particle reaction forces arise on the boundary, see Figure 4.7. For the particles in the inside of the rve, the spatial positions

are assumed to compose in a similar manner as stated in (4.18),

$$\boldsymbol{x}_i = \overline{\boldsymbol{F}} \bullet [\boldsymbol{X}_i + \boldsymbol{\Xi}_i] \,, \qquad \forall i \in \mathscr{I}. \tag{4.26}$$

The bulk is driven by the prescribed displacements of the boundary particles. For the rve to be in a state of quasi-static equilibrium, we demand the inner particle forces to vanish, see Figure 4.7.

$$\begin{aligned} \boldsymbol{x}_i &= \overline{\boldsymbol{F}} \bullet \boldsymbol{X}_i, && \forall i \in \mathscr{B}, \\ \boldsymbol{f}_i &= \boldsymbol{0}, && \forall i \in \mathscr{I}. \end{aligned} \tag{4.27}$$

Please note that the global equilibrium, $\sum_{i \in \mathscr{P}} \boldsymbol{f}_i = \boldsymbol{0}$, is fulfilled once more.

Remark 4.4 (Computational implementation of the restricted TAYLOR assumption) Opposed to the assumption of TAYLOR and VOIGT, the numerical implementation of the restricted TAYLOR assumption demands the need of storing variables which belong to the microscopic structure. Solely assuming a linear force-overlap relation, we can reduce the storing procedure to the spatial positions of the particle aggregate. Doing so, we allow the inside of the rve to undergo a continuous evolution. Each macroscopic iteration/load step starts with a microstructure, developed at the last converged solution from the previous macroscopic load step. Thereby, each prescribed deformation of the boundary particles is followed by a dynamic relaxation procedure, see Table 4.1.

1. loop over all load steps
   a. load history data
   b. compute current positions of the boundary particles
      $\boldsymbol{x}_i^{n+1} = \overline{\boldsymbol{F}} \bullet \boldsymbol{X}_i \quad \forall i \in \mathscr{B}$
   c. relax rve (see Table 4.4)
   d. save history data

Table 4.1.: Overall microscopic computations including the application of restricted TAYLOR boundary conditions.

4.3.4. Periodic boundary conditions

While the previously introduced boundary conditions are feasible on various kinds of rve shapes, e.g., circles or polygons, the application of periodic boundary conditions requires the rve to possess geometric periodic boundary faces. Thus, periodic

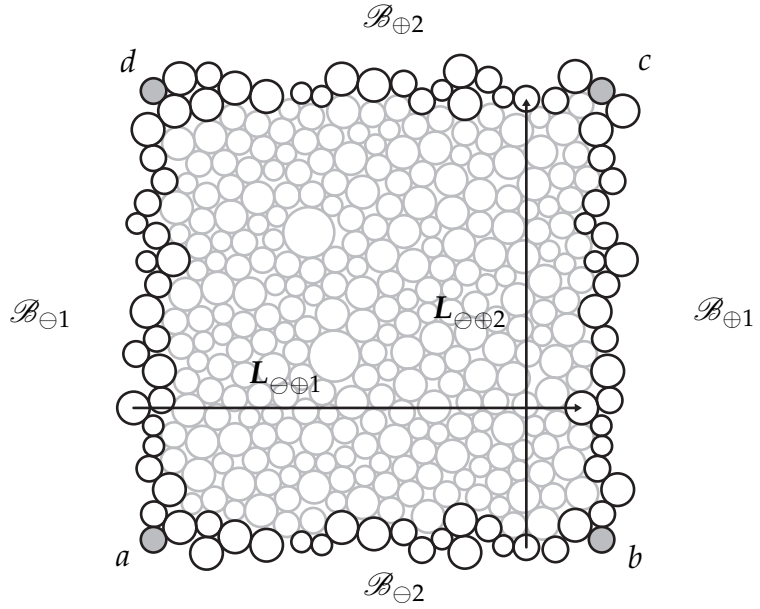

Figure 4.8.: Definition of the negative and positive boundary particle set, denoted by $\mathscr{B}_{\ominus}$ and $\mathscr{B}_{\oplus}$, respectively. Black colored grains belong to the boundary. Particles in gray belong to the interior. The vectors $\boldsymbol{L}_{\ominus\oplus}$ denote the horizontal and vertical branch vectors between the opposite boundaries.

boundary conditions are solely applicable if the reference rve is some kind of parallelepiped. Note that the parallelepiped faces are not restricted to be linear. During the deformation process, we demand the conservation of the geometrical periodicity of the rve boundary and require the bulk to be in a state of quasi-static equilibrium. To account for the conservation of the geometrical periodicity of the boundary, the boundary fluctuations of geometrically associated material points on the opposite boundaries are demanded to be equal,

$$\boldsymbol{\Xi}_{\oplus} = \boldsymbol{\Xi}_{\ominus}. \tag{4.28}$$

Therein, the indices, $\oplus$ and $\ominus$ denote the associated opposite faces of the rve. The demand stated in (4.28) introduces anti-periodic outward normals on opposite boundaries.

$$\boldsymbol{N}_{\oplus} = -\boldsymbol{N}_{\ominus}. \tag{4.29}$$

Recalling the necessary condition to fulfill the scale transition, we split (4.21) into two integrals over opposite surfaces, denoted by $\partial\Omega_{\oplus}$ and $\partial\Omega_{\ominus}$, respectively.

$$\int_{\partial\Omega} \boldsymbol{\Xi} \otimes \boldsymbol{N} \mathrm{d}A = \int_{\partial\Omega_{\oplus}} \boldsymbol{\Xi}_{\oplus} \otimes \boldsymbol{N}_{\oplus} \mathrm{d}A + \int_{\partial\Omega_{\ominus}} \boldsymbol{\Xi}_{\ominus} \otimes \boldsymbol{N}_{\ominus} \mathrm{d}A = \boldsymbol{0}. \tag{4.30}$$

Inserting (4.28) as well as (4.29), the necessary condition is satisfied. To derive the periodic boundary conditions in their general form, we reformulate (4.18) with respect to the fluctuations and insert the resulting expression into (4.28). Simple manipulations

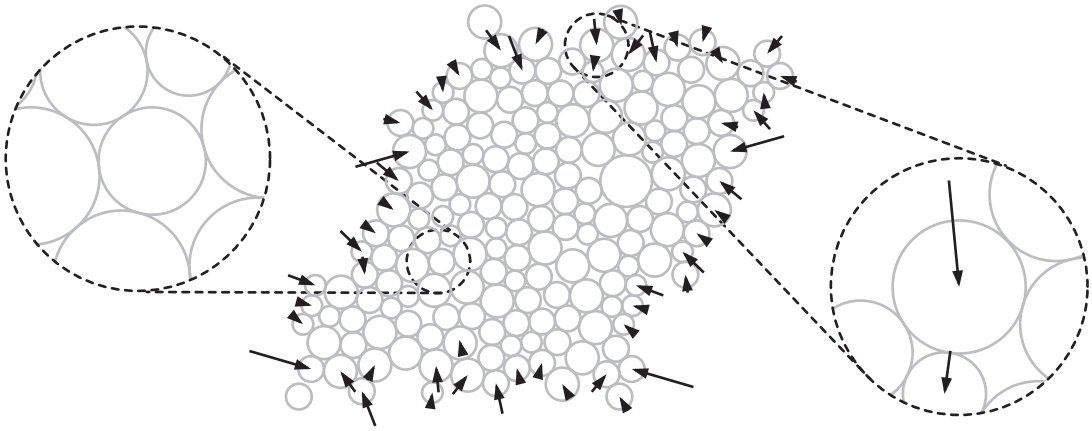

Figure 4.9.: Particle reaction forces: Periodic boundary conditions. The particle reaction forces are depicted in black. A zoom in on the boundary as well as on the bulk is granted. Please observe the anti-periodic nature of the particle reaction forces on the boundary of the rve.

finally lead to:

$$\boldsymbol{x}_{\oplus 1} - \boldsymbol{x}_{\ominus 1} = \overline{\boldsymbol{F}} \bullet \left[\boldsymbol{X}_{\oplus 1} - \boldsymbol{X}_{\ominus 1}\right], \quad \text{and} \quad \boldsymbol{x}_{\oplus 2} - \boldsymbol{x}_{\ominus 2} = \overline{\boldsymbol{F}} \bullet \left[\boldsymbol{X}_{\oplus 2} - \boldsymbol{X}_{\ominus 2}\right]. \tag{4.31}$$

While the definition in (4.31) allows the preservation of the periodicity of the boundary of the rve, it does also allow for rigid body motions. Remedy is found by mapping the four corner points in the manner of TAYLOR, i.e., the individual fluctuations of the rve corners are neglected *a priori*. Resumed, the periodic boundary conditions consist of

$$\begin{aligned} &\boldsymbol{x}_{\oplus} - \boldsymbol{x}_{\ominus} = \overline{\boldsymbol{F}} \bullet \left[\boldsymbol{X}_{\oplus} - \boldsymbol{X}_{\ominus}\right], && \forall \boldsymbol{X}_{\oplus}, \boldsymbol{X}_{\ominus} \in \partial\Omega \setminus \{a,b,c,d\}, \\ &\boldsymbol{x} = \overline{\boldsymbol{F}} \bullet \boldsymbol{X}, && \forall \boldsymbol{X} \in \{a,b,c,d\}, \\ &\mathrm{DIV}\boldsymbol{P} = \boldsymbol{0}, && \text{in } \Omega, \end{aligned} \tag{4.32}$$

whereby a, b, c, d refer to the four corner nodes of the rve. These nodes do not belong to the $\oplus$ or $\ominus$ boundary. Deriving the discrete counter part of the continuous periodic boundary conditions, listed in (4.32) yields:

$$\begin{aligned} &\boldsymbol{l}_{ij} = \overline{\boldsymbol{F}} \bullet \boldsymbol{L}_{ij}, && \forall\, (i,j) \in \{\mathscr{B}_{\ominus} \times \mathscr{B}_{\oplus}\}, \\ &\boldsymbol{x}_i = \overline{\boldsymbol{F}} \bullet \boldsymbol{X}_i, && \forall i \in \{a,b,c,d\}, \\ &\boldsymbol{f}_i = \boldsymbol{0}, && \forall i \in \mathscr{I}. \end{aligned} \tag{4.33}$$

We remark that the branch vectors $\boldsymbol{L}_{\ominus\oplus}$, in vertical as well as in horizontal direction, are constant throughout the whole rve, see Figure 4.8. Based on the overall geometric periodic nature, we colligate the horizontal material branch vector $\boldsymbol{L}_{\ominus\oplus 1}$ to $\boldsymbol{X}_b - \boldsymbol{X}_a$, while its vertical counter part relates to $\boldsymbol{X}_d - \boldsymbol{X}_a$. This particular feature follows from the geometric periodic nature of the rves. The newly introduced sets, i.e., $\mathscr{B}_{\ominus}, \mathscr{B}_{\oplus}$ as well as the four corner particles a, b, c, d are marked in Figure 4.8. Once more, we point out that the corner particles do not belong to either boundary set. Disregarding the four corner particles of the particulate rve, the spatial positions of each particle is

composed by a homogeneous as well as an individual fluctuational displacement part,

$$\boldsymbol{x}_i = \overline{\boldsymbol{F}} \bullet [\boldsymbol{X}_i + \boldsymbol{\Xi}_i] \,, \qquad \forall i \in \mathscr{P} \setminus \{a, b, c, d\} \,. \tag{4.34}$$

Thereby, we emphasize once more that the fluctuations of associated particles on opposite boundary faces are demanded to be accordant.

Remark 4.5 (Computational implementation, periodic boundary conditions) With respect to the computational implementation, we trivially reproduce certain parts of the rve in a periodic manner. Mapping as well as translation of all replica particles is done by periodic placements, i.e., by simply adding or subtracting $\boldsymbol{l}_{\ominus\oplus}$. Thus, no computational expensive calculations are necessary. However, additional particles yield higher contact search times. The overall algorithm compares to Table 4.1, whereby extensions are made in regards to the boundary particles.

1. loop over all load steps
   a. load history data
   b. compute current positions of the corner particles
      $\boldsymbol{x}_i^{n+1} = \overline{\boldsymbol{F}} \bullet \boldsymbol{X}_i \quad \forall i \in \{a, b, c, d\}$
   c. compute current positions of the boundary particles
      $\boldsymbol{x}_j^{n+1} = \boldsymbol{x}_i^{n+1} + \overline{\boldsymbol{F}} \bullet \boldsymbol{L}_{ij} \quad \forall (i, j) \in \{\mathscr{B}_\ominus \times \mathscr{B}_\oplus\}$
   c. relax rve (see Table 4.4)
   d. save history data

Table 4.2.: Overall microscopic computations including the application of periodic boundary conditions.

4.3.5. On the regularity of the global aggregate stiffness

In contrast to the classical fem, the application of standard boundary conditions, see Subsections 4.3.2, 4.3.3 and 4.3.4, is insufficient to guarantee the regularity of the global microscopic aggregate matrix of a general discrete particle assembly. For discrete assemblies, the regularity of the global microscopic aggregate matrix and the jammed state of the single grains are strongly connected. In particular, for a connectivity, solely considering jammed grains, the global microscopic aggregate matrix is guaranteed to be regular and therefore invertible. Using the definition of TORQUATO, TRUSKETT

& DEBENEDETTI [140], a single grain is considered jammed if the grain itself cannot translate while the contacting particles are held fixed in space. While this definition is obsolete under the assumption of TAYLOR, the demand of quasi-static equilibrium requires the distinction of jammed particles. From all particles in the assembly, the aggregate of jammed grains is declared to form the load bearing structure. Naturally, a general particle assembly might include un-jammed particles. These so-called rattlers do not contribute to the load bearing of the structure and thus are not considered throughout the homogenization process. For identification purposes we introduce an additional set of sets, solely including jammed grains. These sets are subsets of $\mathscr{I}$, $\mathscr{B}$ as well as $\mathscr{P}$, and are denoted by a star,

$$\mathscr{I}^* \subseteq \mathscr{I}, \quad \mathscr{B}^* \subseteq \mathscr{B}, \quad \mathscr{P}^* \subseteq \mathscr{P}. \tag{4.35}$$

Attempts to associate the jammed state of a particle to the coordination number, whereby the coordination number reflects the number of contacting grains, are not trivial when considering a general particle assembly, see Figure 4.10 (left). Even though, the depicted setup defines the shaded grain to be jammed, there exist other configurations of the surrounding grains defining the shaded grain as rattler. Focusing on

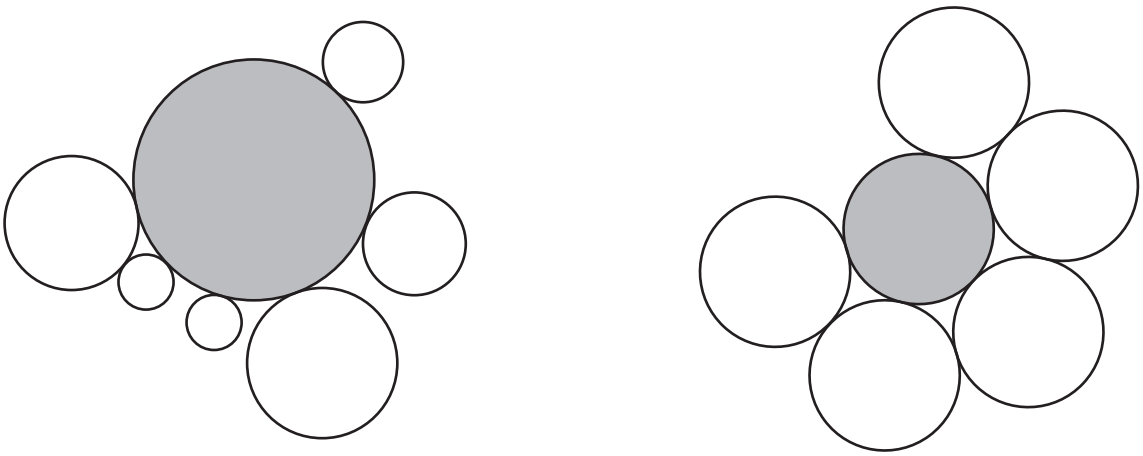

Figure 4.10.: Jammed state of individual grains. The grain of interested is colored in gray. *Left*: Example of polydisperse packings. The coordination number, equal to six, is not meaningful to define the gray colored grain to be jammed. *Right*: Example of monodisperse packings. A coordination number equal to five guarantees the jammed state of the gray colored particle.

a monodisperse packing, which is regarded as a special case, a particle is defined jammed if its coordination number equals five, compare Figure 4.10 (right). Thereby, a change of the setup does not effect the state of the shaded particle. For a general particle assembly in n-dimensional space, TORQUATO & STILLINGER [139] pointed out that essentially $n + 1$ contacting grains are necessary to define the grains of interest to be jammed. These grains are demanded to not all reside on the same hemisphere. Further information concerning jamming itself as well as the definitions of locally jammed,

collectively jammed and strictly jammed particle systems are found in the excellent contributions of DONEV ET AL. [34–36]. Our focus is restricted to detect all jammed grains in the aggregate.

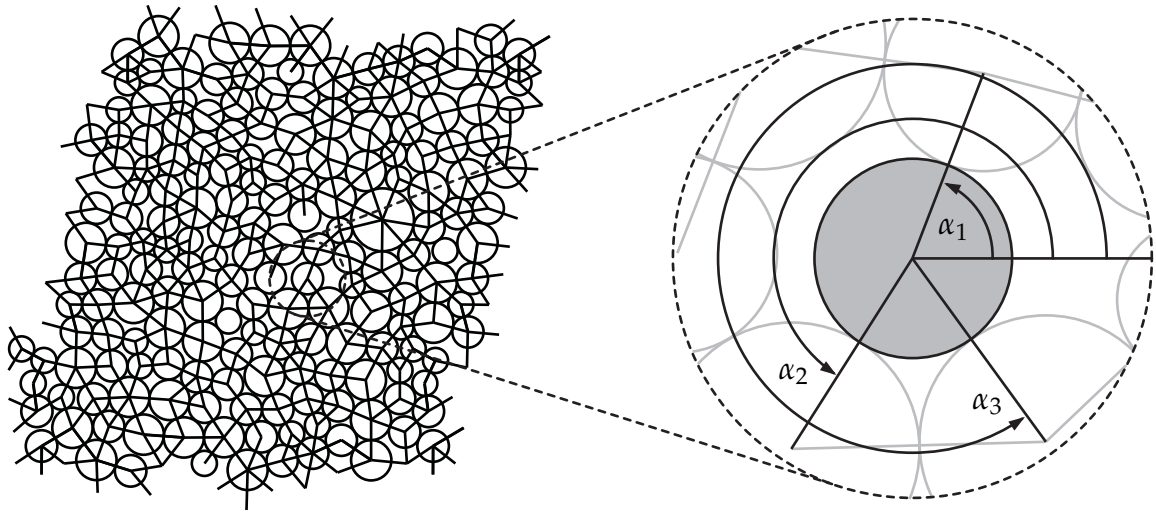

Figure 4.11.: Jammed state of individual grains. Triple angle criterion. *Left*: Particle assembly showing the inter-particle contact network. *Right*: Zoom in on a single grain and its contacts. The angle triple defining the grain jammed is marked.

Remark 4.6 (Computational implementation, regularization) With respect to the efficient implementation, the hemisphere criterion is reduced to a numerically more suitable procedure. Therefore, we introduce an angle triple $\alpha_1, \alpha_2, \alpha_3$, see Figure 4.11 (right). The angles describe the contact directions of three contacting grains. Finding three grains, having angles:

$$\begin{aligned} \alpha_1 &< 180^\circ, \\ \alpha_1 < \alpha_2 &< \alpha_1 + 180^\circ, \\ \alpha_1 + 180^\circ < \alpha_3 &< \alpha_2 + 180^\circ, \end{aligned} \tag{4.36}$$

the grain of interest is defined jammed. Algorithmically, these requirements are nested in a iterative scheme, listed in Table 4.3. Obviously, this algorithm does not consider the special cases of having two or four contacting grains with 180° or 90° between the branch vectors. These cases are handled separately. ■

4.4. The dynamic relaxation method

4.4.1. Explicit vector iteration

The present explicit vector iteration method relies on the central difference time integration scheme. For its application, the non-linear static equation is transferred to a

1. for all particles with fluctuations
   a. place a polar coordinate system in the center of the particle
   b. find a contacting particle with $\alpha_1 = \min\{\alpha\}$

      IF $\alpha_1 \geq 180^\circ$ THEN
        particle is marked as rattler
        repeat = .TRUE.
        GOTO 2.

   c. find a second contacting particle with $\alpha_2 = \max\{\alpha < \alpha_1 + 180^\circ\}$

      IF $\alpha_2 = \alpha_1$ THEN
        particle is marked as rattler
        repeat = .TRUE.
        GOTO 2.

   d. find a second contacting particle with $\alpha_3 = \max\{\alpha < \alpha_2 + 180^\circ\}$

      IF $\alpha_3 \leq \alpha_1 + 180^\circ$ THEN
        particle is marked as rattler
        repeat = .TRUE.

2. IF *repeat* GOTO 1.

Table 4.3.: Iterative algorithm to find rattlers.

dynamic equation. Therefore, an artificial inertial force $\boldsymbol{M} \bullet \ddot{\boldsymbol{x}}$ and a artificial damping force $\boldsymbol{C} \bullet \dot{\boldsymbol{x}}$ are added. The artificial mass and damping matrices are denoted by $\boldsymbol{M}$ and $\boldsymbol{C}$, respectively. Related to the discrete nature, the mass and the damping matrix are diagonal matrices, i.e., $\boldsymbol{M} = \mathrm{diag}\,[\boldsymbol{m}_{11} \cdots \boldsymbol{m}_{\#\mathscr{P}\#\mathscr{P}}]$ with $\boldsymbol{m}_{ii} = \mathrm{diag}\,[m, m]$. Assuming only mass proportional damping, we introduce the artificial damping coefficient γ, such that $\boldsymbol{C} = \gamma \boldsymbol{M}$.

$$\boldsymbol{M} \bullet \left[\ddot{\boldsymbol{x}} + \gamma \dot{\boldsymbol{x}}\right] - \boldsymbol{f} = \boldsymbol{0}. \tag{4.37}$$

The central difference time approximations for the artificial velocity at half time $k + 1/2$, full time k as well as the pseudo acceleration at full time k render to,

$$\dot{\boldsymbol{x}}^{k+1/2} = \frac{\boldsymbol{x}^{k+1} - \boldsymbol{x}^k}{\Delta t}, \quad \dot{\boldsymbol{x}}^k = \frac{\dot{\boldsymbol{x}}^{k+1/2} + \dot{\boldsymbol{x}}^{k-1/2}}{2}, \quad \ddot{\boldsymbol{x}}^k = \frac{\dot{\boldsymbol{x}}^{k+1/2} - \dot{\boldsymbol{x}}^{k-1/2}}{\Delta t}. \tag{4.38}$$

At this point we would like to emphasize that the superscript k and its alternations do not relate to physical time positions, rather than, their functionality are solely restricted to iteration counters. Insertion of (4.38) in (4.37) as well as reordering the terms yields

a formula for the pseudo velocity at $k + 1/2$,

$$\dot{\boldsymbol{x}}^{k+1/2} = \frac{1}{2 + \gamma \Delta t} \left[[2 - \gamma \Delta t] \, \dot{\boldsymbol{x}}^{k-1/2} + 2 \Delta t \, \boldsymbol{M}^{-1} \bullet \boldsymbol{f}^{k} \right]. \tag{4.39}$$

Note that, based on its diagonal form, the inversion of the mass matrix is considered as trivial and does not require high computational costs. In fact, the inverse of the global mass matrix can be constructed in a direct manner. Reordering $(4.38)_1$, the positions at $k + 1$ are calculated.

$$\boldsymbol{x}^{k+1} = \boldsymbol{x}^{k} + \frac{1}{2 + \gamma \Delta t} \left[[2 - \gamma \Delta t] \, \dot{\boldsymbol{x}}^{k-1/2} + 2 \Delta t \, \boldsymbol{M}^{-1} \bullet \boldsymbol{f}^{k} \right] \Delta t. \tag{4.40}$$

Initiation of the algorithm requires knowledge of the pseudo velocity at $-1/2$. Since we assume an overall static behavior, $\dot{\boldsymbol{x}}^{0}$ is set to zero. Using $(4.38)_2$ we find the velocities of the prior and posterior half steps to be equivalent, i.e., $\dot{\boldsymbol{x}}^{-1/2} = -\dot{\boldsymbol{x}}^{1/2}$. Inserting this result in (4.39) as well as rearranging, leads to a definition of the velocity at $1/2$,

$$\dot{\boldsymbol{x}}^{1/2} = \frac{\Delta t}{2} \boldsymbol{M}^{-1} \bullet \boldsymbol{f}^{0}. \tag{4.41}$$

Equivalent to the remaining algorithm, we utilize $(4.38)_1$ to calculate the positions at the next full step. As convergence criterion, we propose the following relative error measurement,

$$\frac{\left|\left| \boldsymbol{f}^{k+1} \right|\right|}{\left|\left| \boldsymbol{f}^{0} \right|\right|} \leq \varepsilon_{\text{tol}}, \tag{4.42}$$

with $\left|\left| \boldsymbol{f}^{k+1} \right|\right|$ relating to the current norm of the particle force vector and $\left|\left| \boldsymbol{f}^{0} \right|\right|$ to the initial norm of the particle force vector. In final the description of the explicit vector iteration method, we observe the absence of the stiffness matrix. As mentioned in the latter, this particular feature makes this method extremely attractive for a large variety of various numerical applications. A pseudo code of the outlined algorithm is presented in Table 4.4

4.4.2. Iteration parameters

The crucial point of explicit vector iteration methods are the right choice of the iteration parameters which guarantee the stability as well as the convergence of the overall algorithm. To obtain these parameters, we follow the outline of UNDERWOOD [143] and evaluate the position errors,

$$\boldsymbol{\epsilon}^{k+1} = \boldsymbol{x}^{k+1} - \boldsymbol{x}^{*}, \qquad \boldsymbol{\epsilon}^{k} = \boldsymbol{x}^{k} - \boldsymbol{x}^{*}, \qquad \boldsymbol{\epsilon}^{k-1} = \boldsymbol{x}^{k-1} - \boldsymbol{x}^{*}. \tag{4.43}$$

1. fix-point iteration loop
   a. compute particle forces for the entire rve
      f^k
   b. compute velocities at half step
      IF $k = 0$ THEN
      $$\dot{x}^{1/2} = \frac{\Delta t}{2} M^{-1} \bullet f^0$$
      ELSE
      $$\dot{x}^{k+1/2} = \frac{1}{2 + \gamma \Delta t} \left[[2 - \gamma \Delta t] \, \dot{x}^{k-1/2} + 2 \Delta t \, M^{-1} \bullet f^k \right]$$
      END IF
   c. compute positions at full step
      $x^{k+1} = x^k + \Delta t \, \dot{x}^{k+1/2}$
   d. convergence check
      IF $\dfrac{\left|\left| f^{k+1} \right|\right|}{\left|\left| f^0 \right|\right|} \geq \varepsilon_{\text{tol}}$ GOTO 1.

Table 4.4.: Pseudocode for the microscopic dynamic relaxation procedure (restricted TAYLOR).

Thereby, we assume that the exact quasi-static solution, denoted by x^*, is known. Inserting these equations in (4.40), as well as sorting the individual terms with respect to the position errors yields an explicit expression between the successive error vectors,

$$\epsilon^{k+1} = [[1 + \beta] \, \mathbf{1} - \alpha A] \, \epsilon^k - \beta \epsilon^{k-1}. \tag{4.44}$$

The matrix A defines as: $A = M^{-1} \bullet K_{\text{n}}$. The relation between the position errors in pseudo time is believed to obey $\epsilon = \kappa \epsilon^n$, with $\kappa < 1$, whereby κ itself is understood as the spectral radius. Obviously, smaller values of κ lead to a faster decay of the position error and thus, to a fast convergence towards the desired quasi-static solution. Inserting the position error relation in (4.44),

$$[A - \lambda \mathbf{1}] \, \epsilon^k = \mathbf{0}, \quad \text{with} \quad \lambda = -\frac{\kappa^2 - [1 + \beta] \, \kappa + \beta}{\alpha \kappa}, \tag{4.45}$$

is obtained. Equation $(4.45)_1$ describes a standard eigenvalue problem with λ being the eigenvalues and ϵ^n the corresponding eigenvectors of the matrix A. Observing (4.45) reveals relations between the eigenvalues of A and the spectral radius κ. Solving the quadratic equation $(4.45)_2$ with respect to κ yields:

$$\kappa_{1,2} = \frac{1 + \beta - \alpha \lambda}{2} \pm \frac{1}{2} \sqrt{[1 + \beta - \alpha \lambda]^2 - 4\beta}. \tag{4.46}$$

Depending on the argument of the square root, three possible solutions are obtained. As proven by PAPADRAKAKIS [114], κ is insured to be a minimum if the solutions of (4.46) are real and equal, i.e., if the square root vanishes. Solely considering this special case, we obtain an expression for the time step as well as for the damping coefficient:

$$\Delta t = \frac{2}{\sqrt{\lambda_{\mathsf{min}} + \lambda_{\mathsf{max}}}}, \quad \text{and} \quad \gamma = 2\sqrt{\frac{\lambda_{\mathsf{min}}\lambda_{\mathsf{max}}}{\lambda_{\mathsf{min}} + \lambda_{\mathsf{max}}}}. \tag{4.47}$$

Note the exclusively dependence on the minimum and maximum eigenvalues of $\boldsymbol{A}$.

Remark 4.7 (Eigenvalues for the periodic case) In case of periodic boundary conditions, the global stiffness matrix as well as the global mass matrix require modification. In particular, we apply a method used by KOUZNETSOVA [70], which relies on the application of a connectivity matrix, denoted by $\boldsymbol{C}$.

$$\boldsymbol{A}_{\mathsf{peri}} = \boldsymbol{K}_{\mathsf{peri}} \bullet \boldsymbol{M}_{\mathsf{peri}}{}^{-1} \tag{4.48}$$

with

$$\boldsymbol{K}_{\mathsf{peri}} = \boldsymbol{C}^t \bullet \boldsymbol{K} \bullet \boldsymbol{C} \quad \text{and} \quad \boldsymbol{M}_{\mathsf{peri}} = \boldsymbol{C}^t \bullet \boldsymbol{M} \bullet \boldsymbol{C}. \tag{4.49}$$

In contrast to continuum mechanics, discrete systems require to account for double considerations of inter-particle boundary quantities. To overcome this problem, related quantities are multiplied by $1/2$. ■

4.5. Representative numerical examples

The introduced dem is demonstrated by two numerical examples, consisting of a uniaxial compression test as well as a simple shear test. The results allow the understanding of the behavior of the relaxation method and provide deeper insight into the influence of the individual boundary conditions. The deformation scenarios are performed on a randomly generated polydisperse rve, containing 300 primary particles. The initial rve is depicted in Figure 4.12 (left), generated by using the previous discussed algorithm. Hence, distinguishing features like geometric periodic boundaries as well as a high packing density are naturally included. Information in regards to the used grain size distribution is given in Table 5.1. The image on the right of Figure 4.12 shows the related contact distribution by means of a so-called contact density function plot. A density function is closely related to the so-called rose-diagram, first published by NIGHTINGALE [102]. It is a common method of depicting directional dependent data and is frequently used in the area of geo-science, see for example FISHER [44] SOKOLOV & O'BRIEN [130]. In contrast to the used density function, the rose-diagram is strongly dependent on the petal width and its point of initiation, see WELLS [155] The contact density function depicts information of the inter-particle contact directions

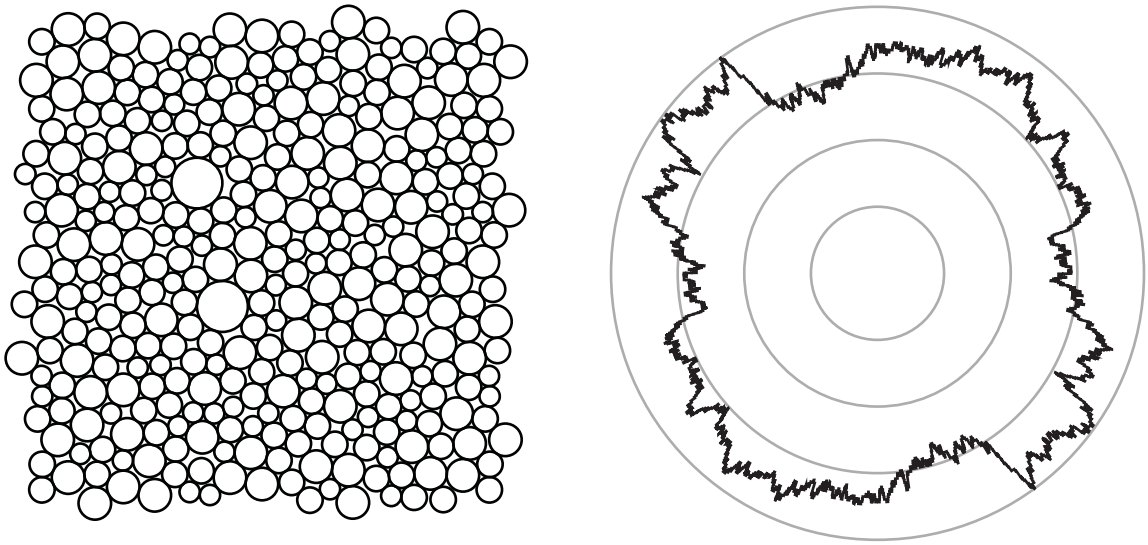

Figure 4.12.: *Left*: Undeformed rve, containing 300 primary particles. *Right*: Contact density function of the undeformed rve.

as well as their frequency of occurrence, see MEIER ET AL. [85]. We remark that this distinguished method of plotting the directional information of the rve is used as a measure of isotropy. In case of an isotropic rve, the contact density function shows a circular plot. Obviously, density function plots strongly depend on the angle of influence, whereby a larger angle smoothes the output. For all depicted plots, the angle of influence is set to 25°. Therefore, we regard the selected rve as somehow isotropic.

4.5.1. Microscopic investigations - uni-axial compression

As a first example, we consider a uni-axial compression test in horizontal direction. The compression is applied by the macroscopic deformation gradient $\overline{\boldsymbol{F}} = \delta_{ij}\boldsymbol{e}_i \otimes \boldsymbol{e}_j - \lambda \boldsymbol{e}_k \otimes \boldsymbol{e}_k$, whereby k is set to 1. The loading parameter is chosen to $\lambda \in [0 \rightarrow 0.3]$. Figure 4.13 shows the algorithmic specific results in regards to the restricted TAYLOR and the periodic boundary conditions. We apply the deformation in a uniform manner and perform 300 load steps, see Figure 4.13 (top left). Depending on the applied boundary conditions, each load step is followed by a deformation dependent number of relaxation steps, see Figure 4.13 (bottom left). The relative convergence threshold is set to 1E−08. We observe that the mean number of iteration steps is considerably low. Nevertheless, peaks are existing. These artifacts relate to large movement or reorientation of single particles or particle clusters, ultimately effecting the majority of all particles. In case of the periodic boundary condition, we observe four main peaks. The peak at load step 171 is investigated in detail in the following. Therefore, we plot the particle configuration of the load steps 170 and 171, see Figure 4.14 (left). Particles denoted in gray belong to the 170^{th} load step. Particles of the 171^{st} load step are colored in black. While this image allows for a first impression of the motion of the individual grains,

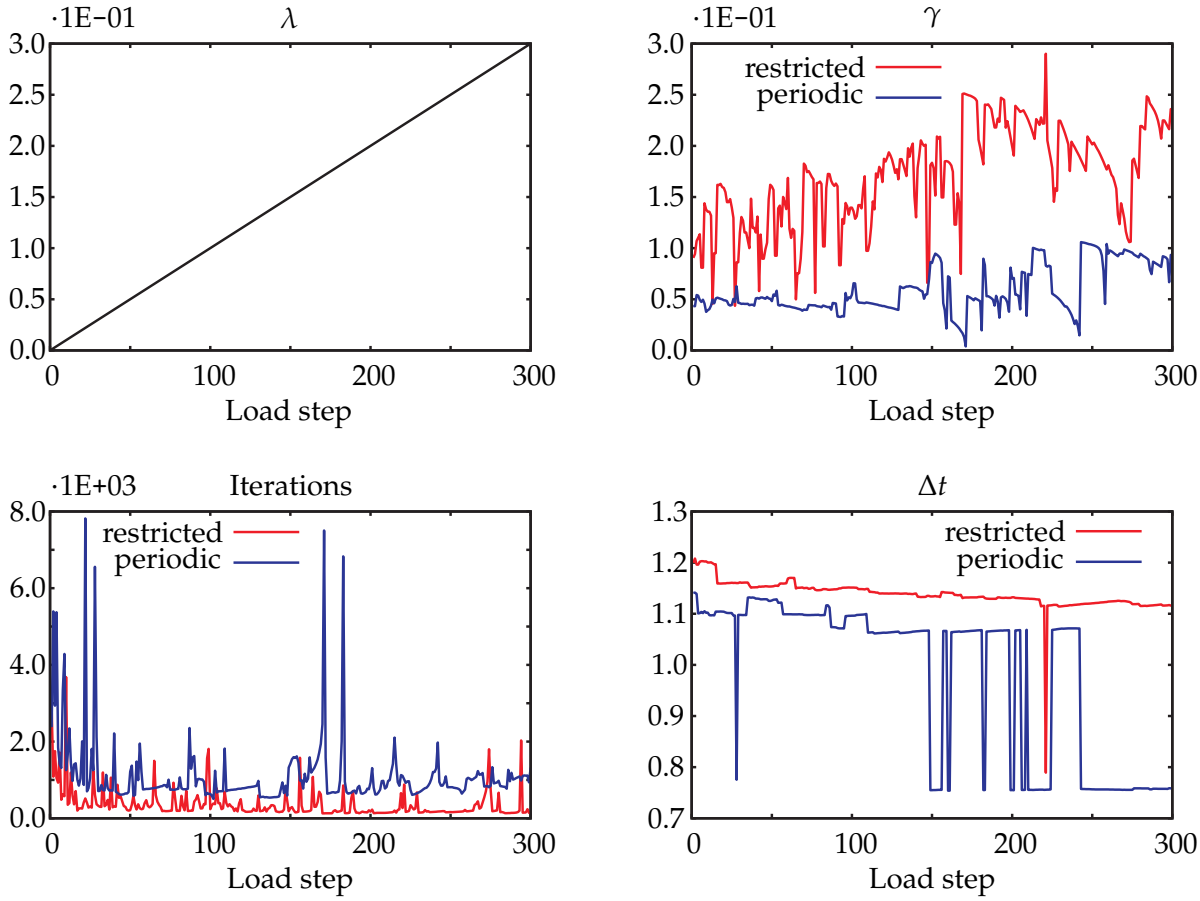

Figure 4.13.: Algorithmic results: Uni-axial compression. *Top left*: Loading parameter λ over the load steps. *Top right*: Damping coefficient γ over the load steps. *Bottom left*: Number of iterations over the load steps. *Bottom right*: Time step size Δt over the load steps.

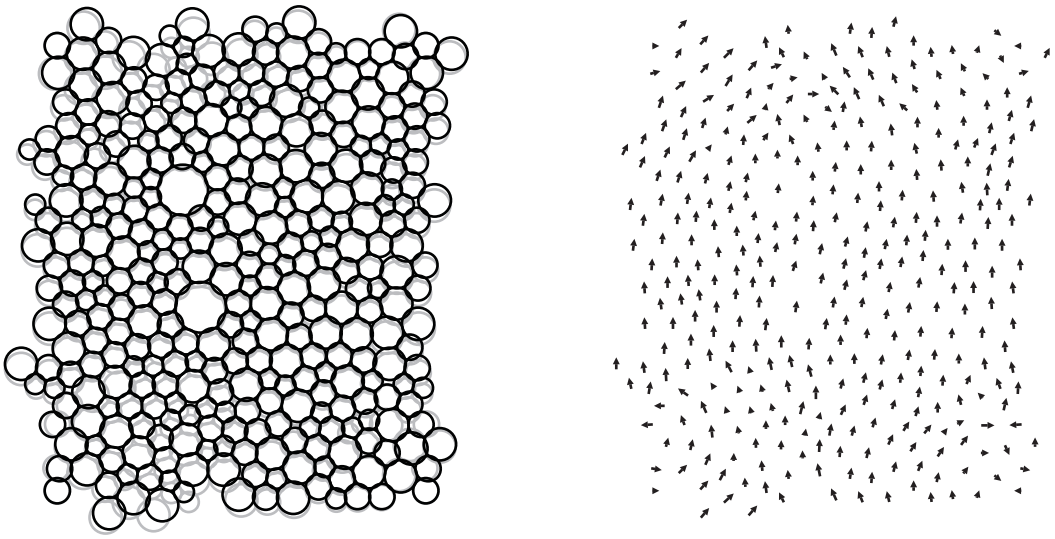

Figure 4.14.: Investigation on large displacements under periodic boundary conditions. *Left*: Particle setup for two load steps. Gray colored grains belong to the 170^{th} load step, while black particles refer to load step 171. *Right*: Unscaled depiction of particle displacements between the load step 170 and 171.

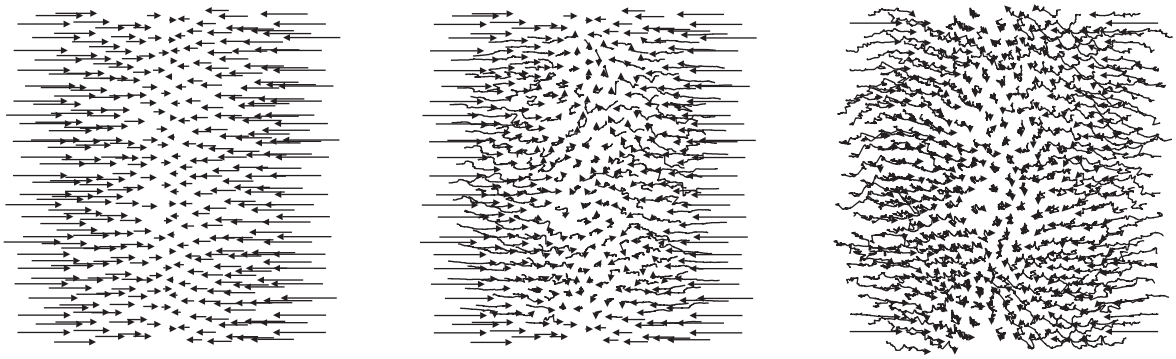

Figure 4.15.: Motion of the individual grains by trace lines: Uni-axial compression. *Left*: Assumption of TAYLOR. *Center*: Restricted TAYLOR assumption. *Right*: Periodic boundary conditions.

the plot on the right of Figure 4.14 provides deeper insight. Therein, the displacement between the 170^{th} and 171^{st} load step is plotted by vectors. Close observation reveals a large shift in vertical direction of almost all particles in the rve. Please note that the magnitude of the shift is considerably larger than the applied deformation, as well as that its direction is orthogonal to the direction of loading. Obviously, such motions are solely possible in the case of periodic boundary conditions. The magnitude of the damping coefficients and the time step size are depicted in the top right and bottom right images of Figure 4.13. We notice a very active behavior of the damping coefficient for both boundary conditions. Furthermore, both damping coefficient show an increasing behavior as the deformation is increased. The time step size, when compared to the damping coefficient, shows a rather uniform and decreasing tendency. Nevertheless, jumps are present for both boundary conditions.

The total motion of the individual grains is shown in Figure 4.15 by means of particle trace lines. The image to the right relates to the assumption of TAYLOR, the center image to the restricted TAYLOR assumption and the image to the left to the periodic boundary conditions. The differences between the individual plots are remarkable and show the nature of the individual boundary conditions in a comprehensive way. As expected, the trace lines related to the assumption of TAYLOR describe linear motions of all particles, solely orientated in the direction of loading. Naturally, assuming the point of origin in the rve center yields the outer particles to translate a longer distance. The linear motion repeats for the boundary particles of the rve, subjected to the restricted TAYLOR assumption. In contrast, we find the free motion of the bulk to be well defined. Please observe that the motion of the inner grains is not restricted to the direction of loading. The trace lines related to the periodic boundary conditions display a rather chaos like behavior, which solely orders by close observation. Than, one is able to detect periodic movements of the boundary particles as well as linear motions of the four corner grains. In addition to the restricted TAYLOR assumption, we not only find the inner grains to translate in directions other than the direction of loading, but we as well observe the boundary particles to do so.

Next, we study the inter-particle connectivity as well as the direction of force flux under different boundary conditions. A prominent way to depict both features is the so-called force network plot, whereby each branch vector is scaled by the related inter-particle overlap, see, e.g., Figure 4.16 (left column). Obviously, based on the amount of information, detailed statements are hard to conceive. However, the force network plot allows for a first impression as well as for a good overview of the underlying information. Particular information regarding the inter-particle connectivity as well as the direction of force flux are extracted by means of density function plots. Therefore, the complete contact network is abstracted by the previous introduced contact density function. Data concerning the direction of force flux is depicted by a scaled density function plot, the so-called force density function, see, e.g., Figure 4.16 (right column). The function itself constructs by using overlap scaled direction information as well as their frequency of occurrence. The output is related to the measure of hydrostatic state, whereby a hydrostatic state is represented as a circle. Using all three representations, i.e., the force network, the contact density function as well as the force density function, allows a qualitative study of influence of the different boundary conditions. At first, following the previously introduced order, we tend to the assumption of TAYLOR, see Figure 4.16. Therein, each row relates to a specific state of deformation, identified by the loading parameter λ. The first row shows snap shots for $\lambda = 0.1$. The consequent rows of images relate to loading parameters of 0.2 and 0.3. Different sources of information are ordered by columns, whereby the first column shows the force network plots, the second column shows the contact density function plots and the third column shows the force density function plots. Stepping to the first column, we find an increase of the magnitude of the force chains under loading. This is noticed by the increasing line thickness of the plotted network. Developing force chains, sometimes called solid-paths, show a strong directional dependence. In particular, one notices the thickness enlargement in, or close to, the direction of loading. Branches orthogonal to the direction of loading are observed to be rather thin. Solely considering the first column, the network itself does not seem to extend or alter significantly. This position has to be revised when considering the second column which depicts the overall contact network: By loading, a change of the contact network is observed. A significant increase or decrease of inter-particle contacts is not visible, however, the contact density function plots reveal branch rotations towards the vertical axis. This observation aligns with the applied homogeneous mapping of all grains. Overall, the nearly isotropic response of the initial packing alters to a rather anisotropic one. The plots in the last column underline the previous statement of the relation of the branch thickness and the direction of loading. One finds plot spreading in, or close to, the direction of loading. Orthogonal to the direction of loading, plot necking is observed. Hence, applying the assumption of TAYLOR, the depicted images reveal a strong relation between the solid paths, i.e., the direction of force flux through the rve, and the loading direction: The solid paths and the direction of loading are well aligned. Results concerning the restricted TAYLOR assumption are plotted in Figure 4.17. The previously introduced order of load steps as well as information sources is retained. Starting with the force network plots, see Figure 4.17 (left column), one notices an evolution sequence of individual force chains. Based on the subjected boundary condition, the resulting images

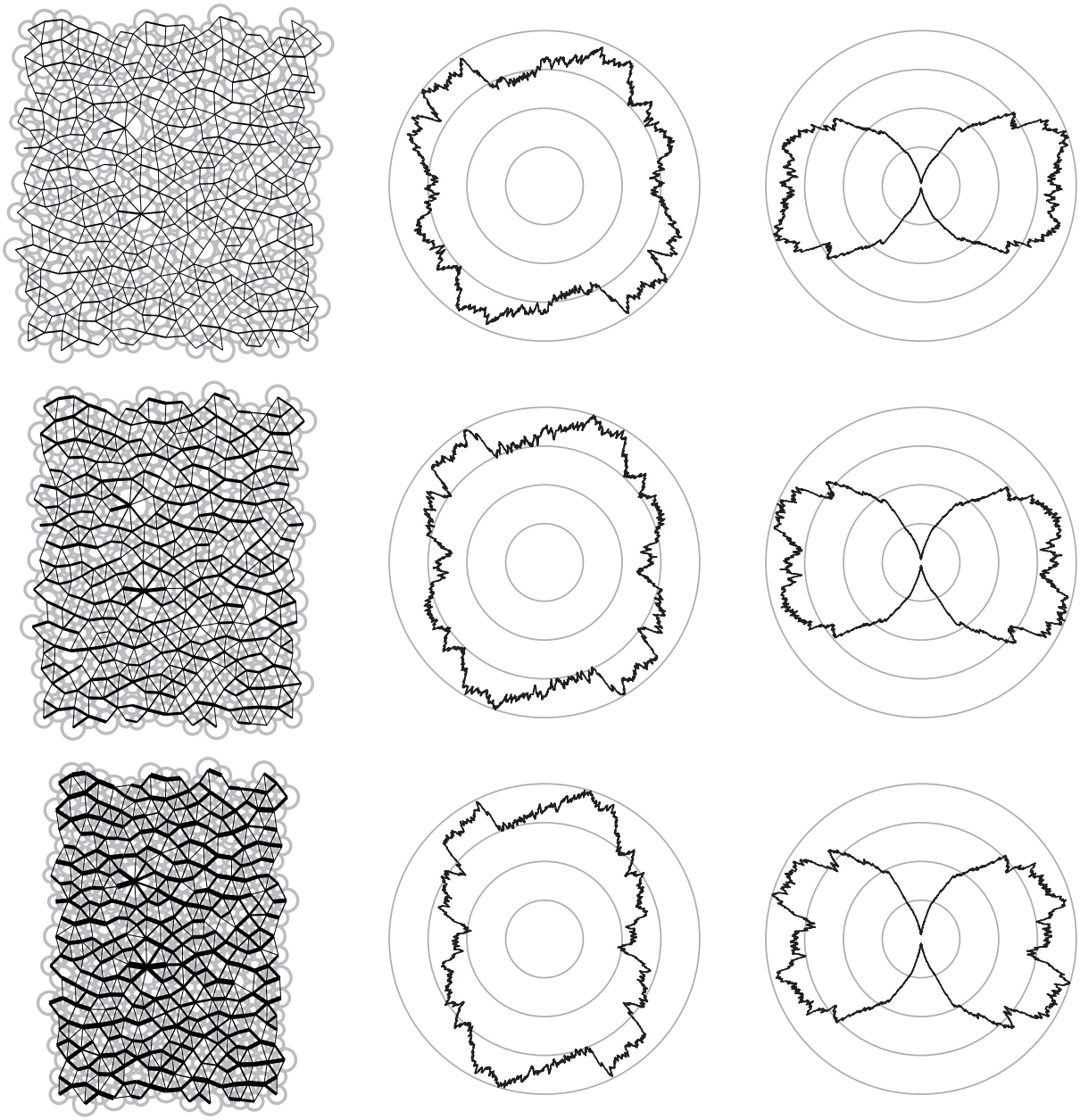

Figure 4.16.: Uni-axial compression: TAYLOR assumption. Each row relates to a state of deformation, starting in the top row with $\lambda = 0.1$ and increasing by 0.1 to the bottom row of $\lambda = 0.3$. *Left column*: Inter-particle force network. *Center column*: Contact density function. *Right column*: Force density function. The angle of influence is set to 25°.

do not compare to the previously discussed outputs of the assumption of TAYLOR. In particular, we remark the arbitrary run of the solid-paths which, initially, are not solely orientated along the direction of loading. The sequence of images shows the existence of complicated networks, altering between the single snap shots. Nevertheless, certain distinct solid-paths are visible throughout the deformation process. Concentrating on the boundary of the rve, one detects a significant similarity to the assumption of TAYLOR, i.e., the perfect matching of the force chains between boundary particles. Obviously, this feature relates to the nature of the restricted TAYLOR assumption. Informa-

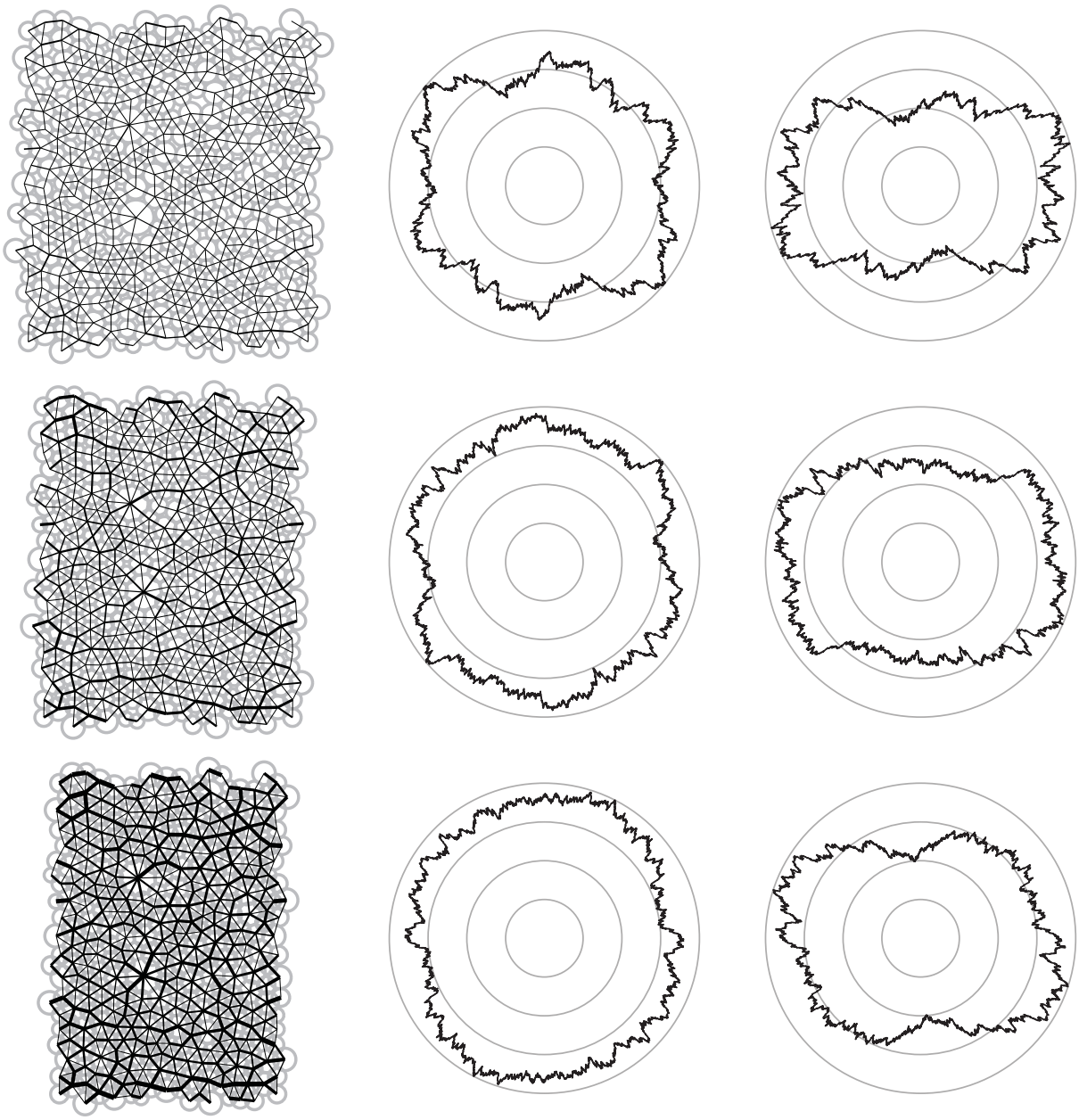

Figure 4.17.: Uni-axial compression: Restricted TAYLOR assumption. Each row relates to a state of deformation, starting in the top row with $\lambda = 0.1$ and increasing by 0.1 to the bottom row of $\lambda = 0.1$. *Left column*: Inter-particle force network. *Center column*: Contact density function. *Right Column*: Force density function. The angle of influence is set to 25°.

tion in regards to the contact network is depicted in the center column of Figure 4.17. We observe a well balanced contact density function at all times, whereby certain directions seem to be preferred at different stages. While the first image shows a rather star like shape, the remaining plots are considered to be rather smooth. This change of shape, not noticed under the assumption of TAYLOR, relates to the ability of the bulk to develop and relax. The right column of Figure 4.17 shows the force density function of the observed loading stages. We notice a behavior which confirms the results of the assumption of TAYLOR. Basically, one finds the direction of force flux in alignment with

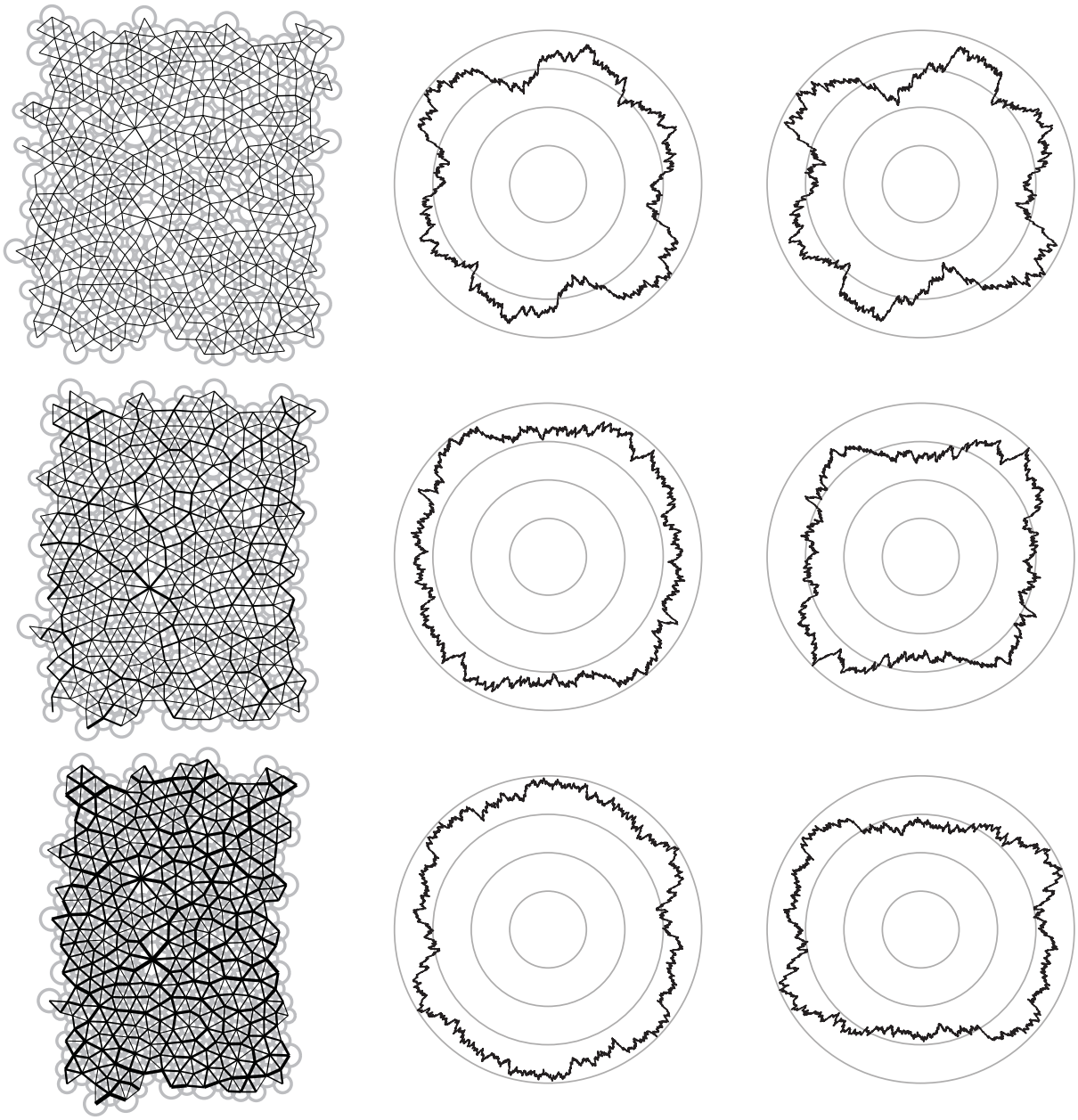

Figure 4.18.: Uni-axial compression: Periodic boundary conditions. Each row relates to a state of deformation, starting in the top row with $\lambda = 0.1$ and increasing by 0.1 to the bottom row of $\lambda = 0.3$. *Left column*: Inter-particle force network. *Center column*: Contact density function. *Right column*: Force density function. The angle of influence is set to 25°.

the direction of loading. The previously observed necking is not as pronounced. As last boundary condition, we study the influence of the periodic boundary conditions. The related results are depicted in Figure 4.18 and follow the previously introduced arrangement. By investigating the force network plots, one finds similarities with the output of the restricted TAYLOR assumption. Specifically, we remark the incisive force network, which itself seems well balanced. Yet, we observe rather distinctive network changes between the singe snap shots as well as the absence of the previously noticed boundary force chains. Instead, we observe solid-paths which cross the boundary in

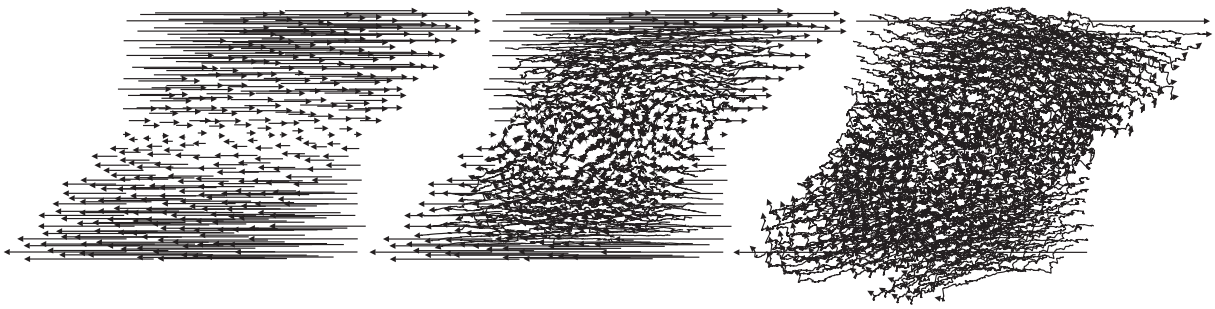

Figure 4.19.: Motion of the individual grains by trace lines: Simple shear deformation. *Left*: Assumption of TAYLOR. *Center*: Restricted TAYLOR assumption. *Right*: Periodic boundary conditions.

a periodic manner, reflecting the nature of the underlying assumption of periodicity. Gathering the available information of the center column of Figure 4.18, one recognizes once more, a behavior similar to the restricted TAYLOR assumption. In particular, the shape of the contact density function as well as its change of shape strongly confirm between the two boundary conditions. Remarkable results are presented in the last column of Figure 4.18. Therein, strong similarities between the contact density function and the force density function attract our attention. In particular, the first row of images seem very much alike, pointing not only to a well balanced but also well utilized contact network. With increasing load, this significant feature slowly fades out, finally leading to the previously noticed alignment between the direction of loading and the direction of force flux.

4.5.2. Microscopic investigations - simple shear

For closer observations, we perform a simple shear test in horizontal direction. To ensure the stability of the rves throughout the shearing process, each rve is compressed in a bi-axial manner. In particular, we apply the macroscopic deformation gradient tensor $\overline{\boldsymbol{F}} = \delta_{ij}\left[1-\lambda_c\right]\boldsymbol{e}_i \otimes \boldsymbol{e}_j$. The bi-axial compression is applied in 10 uniform load steps with $\lambda_c \in [0 \rightarrow 0.01]$. Hereupon, shear deformation is subjected by $\overline{\boldsymbol{F}} = \delta_{ij}\left[1-\lambda_c\right]\boldsymbol{e}_i \otimes \boldsymbol{e}_j + \lambda_s \boldsymbol{e}_1 \otimes \boldsymbol{e}_2$, whereby λ_c is set to 0.01 throughout the shearing. In the sequent, we exclusively focus on the results of the shearing deformation and leave the initially applied compression unconsidered. Trace lines of the considered deformation under different boundary conditions are depicted in Figure 4.19. Once more we observe the differences between the individual boundary conditions. In contrast to the previously considered deformation, trace lines with respect to the simple shear deformation show a rather strong fluctuational behavior. To study the inter-particle connectivity as well as the direction of force flux, we utilize the introduced plotting methods. The results in regards to the assumption of TAYLOR are depicted in Figure 4.20. The first row of plots relates to a loading stage of $\lambda_s = 0.333$, the second row to $\lambda_s = 0.666$ and the bottom row to $\lambda_s = 1$. The related force network plots show behaviors which relate to the observations under uni-axial compression. In particular, we notice an increase of line thickness of the solid paths, which correlates to the loading stage. Considering the homogeneous mapping of all grains, the orientation of the

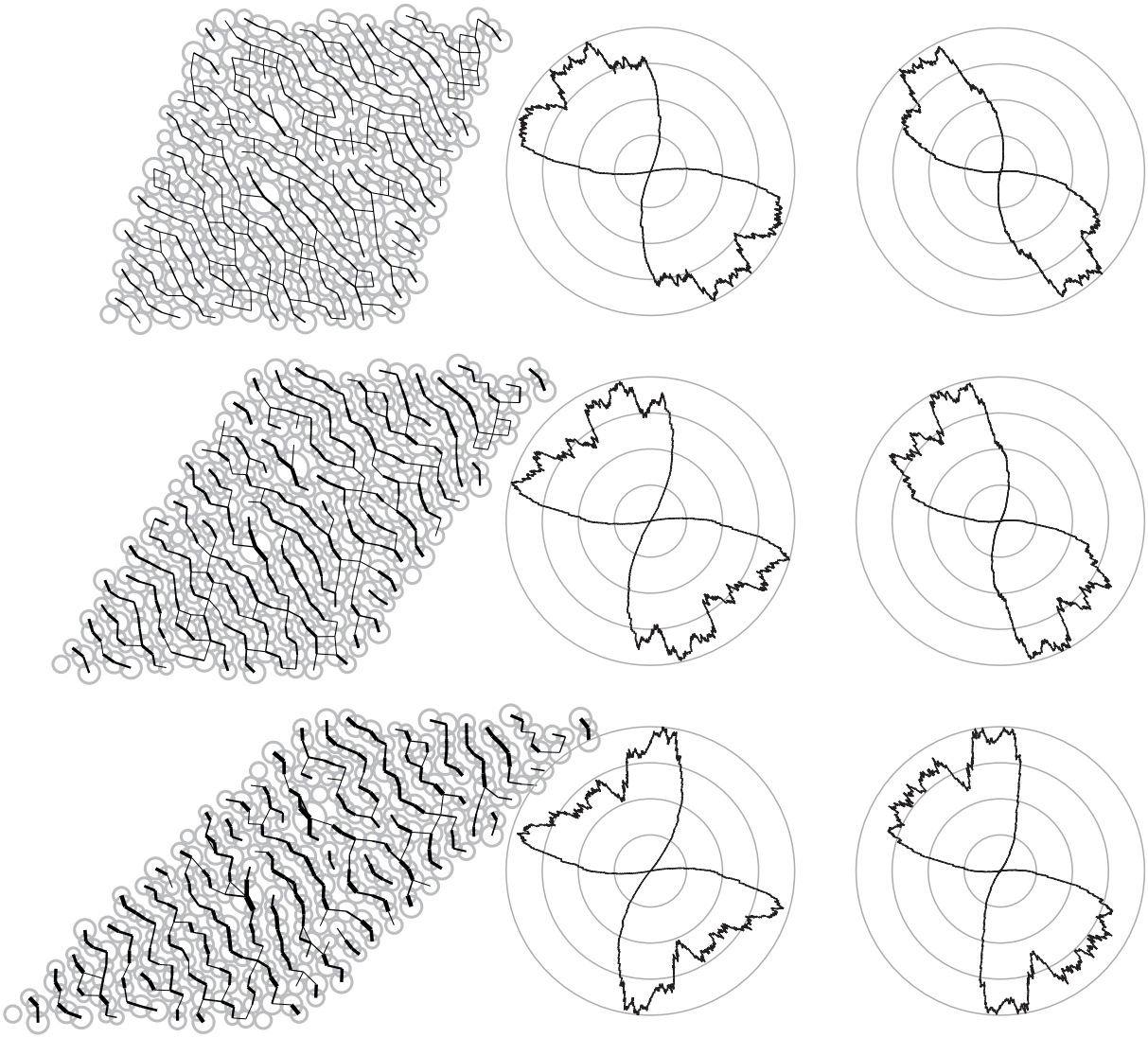

Figure 4.20.: Simple shear deformation: TAYLOR assumption. Each row relates to a state of deformation, starting in the top row with $\lambda_s = 0.333$ and increasing by 0.333 to the bottom row of $\lambda_s = 1.0$. *Left column*: Inter-particle force network. *Center column*: Contact density function. *Right column*: Force density function. The angle of influence is set to 25°.

branches is once more related to the deformation process. Under the present form of loading, the run of the solid paths appear to be orthogonal to the line of elongation. In the direction of elongation, nearly no branching is observed. The contact density function plots support the observations in regards to the force network plots. We point out the directional dependence of the branch network, oriented orthogonal to the direction of elongation. Comparing the single snap shots, the spreading of the primary axis flares gradually, while the necking remains. The force density plots are considered to be qualitatively matchable to the discussed contact density plots. Especially, features like the direction dependence, the flaring as well as the necking are remarkable. These similarities indicate a well utilized contact network, whereby the network itself shows a rather anisotropic nature. Figure 4.21 plots the results in regards to the restricted TAYLOR assumption. The order as well as the loading relation of the images is kept to match the previously discussed results. The obtained force network plots show a

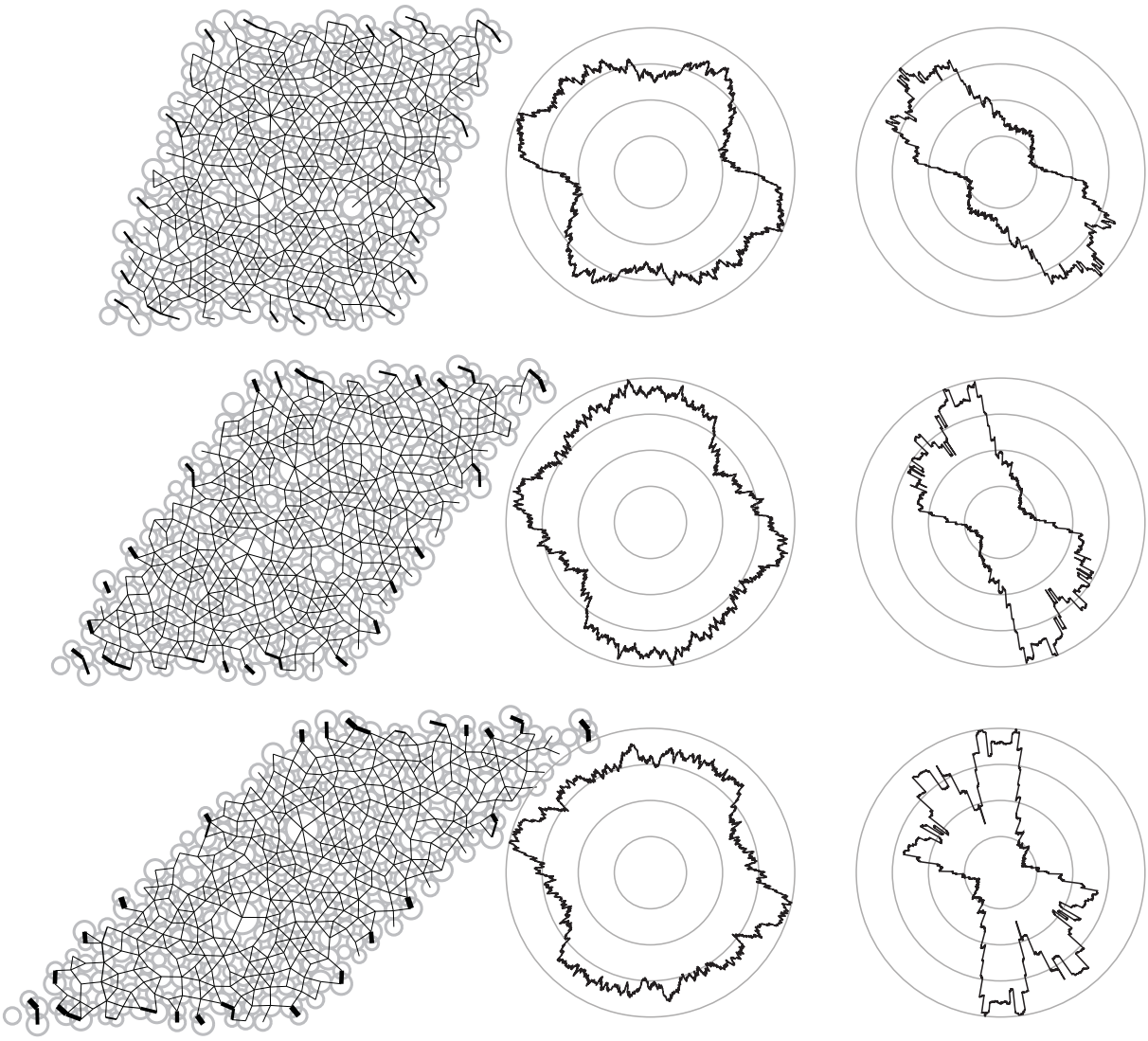

Figure 4.21.: Simple shear deformation: Restricted TAYLOR assumption. Each row relates to a state of deformation, starting in the top row with $\lambda_s = 0.333$ and increasing by 0.333 to the bottom row of $\lambda_s = 1.0$. *Left column*: Inter-particle force network. *Center column*: Contact density function. *Right column*: Force density function. The angle of influence is set to 25°.

well developed bulk network. Therein, only minor fluctuations in regards to the magnitude of the inter-particle contact forces between the inner grains are recognized. In contrast to the nearly even distribution of the force network of the bulk, strong force chains between boundary particles are visible. In particular, one might assume that the particle forces of the bulk may be considered to be neglectable. Their distinguishing character strongly relates to the nature of the applied boundary condition, already discussed for the uni-axial compression test. The contact density function plots show the existence of a well developed contact network for all depicted loading stages. Preferred contact directions are visible throughout all stages, whereby under the increase of loading rise of distinctness is noticed. Gathering the information of the contact force density functions, the previous assumption is verified, i.e., the contact forces between boundary particles are considered to be critical. Essentially, we find that the overall force flux information is strongly distorted by the boundary particles. Plots related to

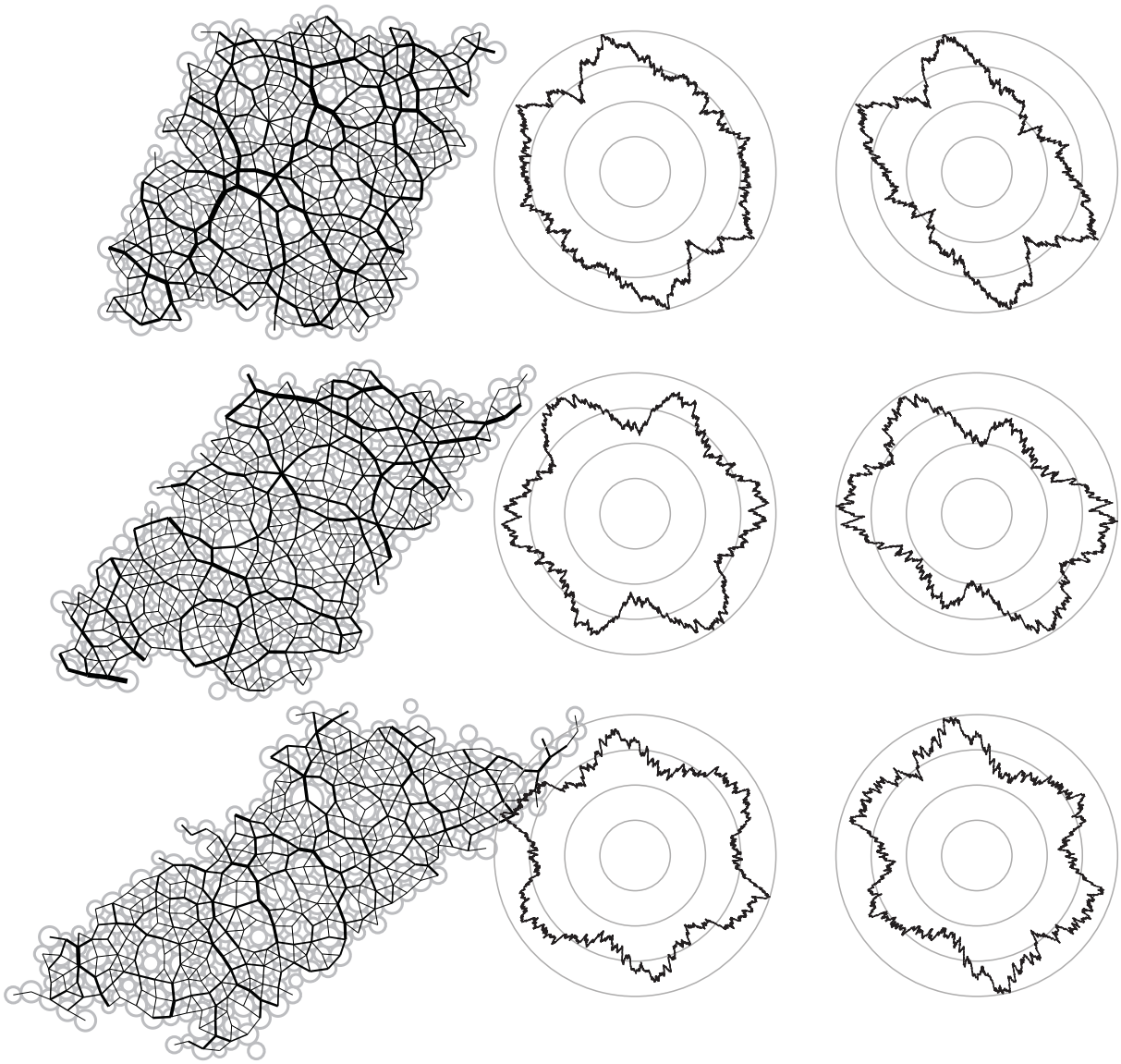

Figure 4.22.: Simple shear deformation: Periodic boundary conditions. Each row relates to a state of deformation, starting in the top row with $\lambda_s = 0.333$ and increasing by 0.333 to the bottom row of $\lambda_s = 1.0$. *Left column*: Inter-particle force network. *Center column*: Contact density function. *Right column*: Force density function. The angle of influence is set to 25°.

the periodic boundary conditions are depicted in Figure 4.22, ordered as described in the latter. Throughout the depicted force network plots, one observes well balanced force networks which demonstrate the periodic character of the underlying boundary conditions. In contrast to the remaining boundary conditions, a decrease in the particle contact forces with increasing shear is observed. On the first view, the arrangement of the boundary grains reflects disorder, however, their geometric periodicity is conserved. The contact density functions in Figure 4.22 show similarities to the contact density functions under the restricted TAYLOR assumption, depicted in Figure 4.21. Especially the star like shape, pointing to a well developed contact network, is noticeable. The sequence of the force density function depicts a sound developed force network which shows minor directional dependence. Similarities between the contact

density function plots and the force density function plots are obvious and underline the utilization of the inter-particle contact network.

5. Discrete homogenization

5.1. Introduction

The development of appropriate expressions of a macroscopic stress of confined discrete matter is discussed in this chapter. Stress as a continuum measure is related to an infinitesimal region of continuous media. Tending to the locally attached discrete and unbonded microstructure, we emphasize that a meaningful microscopic stress measure is undefinable across the boundaries of the individual grains. However, viewing each grain as a deformable continuum, the usual definition of stress is applicable within each grain. Enforcing the concept of volume averaging in the manner of HILL [58] and WEBER [153], the locally underlying inhomogeneous microstructure is homogenized. This particular method of bridging the length scales is founded on two assumptions of the locally attached microstructure. It is assumed that the microstructure is macroscopically small enough to convey solely local information. At the same time, the microstructure is demanded to be microscopically large enough to be statistically sound. Satisfying both demands allows to define a meaningful macroscopic stress measure, which incorporates information of the locally attached discrete microstructure. Certain formulations of the macroscopic stress of discrete matter exist, see, e.g., BAGI [3], DRESCHER & DE JOSSELIN DE JONG [37], CHRISTOFFERSEN, MEHRABADI & NEMAT-NASSER [21] and ROTHENBURG & SELVADURAI [124]. However, the provided stress measures do not incorporate the influence of different microscopic boundary conditions. Our focus is on presenting macroscopic stress expressions of confined particulate media, tailored with respect to select microscopic boundary conditions. We provide the reader with two alternatives to define a general expression of the macroscopic stress. At first, in the manner of TADMOR ET AL. [135], we relate the macroscopic energy density of a point in a continuum to the volume averaged energy density of the discrete particle assembly. Derivation of the identified macroscopic energy density with respect to the macroscopic deformation gradient yields an expression of the general macroscopic PIOLA stress. The second approach is based on the identity of virtual work between the macroscopic continuum and the locally attached discrete microstructure. Relating the virtual work expressions yields a general definition of the macroscopic PIOLA stress. This general definition does not include an assumption in regards to microscopic boundary conditions. Subjecting microscopic boundary conditions to the derived general stress expressions yields the loss of generality and results in microscopic boundary condition specific macroscopic stress formulations. We provide stress formulations for the assumption of TAYLOR, the restricted TAYLOR assumption, as well as for the periodic boundary conditions. Related measures are published by BORJA & WREN [13], DETTMAR [33], MIEHE & DETTMAR [91] or WREN & BORJA [159]. Even though the proposed schemes allow for the periodic deformation of the microscopic

rve, particle flux is not addressed. Particle flux itself defines as the process of particles crossing the predefined boundary particle set and interact with periodically replicated particles. We seize the challenge of considering particle flux and provide proper stress reformulations.

5.2. General macroscopic stress

This section describes the derivation of a general macroscopic PIOLA stress. To begin, we define the macroscopic energy density by means of the energy of the particulate aggregate. Therefore, we utilize a standard volume averaging procedure. The obtained relation between the two scales builds the basis of the proposed homogenization strategy. Linearizing the energetic scale relation with respect to the macroscopic deformation gradient tensor yields a general expression of the macroscopic PIOLA stress. A remark, concerning the derivation of the general macroscopic PIOLA stress in terms of the virtual work identity between the macro and the microscale finalizes this section.

5.2.1. Macroscopic potential energy density

Starting with the microscopic energy of the particle assembly, see (4.6), we focus on relating this particular result to the macroscale. We find an energy density with respect to the material configuration to be an appropriate quantity to relate between the two scales. Smearing out the microscopic potential energy over the volume of the undeformed rve, i.e., we simply divide (4.6) by the undeformed volume of the microscopic rve, yields a macroscopic energy density,

$$\overline{\Phi}^{n+1} = \left\langle \Phi^{n+1} \right\rangle = \frac{1}{2V_{\text{rve}}} \sum_{i \in \mathscr{P}^*} \sum_{\substack{j \in \mathscr{P}^* \\ j \neq i}} \Phi_{ij}^{n+1}. \tag{5.1}$$

The triangular brackets in (5.1) denote the volume averaging procedure of an overall quantity, $\langle \bullet \rangle = 1/V_{\text{rve}} \bullet$, whereby V_{rve} refers to the volume of the undeformed rve. We define the volume of the rve by a poly-line, connecting the centers of the boundary particles, see Figure 5.1 (left). Obtaining a polygonal area is considered to be complicated and computationally expensive. However, the present choice of rves, i.e., rves incorporating a geometric periodic boundary, allow the calculation of their volume in an efficient way. We relate the polygonal area to an area which is spanned by the two branch vectors $\boldsymbol{L}_{ab}$ and $\boldsymbol{L}_{ad}$, see Figure 5.1 (right). Thus, in this particular case, the volume of the rve computes to $V_{\text{rve}} = ||\boldsymbol{L}_{ab} \times \boldsymbol{L}_{ad}||$. Pointing out that this research solely considers square rves, one might compute the initial volume of the rve by $V_{\text{rve}} = ||\boldsymbol{L}_{ab}||^2 = ||\boldsymbol{L}_{ad}||^2 = ||\boldsymbol{L}_{\ominus\oplus}||^2$.

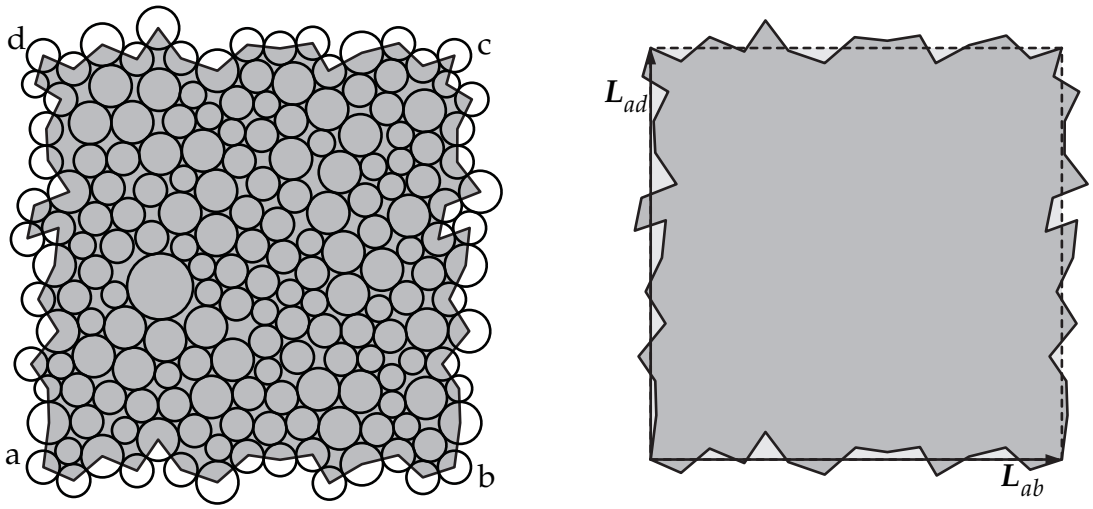

Figure 5.1.: Volume of an geometric periodic rve. *Left*: Granular rve. The area, considered as the volume of the rve, is shaded in gray. Corner particles are marked by lower case letters. *Right*: Relation between the actual rve area (shaded in gray) and the area spanned by the branch vectors $\boldsymbol{L}_{ab}$ and $\boldsymbol{L}_{ad}$.

5.2.2. General macroscopic stress - energy approach

In classical continuum mechanics, the PIOLA stress associates to the total derivative of a potential function, i.e., Φ is linearized with respect to the deformation gradient, $\boldsymbol{P} = \mathrm{d}\Phi/\mathrm{d}\boldsymbol{F}$. Applying this relation to colligate the macroscopic PIOLA stress to the macroscopic energy density, we take the total derivative of the macroscopic energy density, see (5.1), with respect to the macroscopic deformation gradient. Recalling the dependence of the microscopic fluctuations, i.e., $\boldsymbol{\Xi}_i\left(\overline{\boldsymbol{F}}\right)$, the expression of the macroscopic PIOLA stress yields,

$$\overline{\boldsymbol{P}} = \frac{\mathrm{d}\overline{\Phi}}{\mathrm{d}\overline{\boldsymbol{F}}} = \frac{\partial\overline{\Phi}}{\partial\overline{\boldsymbol{F}}} + \sum_{m\in\mathscr{F}^*} \frac{\partial\overline{\Phi}}{\partial\boldsymbol{\Xi}_m} \bullet \frac{\partial\boldsymbol{\Xi}_m}{\partial\overline{\boldsymbol{F}}}. \tag{5.2}$$

We can identify two shares which contribute to the general macroscopic stress of the particle aggregate. The first term, i.e., the partial derivative of the macroscopic potential with respect to the macroscopic deformation gradient, does not include any fluctuational contributions. The second term relates to the fluctuations. Naturally, the last share only incorporates contributions of particles which hold fluctuations, i.e., are not linear dependent on the macroscopic deformation gradient tensor. These particles combine in set $\mathscr{F}^*$, which is a subset of $\mathscr{P}^*$. In the following, we tend to the individual derivatives in (5.2). The reader is advised that the non-trivial derivatives, i.e., the partial derivative of the individual fluctuations with respect to the macroscopic deformation gradient tensor, are listed in Appendix A.3. Inserting the introduced relation between the pair and the global potential, see (4.6), as well as considering that the

second term solely contributes for $i = m$ or $j = m$, (5.2) is re-casted.

$$\overline{\boldsymbol{P}} = \frac{1}{2V_{\text{rve}}} \left[\sum_{i \in \mathscr{P}^*} \sum_{\substack{j \in \mathscr{P}^* \\ j \neq i}} \frac{\partial \Phi_{ij}}{\partial \overline{\boldsymbol{F}}} + 2 \sum_{i \in \mathscr{F}^*} \sum_{\substack{j \in \mathscr{P}^* \\ j \neq i}} \frac{\partial \Phi_{ij}}{\partial \boldsymbol{\Xi}_i} \bullet \frac{\partial \boldsymbol{\Xi}_i}{\partial \overline{\boldsymbol{F}}} \right]. \tag{5.3}$$

The first derivative, i.e., taking the partial derivative of the pair potential with respect to the macroscopic deformation gradient, becomes:

$$\frac{\partial \Phi_{ij}}{\partial \overline{\boldsymbol{F}}} = \boldsymbol{f}_{ij} \otimes \left[\overline{\boldsymbol{F}}^{-1} \bullet \boldsymbol{l}_{ij} \right]. \tag{5.4}$$

Please observe that $\boldsymbol{L}_{ij} + \boldsymbol{\Xi}_j - \boldsymbol{\Xi}_i$ is replaced by $\overline{\boldsymbol{F}}^{-1} \bullet \boldsymbol{l}_{ij}$ to shorten the expression. The partial derivative of the pair potentials with respect to the individual particle fluctuations reads:

$$\frac{\partial \Phi_{ij}}{\partial \boldsymbol{\Xi}_i} = -\boldsymbol{f}_{ij} \bullet \overline{\boldsymbol{F}}. \tag{5.5}$$

Recalling the statement of reciprocal forces, see (4.9), the definition of the branch vector, given in (3.4) as well as the postulation of the particle force, i.e., $\boldsymbol{f}_i = \sum_{j \in \mathscr{P}^*} \boldsymbol{f}_{ij}$, the explicit expression of the macroscopic PIOLA stress yields:

$$\overline{\boldsymbol{P}} = -\frac{1}{V_{\text{rve}}} \left[\sum_{i \in \mathscr{P}^*} \boldsymbol{f}_i \otimes \left[\overline{\boldsymbol{F}}^{-1} \bullet \boldsymbol{x}_i \right] + \sum_{i \in \mathscr{F}^*} \boldsymbol{f}_i \bullet \overline{\boldsymbol{F}} \bullet \frac{\partial \boldsymbol{\Xi}_i}{\partial \overline{\boldsymbol{F}}} \right]. \tag{5.6}$$

Remark 5.1 (General macroscopic stress - virtual work consideration) The central point of this remark is the application of the so-called HILL-MANDEL theorem. Enforcing the HILL-MANDEL theorem, the virtual work on the macroscale, denoted by $\delta\overline{\mathcal{W}}$, is related to the volume average of the microscopic virtual work $\langle \delta\mathcal{W} \rangle$,

$$\delta\overline{\mathcal{W}} = \langle \delta\mathcal{W} \rangle. \tag{5.7}$$

This particular identity represents the common point of departure to derive an expression for the macroscopic PIOLA stress. The virtual work on the macroscale level is expressed by a double contraction of the macroscopic PIOLA stress $\overline{\boldsymbol{P}}$ and the infinitesimal macroscopic deformation gradient tensor $\delta\overline{\boldsymbol{F}}$,

$$\delta\overline{\mathcal{W}} = \overline{\boldsymbol{P}} : \delta\overline{\boldsymbol{F}}. \tag{5.8}$$

On the microscopic level, the volume average of the microscopic virtual work has to be equivalent to the sum of the virtual work, which is performed on the single grains. The

virtual work regarding a single particle contact is expressed by the single contraction between the negative particle contact force and the virtual displacement of the particle.

$$\delta \mathcal{W}_{ij} = -\boldsymbol{f}_{ij} \bullet \delta \boldsymbol{u}_i. \tag{5.9}$$

The reader is advised that the virtual displacement $\delta \boldsymbol{u}_i$ relates to the enlargement of the overlap and thus conjugates to the negative contact force. Hence, both quantities always join a positive virtual work expression. The virtual work performed on a single particle equals:

$$\delta \mathcal{W}_i = \sum_{\substack{j \in \mathscr{P}^* \\ j \neq i}} \delta \mathcal{W}_{ij} = -\sum_{\substack{j \in \mathscr{P}^* \\ j \neq i}} \boldsymbol{f}_{ij} \bullet \delta \boldsymbol{u}_i. \tag{5.10}$$

Summation over all relevant particles results in the total virtual work on the microscale level. Applying the averaging procedure for overall quantities, i.e., dividing the total virtual work by the volume of the rve, yields the volume average of the virtual work contribution on the microscale level,

$$\langle \delta \mathcal{W} \rangle = -\frac{1}{V_{\mathsf{rve}}} \sum_{i \in \mathscr{P}^*} \sum_{\substack{j \in \mathscr{P}^* \\ j \neq i}} \boldsymbol{f}_{ij} \bullet \delta \boldsymbol{u}_i. \tag{5.11}$$

Using the relation between the reciprocal contact forces, see (4.9), as well as the field condition $\boldsymbol{l}_{ij} - \boldsymbol{L}_{ij} = \boldsymbol{u}_j - \boldsymbol{u}_i$, (5.11) is re-casted to:

$$\langle \delta \mathcal{W} \rangle = \frac{1}{2V_{\mathsf{rve}}} \sum_{i \in \mathscr{P}^*} \sum_{\substack{j \in \mathscr{P}^* \\ j \neq i}} \boldsymbol{f}_{ij} \bullet \delta \left[\boldsymbol{l}_{ij} - \boldsymbol{L}_{ij} \right]. \tag{5.12}$$

Therein, each virtual work contribution relates to a single contraction between the contact forces $\boldsymbol{f}_{ij}$ and the corresponding, infinitesimal changed length of the branch vector $\delta \left[\boldsymbol{l}_{ij} - \boldsymbol{L}_{ij} \right]$. Writing out the variation of the change of the branch vector yields,

$$\delta \left[\boldsymbol{l}_{ij} - \boldsymbol{L}_{ij} \right] = \delta \overline{\boldsymbol{F}} \bullet \left[\overline{\boldsymbol{F}}^{-1} \bullet \boldsymbol{l}_{ij} \right] + \overline{\boldsymbol{F}} \bullet \left[\frac{\partial \boldsymbol{\Xi}_j}{\partial \overline{\boldsymbol{F}}} - \frac{\partial \boldsymbol{\Xi}_i}{\partial \overline{\boldsymbol{F}}} \right] \boldsymbol{:} \delta \overline{\boldsymbol{F}}. \tag{5.13}$$

Inserting (5.13) into (5.12), followed by some simple manipulation as well as considerations regarding the summation ranges, equates to:

$$\langle \delta \mathcal{W} \rangle = -\frac{1}{V_{\mathsf{rve}}} \left[\sum_{i \in \mathscr{P}^*} \boldsymbol{f}_i \otimes \left[\overline{\boldsymbol{F}}^{-1} \bullet \boldsymbol{x}_i \right] + \sum_{i \in \mathscr{P}^*} \boldsymbol{f}_i \bullet \overline{\boldsymbol{F}} \bullet \frac{\partial \boldsymbol{\Xi}_i}{\partial \overline{\boldsymbol{F}}} \right] \boldsymbol{:} \delta \overline{\boldsymbol{F}}. \tag{5.14}$$

Comparing (5.8) and (5.14), we conclude a general description for the macroscopic

PIOLA stress

$$\overline{\boldsymbol{P}} = -\frac{1}{V_{\text{rve}}} \left[\sum_{i \in \mathscr{P}^*} \boldsymbol{f}_i \otimes \left[\overline{\boldsymbol{F}}^{-1} \bullet \boldsymbol{x}_i \right] + \sum_{i \in \mathscr{F}^*} \boldsymbol{f}_i \bullet \overline{\boldsymbol{F}} \bullet \frac{\partial \Xi_i}{\partial \overline{\boldsymbol{F}}} \right]. \tag{5.15}$$

The macroscopic PIOLA stress, obtained from the virtual work statement, see (5.15), clearly shows the equivalence to the PIOLA stress stated in (5.6). Thus, both approachs, i.e., the virtual work and the energy approach, lead to the same general expression of the macroscopic PIOLA stress. We favor the approach of deriving the macroscopic PIOLA stress by relating the microscopic and the macroscopic energy densities. ■

Remark 5.2 (Sign convention of the macroscopic stress) We remark that the derived stresses confirm to the standard sign convention of classical continuum mechanics, i.e., pressure is indicated by a negative sign, whereas tensile stress is indicated by positive quantities. ■

5.3. Boundary specific macroscopic stress

Thus far, the expression of the macroscopic PIOLA stress is of a general form, i.e., no microscopic boundary conditions are included in the stress formulation. Application of microscopic boundary conditions to these general expressions allows the derivation of microscopic boundary condition specific macroscopic stresses. In view of the discussed boundary conditions, we restricted this study to the assumption of TAYLOR, the restricted TAYLOR assumption and the periodic boundary conditions.

5.3.1. Macroscopic stress - Taylor assumption

At first we consider the assumption of TAYLOR, described in Subsection 4.3.2. As pointed out, under this kind of boundary conditions the microscopic individual particle fluctuations are neglected in the whole rve, i.e., $\Xi_i = \boldsymbol{0}, \forall i \in \mathscr{P}$. Hence, each spatial particle position is described by $\boldsymbol{x}_i = \overline{\boldsymbol{F}} \bullet \boldsymbol{X}_i, \forall i \in \mathscr{P}$. Consequently, the second summation in (5.15) disappears and the macroscopic PIOLA stress computes to,

$$\overline{\boldsymbol{P}} = \frac{1}{V_{\text{rve}}} \sum_{i \in \mathscr{P}} \boldsymbol{r}_i \otimes \boldsymbol{X}_i. \tag{5.16}$$

In general, one finds the particle reaction forces to be non zero for the individual grains, see Figure 4.6. Nevertheless, we remark once more that the sum of all reaction forces vanishes over the entire rve. We observe that the macroscopic PIOLA stress, concerning the assumption of TAYLOR, consists of a volume weighted summation of the tensor product between the particle reaction forces in the spatial and the particle positions in the material configuration over all particles in the rve. Using (2.5) transfers the

macroscopic PIOLA stress to the macroscopic CAUCHY stress,

$$\overline{\boldsymbol{\sigma}} = \frac{1}{v_{\mathsf{rve}}} \sum_{i \in \mathscr{P}} \boldsymbol{r}_i \otimes \boldsymbol{x}_i, \tag{5.17}$$

where v_{rve} refers to the volume of the rve in the spatial configuration, i.e., $v_{\mathsf{rve}} = \overline{J} V_{\mathsf{rve}}$. Manipulation of (5.17) demonstrates the expected symmetry of the macroscopic CAUCHY stress.

$$\overline{\boldsymbol{\sigma}} = -\frac{1}{2v_{\mathsf{rve}}} \sum_{i \in \mathscr{P}} \sum_{\substack{j \in \mathscr{P} \\ j \neq i}} E_{ij} \mathscr{H}\Big(\varepsilon_{ij}\Big)\, \varepsilon_{ij} \Big|\Big| \boldsymbol{l}_{ij} \Big|\Big| \, \boldsymbol{n}_{ij} \otimes \boldsymbol{n}_{ij} \tag{5.18}$$

The symmetry itself is expressed by the dyadic product between the contact normal vectors in the spatial configuration. As pointed out by WELLMANN, LILLIE & WRIGGERS [154], the macroscopic stress is directly proportional to the contact stiffness. Equation (5.18) reveals that this proportionality is introduced by the inter-particle contact forces.

5.3.2. Macroscopic stress - restricted Taylor assumption

In the case of the restricted TAYLOR assumption, particles of set $\mathscr{B}$ are mapped by the macroscopic deformation gradient and do not include superimposed fluctuational parts, see (4.27). However, particles of the bulk contain a fluctuational part, leading to $\mathscr{F}^* = \mathscr{I}^*$. These grains are demanded to finally reach their equilibrium positions, resulting to zero particle forces, i.e., $\boldsymbol{f}_i = \boldsymbol{0} \quad \forall\, i \in \mathscr{F}^*$. Applying this consideration to (5.6), the second summation disappears. Particle reaction forces on the boundary do, in general, not vanish, compare Figure 4.7. As a result, the restricted TAYLOR specific expression of the macroscopic PIOLA stress becomes,

$$\overline{\boldsymbol{P}} = \frac{1}{V_{\mathsf{rve}}} \sum_{i \in \mathscr{B}} \boldsymbol{r}_i \otimes \boldsymbol{X}_i. \tag{5.19}$$

While similarities between (5.16) and (5.19) are obvious, the main difference is found in the definition of the summation limits. As a result of the relaxed internal aggregate, contributions from the inner particles drop out, reducing the summation limit to a summation over the boundary particles. Hence, by applying the restricted TAYLOR assumption on the microscale level, the macroscopic PIOLA stress solely defines by quantities of the boundary particles. Pushing the macroscopic PIOLA stress to the spatial configuration leads to an expression of the macroscopic CAUCHY stress,

$$\overline{\boldsymbol{\sigma}} = -\frac{1}{2v_{\mathsf{rve}}} \sum_{i \in \mathscr{B}} \sum_{\substack{j \in \mathscr{P}^* \\ j \neq i}} E_{ij} \mathscr{H}\Big(\varepsilon_{ij}\Big)\, \varepsilon_{ij} \Big|\Big| \boldsymbol{l}_{ij} \Big|\Big| \, \boldsymbol{n}_{ij} \otimes \boldsymbol{n}_{ij}. \tag{5.20}$$

Differences in comparison to the macroscopic CAUCHY stress of the TAYLOR-VOIGT assumption are noticed in the first summation limit of (5.20), while the expression $\boldsymbol{n}_{ij} \otimes \boldsymbol{n}_{ij}$ is responsible once more for the symmetry of the macroscopic CAUCHY stress.

5.3.3. Macroscopic stress - periodic boundary conditions

The last microscopic boundary conditions under consideration are the periodic boundary conditions. Similar to the restricted TAYLOR assumption, the inner particles must find their equilibrium positions, yielding to zero particle forces of the inner particles. Furthermore, individual particle fluctuations of associated boundary particles are defined to be equal, $\boldsymbol{\Xi}_{\ominus} = \boldsymbol{\Xi}_{\oplus}$, while their reaction forces are anti-periodic, $\boldsymbol{r}_{\ominus} = -\boldsymbol{r}_{\oplus}$, see Figure 4.9. Additional application of the relation between particles on the opposite boundary, i.e., $\boldsymbol{L}_{\ominus\oplus} = \boldsymbol{X}_{\oplus} - \boldsymbol{X}_{\ominus}$, allows to compact (5.6).

$$\overline{\boldsymbol{P}} = -\frac{1}{V_{\mathsf{rve}}} \left[\sum_{i \in \mathscr{B}^*_{\oplus}} \boldsymbol{f}_i \otimes \boldsymbol{L}_{\ominus\oplus} + \sum_{i \in \{a,b,c,d\}} \boldsymbol{f}_i \otimes \boldsymbol{X}_i \right]. \tag{5.21}$$

Recalling the relation between the material branch vectors $\boldsymbol{L}_{\ominus\oplus}$ and the corner particles, (5.21) is transformed.

$$\overline{\boldsymbol{P}} = \frac{1}{V_{\mathsf{rve}}} \sum_{i \in \{a,b,c,d\}} \boldsymbol{r}^{\star}_i \otimes \boldsymbol{X}_i, \tag{5.22}$$

with

$$\boldsymbol{r}^{\star}_a = \boldsymbol{r}_a - \sum_{i \in \mathscr{B}^*_{\oplus}} \boldsymbol{r}_i, \quad \boldsymbol{r}^{\star}_b = \boldsymbol{r}_b + \sum_{i \in \mathscr{B}^*_{\oplus 1}} \boldsymbol{r}_i, \quad \boldsymbol{r}^{\star}_c = \boldsymbol{r}_c, \quad \boldsymbol{r}^{\star}_d = \boldsymbol{r}_d + \sum_{i \in \mathscr{B}^*_{\oplus 2}} \boldsymbol{r}_i, \tag{5.23}$$

whereby $\mathscr{B}^*_{\oplus 1}$ and $\mathscr{B}^*_{\oplus 2}$ refer to the positive boundaries of the horizontal and vertical direction of the rve, compare Figure 4.8. Please observe the compactness of the above expression, solely consisting of the summation of the dyadic products between combined particle reaction forces at the corners of the rve and their initial positions. This compact representation of the macroscopic PIOLA stress tensor correlates to its continuous counterpart, derived by KOUZNETSOVA, GEERS & BREKELMANS [69]. The expression in (5.23) is pushed forward to the spatial configuration, yielding the macroscopic CAUCHY stress. While the macroscopic CAUCHY stress for the case of periodic boundary conditions on the microscale is expressed by,

$$\overline{\boldsymbol{\sigma}} = \frac{1}{v_{\mathsf{rve}}} \sum_{i \in \{a,b,c,d\}} \boldsymbol{r}^{\star}_i \otimes \boldsymbol{x}_i, \tag{5.24}$$

the presentation of its symmetry ends up in expression (5.20) and is thus not repeated.

Remark 5.3 (Consideration of particle flux) In contrast to the application of periodic boundary conditions in the continuous case, unbounded discrete granular assemblies require the consideration of particle flux between the periodic cells. Particle flux may arise if gaps between neighboring boundary particles of set $\mathscr{B}$ reach a critical limit. This critical limit is strongly related to the incorporated grain size distribution as well as on the loading state of the rve. Gap emergence between neighboring boundary particles strongly relates to the soft nature of the periodic boundary conditions subjected to the granular assemblies under consideration. Based on the dense packing of the considered rves, particle flux itself attracts attention if particles from the inner particle set $\mathscr{I}$ contact with replicated particles, see Figure 5.3 (center row). Neglecting such contact events, i.e., simply applying the derived expression for the macroscopic stress, see (5.24), yields to the loss of symmetry of the macroscopic CAUCHY stress, see Figure 5.2 (left). The phenomena of the loss of symmetry basically explains by a violation

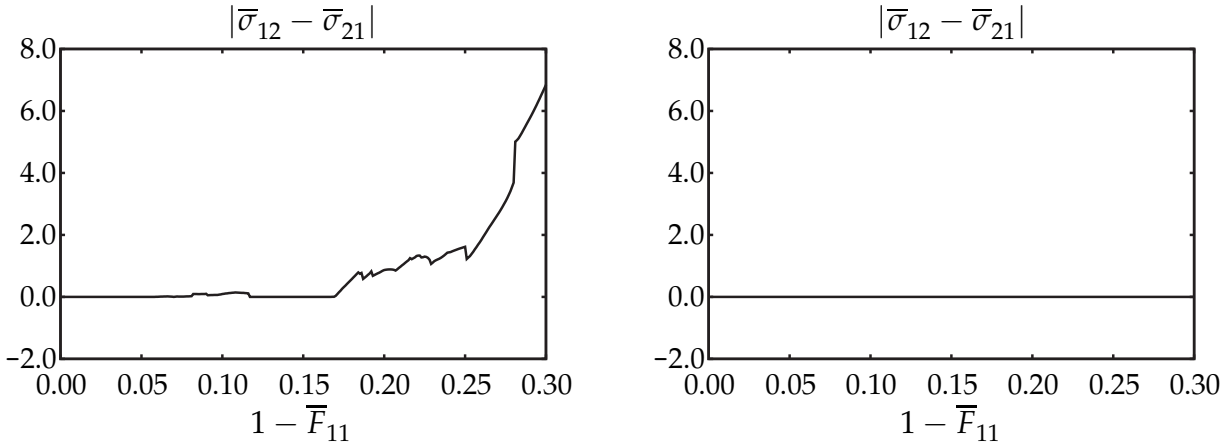

Figure 5.2.: Absolute values of the difference between the shear components of the macroscopic CAUCHY stress under periodic boundary conditions. Uni-axial compression in horizontal direction. *Left*: Unmodified expression, see (5.24). *Right*: Periodically enhanced expression, including additional boundary particle sets.

of $(4.33)_3$, i.e., the requirement of internal equilibrium. As one possible solution we propose an extension of the periodic cell by periodically enhancing the boundary particle set, compare Figure 5.3 (bottom row). Therein, the boundary set enhancement is illustrated by a change of the poly-line, connecting the centers of the boundary particles. In particular, one of the contacting grains and its replica particle, i.e., B and B′ in the depicted example, are used to enhance the boundary particle set. Using this kind of enhancement of the boundary particle set, the obtained macroscopic CAUCHY stress is guaranteed to be symmetric, see Figure 5.2 (right). Note that the extension by A and A′ will lead to the same results with respect to the macroscopic stress. Naturally, such an enhancement yields to the reduction of the inner particle set. Please note that this reformulation is solely required during the computation of the macroscopic stress and tangent. During the microscopic relaxation process no alternations of the

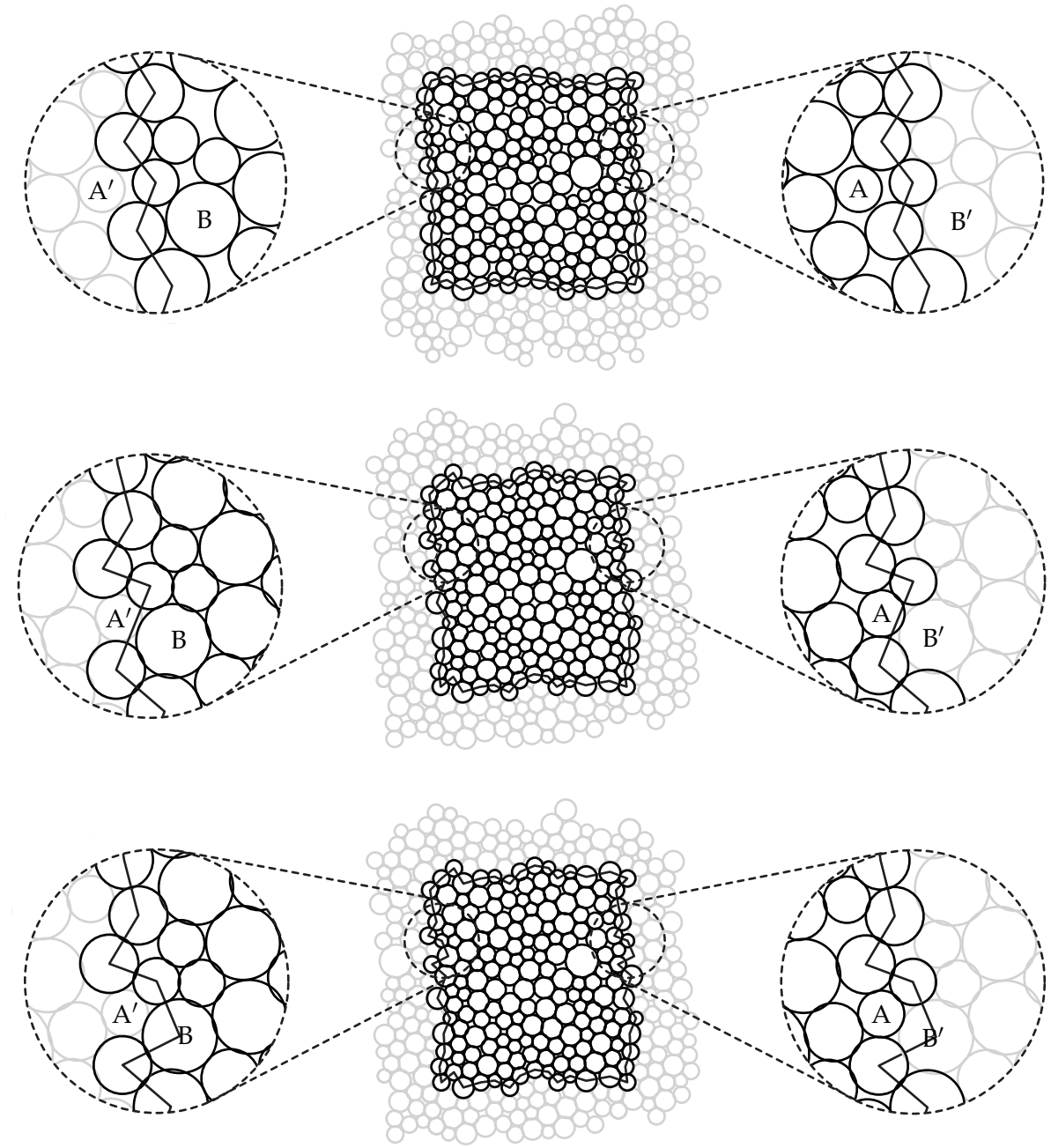

Figure 5.3.: Boundary reformulation under periodic boundary conditions. The process of reformulation is triggered by contacts between inner particles of the rve and replica particles. Primary particles of interest are denoted by capital letter. Upper case letters including a prime distinguish replica particles of interest. *Top row*: Initial undeformed configuration. *Center row*: Deformed configuration, original boundary. *Bottom row*: Deformed configuration, altered boundary.

inner or boundary particle set are performed. A similar phenomena, i.e., the contact between particles from different boundaries, yields to the mentioned asymmetry of the macroscopic CAUCHY stress as well. Once more, remedy is found by extending the summation limit and incorporating the additional required particles. ■

5.4. Representative numerical examples

The proposed computational homogenization is illustrated by selected numerical examples. Therefore, we generate three sets of rves. Each set contains 15 randomly generated rves. The individual sets differ in terms of their primary number of grains. The used grain size distribution data is listed in Table 5.1. At first, we subject uni-axial com-

Table 5.1.: Input parameters: 150, 300 and 600 primary particles.

grain ∅ $[mm]$	150 particles [/]	300 particles [/]	600 particles [/]
0.315	0	0	0
0.250	1	2	4
0.160	40	80	160
0.125	74	148	296
0.100	35	70	140

pression as well as simple shear to all three sets. These test, described in Section 4.5, are performed in horizontal and vertical direction. Quantities of interest are the macroscopic CAUCHY stress as well as the macroscopic energy density. Having studied the macroscopic output under basic deformation scenarios, we tend to the application of cyclic loading.

5.4.1. Macroscopic investigations - uni-axial compression

The Figures 5.4, 5.5 as well as 5.6 show the resulting mean values of the macroscopic CAUCHY stress and energy density in regards to the three different boundary conditions. Error bars depict the corresponding standard deviation. The partitioning of the figures is kept identical. The left and the right column refer to the horizontal and vertical compression tests, respectively. The top rows show the mean values of the macroscopic CAUCHY stress components in horizontal and vertical direction. The stress components in horizontal direction are plotted by solid lines, while dashed lines are used for the stress components in the vertical direction. The center rows depict the mean values of the shear components of the macroscopic CAUCHY stress, while the mean values of the macroscopic energy density are plotted in the bottom rows. Figure 5.4 depicts the results concerning the assumption of TAYLOR. Overall, the uni-axial compression tests demonstrate a good agreement for all rves, whereby the coarse scale smoothness as well as the grouped arrangement of the individual quantities is remarkable. The error bars are considerably small, whereby a slightly increasing behavior in terms of the shear components is noticed. A linear stress behavior in the direction of loading is observed. Orthogonal to the direction of loading, the stress response is non-linear, having an increasing slope. The increase of slope points to the rise of particle contacts and agrees with the microscopic observations. In particular, we remark that the stress

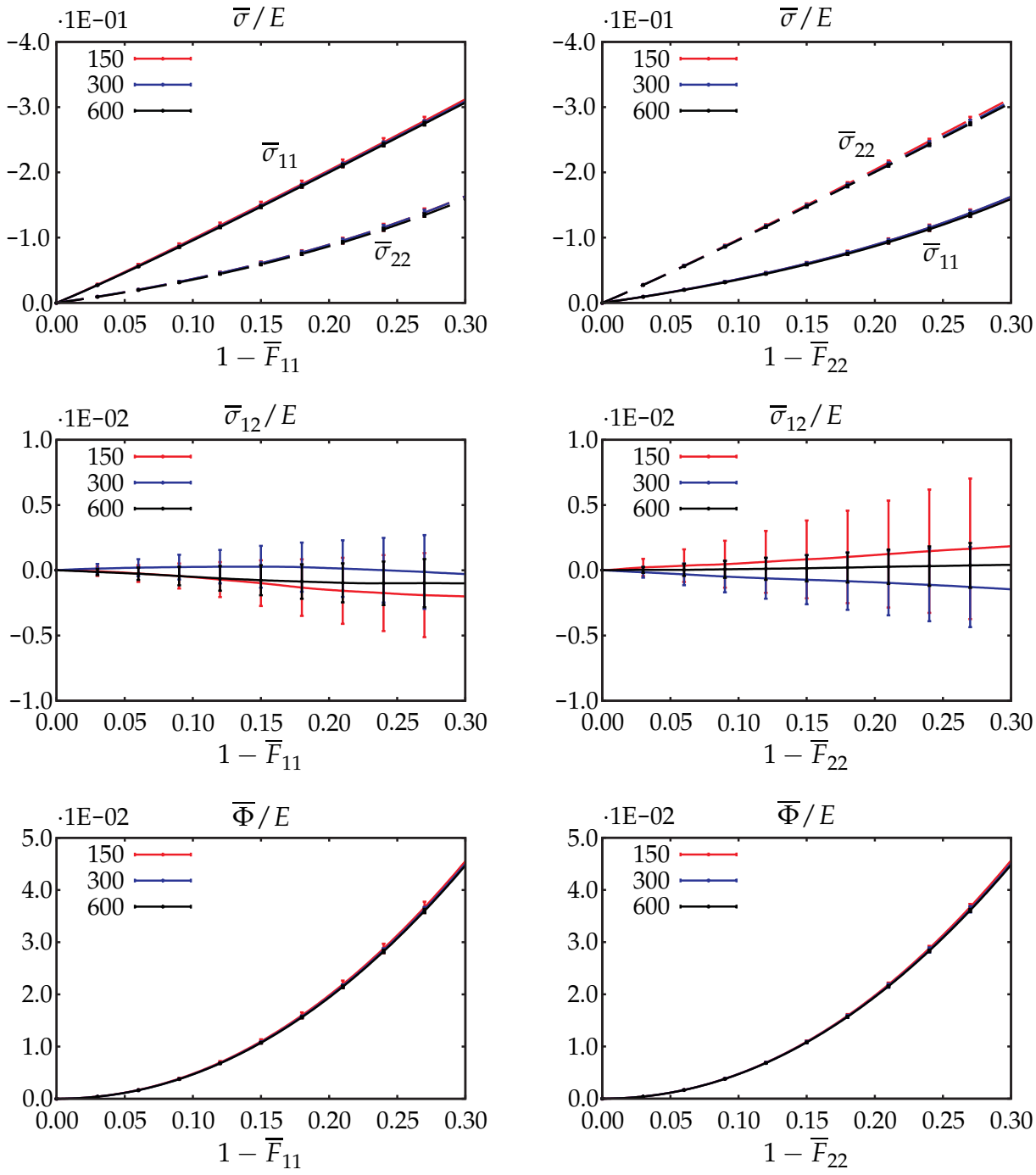

Figure 5.4.: Macroscopic quantities under uni-axial compression: Assumption of TAYLOR. Error bars show the standard deviation. All curves and error bars are scaled by the normal contact stiffness. *Left column*: Horizontal compression. *Right column*: Vertical compression. *Top row*: Macroscopic CAUCHY stress. Solid lines denote the stress component in horizontal direction, while dashed lines refer to the vertical stress component. *Center row*: Shear component of the macroscopic CAUCHY stress. *Bottom row*: Macroscopic energy density.

in loading direction shows a rather stiff behavior. The mean values of the shear stress components reveal the tendency to lean towards a value of zero as the number of particles increases. The macroscopic energy densities show a uniform character for all sets of rves. In particular, their response somehow resembles the used one-sided harmonic

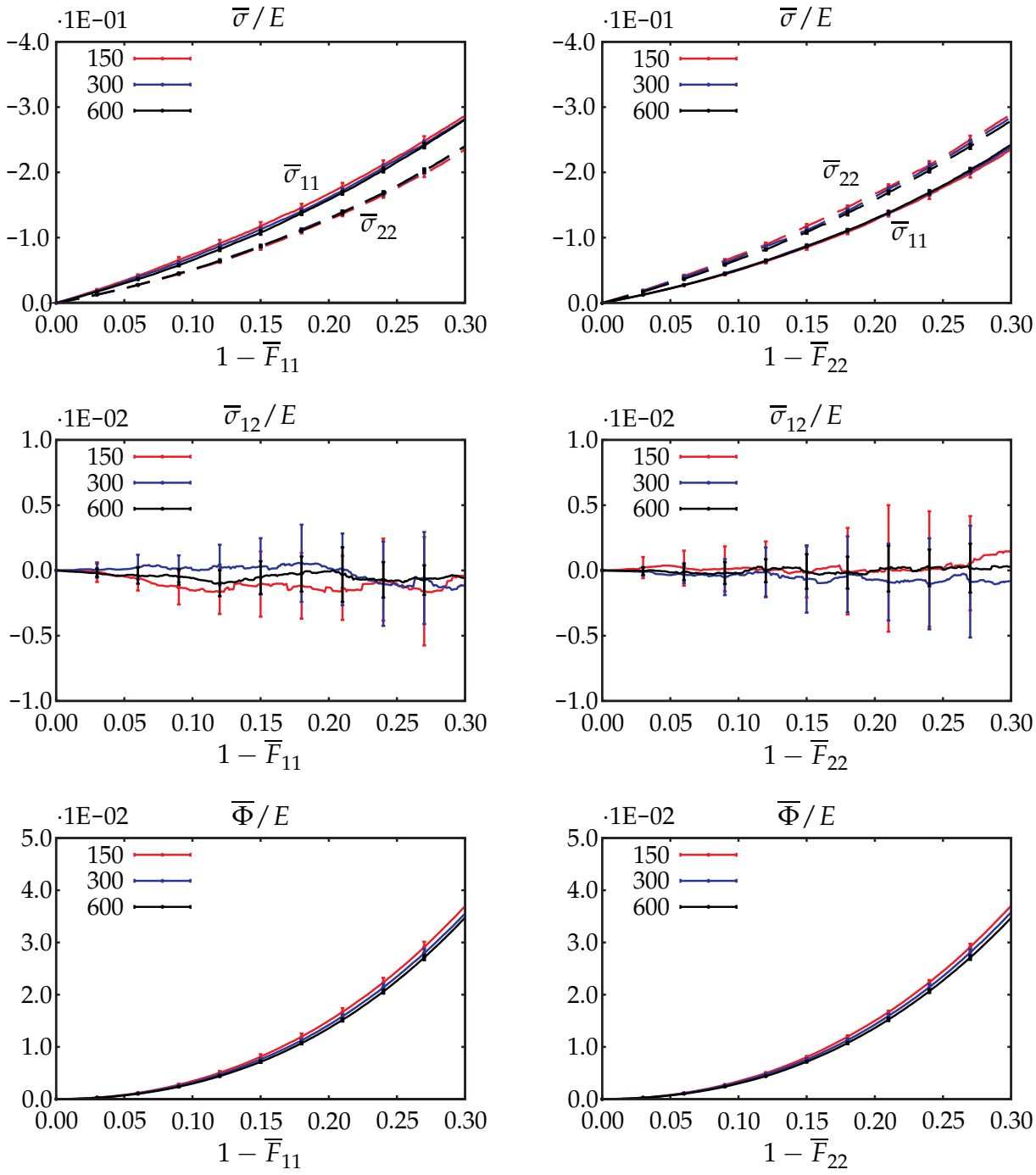

Figure 5.5.: Macroscopic quantities under uni-axial compression: Restricted TAYLOR boundary condition. Error bars show the standard deviation. All curves and error bars are scaled by the normal contact stiffness. *Left column*: Horizontal compression. *Right column*: Vertical compression. *Top row*: Macroscopic CAUCHY stress. Solid lines denote the stress component in horizontal direction, while dashed lines refer to the vertical stress component. *Center row*: Shear component of the macroscopic CAUCHY stress. *Bottom row*: Macroscopic energy density.

contact potential, compare Figure 4.2. A global comparison between the graphs belonging to the horizontal and vertical compression, i.e., the left and right column of Figure 5.4, reveals a good agreement, considering the switched direction of loading. The mean value CAUCHY stress and energy density curves obtained by applying the

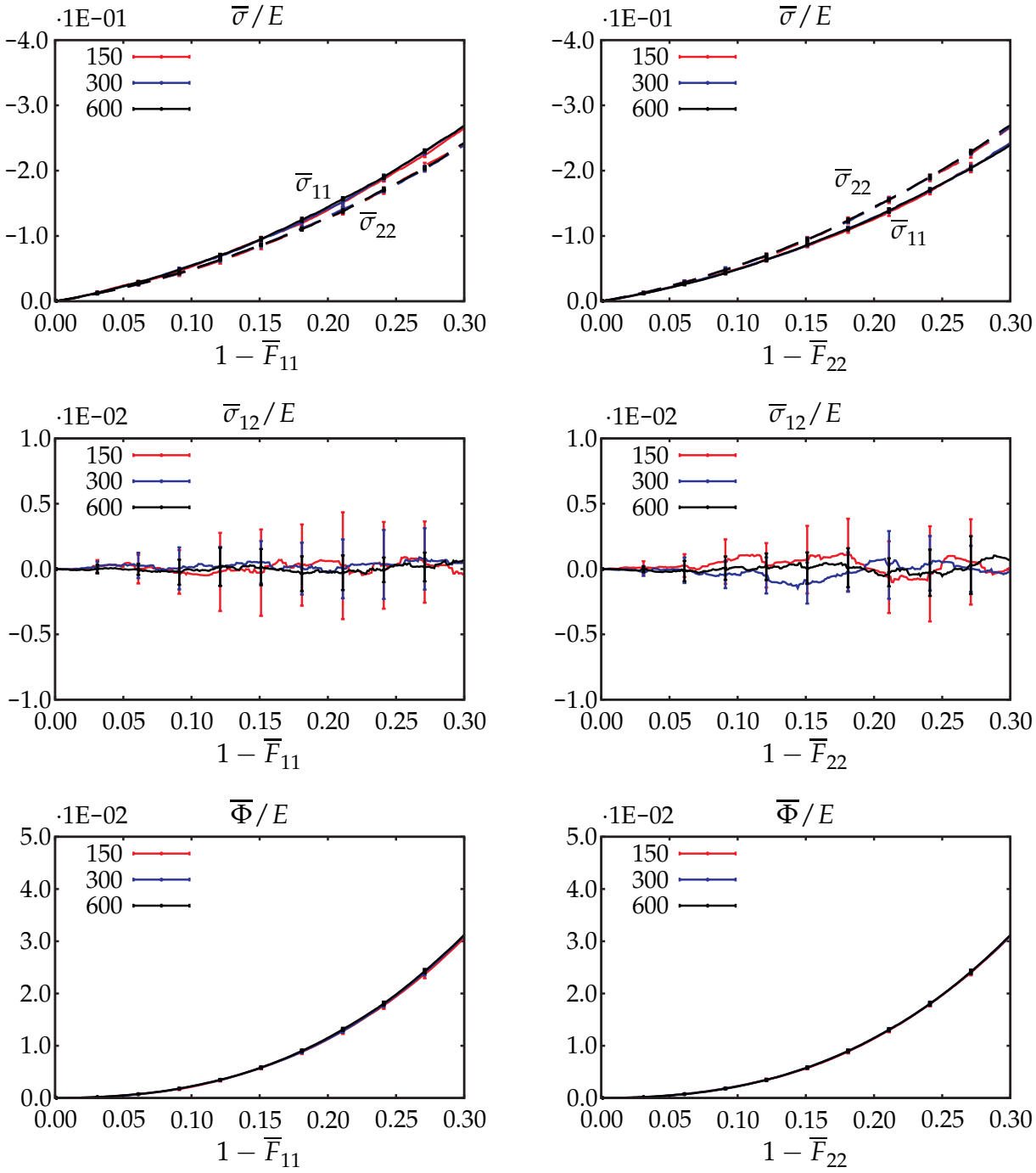

Figure 5.6.: Macroscopic quantities under uni-axial compression: Periodic boundary condition. Error bars show the standard deviation. All curves and error bars are scaled by the normal contact stiffness. *Left column*: Horizontal compression. *Right column*: Vertical compression. *Top row*: Macroscopic CAUCHY stress. Solid lines denote the stress component in horizontal direction, while dashed lines refer to the vertical stress component. *Center row*: Shear component of the macroscopic CAUCHY stress. *Bottom row*: Macroscopic energy density.

restricted TAYLOR boundary condition are plotted in Figure 5.5. Similar to the results produced by applying the assumption of TAYLOR, the overall impression of the obtained results is satisfactory. We point out the arrangement of the individual curves, gathered in individual groups. Once more, we find the standard deviation to be con-

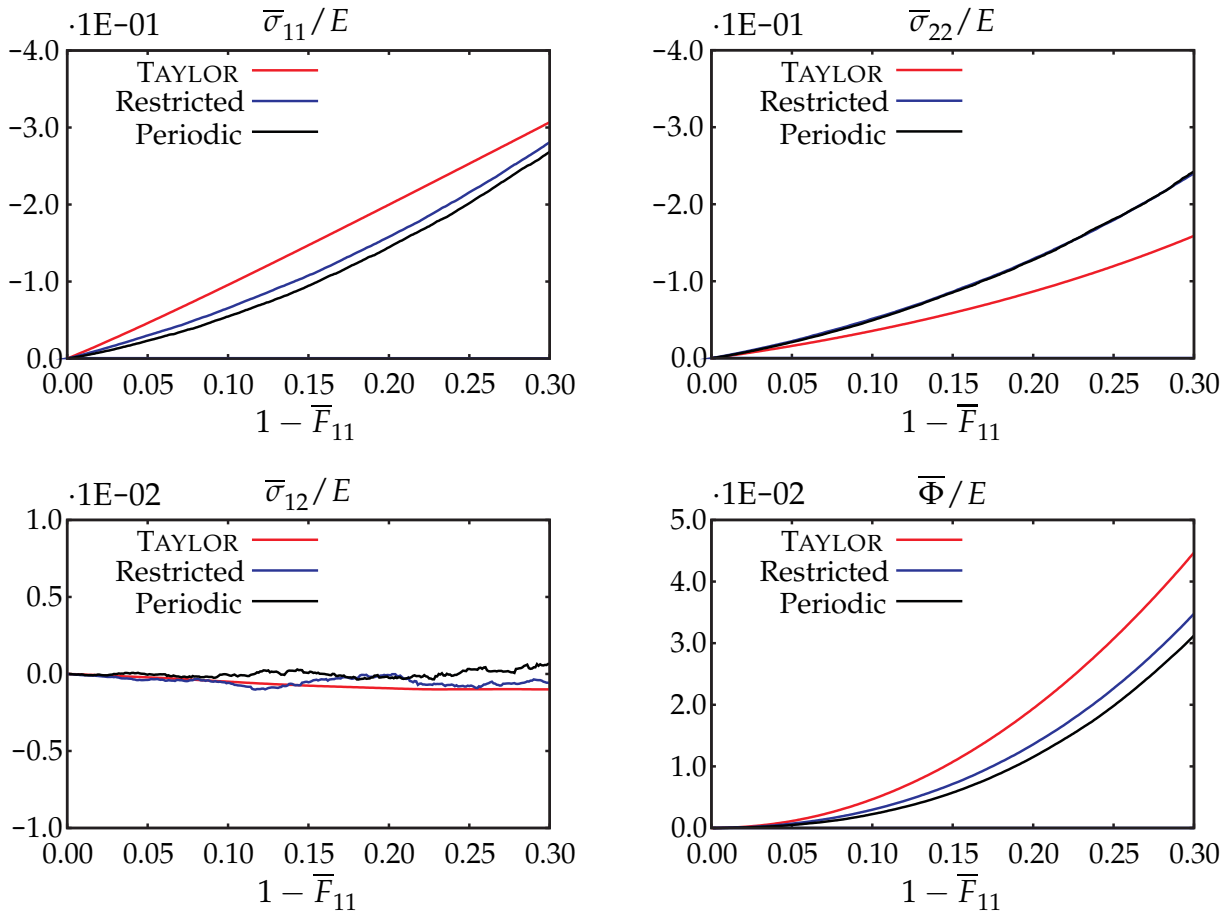

Figure 5.7.: Comparison of mean values of macroscopic quantities under horizontal compression. Curves related to the Taylor assumption are denoted in red, while blue and black curves refer to the restricted Taylor and periodic boundary condition, respectively. *Top left*: Horizontal component of the macroscopic CAUCHY stress. *Top right*: Vertical component of the macroscopic CAUCHY stress. *Bottom left*: Shear component of the macroscopic CAUCHY stress. *Bottom right*: Macroscopic energy density.

siderably small. The normal stress components bare a non-linear and macroscopically smooth behavior. In both directions, we notice an increasing slope, i.e., increase of particle contacts. The mean values of the shear stress components balance around a value of zero. Thereby, in contrast to the mean values of the normal stress components, a rough and non-smooth behavior is observed. The output of the macroscopic energy density qualitatively resembles the results of the assumption of TAYLOR. Computational results related to the periodic boundary conditions are plotted in Figure 5.6. As for the previous results, the macroscopic smoothness as well as their accordance is noteworthy. The two normal stresses show an almost identical non-linear behavior. In the case of the shear stress components, the rough trend of the previously discussed boundary condition is continued. The plots depicting the macroscopic energy densities are almost identical and describe a non-linear behavior. Having studied the individual results, the interest is on examining the resemblances and differences. Therefore, and in particular for a better observation, the obtained mean values of the averaged quantities are combined and replotted, compare Figure 5.7. Reviewing the similarities regarding the interchanged directions of loading, we restrict this investigation to the compression in horizontal direction. As representative quantities, we select the mean

values of the rves containing 600 primary particles. Observe that the related error bars are neglected. We start with the graph containing plots of the macroscopic energy density, depicted in the lower right diagram of Figure 5.7. Recall that the microscopic potential energy represents the quantity which is minimized on the micro scale level. The macroscopic stresses correspond to precise derivatives of the volume average of this quantity. Hence, we emphasize that the macroscopic energy density represents the only quantity which allows a true ranking between the different boundary conditions. As expected, we observe the TAYLOR assumption to deliver an overall stiff response. The answer linked to the restricted TAYLOR boundary conditions is considered to be intermediate. The softest output follows by application of periodic boundary conditions. The mean values of the stress component $\overline{\sigma}_{11}$, shown in the upper left diagram of Figure 5.7, reveal an identical ranking as for the values of the mean energy density. We find the response of the rves under the assumption of TAYLOR to be the stiffest as well as to be linear. The outcome in regards to the restricted TAYLOR assumption yields a softer, non-linear answer. The feedback related to the periodic boundary conditions shows similarities to the feedback of the restricted TAYLOR assumption. However, we witness the periodic boundary conditions to present the softest response. The observations of the mean values of the $\overline{\sigma}_{22}$ stress components show a rather unexpected outcome. Thereby, the assumption of TAYLOR yields the softest response, while the reactions of the restricted TAYLOR assumption and the periodic boundary conditions are stiffer and almost identical. The switched ranking explains by the ability of relaxation, i.e., the load is carried more equally throughout the rve. The shear component $\overline{\sigma}_{12}$, plotted in the lower left diagram of Figure 5.7, reveals a remarkable accordance between the results. Hereby, we remark the steady outcome for a compression between 0% and 10% and the slight deviation for higher compressions.

5.4.2. Macroscopic investigations - simple shear

The outcome of the simple shear deformations are plotted in Figure 5.8, 5.9 and 5.10. These images depict the mean value results, including their standard deviation. The arrangement of the individual figures is equivalent to the presentation of the uni-axial compression results. Macroscopic CAUCHY stress components and macroscopic energy densities in terms of the assumption of TAYLOR are depicted in Figure 5.8. We observe a well alignment of all curves throughout the graphs. However, in comparison to the results under uni-axial compression, the present output shows larger variation as well as deviation. The normal components of the macroscopic CAUCHY stress demonstrate a non-linear behavior, having a decreasing slope. The decrease in slope associates with loss of particle contacts. Horizontal and vertical stress components show significant differences in their final values, while their initial paths equal. The answers of the shear components of the macroscopic CAUCHY stress show a peak at approximately $\lambda_s = 0.6$. This feature is visible for both directions of loading. An interesting behavior is displayed by the macroscopic energy density plots. At first, one notices a non-linear output with increasing slope. Under additional loading, the non-linear response changes the sign of slope. Such a behavior of the energy corresponds to the energy produced during shearing of two grains. Figure 5.9 provides

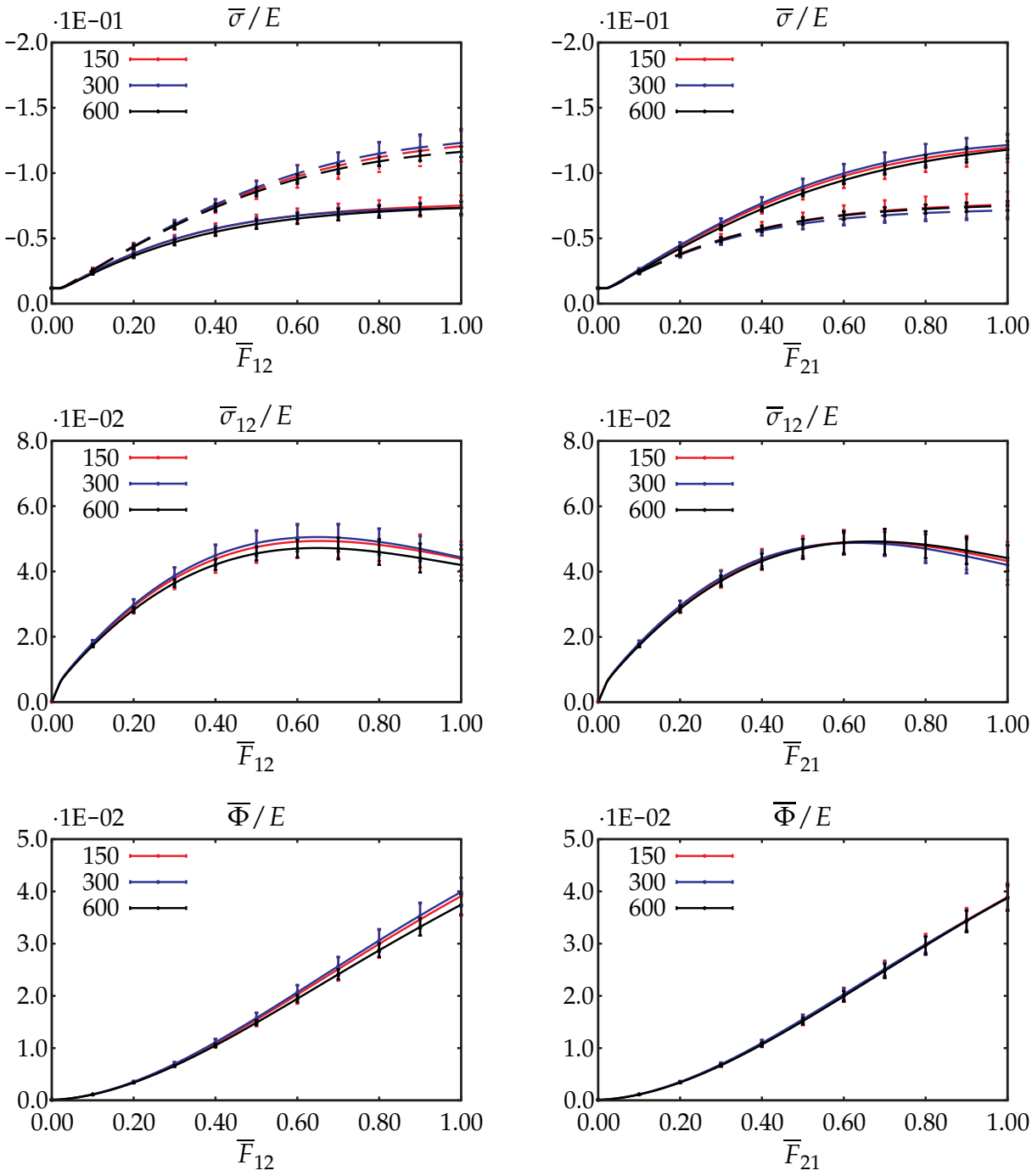

Figure 5.8.: Macroscopic CAUCHY stress and energy density in regards to the assumption of TAYLOR. Error bars show the standard deviation. All curves and error bars are scaled by the normal contact stiffness. Left column: Simple shear in horizontal direction. Right column: Simple shear in vertical direction Top row: Macroscopic CAUCHY stress. Solid lines refer to the horizontal stress component, whereby dashed lines denote the vertical stress component. Center row: Macroscopic shear stress. Bottom row: Macroscopic energy density.

details in terms of the restricted TAYLOR assumption. Across all responses one observes similarities to the assumption of TAYLOR, however, the macroscopic CAUCHY stress plots show a rather rough output. Increasing the number of particles seems to smooth out the overall rough nature and yields a softer response. Yet, the depicted

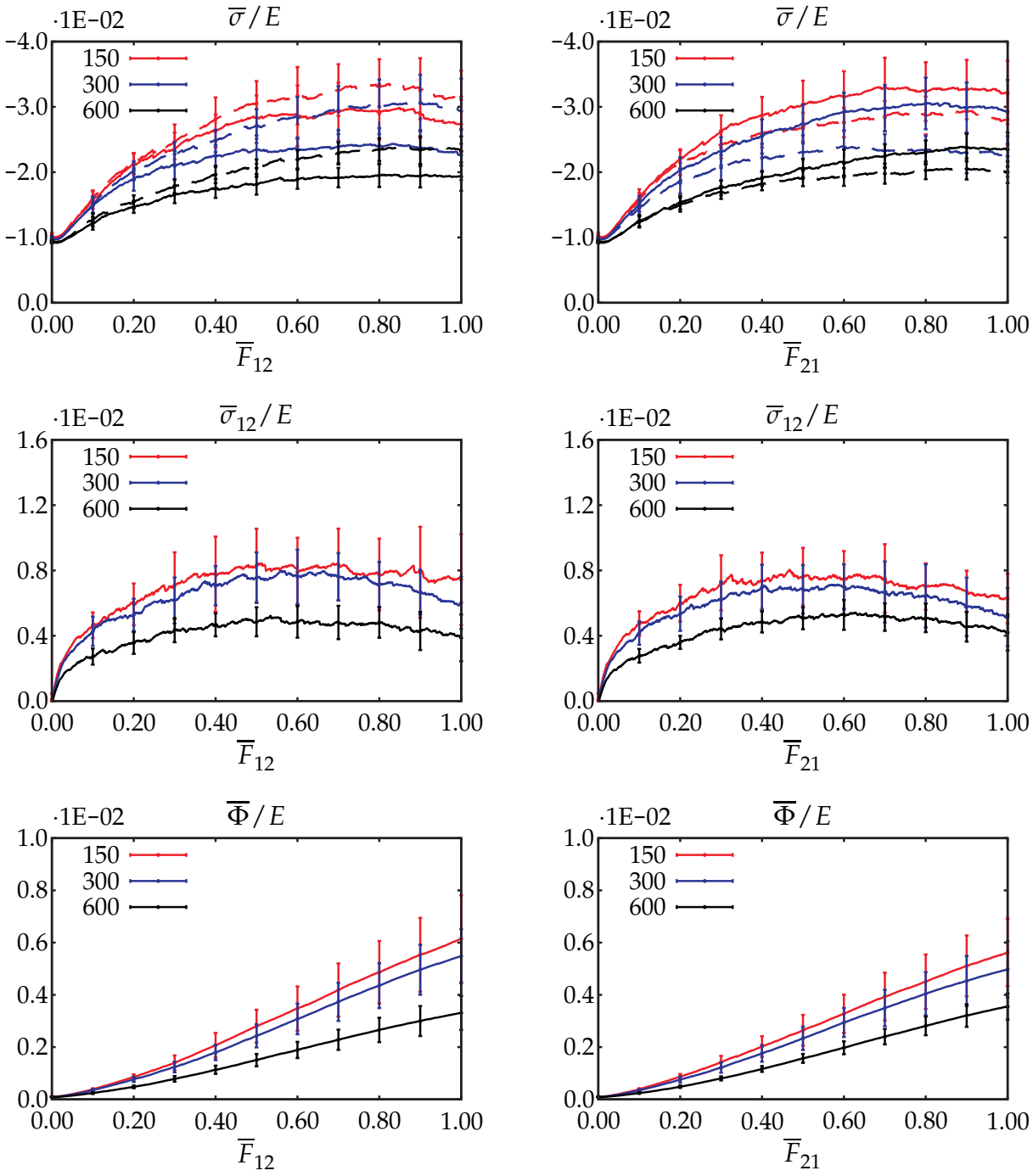

Figure 5.9.: Macroscopic CAUCHY stress and energy density in regards to the restricted TAYLOR boundary condition. Error bars show the standard deviation. All curves and error bars are scaled by the normal contact stiffness. Left column: Simple shear in horizontal direction. Right column: Simple shear in vertical direction Top row: Macroscopic CAUCHY stress. Solid lines refer to the horizontal stress component, whereby dashed lines denote the vertical stress component. Center row: Macroscopic shear stress. Bottom row: Macroscopic energy density.

curves do not converge to a meaningful function. Concerning the subjected deformation and boundary conditions, this observation indicates that neither rve contains a sufficient number of grains to be representative. Similar behaviors are noticed for the energy density plots. However, these graphs reveal a macroscopic smooth behav-

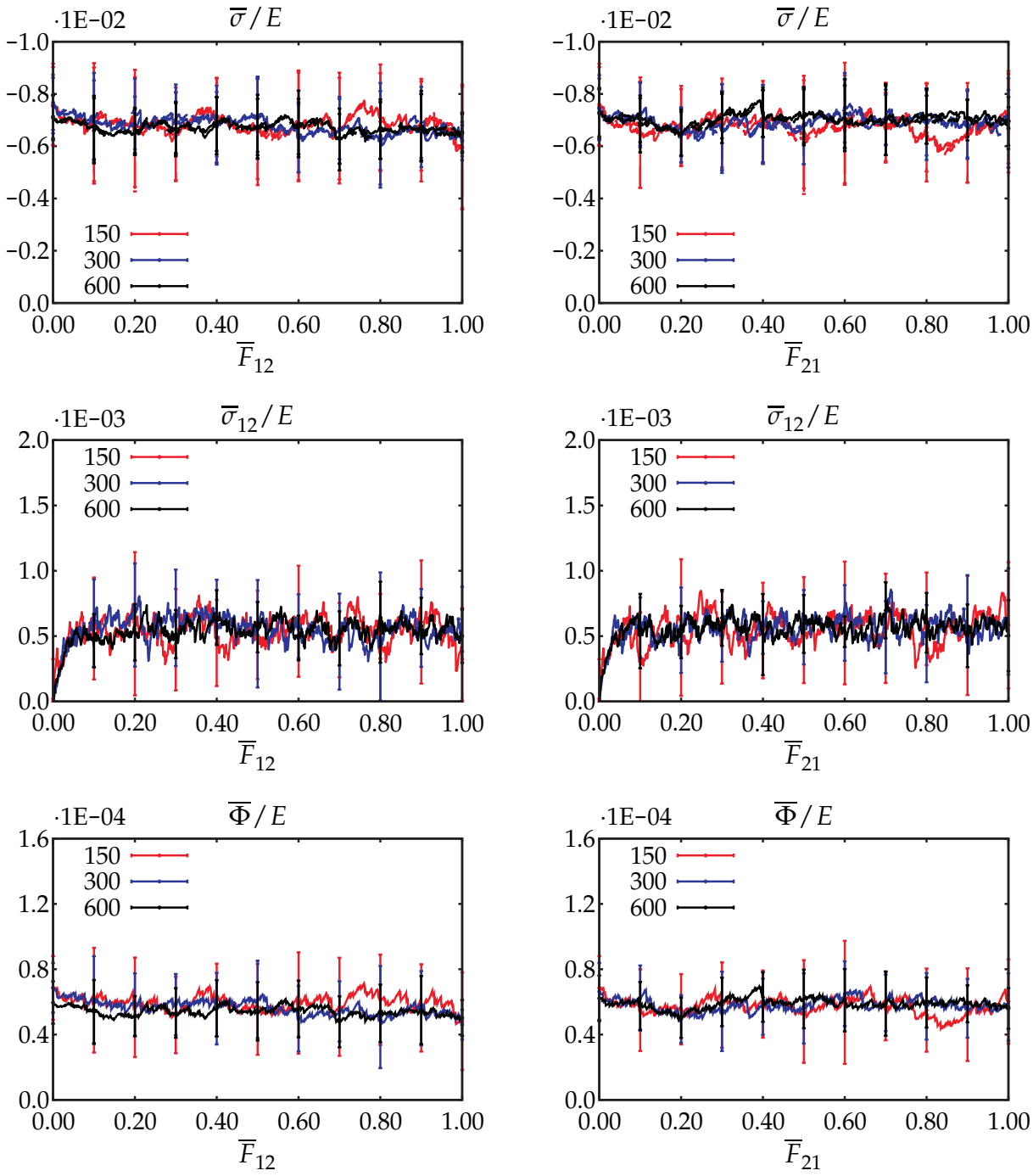

Figure 5.10.: Macroscopic CAUCHY stress and energy density in regards to the periodic boundary condition. Error bars show the standard deviation. All curves and error bars are scaled by the normal contact stiffness. Left column: Simple shear in horizontal direction. Right column: Simple shear in vertical direction Top row: Macroscopic CAUCHY stress. Solid lines refer to the horizontal stress component, whereby dashed lines denote the vertical stress component. Center row: Macroscopic shear stress. Bottom row: Macroscopic energy density.

ior. The depicted error bars decrease under the increase of grains. Periodic boundary conditions related macroscopic results are depicted in Figure 5.10. The plotted components of the macroscopic stress and energy densities reveal a very rough response. Despite their roughness, the difference in the number of microscopic grains does not

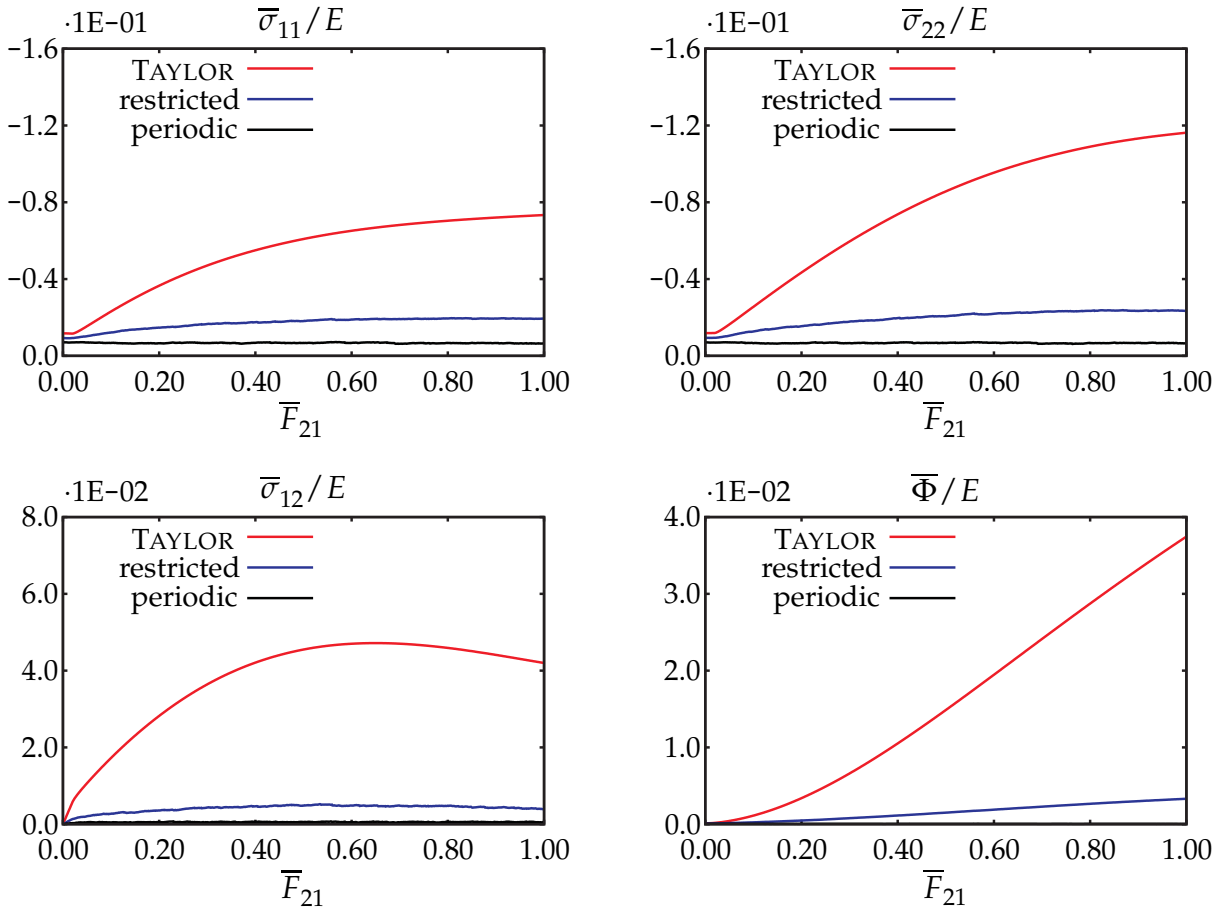

Figure 5.11.: Comparison of mean values of volume averaged quantities with respect to the different boundary conditions under horizontal simple shear. Taylor boundary conditions are denoted in red, while blue and black curves refer to the restricted Taylor and the periodic boundary condition, respectively.

effect the overall macroscopic output majorly. Loosely speaking, we almost obtain equivalent macroscopic answers for different numbers of particles. This observation points to a sufficient number of grains in all sets of rves. Tending to the two top graphs of Figure 5.10, one observes almost identical responses of the horizontal and vertical components of the macroscopic CAUCHY stress for both directions of loading. Overall, all six curves in the top two plots reveal a slightly decreasing behavior. The shear components of the macroscopic CAUCHY stress are shown in the center row of Figure 5.10. At first, we notice an increasing behavior which delineates for $\overline{F}_{12} \in [0 \rightarrow 0.1]$ and for $\overline{F}_{21} \in [0 \rightarrow 0.1]$, respectively. Thereafter, disregarding the fluctuational behavior, all responses may be accounted as almost constant. The outputs of the macroscopic energy densities, plotted in the bottom row of Figure 5.10, qualitatively compare to the results of the horizontal and vertical components of the macroscopic CAUCHY stress. Leaving the fuzzy nature of the energy density outputs unconsidered, one observes a slight decrease under increasing shear deformation. To improve the quality of comparison between the obtained results, we once more plot the mean values of the rves containing 600 primary particles, see Figure 5.11. Based on the accordance between the horizontal and vertical shear responses, we exclusively restrict this comparison to the horizontal simple shear deformation results. Starting by comparing the results regarding the macroscopic energy densities, located in the lower graph of Figure 5.11, one

observes significant differences between the individual results. These differences are visible throughout the range of deformation. While the assumption of TAYLOR delivers a very stiff response, the restricted TAYLOR output is considered to be rather soft. The difference between the two answers is remarkable and does not compare to the previous obtained responses under uni-axial compression. An even more impressive result stems from the application of periodic boundary conditions. Thereby, related to the graph scale, the received energy density curve coincides with the horizontal axis of the graph, pointing to an extremely soft output. Evidently, these varieties strongly relate to the relaxation ability under different boundary conditions. The remaining plots depict the components of the macroscopic CAUCHY stress. The two images in the top row of Figure 5.11 relate to the horizontal and vertical components of the considered stress measure. For the TAYLOR as well as the restricted TAYLOR boundary condition one observes monotonously increasing behaviors. The assumption of TAYLOR delivers the stiffest reply. Curves related to the periodic boundary conditions show a slightly decreasing linear trend. Please note that the afore mentioned strong fluctuational behavior is not visible at the employed graph scale. Shear components of the macroscopic CAUCHY stress are shown in the bottom left graph of Figure 5.11. Once again, we find the priorly discussed differences with respect to the response stiffness. Noteworthy is the periodic boundary condition output, describing an almost constant function with minimal value.

5.4.3. Macroscopic investigations - cyclic loading

We perform cyclic loading of 15 rves, having 150 primary particles. Related to the nature of the TAYLOR boundary conditions, we solely perform the cyclic loading by subjecting restricted TAYLOR as well as periodic boundary conditions. At first, the rves are compressed in a bi-axial manner, i.e., we apply the macroscopic deformation gradient $\overline{\boldsymbol{F}} = \delta_{ij}\left[1-\lambda_c\right]\boldsymbol{e}_i \otimes \boldsymbol{e}_j$. The loading parameter, governing the compression, is set to $\lambda_c \in [0 \rightarrow 0.01]$. The compression is applied in 10 uniform load steps. Reaching the compressed state, the shearing deformation is initiated. Shearing applies by $\overline{\boldsymbol{F}} = \delta_{ij}\left[1-\lambda_c\right]\boldsymbol{e}_i \otimes \boldsymbol{e}_j + \lambda_s \boldsymbol{e}_1 \otimes \boldsymbol{e}_2$. The loading parameter λ_c is held constant during the shearing, i.e., $\lambda_c = 0.01 = \mathsf{const}$. The loading parameter λ_s, which defines the shear deformation, applies in three stages $[0 \rightarrow 0.5]$, $[0.5 \rightarrow -0.5]$ and $[-0.5 \rightarrow 0]$. The complete cycle uses 2000 uniform load steps, each followed by a deformation dependent number of relaxation steps. The obtained results are combined in Figure 5.12. We plot the mean values of the individual macroscopic stress components as well as the macroscopic energy densities. The deviation depicts by error bars. Studying the plots, one witnesses history dependent answers in all graphs, whereby the soft nature of the periodic boundary conditions reveals minor history dependence. Recalling that the contact relation between the grains is described by a linear elastic model, the obtained history effects must exclusively relate to microscopic topology changes as well as the continuous evolution of the inter-particle contact network. At first, we tend to the restricted TAYLOR related results. Following the path of the normal stress components, see Figure 5.12 (Top row), we observe an increase of stress for each state of $\overline{F}_{12} = 0$. This

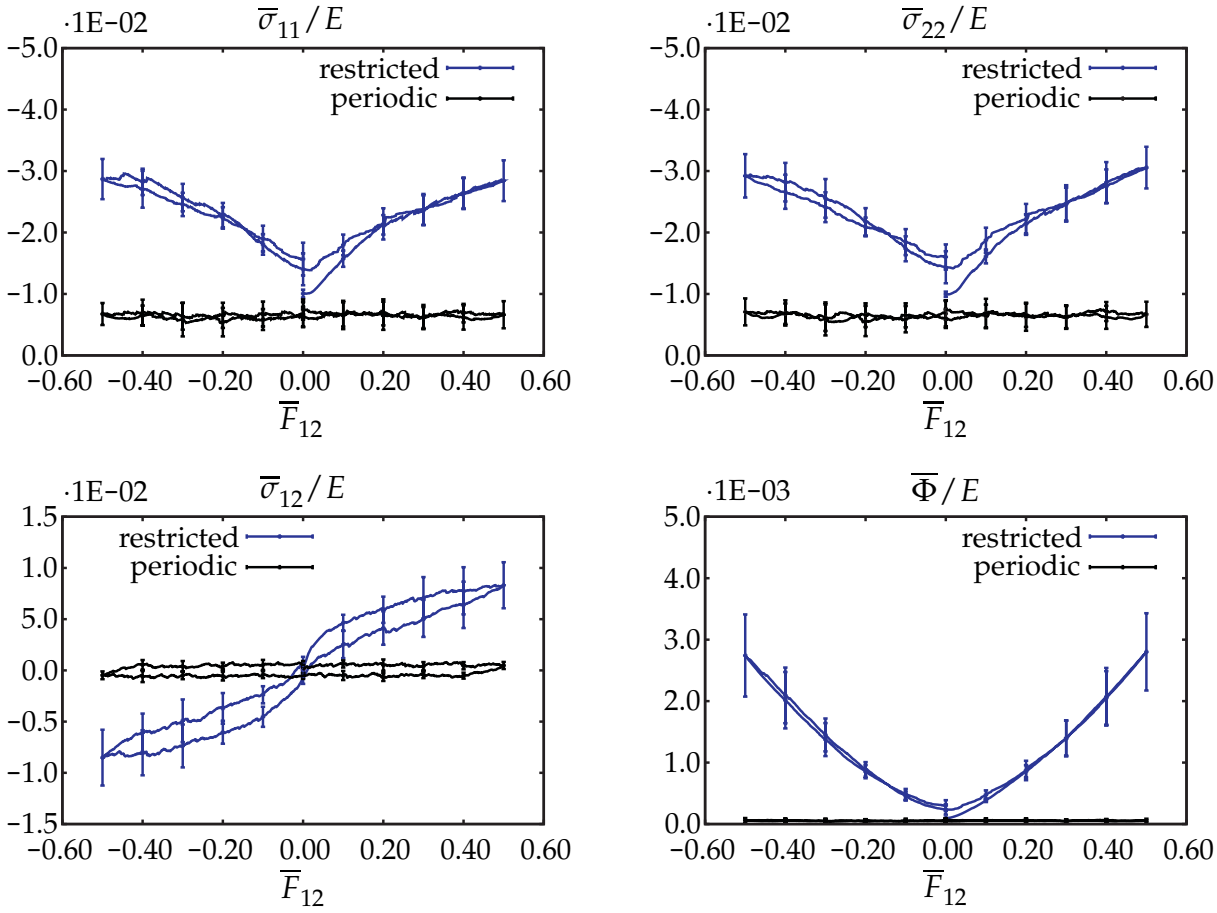

Figure 5.12.: Macroscopic quantities under cyclic loading: Restricted TAYLOR assumption and periodic boundary conditions. Error bars show the standard deviation. All curves and error bars are scaled by the normal contact stiffness. *Top left*: Macroscopic stress component in horizontal direction. *Top right*: Macroscopic stress component in vertical direction. *Bottom left*: Shear component of the macroscopic CAUCHY stress. *Bottom right*: Macroscopic energy density.

recognition reveals that irreversible inter-locking and reformation of the grains takes place, enforcing the granular structures to try to expand their volume. This effect, also known as REYNOLDS' principle of dilatancy [118], is also visible in the energy density plot, compare Figure 5.12 (Bottom right). The performed shearing is volume preserving, i.e., $v_{\text{rve}} = 0.01^2 V_{\text{rve}} = \text{const}$, thus, the energy density plot describes the overall increase and decrease of the inter-particle overlaps. The graph relating to the shear components of the macroscopic CAUCHY stress shows hysteresis, underlining the previously discussed fact of microscopic topology changes. By focusing on the periodic boundary condition related results, one identifies only minor changes in the horizontal as well as vertical macroscopic stress components. Nevertheless, evolution of the grain scale structure exhibits by fuzzy and unsteady output. The overall consistency of both functions, i.e., the absence of stress increase or stress decrease, strongly relates to the soft nature of the periodic boundary conditions. In detail, the soft nature does not allow for constant long-lasting grain inter-locking. Rather than, periodic boundary shifts are noticed, releasing occurring stresses. Still, turning towards the shear component of the macroscopic CAUCHY stress, one observes a distinctive hysteresis pattern, apparently related to the continuous evolution and topology changes.

6. Fem - dem coupling

6.1. Introduction

Commonly applied non-linear fem implementations typically rely on an implicit solution strategy of the NEWTON-RAPHSON type. One distinguishing feature of this particular choice is found in the rapid convergence towards the solution of the system of non-linear equations. Locally, i.e., close to the solution, one may observe a quadratic convergence behavior. In relation to the considered computational homogenization method, fast convergence behavior on the continuous level, i.e., a limited number of macroscopic iterations, is of great importance to restrict the microscopic calculations to a minimum. NEWTON-RAPHSON type schemes require knowledge of the linearized residual forces, the so-called tangent or HESSIAN matrix. Its setup requires additional computational performance, however, in comparison to the computational effort on the microscale, the setup itself as well as solution of the arising system of linear equations is considerably low. The majority of computational power is needed for the grain scale computations. One ingredient of the macroscopic stiffness of a material point is the related macroscopic tangent operator. Classical continuum formulations utilize elasto-plastic constitutive laws, in general related to phenomenological models. Pioneering attempts to model granular matter in a continuum framework are for example found in the works of DRUCKER, GIBSON & HENKEL [38], GOODMAN & COWIN [48], GUDEHUS [50] or ROSCOE, SCHOFIELD & WROTH [123]. The inclusion of plasticity allows for macroscopic energy dissipation, in reality related to microscopic grain reorganization and dislocation. Basic elasto-plastic formulations require insight of the elastic and plastic moduli, the POISSON ratio as well as a yield criterion. Distinguishing granular features like REYNOLDS' dilatancy require more sophisticated continuum formulations which allow for the incorporation of the dilatancy angle. This particular quantity represents the plastic volume change over the plastic shear strain. Approaches used in classical continuum mechanics do not consider the influence of the individual grains, their interaction as well as their topological placement.

We present an intuitive formulation of the macroscopic tangent operator which does not depend on phenomenological assumptions on the macroscale level. Instead, the macroscopic tangent operator is founded on the introduced volume average of the microscopic contact energy. Thus, it is solely based on microscopic quantities. Related works of CHANG & MISRA [19, 20] focus on the description and simulation of macroscopic quantities of granular matter by considering the microscopic nature. Focal point is the assumption of TAYLOR under small deformations and fixed inter-particle connectivity. An extension to different boundary conditions is presented in [98], however, the assumption of a fixed inter-particle contact network as well as small strain are retained. Macroscopic dissipation and irreversible changes in volume stay unconsidered.

Our formulation permits contact breaking and forming between the discrete grains. In combination with a large strain framework, reorganization as well as dislocation of individual grains or grain groups naturally arise in the discrete system.

6.2. General macroscopic tangent operator

With the definition of the general macroscopic PIOLA stress at hand we approach the derivation of the corresponding general macroscopic tangent operator. The general macroscopic tangent constructs by linearizing the general expression of the macroscopic PIOLA stress with respect to the macroscopic deformation gradient. Recalling the relation between the macroscopic energy density and the general macroscopic PIOLA stress, see (5.2), one finds the general macroscopic tangent to equate to the second total derivative of the macroscopic energy density with respect to the macroscopic deformation gradient.

$$\overline{\mathbb{A}} = \frac{\mathrm{d}^2\overline{\Phi}_{\mathsf{n}}}{\mathrm{d}\overline{\boldsymbol{F}} \otimes \mathrm{d}\overline{\boldsymbol{F}}} = \frac{\mathrm{d}\overline{\boldsymbol{P}}}{\mathrm{d}\overline{\boldsymbol{F}}} = \frac{\partial^2\overline{\Phi}_{\mathsf{n}}}{\partial\overline{\boldsymbol{F}} \otimes \partial\overline{\boldsymbol{F}}} + \sum_{m\in\mathscr{F}^*} \frac{\partial^2\overline{\Phi}_{\mathsf{n}}}{\partial\overline{\boldsymbol{F}} \otimes \partial\Xi_m} \bullet \frac{\partial\Xi_m}{\partial\overline{\boldsymbol{F}}} + \overline{\mathbb{O}}, \tag{6.1}$$

with

$$\overline{\mathbb{O}} = \sum_{r\in\mathscr{F}^*} \left[\frac{\mathrm{d}}{\mathrm{d}\overline{\boldsymbol{F}}} \left[\frac{\partial\overline{\Phi}_{\mathsf{n}}}{\partial\Xi_r} \right] \bullet \frac{\partial\Xi_r}{\overline{\boldsymbol{F}}} + \frac{\partial\overline{\Phi}_{\mathsf{n}}}{\partial\Xi_r} \bullet \frac{\mathrm{d}}{\mathrm{d}\overline{\boldsymbol{F}}} \left[\frac{\partial\Xi_r}{\partial\overline{\boldsymbol{F}}} \right] \right]. \tag{6.2}$$

Based on the requirement of static equilibrium at the time of scale transition, the fourth order tensor $\overline{\mathbb{O}}$ is zero for all considered boundary conditions, see (A.9). Inspecting (6.1), one detects two main contributions. Equivalent to (5.2), we identify a fluctuational dependent as well as a fluctuational independent share. The first term, i.e., the second derivative of the macroscopic energy density with respect to the macroscopic deformation gradient, shows the fluctuational independent part. The second term denotes the fluctuational dependent contribution. This share consists of a summation over all particles which include a fluctuational displacement part. By inserting (4.6), as well as (A.14) we obtain:

$$\begin{aligned} \overline{\mathbb{A}} \;=\; & \frac{1}{2V_{\mathsf{rve}}} \sum_{i\in\mathscr{P}^*} \sum_{\substack{j\in\mathscr{P}^* \\ j\neq i}} \frac{\partial^2\Phi_{\mathsf{n}ij}}{\partial\overline{\boldsymbol{F}} \otimes \partial\overline{\boldsymbol{F}}} \\ & - \frac{1}{V_{\mathsf{rve}}} \sum_{\substack{k\in\mathscr{P}^* \\ k\neq m}} \sum_{m\in\mathscr{F}^*} \sum_{n\in\mathscr{F}^*} \sum_{\substack{l\in\mathscr{P}^* \\ l\neq n}} \frac{\partial^2\Phi_{\mathsf{n}km}}{\partial\overline{\boldsymbol{F}} \otimes \partial\Xi_m} \bullet \overline{\boldsymbol{F}}^{-1} \bullet \left[\boldsymbol{K}^{-1}\right]_{nm} \bullet \overline{\boldsymbol{F}}^{-t} \bullet \frac{\partial^2\Phi_{\mathsf{n}ln}}{\partial\Xi_n \otimes \partial\overline{\boldsymbol{F}}}. \end{aligned} \tag{6.3}$$

We remark that $\left[\boldsymbol{K}^{-1}\right]_{nm}$ refers to a two by two entry of the inverted microscopic aggregate matrix. Next we tend to the individual derivatives in (6.3). Taking the second derivative of the contact energy with respect to the macroscopic deformation gradient

becomes:

$$\frac{\partial^2 \Phi_{\mathrm{n}ij}}{\partial \overline{\boldsymbol{F}} \otimes \partial \overline{\boldsymbol{F}}} = -\boldsymbol{k}_{ij} \overline{\otimes} \left[\left[\overline{\boldsymbol{F}}^{-1} \cdot \boldsymbol{l}_{ij} \right] \otimes \left[\overline{\boldsymbol{F}}^{-1} \cdot \boldsymbol{l}_{ij} \right] \right]. \tag{6.4}$$

Therein, $\boldsymbol{k}_{ij}$ denotes a contribution of the microscopic aggregate stiffness, defined in $(4.11)_2$. The mixed second derivative of the contact energy with respect to the macroscopic deformation gradient and the individual microscopic fluctuations yields:

$$\frac{\partial^2 \Phi_{\mathrm{n}km}}{\partial \overline{\boldsymbol{F}} \otimes \partial \boldsymbol{\Xi}_m} = -\left[\left[\boldsymbol{k}_{km} \cdot \overline{\boldsymbol{F}} \right] \overline{\otimes} \overline{\boldsymbol{F}}^{-1} \right] \cdot \boldsymbol{l}_{km} + \boldsymbol{f}_{km} \otimes \boldsymbol{1}. \tag{6.5}$$

Again, we confirm the presence of a contribution of the microscopic aggregate stiffness. Furthermore, we observe the inclusion of the particle contact force $\boldsymbol{f}_{km}$. For completeness, the third order tensor $\partial^2 \Phi_{ln} / \left[\partial \boldsymbol{\Xi}_n \otimes \partial \overline{\boldsymbol{F}} \right]$ attracts the attention. Considering the derivative in (6.5), its explicit expression is found by a simple permutation of the tensor basis.

$$\frac{\partial^2 \Phi_{\mathrm{n}ln}}{\partial \boldsymbol{\Xi}_n \otimes \partial \overline{\boldsymbol{F}}} = -\overline{\boldsymbol{F}}^t \cdot \boldsymbol{k}_{nl} \otimes \left[\overline{\boldsymbol{F}}^{-1} \cdot \boldsymbol{l}_{ln} \right] + [\boldsymbol{1} \overline{\otimes} \boldsymbol{1}] \cdot \boldsymbol{f}_{ln}. \tag{6.6}$$

6.3. Boundary specific macroscopic tangent

Similar to the general macroscopic PIOLA stress, presented in (5.6) as well as (5.15), the corresponding general macroscopic tangent operator is fit to relate to desired boundary conditions. A more precise discussion of the boundary condition specific tangent operators is found in the upcoming subsections.

6.3.1. Macroscopic tangent - Taylor assumption

Adopting the assumption of TAYLOR, individual particle fluctuations are neglected and thus are assumed to be zero. Under this assumption, the volume average of the microscopic potential energy solely depends on the macroscopic deformation gradient, i.e., $\overline{\mathbb{A}} = \overline{\mathbb{A}}\left(\overline{\boldsymbol{F}}\right)$. Thus, the second term of (6.3) disappears. The macroscopic tangent is expressed by the second derivative of the volume average of the microscopic potential energy with respect to the macroscopic deformation gradient,

$$\overline{\mathbb{A}} = \frac{\mathrm{d}^2 \overline{\Phi}}{\mathrm{d} \overline{\boldsymbol{F}} \otimes \mathrm{d} \overline{\boldsymbol{F}}} = \frac{\mathrm{d} \overline{\boldsymbol{P}}}{\mathrm{d} \overline{\boldsymbol{F}}} = -\frac{1}{2 V_{\mathrm{rve}}} \sum_{i \in \mathscr{P}^*} \sum_{\substack{j \in \mathscr{P}^* \\ j \neq i}} \boldsymbol{k}_{ij} \overline{\otimes} \left[\boldsymbol{L}_{ij} \otimes \boldsymbol{L}_{ij} \right]. \tag{6.7}$$

Observe that the absence of the microscopic fluctuations allows us to replace $\overline{\boldsymbol{F}}^{-1} \cdot \boldsymbol{l}_{ij}$ by $\boldsymbol{L}_{ij}$. Based on the restriction of the summation, i.e., $j \neq i$, only off-diagonal terms of the microscopic stiffness matrix are processed. We expand (6.7) by using the definition of the material branch vector $\boldsymbol{L}_{ij} = \boldsymbol{X}_j - \boldsymbol{X}_i$. Thereby, recall that the material fluctu-

ations are zero for the assumption of TAYLOR. By reordering as well as by applying (4.14), (6.7) is compacted.

$$\overline{\mathbb{A}} \;=\; \frac{1}{V_{\mathsf{rve}}} \sum_{i\in\mathscr{P}^*} \sum_{j\in\mathscr{P}^*} \boldsymbol{k}_{ij} \overline{\otimes} \left[\boldsymbol{X}_i \otimes \boldsymbol{X}_j \right], \tag{6.8}$$

The compaction introduces an expansion of the summation ranges, i.e., in contrast to (6.7), (6.8) considers diagonal and off-diagonal terms of the microscopic aggregate matrix.

Remark 6.1 (On an analytical macroscopic tangent) Let us consider the possibility of estimating the macroscopic tangent in an analytical manner. For simplicity, we restrict this investigation to a regular square grid of monodisperse particles. The particles are placed so that all overlaps are equal to zero, i.e., there exists contact between the grains but no contact force is generated. Thus, the branch vectors between the grains are set to the sum of the particle radii, $\boldsymbol{l}_{ij} = \boldsymbol{l} = 2r$. Postulating the contact stiffness to be equivalent for all inter-particle contacts, we replace the contact specific stiffness E_{ij} by the single stiffness E. Correlating to the rectangular and equidistant nature of the rve, each direction contains $\#\mathscr{P} - \sqrt{\#\mathscr{P}}$ contacts. Thus, the total number of contacts inside the rve yields $2\left[\#\mathscr{P} - \sqrt{\#\mathscr{P}}\right]$ in total. The volume of the rve is expressed by the uniform particle radii as well as the number of contacts.

$$V_{\mathsf{rve}} = 4r^2 \left[\#\mathscr{P} - 2\sqrt{\#\mathscr{P}} + 1\right]. \tag{6.9}$$

Inserting the latter considerations in (6.7) as well as recalling the regularity of the assumed grid, the macroscopic tangent operator is reduced to:

$$\overline{\mathbb{A}} = E \left[1 + \frac{\sqrt{\#\mathscr{P}} - 1}{\left[\#\mathscr{P} - 2\sqrt{\#\mathscr{P}} + 1\right]} \right] \mathbf{1} \overline{\otimes} \mathbf{1}. \tag{6.10}$$

Equation (6.10) shows that under the latter presumptions, the macroscopic tangent stiffness solely depends on the number of contacting grains in the system.

$$\operatorname*{Lim}_{\#\mathscr{P}\to\infty} \left(1 + \frac{\sqrt{\#\mathscr{P}} - 1}{\left[\#\mathscr{P} - 2\sqrt{\#\mathscr{P}} + 1\right]} \right) = 1. \tag{6.11}$$

We note, for the contacting number of grains tending towards infinity, the macroscopic stiffness equates the microscopic contact stiffness E. This phenomena discloses the relation between the material behavior of a discrete aggregate model and an continuum model, i.e., for an unlimited number of contacting grains we obtain a continuum response. Furthermore, (6.11) indicates that less contacting grains, i.e., contacting grains

with a larger diameter, result into a rather stiff behavior of the macroscopic tangent. Concluding, we remark that rves having the same number of particles can result into completely different responses solely related to their contact network. However, assuming that the contact network of the generated rves is arbitrarily, the rectangular and equidistant rve will yield the stiffest responds. ■

6.3.2. Macroscopic tangent - restricted Taylor assumption

In contrast to the tangent operator related to the TAYLOR assumption, the tangent operator belonging to the restricted TAYLOR assumption does depend on the microscopic fluctuations, $\overline{\mathbb{A}} = \overline{\mathbb{A}}\left(\overline{\boldsymbol{F}}, \boldsymbol{\Xi}\left(\overline{\boldsymbol{F}}\right)\right)$. At present, the fluctuations are present for all inner particles. For the particles on the boundary, fluctuations are set to zero. Hence, the set of fluctuational dependent grains is equal to $\mathscr{I}^*$. Replacing $\mathscr{F}^*$ by $\mathscr{I}^*$ in (6.3), we set the initial definition of the macroscopic tangent in regards to the restricted TAYLOR assumption.

$$\begin{aligned}\overline{\mathbb{A}} &= \frac{1}{2V_{\mathsf{rve}}}\sum_{i\in\mathscr{P}^*}\sum_{\substack{j\in\mathscr{P}^*\\ j\neq i}}\frac{\partial^2\Phi_{\mathsf{n}ij}}{\partial\overline{\boldsymbol{F}}\otimes\partial\overline{\boldsymbol{F}}}\\ &- \frac{1}{V_{\mathsf{rve}}}\sum_{\substack{k\in\mathscr{P}^*\\ k\neq m}}\sum_{m\in\mathscr{I}^*}\sum_{n\in\mathscr{I}^*}\sum_{\substack{l\in\mathscr{P}^*\\ l\neq n}}\frac{\partial^2\Phi_{\mathsf{n}km}}{\partial\overline{\boldsymbol{F}}\otimes\partial\boldsymbol{\Xi}_m}\cdot\overline{\boldsymbol{F}}^{-1}\cdot\left[\boldsymbol{K}^{-1}\right]_{nm}\cdot\overline{\boldsymbol{F}}^{-t}\cdot\frac{\partial^2\Phi_{\mathsf{n}ln}}{\partial\boldsymbol{\Xi}_n\otimes\partial\overline{\boldsymbol{F}}}. \end{aligned} \tag{6.12}$$

Keeping in mind the influence of the microscopic fluctuations, one treats the first term of (6.12) as done under the assumption of TAYLOR. As result we obtain:

$$\frac{1}{2V_{\mathsf{rve}}}\sum_{i\in\mathscr{P}^*}\sum_{\substack{j\in\mathscr{P}^*\\ j\neq i}}\frac{\partial^2\Phi_{\mathsf{n}ij}}{\partial\overline{\boldsymbol{F}}\otimes\partial\overline{\boldsymbol{F}}} = \frac{1}{V_{\mathsf{rve}}}\sum_{i\in\mathscr{P}^*}\sum_{j\in\mathscr{P}^*}\boldsymbol{k}_{ij}\overline{\otimes}\left[\left[\overline{\boldsymbol{F}}^{-1}\cdot\boldsymbol{x}_i\right]\otimes\left[\overline{\boldsymbol{F}}^{-1}\cdot\boldsymbol{x}_j\right]\right], \tag{6.13}$$

where we, similar to (5.4), replaced $\boldsymbol{X}_i + \boldsymbol{\Xi}_i$ by $\overline{\boldsymbol{F}}^{-1}\cdot\boldsymbol{x}_i$. Obviously, the expression in (6.13) correlates to (6.8). In particular, (6.8) can be deduced by (6.13), demanding the individual microscopic fluctuations to be zero. Pointing the attention to the second share of (6.12), we first investigate on the influence of the summation over the index l. This index is only present in the last term and allows an isolated modification of the term of interest: Based on the commutative law, the expression is parted. Its first share is reformulated, using the definition of the spatial branch vector as well as the identity in (4.14). As an important result, the summation restriction $l \neq n$ is neutralized, allowing the consideration of diagonal entries of the microscopic aggregate stiffness. In case of the second share, the summation restricts to the inter-particle contact forces, finally leading to the negative particle force. Combined we find:

$$\sum_{\substack{l\in\mathscr{P}^*\\ l\neq n}}\frac{\partial^2\Phi_{\mathsf{n}ln}}{\partial\boldsymbol{\Xi}_n\otimes\partial\overline{\boldsymbol{F}}} = \sum_{l\in\mathscr{P}^*}\overline{\boldsymbol{F}}^t\cdot\boldsymbol{k}_{nl}\otimes\left[\overline{\boldsymbol{F}}^{-1}\cdot\boldsymbol{x}_l\right] - [\boldsymbol{1}\overline{\otimes}\boldsymbol{1}]\cdot\boldsymbol{f}_n. \tag{6.14}$$

An identical procedure is performed on the first term of (6.12).

$$\sum_{\substack{k\in\mathscr{P}^*\\k\neq m}} \frac{\partial^2\Phi_{\mathsf{n}km}}{\partial\overline{\boldsymbol{F}}\otimes\partial\boldsymbol{\Xi}_m} = \sum_{k\in\mathscr{P}^*}\left[\left[\boldsymbol{k}_{km}\bullet\overline{\boldsymbol{F}}\right]\overline{\otimes}\overline{\boldsymbol{F}}^{-1}\right]\bullet\boldsymbol{x}_k - \boldsymbol{f}_m\otimes\boldsymbol{1}. \tag{6.15}$$

Substitution of (6.13), (6.14) and (6.15) in (6.12) as well as considering the demand $\boldsymbol{f}_i = \boldsymbol{0}, \forall i\in\mathscr{I}$ yields:

$$\begin{aligned}\overline{\mathbb{A}} &= \frac{1}{V_{\mathsf{rve}}}\sum_{i\in\mathscr{P}^*}\sum_{j\in\mathscr{P}^*}\boldsymbol{k}_{ij}\overline{\otimes}\left[\left[\overline{\boldsymbol{F}}^{-1}\bullet\boldsymbol{x}_i\right]\otimes\left[\overline{\boldsymbol{F}}^{-1}\bullet\boldsymbol{x}_j\right]\right]\\ &- \frac{1}{V_{\mathsf{rve}}}\sum_{k\in\mathscr{P}^*}\sum_{m\in\mathscr{F}^*}\sum_{n\in\mathscr{F}^*}\sum_{l\in\mathscr{P}^*}\boldsymbol{k}_{km}\bullet\left[\boldsymbol{K}^{-1}\right]_{nm}\bullet\boldsymbol{k}_{nl}\overline{\otimes}\left[\left[\overline{\boldsymbol{F}}^{-1}\bullet\boldsymbol{x}_k\right]\left[\overline{\boldsymbol{F}}^{-1}\bullet\boldsymbol{x}_l\right]\right]\end{aligned} \tag{6.16}$$

At this point, we are able to combine the two shares in (6.16). Therefore, we identify the index k with the index i as well as the index l with the index j. Observing that:

$$\boldsymbol{k}_{ij} - \sum_{m\in\mathscr{F}^*}\sum_{n\in\mathscr{F}^*}\boldsymbol{k}_{im}\bullet\left[\boldsymbol{K}^{-1}\right]_{nm}\bullet\boldsymbol{k}_{nj} = \boldsymbol{0} \quad\forall\quad i,j\in\mathscr{P} \quad\text{with}\,\{i,j\}\cap\mathscr{I}\neq\emptyset, \tag{6.17}$$

we end up with the definition of the macroscopic tangent in terms of the restricted TAYLOR assumption.

$$\overline{\mathbb{A}} = \frac{1}{V_{\mathsf{rve}}}\sum_{i\in\mathscr{B}^*}\sum_{j\in\mathscr{B}^*}\left[\boldsymbol{k}_{ij} - \sum_{m\in\mathscr{F}^*}\sum_{n\in\mathscr{F}^*}\boldsymbol{k}_{im}\bullet\left[\boldsymbol{K}^{-1}\right]_{nm}\bullet\boldsymbol{k}_{nj}\right]\overline{\otimes}\left[\boldsymbol{X}_i\otimes\boldsymbol{X}_j\right] \tag{6.18}$$

The term including the aggregate stiffness entries defines a SCHUR complement, also known as static condensation, see TURNER ET AL. [142] or WILSON [158]. Thereby, the response of the entire bulk, i.e., the group of grains which does not experience reaction forces, is transferred to the boundary particles.

6.3.3. Macroscopic tangent - periodic boundary conditions

Under the consideration of periodicity in the material as well as spatial configuration, the derivation of the periodic boundary conditions related tangent follows an identical procedure as described in Subsection 6.3.2. We remark that the spatial periodicity renders the use of the introduced periodic stiffness matrix as well as its entries, see $(4.49)_1$.

$$\overline{\mathbb{A}} = \frac{1}{V_{\mathsf{rve}}}\sum_{i\in\{a,b,c,d\}}\sum_{j\in\{a,b,c,d\}}\boldsymbol{k}^{\star}_{\mathsf{peri}\,ij}\overline{\otimes}\left[\boldsymbol{X}_i\otimes\boldsymbol{X}_j\right] \tag{6.19}$$

with

$$\boldsymbol{k}^{\star}_{\text{peri}\,ij} = \boldsymbol{k}_{\text{peri}\,ij} - \sum_{m\in\mathscr{I}^{*},\mathscr{B}^{*}_{\ominus}} \sum_{n\in\mathscr{I}^{*},\mathscr{B}^{*}_{\ominus}} \boldsymbol{k}_{\text{peri}\,im} \bullet \left[\boldsymbol{K}_{\text{peri}}{}^{-1}\right]_{nm} \bullet \boldsymbol{k}_{\text{peri}\,nj}. \tag{6.20}$$

Please observe the static condensation with respect to the four corner particles, denoted by a, b, c, d. The obtained representation of the macroscopic tangent states the discrete counter part to the continuous macroscopic tangent, derived by KOUZNETSOVA [70].

6.4. Representative numerical examples

The successful implementation of the proposed computational homogenization strategy is presented in this section. All macroscopic computations are performed by using the finite element analysis program feap. The microscopic discrete element program, realized by a parallel fortran code, is attached by utilizing the provided user-material interface of feap. We perform three well-chosen numerical experiments. At first we discuss a simple rectangular block, subjected to pressure and deformation, see Subsection 6.4.1. This macroscopically trivial example enables to focus on the macroscopic convergence behavior of the residual and to investigate on a macroscopically noticeable feature which emerges from microscopic topology changes, the so-called REYNOLDS' dilatancy. Microscopically, we consider the introduced set of boundary conditions, including the assumption of TAYLOR, the restricted TAYLOR assumption and the periodic boundary conditions. Subsequently, we turn to a bi-axial compression test, see Subsection 6.4.2, as well as to a slope stability problem, compare Subsection 6.4.3. Thereby, based on the individual problem size, we restrict the selection of applied microscopic boundary conditions. In particular, the bi-axial compression test is performed under the assumption of TAYLOR as well as under the restricted TAYLOR assumption. In case of the slope stability problem we exclusively consider the assumption of TAYLOR.

6.4.1. Rectangular block.

To demonstrate the proposed multiscale algorithm, we select a simple quadratic macroscopic structure shown in Figure 6.1 (left). The structure has dimensions 100 mm $\times$ 100 mm and is discretized by nine Q1 finite elements. The left and the bottom side of the structure are subjected to homogeneous DIRICHLET boundary conditions, see Figure 6.1 (left). Pressure, denoted by p, is applied on the right side. For the present numerical experiment we consider three different side pressures. We take into account $p \in \{0.1, 0.2, 0.3\}$ N/mm^2. Each finite element has a number of four GAUSS-points. Locally, i.e., GAUSS-point based, we attach a microscopic rve to account for the macroscopic constitutive model. The selected rve is depicted on the right side of Figure 6.1. The considered grain assembly contains 150 primary particles and is generated by using the introduced generation algorithm, see Chapter 3. Data concerning the grain size distribution is listed in Table 5.1. The normal contact stiffness between the mi-

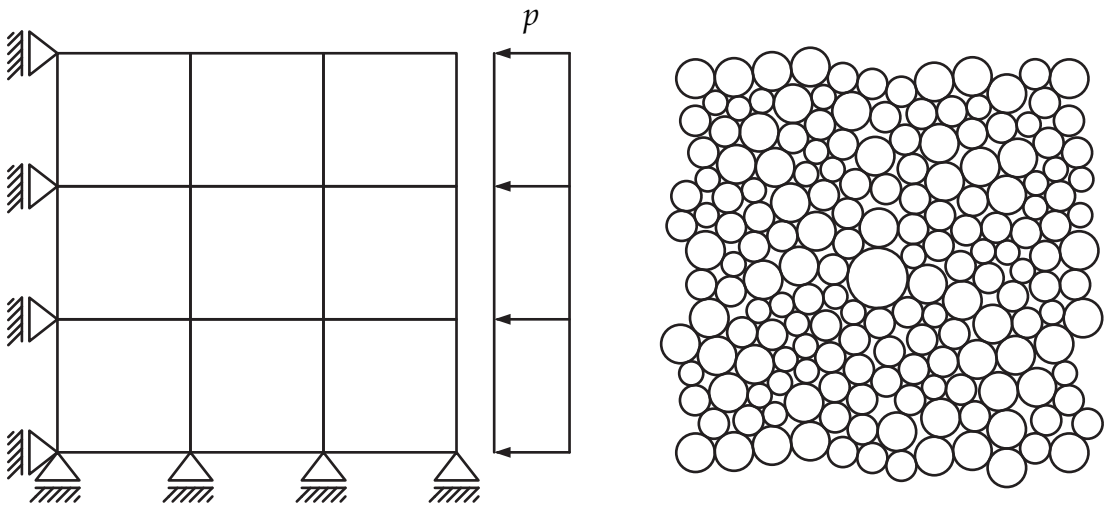

Figure 6.1.: Rectangular block example. *Left*: Initial undeformed macroscopic structure, discretized with nine Q1 finite elements. The physical dimensions are set to 100 mm $\times$ 100 mm. Homogeneous DIRICHLET boundary conditions are depicted. A pressure is applied on the right side of the structure. *Right*: Microscopic rve, containing 150 primary grains.

croscopic grains is chosen to 50 N/mm. Please observe that the microscopic contact stiffness is the only physical parameter that we provide. The complete loading process divides into two parts. Initially, holding the vertical displacement of the upper edge equal to zero, the pressure p is applied. During this step the initial contact network is build and extended. Thereafter, keeping the side pressure constant, the nodes of the upper edge are displaced downwards. We aim to reach a prescribed vertical displacement of $u_v = 3$ mm. As macroscopic solution procedure we utilize a standard NEWTON-RAPHSON iteration scheme, enhanced by a line search procedure. Microscopically, the outlined dynamic relaxation procedure, compare Section 4.4, is used. The macroscopic convergence behavior of the residual is demonstrated by selecting the examples using $p = 0.2$ N/mm^2. Thereby, each introduced boundary condition is individually documented in the Tables 6.1 – 6.3. Even though we only provide results for selected macroscopic load steps (mls), the therein listed information reflects the overall observed convergence behavior. For both TAYLOR assumptions quadratic convergence on the macroscale level is achieved without difficulty, see Table 6.1 and 6.2. This associates to the restricting and well supporting nature of the TAYLOR based boundary conditions. Problems may arise applying periodic boundary conditions, compare the last column of Table 6.3. In this particular mls we observe a slow convergence throughout almost all iterations. Exclusively the last iteration step demonstrates the desired characteristic of a quadratic convergence behavior. This specific observance reflects the soft nature of the periodic boundary conditions, allowing the straightforward transfer of microscopic discrete information to the continuous macroscale, unaffected by microscopic boundary effects. Hence, macroscopic non-smoothness is to

Table 6.1.: Macroscopic convergence behavior of selected mls, rectangular block example: TAYLOR assumption, $p = 0.2$ N/mm^2.

iter	mls 4	mls 7	mls 11	mls 15	mls 22	mls 28
1	1.000E+00	1.000E+00	1.000E+00	1.000E+00	1.000E+00	1.000E+00
2	1.461E-02	2.239E-02	5.565E-02	2.500E-02	2.291E-01	1.081E-01
3	1.649E-07	5.197E-07	2.330E-04	4.137E-04	2.475E-02	9.838E-03
4	5.774E-14	7.830E-14	2.801E-09	1.534E-06	1.108E-03	1.297E-04
5				5.560E-14	2.192E-06	1.903E-10
6					4.015E-14	

Table 6.2.: Macroscopic convergence behavior of selected (mls), rectangular block example: Restricted TAYLOR assumption, $p = 0.2$ N/mm^2.

iter	mls 4	mls 7	mls 11	mls 15	mls 22	mls 28
1	1.000E+00	1.000E+00	1.000E+00	1.000E+00	1.000E+00	1.000E+00
2	2.334E-02	6.490E-02	5.565E-02	1.947E-01	5.924E-02	8.428E-02
3	6.071E-04	7.710E-04	2.330E-04	2.900E-02	2.998E-01	2.025E-03
4	4.397E-08	4.485E-09	2.801E-09	3.322E-02	8.112E-02	5.314E-07
5	3.740E-14			2.164E-03	5.054E-03	1.493E-13
6				1.898E-06	3.996E-05	
7				1.543E-12	9.961E-10	

Table 6.3.: Macroscopic convergence behavior of selected mls, rectangular block example: Periodic boundary conditions, $p = 0.2$ N/mm^2.

iter	mls 4	mls 7	mls 11	mls 15	mls 22	mls 28
1	1.000E+00	1.000E+00	1.000E+00	1.000E+00	1.000E+00	1.000E+00
2	1.511E-01	4.495E-02	1.056E-01	1.292E-01	7.959E-02	8.483E-02
3	1.560E-01	1.068E-02	5.046E-02	3.137E-01	2.958E-02	4.209E-02
4	1.024E-02	4.178E-04	5.337E-03	5.338E-03	3.688E-04	2.473E-02
5	3.259E-04	6.676E-06	4.798E-04	2.764E-05	2.909E-08	3.481E-04
6	3.461E-08	5.830E-11	1.080E-07	8.489E-11	4.274E-13	7.253E-04
7	1.430E-12		2.743E-11			2.202E-05
8						6.865E-10

be expected, possibly leading to poor macroscopic convergence. Next, we concentrate on the macroscopic dilatancy behavior, compare Remark 6.2, and the resultant vertical force f_v, measured at the bottom of the macroscopic structure. We define the macroscopic measure of dilatancy as, $\Delta = (v_{\text{spe}}/V_{\text{spe}} - 1)100$, where v_{spe} denotes

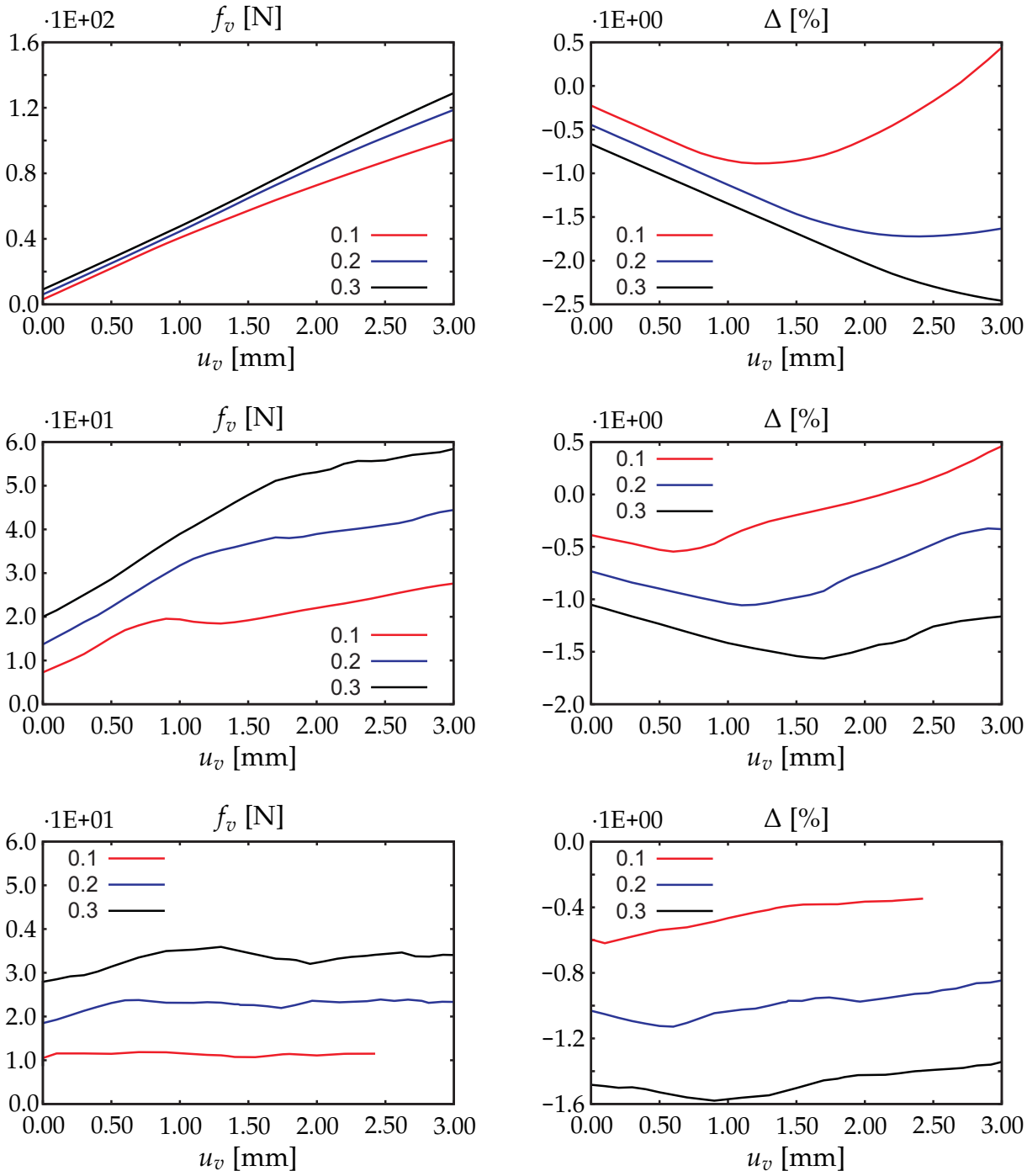

Figure 6.2.: Comparison of macroscopic results for different side pressures. *Left column*: Resultant vertical force on the bottom of the structure. *Right column*: Overall dilatancy of the structure. *Top row*: TAYLOR assumption. *Center row*: Restricted TAYLOR assumption. *Bottom row*: Periodic boundary conditions.

the current volume of the specimen and V_{spe} the initial volume of the structure. Subsequently, a negative dilatancy measure relates to a relative volume decrease, while a

positive dilatancy measure indicates relative volume increase. Results concerning both quantities are combined in Figure 6.2, depicted with respect to the prescribed vertical displacement of the upper edge of the macroscopic structure. The single graphs are ordered by the used boundary conditions. Starting from the top of Figure 6.2 we consider the assumption of TAYLOR, the restricted TAYLOR assumption and the periodic boundary conditions. Keeping in mind the outcome of the preceding chapters, the obtainment applying the assumption of TAYLOR reflects the documented findings of macroscopic smoothness. For the considered range of deformation, the obtained vertical force shows an initial linear branch followed by an almost not noticeable non-linear behavior. The order of the individual curves colligates to the applied pressure, i.e., higher side pressure yields higher resultant forces f_v. The range of linearity increases under the increase of side pressure. This feature is even more vivid for the dilatancy measure. Thereby, we observe a linear decrease and a subsequent monotonously non-linear increase in volume. In the case of the restricted TAYLOR assumption we observe similarities to the just discussed results. These similarities include the order of the individual curves, the presence of initial linear branches as well as their dependence on the applied side pressure. Yet, both graphs reveal the range of linearity to be significantly shorter. The following non-linear response depicts a rather rough outcome, pointing to topology changes of the discrete microscopic nature. In this context, small regions of softening are noticed. Under the application of periodic boundary conditions we find the order with respect to the applied side pressure to match the previous discussed results. Contrary, the obtained plots show a rather rough and a locally non-smooth macroscopic output. Furthermore, both graphs reveal strong fluctuational behaviors which include regions of softening. These reflections correspond to the soft nature of the periodic boundary conditions. Initial linearity is exclusively observed in a very small region of the depicted plots. Dilatancy features are visible; however, compared to the already discussed boundary conditions their course is not as pronounced. With respect to the curve corresponding to a side pressure of $p = 0.1\,\mathrm{N/mm^2}$ we were not able to compute any further. Reasons are related to the rough and non-smooth nature which requires infinitesimal small load increments. Combined we can adhere that the proposed computational homogenization scheme allows the projection of microstructural based granular typical features to the continuous macroscale.

Remark 6.2 (REYNOLD's dilatancy) One distinguishing behavior of particulate media was first described by REYNOLDS [118] in 1885. His observation identifies a relation between the change of the overall volume of a granular specimen and the applied load / deformation. While most materials decrease their overall volume under pressure, particulate media can increase their overall volume. This reaction, the so-called REYNOLDS' dilatancy principle, is based on the particulate nature of granular materials. In detail, a well packed granular assembly generally increases its overall volume, i.e., its pore volume, before it finally decreases in size. Naturally, the volume of the grains themselves stays constant during this process. The matter for such transformations is based on the interlocking grains which need to move around one another. In focus of this contribution the REYNOLDS' dilatancy principle is regarded as a macro-

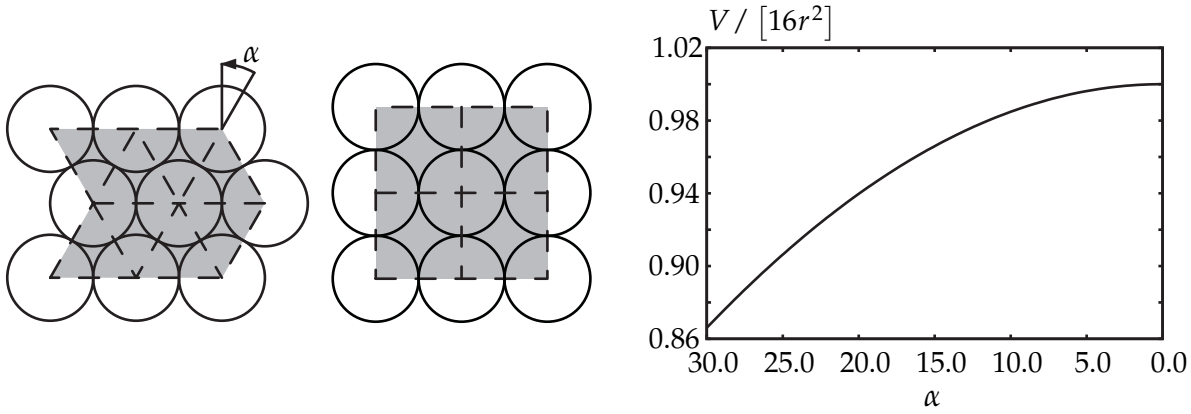

Figure 6.3.: Basic example of the REYNOLDS' dilatancy principle. *Left*: Initial dense particle configuration with the network angle $\alpha = 30°$. The area of interest is shaded in gray. The contact network is denoted by dashed lines. *Center*: Final, compressed, particle structure. The network angle is equal to $0°$. *Right*: Relation between the volume of the closed hull and the network angle α. The ordinate shows the increase of the overall volume of the closed hull, depending on the network angle α.

scopic noticeable effect, caused by the topology changes of the microstructure. The most prominent example of the REYNOLDS' dilatancy principle can be observed during a walk on wet sand, e.g., a beach. Thereby we can note that sand around a footprint dries out under pressure. This phenomena is due to the dilatancy of the sand. Reorganization, based on the applied foot pressure, increases the pore volume and allows the water to enter in between. For a better illustration and understanding of this distinguishing behavior, we study a particle assembly containing nine uniform perfect grains with radii r. As a measurement, we introduce the network angle α, shown in Figure 6.3 (left). For $\alpha = 30°$, Figure 6.3 (center), we obtain the so-called closest packing. This hexagonal particle arrangement, often compared to crystal lattices, is, if extended periodically, distinguished by six contacts per particle. In a two dimensional monodisperse packing, six contacts per particle represent the maximum number of grains being able to contact simultaneously. Furthermore, we find three principal contact directions, having an internal angle of $60°$. The contact network is illustrated by dotted lines which connect the particle centers. The volume of interest, surrounded by a closed hull, is shaded. We define the closed hull as the polyline connecting the particle centers. Using the introduced network angle α, the volume enclosed by the closed hull yields to

$$V(\alpha) = 16r^2 \cos\alpha. \tag{6.21}$$

Thus, the enclosed volume of the initial particle configuration equates to approximately $13.86r^2$. Imagining a compression of the particle assembly by rigid walls from the left and from the right side finally results into the configuration shown in the center of Figure 6.3. During the process of deformation we find the particle volume inside the closed hull to be constant, while we can also observe that the pore volume between

the single grains increases strictly monotonously, see Figure 6.3 (right). This pore expansion reflects the REYNOLDS' dilatancy principle. In the deformed configuration the network angle α to be equal to 0°. This type of arrangement, also known as the cubic lattice packing of monodisperse particles in two dimensions, is distinguished by a number of four contacts per particle. The cubic lattice structure leads to a volume of the closed hull equal to $16.00r^2$. ■

6.4.2. Bi-axial compression test

A rather large example, based on a bi-axial compression test, see for example KANEKO ET AL. [64], is discussed in this subsection. With respect to the microscopic boundary conditions, we focus on applying the outlined TAYLOR assumption, as well as the restricted TAYLOR assumption. The structure on the macroscale has the dimensions 50 mm $\times$ 100 mm and is discretized by 50 Q1 finite elements. We solely use one physical parameter on the microscale, the contact stiffness between the individual grains, $E = 50$ N/mm. The upper and the lower surface are subjected to displacement boundary conditions, see Figure 6.4, (left). The left and the right side of the specimen are subjected to a confining surface pressure of 0.2 N/mm . Each macroscopic GAUSS-point is connected to an microscopic rve, containing 88 particles. Four GAUSS-points of interest are marked. The loading procedure consists of two steps.

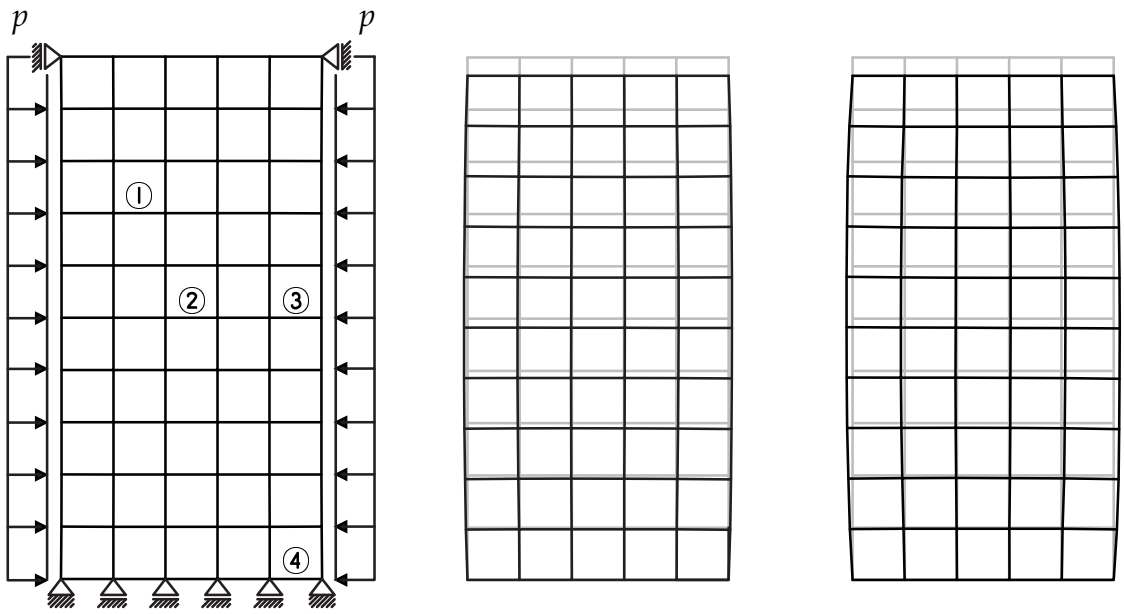

Figure 6.4.: Bi-axial compression test. *Left*: Macroscopic structure, discretized by 50 Q1 finite elements. Homogeneous DIRICHLET boundary conditions are depicted. *Center*: Comparison between the undeformed and the deformed specimen: TAYLOR assumption. *Right*: Comparison between the undeformed and the deformed specimen: restricted TAYLOR assumption.

Table 6.4.: Macroscopic convergence behavior of selected mls, bi-axial compression test: TAYLOR assumption.

mls	iteration 1	iteration 2	iteration 3	iteration 4	iteration 5
2	1.000E+00	2.925E-04	2.797E-08	8.254E-20	
6	1.000E+00	3.600E-05	5.981E-10	1.968E-23	
10	1.000E+00	1.898E-03	2.551E-06	6.749E-11	7.009E-25
17	1.000E+00	1.525E-02	1.308E-04	2.845E-08	6.702E-19

Table 6.5.: Macroscopic convergence behavior of selected mls, bi-axial compression test: Restricted TAYLOR assumption.

mls	iteration 1	iteration 2	iteration 3	iteration 4	iteration 5
2	1.000E+00	4.868E-04	5.047E-07	1.278E-14	3.214E-23
6	1.000E+00	1.456E-03	1.588E-07	1.467E-16	2.638E-28
10	1.000E+00	1.092E-02	2.373E-05	2.709E-09	5.846E-19
17	1.000E+00	1.580E-03	6.638E-06	4.723E-10	3.527E-19

At first, the specimen is subjected to the confining pressure, while the vertical displacement of the upper and lower surface are held fixed. Afterwards, holding the confinement pressure constant, the vertical displacement is applied to the top surface. Table 6.4 and 6.5 show the macroscopic convergence behavior regarding the TAYLOR and restricted TAYLOR assumption. The deformed shapes of the specimens are depicted in Figure 6.4 (center, right). Comparing the outline of the deformed specimens, the application of the restricted TAYLOR assumption yields an overall larger curvature. The corresponding macroscopic force-displacement plots are depicted in Figure 6.5, (right). In particular, we present the macroscopic axial force axial displacement (f_v–u_v) relations for two microscopic boundary conditions. We observe remarkable differences between the two graphs which are in coherence with the deformation plots. While the application of the TAYLOR boundary condition delivers a stiff and almost linear force-displacement behavior, the use of the restricted TAYLOR boundary conditions results in a softer non-linear result. The non-linear behavior on the macroscale relates to the reorganization, as well as the forming and breaking of inter-particle contacts of the microscopic grains. This observation becomes clearer when tending to the dilatancy measure, see Figure 6.5. Utilizing the TAYLOR assumption, the relative dilatancy measure monotonously decreases up to a axial displacement of approximately 3%. Thereafter, we notice a slight volume increase. The minimum of the relative dilatancy measure has a value of $\Delta \approx -1.86\%$. The restricted TAYLOR assumption delivers a different result. We observe a dilatancy principle conforming behavior, i.e., a volume decrease, followed by a volume increase. The minimum of the dilatancy measure corresponds to a axial displacement of approximately 1.25%. The minimum value of the relative dilatancy measure is found to be approximately -1.10%. Relating the dilatancy plot to the axial force plot, the relation between the microscopic grain reorganization and the macroscopic non-linear force graph is visible. In particular, the reorganization, as

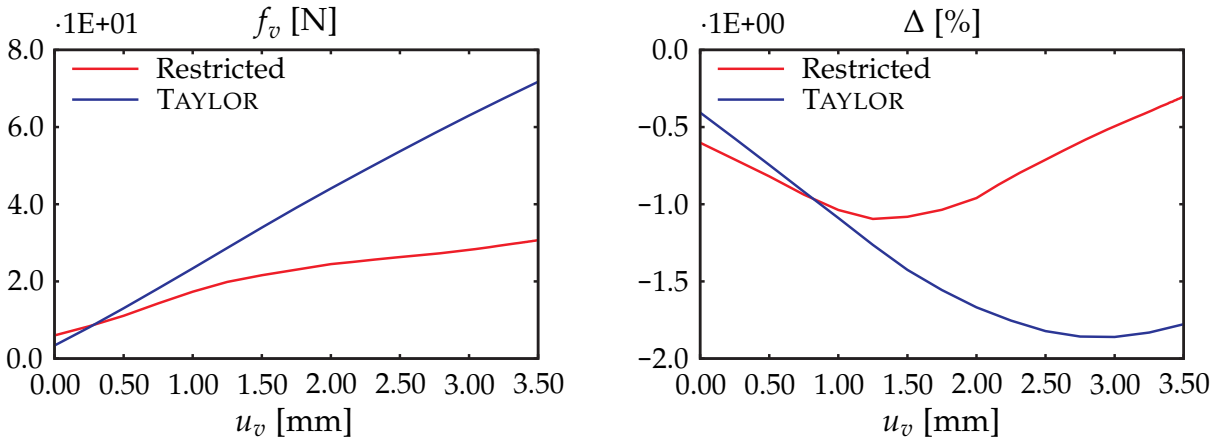

Figure 6.5.: Comparison of macroscopic quantities in response to different microscopic boundary conditions, bi-axial compression test. *Left*: Macroscopic axial force; the abscissa shows the axial displacement, while the ordinate depicts the total axial force. *Right*: Macroscopic dilatancy; the plot shows the overall dilatancy over the axial displacement of the specimen.

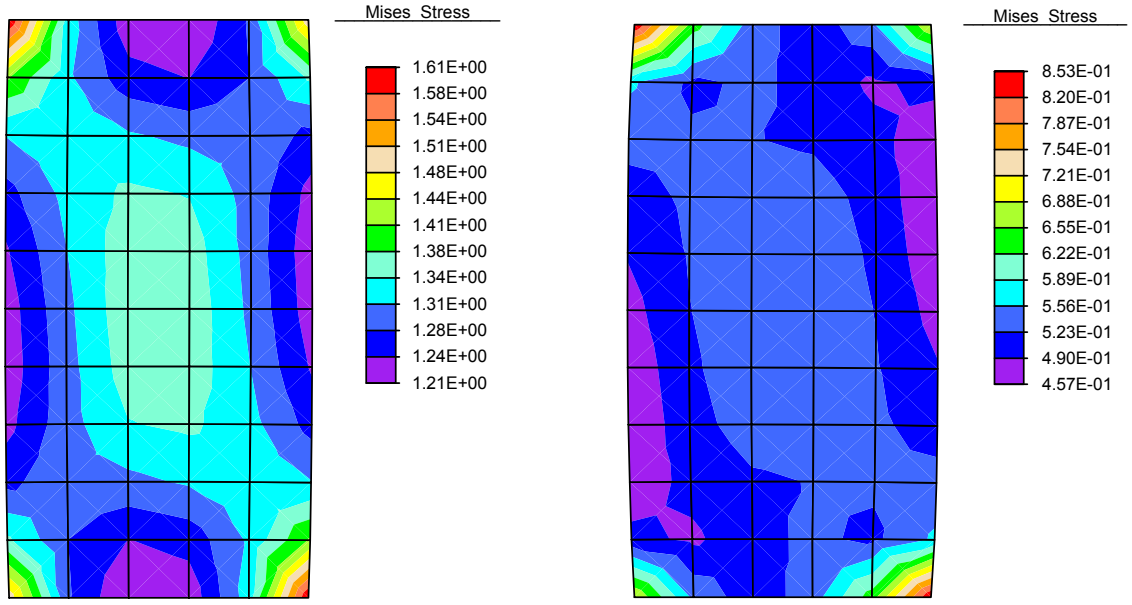

Figure 6.6.: Deformed bi-axial specimen depicting VON MISES stress. *Left*: Assumption of TAYLOR. *Right*: Restricted TAYLOR assumption.

well as the forming and breaking of the inter-particle contacts of the microscopic grains leads to a loss of the macroscopic stiffness, i.e., at the point where volume increase is noticed, the gradient of the macroscopic axial force changes. Figure 6.6 presents the contour plots of the so-called VON MISES stress. The VON MISES stress computes by using the introduced CAUCHY stress, $\overline{\sigma}_{\text{mises}} = \sqrt{3/2\ \overline{\sigma}^{\text{dev}} : \overline{\sigma}^{\text{dev}}}$, where $\overline{\sigma}^{\text{dev}}$ denotes the deviatoric part of the macroscopic CAUCHY stress. Initiation of potential failure

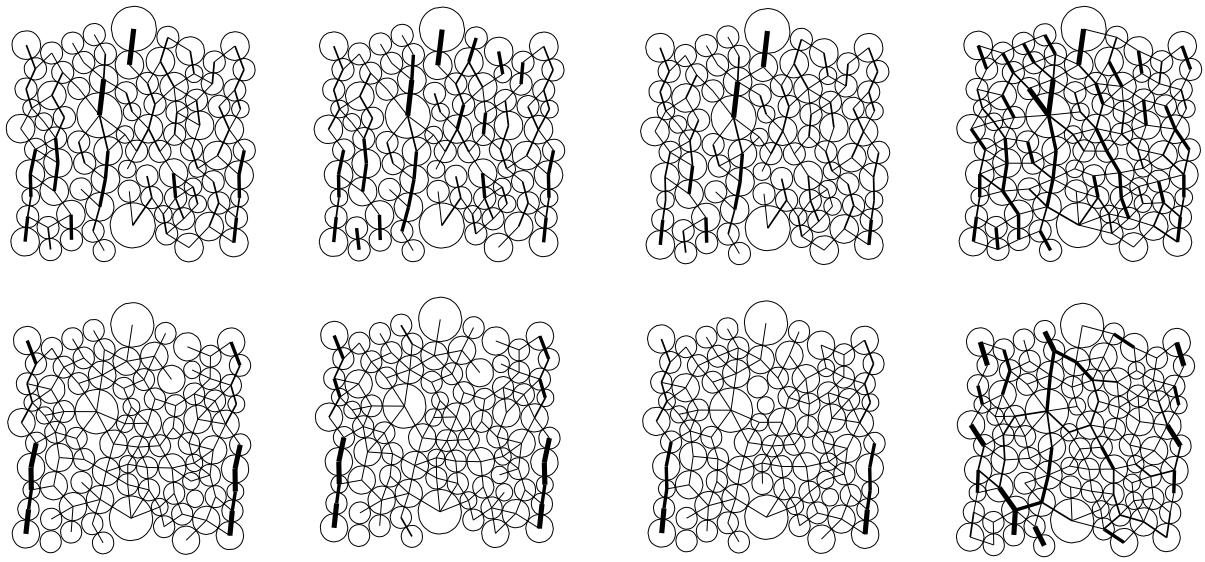

Figure 6.7.: Zoom in on selected micro structures. Sampling points are indicated in Figure 6.4. The rves are ordered in an ascending manner and correspond to an axial displacement of 3.5 mm. The plots show the branch network, whereby the line thickness qualitatively corresponds to the magnitude of the contact force. *Top*: Assumption of TAYLOR. *Bottom*: Restricted TAYLOR assumption.

zones of localized deformation are visible at the upper left and the lower right corner for both microscopic boundary conditions. Deformed rves, related to the in Figure 6.4 (left) indicated sampling points, pointed out by ①, ②, ③ and ④, are depicted in Figure 6.7. The rves in the top row of Figure 6.7 relate to the assumption of TAYLOR. Conforming to the applied boundary condition, i.e., all particle positions are *a priori*prescribed, unbalanced force networks run through the rves. The micro structures, deformed under the restricted TAYLOR assumption, are presented in the bottom row of Figure 6.7. In contrast to the assumption of TAYLOR, a balanced force network is observed for the bulk. Nevertheless, the boundaries of the rves show unbalanced force networks, which are in agreement to the nature of the applied boundary conditions, i.e., while the positions of the boundary particles are prescribed by the macroscopic deformation gradient, the bulk is required to relax.

6.4.3. Slope stability problem

This subsection discusses a slope stability problem, initially introduced by ZIENKIEWICZ & PANDE [161]. The in Figure 6.8 depicted slope is subjected to dead load combined with a load originating from a massless strip footing subjected to an eccentric force. The massless strip footing has a length of 23.25 m. The physical parameters of the macroscopic and microscopic calculations are listed in Table 6.6. The overall structure is discretized by 380 Q1 finite elements. An rve, containing 700 particles, is used on the microscale level. The loading process is divided in two stages. In the first stage, the gravity load is applied, using one load step. The second stage uses twenty load steps to apply the eccentric point load. The convergence of a relative energy norm is

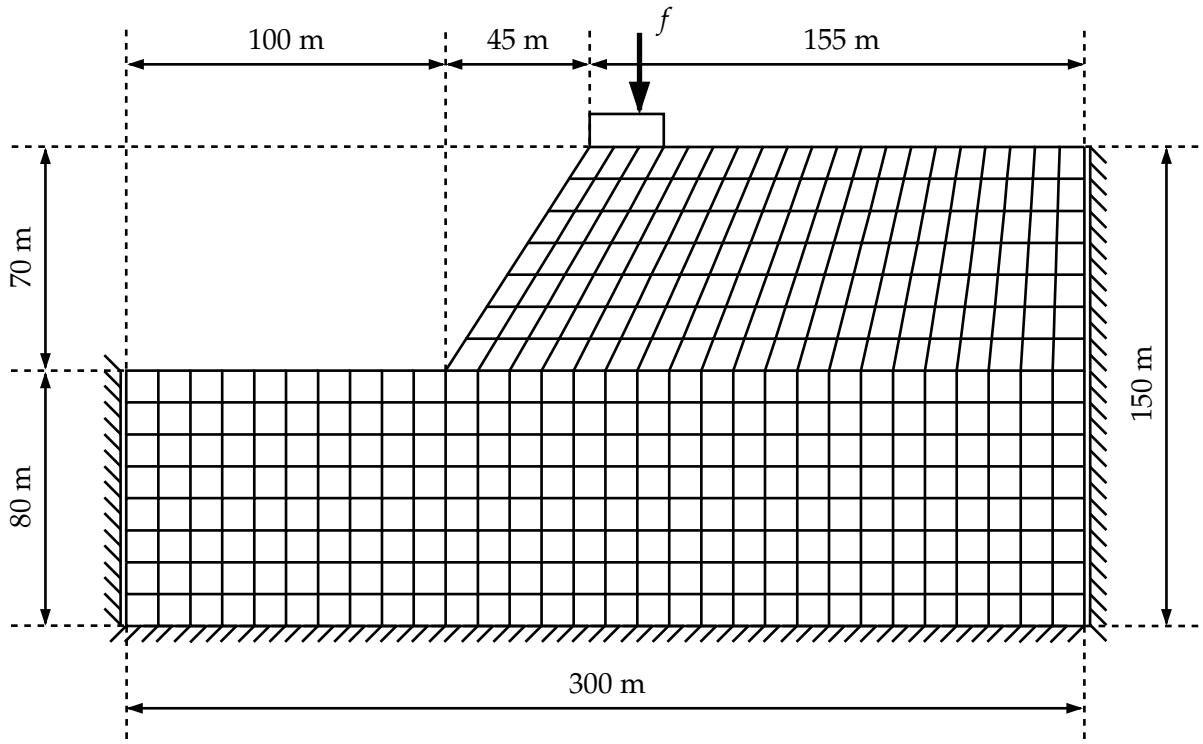

Figure 6.8.: Undeformed mesh of the slope stability problem. Boundary conditions are depicted. The structure is meshed with 380 Q1 finite elements. The massless footing is subjected to an eccentric point load f. The eccentricity equals 3.875 m

Table 6.6.: Physical parameters of the slope stability problem.

Macroscopic mass density	2.5E+03	[kg/m^3]
Macroscopic load	-4.0E+07	[N]
Microscopic contact stiffness	2.8E+07	[N/m]

Table 6.7.: Macroscopic convergence behavior of selected mls, slope stability test: TAYLOR assumption.

mls	iteration 1	iteration 2	iteration 3	iteration 4	iteration 5
6	1.000E+00	3.341E-04	2.308E-08	7.110E-16	3.441E-26
10	1.000E+00	3.940E-04	1.503E-08	7.415E-16	5.014E-26
15	1.000E+00	1.322E-03	1.999E-07	6.114E-14	4.023E-26
18	1.000E+00	4.817E-03	3.816E-06	7.276E-12	5.932E-24

presented for selected load steps, see Table 6.7. Figure 6.9 depicts a contour plot of the macroscopic VON MISES stress. An initial localization, initiated at the maximum VON

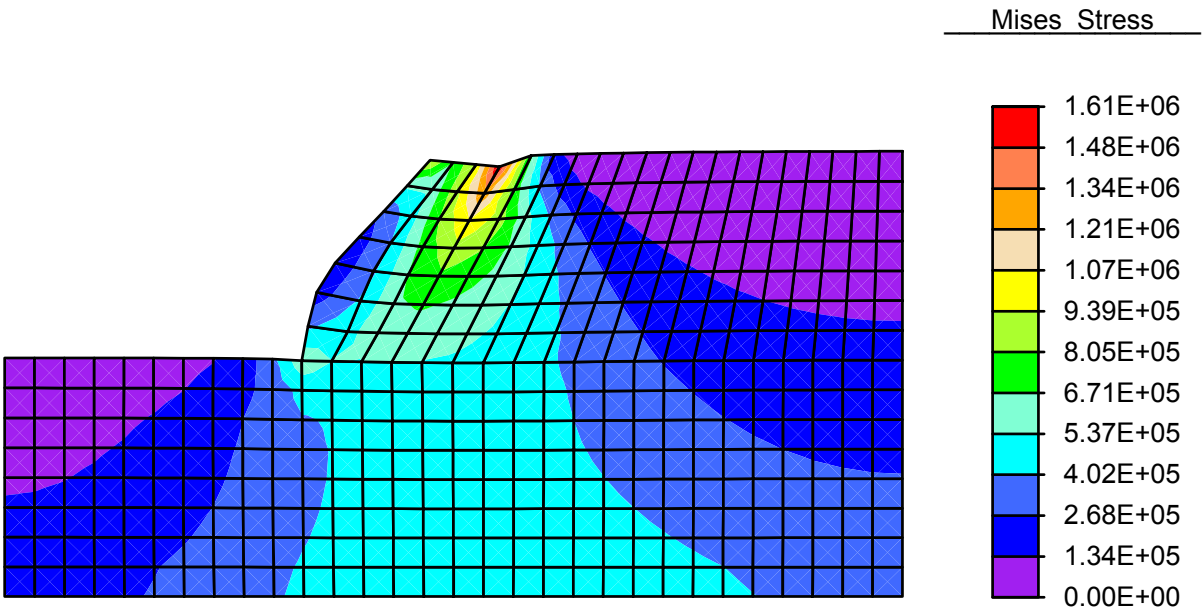

Figure 6.9.: Deformed mesh of the slope stability problem. The macroscopic VON MISES stress is plotted.

MISES stress is noted.

7. Interparticle friction

7.1. Introduction

At this point, we tend to the incorporation of inter-particle friction. Inter-particle friction describes one form of possible energy dissipation on the grain-scale level. Next to the presence of dilatancy, inter-particle friction is accounted as a principle of granular assemblies, compare DURAN [39]. The formulation of frictional contact has a long history of research. In the early stages of the dem, tangential friction is modeled by introducing linear elastic spring devices, in association with the relative tangential displacement of contacting grains. Thereby, the elastic response of the spring is governed by a MOHR-COULOMB law of friction, yielding to the effect of energy dissipation, see for example [27–29]. Although this specific model provides reasonable macroscopic results which are in good agreement with the performed experiments, it does not incorporate the history of the contact itself. Mechanically more advanced, but also rather expensive models are presented by VU-QUOC & ZHANG [146], VU-QUOC, ZHANG & WALTON [149], WALTON [151] and WALTON & BRAUN [152]. Yet, these models are phenomenological based. We attempt to derive a frictional tangential inter-particle contact model by applying a variational approach. In the context of continuum mechanics, variational approaches are used by numerous investigators to describe dissipative processes, see for example COMI & PEREGO [22] for elasto-plasticity or ORTIZ & STAINIER [111] for visco-plasticity. Recently, ORTIZ & PANDOLFI employed a variational approach to define a formulation of the Cam-clay theory of plasticity, see [110]. In MIEHE [89] and MIEHE, SCHOTTE & LAMBRECHT [93] a variational approach is extended to allow the variational formulation of homogenization of inelastic microstructures.

We deploy a variational model to define an inter-particle tangential friction forces. The adopted procedure relies on the minimization of a general work function with respect to the internal variables, whereby the generalized work function includes an elastic and an inelastic contribution. Internal variables are updated subsequently during the minimization process. The result of the minimization process defines an incremental potential. The incremental potential is used to define the elastic tangential contact force as well as the related couples. A discrepancy between the obtained results does not allow for the conservation of the global angular momentum. We provide the reader with a suitable algorithmic update procedure to circumvent this problem.

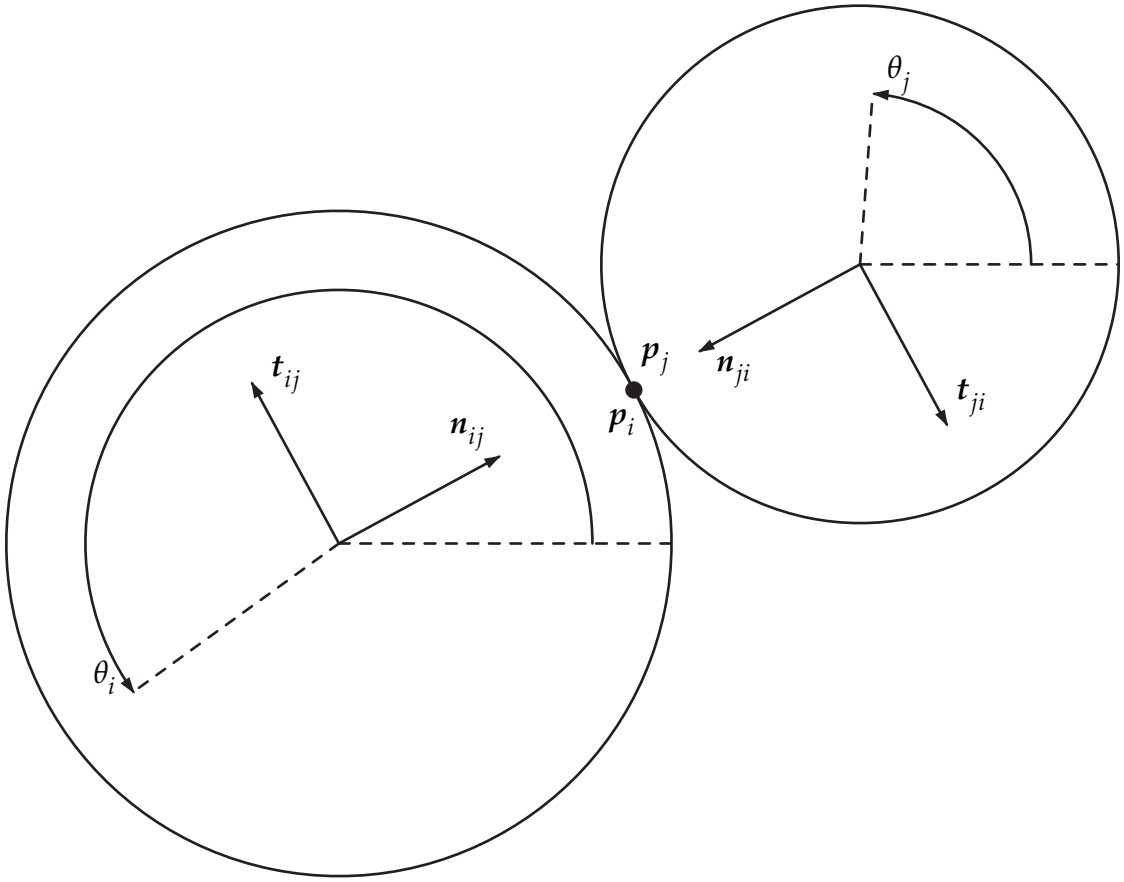

Figure 7.1.: Two particles in contact

7.2. Frictional extension

This section provides a frictional extension to the smooth dem, presented in Chapter 4. The kinematics with respect to the smooth contact are enhanced by introducing the inter-particle slip. In terms of the frictional enrichment, the inter-particle slip represents a primary variable. Next, we define the reduced incremental potential which allows for a derivation of the tangential contact forces. This section closes with remarks on the microscopic boundary conditions as well as on the macroscopic stress calculation.

7.2.1. Inter-particle kinematics

To set the stage for the introduction of a tangential energy storage function as well as for the CLAUSIUS-PLANCK inequality, the reader's attention is directed to the definition of a kinematic variable, the total inter-particle slip γ. The total inter-particle slip,

decomposable into an elastic and a plastic part,

$$\gamma_{ij} = \gamma_{\mathrm{el}ij} + \gamma_{\mathrm{pl}ij}, \tag{7.1}$$

is derived from the rate of the total inter-particle slip. The elastic part of the total slip is related to the adhesion between contacting grains, while the plastic share is interpreted as sliding between the objects. We define the total inter-particle slip by its rate. Therefore, we observe the velocities of the points $\boldsymbol{p}_i$ and $\boldsymbol{p}_j$, positioned at the point of contact, see Figure 7.1. These velocities are described by:

$$\dot{\boldsymbol{p}}_i = \dot{\boldsymbol{x}}_i + \dot{\theta}_i r_i \frac{\left|\left|\boldsymbol{l}_{ij}^{n+1}\right|\right|}{r_i + r_j} \boldsymbol{t}_{ij} \quad \text{and} \quad \dot{\boldsymbol{p}}_j = \dot{\boldsymbol{x}}_j + \dot{\theta}_j r_j \frac{\left|\left|\boldsymbol{l}_{ij}^{n+1}\right|\right|}{r_i + r_j} \boldsymbol{t}_{ji}. \tag{7.2}$$

The translational velocity of the particles are denoted by $\dot{\boldsymbol{x}}_i$ and $\dot{\boldsymbol{x}}_j$, while the rotational velocities are indicated by $\dot{\theta}_i$ and $\dot{\theta}_j$. In contrast to the standard definition of the velocity of a point on a rigid body, (7.2) includes the scaling factor $\left|\left|\boldsymbol{l}_{ij}^{n+1}\right|\right| / \left[r_i + r_j\right]$. The scaling compensates for the allowed inter-particle overlap between the contacting grains. Note, with respect to the assumption of rigidity, we select the introduced scaling factor to be constant during the overall derivation process. The unit vectors $\boldsymbol{t}_{ij}$ and $\boldsymbol{t}_{ji}$ indicate the tangential direction and comply to,

$$\boldsymbol{t}_{ij} = -\boldsymbol{t}_{ji}, \qquad \boldsymbol{t}_{ij} = \boldsymbol{\Omega} \cdot \boldsymbol{n}_{ij}. \tag{7.3}$$

Similar to the branch and the normal vector, compare (3.4), the first index of the unit tangential vector indicates the position of origin. The matrix $\boldsymbol{\Omega}$, termed alternation matrix, compare CUNDALL & STRACK [27], specifies a standard two dimensional rotation matrix which is evaluated for a fixed angle of 90°. Subtracting the velocity of point $\boldsymbol{p}_j$ from the velocity of point $\boldsymbol{p}_i$ and projecting the result on the tangential contact direction yields the definition of the total tangential inter-particle slip rate,

$$\dot{\gamma}_{ij} = \left[\dot{\boldsymbol{p}}_i - \dot{\boldsymbol{p}}_j\right] \cdot \boldsymbol{t}_{ij} = \left[\dot{\theta}_i r_i + \dot{\theta}_j r_j\right] \frac{\left|\left|\boldsymbol{l}_{ij}^{n+1}\right|\right|}{r_i + r_j} - \dot{\boldsymbol{l}}_{ij} \cdot \boldsymbol{t}_{ij}. \tag{7.4}$$

Assuming the total inter-particle slip to be linear between the nodes of loading, we apply a standard backward EULER integration scheme to obtain a discrete expression for the total inter-particle slip,

$$\gamma_{ij}^{n+1} = \gamma_{ij}^{n} + \left[\left[\theta_i^{n+1} - \theta_i^{n}\right] r_i + \left[\theta_j^{n+1} - \theta_j^{n}\right] r_j\right] \frac{\left|\left|\boldsymbol{l}_{ij}^{n+1}\right|\right|}{r_i + r_j} - \left|\left|\boldsymbol{l}_{ij}^{n}\right|\right| \boldsymbol{t}_{ij}^{n} \cdot \boldsymbol{n}_{ij}^{n+1}. \tag{7.5}$$

The derived expression includes the incremental update of the inter-particle slip. This update is composed by two shares. The first part of the slip update stems from pure

particle rotation. The second part colligates to the slip update which is introduced by pure particle translation. Hence, assuming the temporal change of the contact direction to be zero, this term nullifies.

7.2.2. Reduced incremental potential

With the definition of the total inter-particle slip at hand, we postulate an energy storage function,

$$\Phi_{\mathrm{t}ij}^{n+1} = \frac{1}{2}\mathscr{H}\left(\varepsilon_{ij}^{n+1}\right)\left[E_{\mathrm{t}ij}\left[\gamma_{\mathrm{el}ij}^{n+1}\right]^2 + h_{ij}\left[\alpha_{ij}^{n+1}\right]^2\right]. \tag{7.6}$$

This function is based on the elastic share of the total inter-particle slip, as well as on the internal hardening variable α_{ij}. The tangential contact stiffness is denoted by $E_{\mathrm{t}ij}$, while the hardening modulus is defined by h_{ij}. Considering the results of MINDLIN [97], we relate the tangential contact stiffness to the normal contact stiffness by $E_{\mathrm{t}} = \vartheta E_{\mathrm{n}}$ with $\vartheta \in [2/3, 1]$. Similar to the normal contact, the included HEAVISIDE function leads to a one-sided harmonic character of the stored energy function. We remark that the HEAVISIDE function acts on the particle overlap. Hence, for separated grains, the energy storage function yields a value of zero. For a single contact, the discrete CLAUSIUS-PLANCK inequality reads,

$$\mathcal{D}_{ij}^{n+1} = f_{\mathrm{t}ij}^{n+1}\dot{\gamma}_{ij}^{n+1} - \dot{\Phi}_{\mathrm{t}ij}^{n+1} \geq 0, \tag{7.7}$$

including the discrete internal dissipation power, $\mathcal{D}_{ij}^{n+1}$, the tangential stress power, $f_{\mathrm{t}ij}^{n+1}\dot{\gamma}_{ij}^{n+1}$, and the rate of the energy storage function, $\dot{\Phi}_{\mathrm{t}ij}^{n+1}$. Using the chain rule, the rate of the energy storage function yields,

$$\dot{\Phi}_{\mathrm{t}ij}^{n+1} = \frac{\partial \Phi_{\mathrm{t}ij}^{n+1}}{\partial \gamma_{ij}^{n+1}}\dot{\gamma}_{ij}^{n+1} + \frac{\partial \Phi_{\mathrm{t}ij}^{n+1}}{\partial \gamma_{\mathrm{pl}ij}^{n+1}}\dot{\gamma}_{\mathrm{pl}ij}^{n+1} + \frac{\partial \Phi_{\mathrm{t}ij}^{n+1}}{\partial \alpha_{ij}^{n+1}}\dot{\alpha}_{ij}^{n+1}. \tag{7.8}$$

Insertion of (7.8) in (7.7), reorganization of the result and the application of the COLEMAN-NOLL argument result in a definition of the magnitude of the discrete tangential contact force, as well as in a reduced discrete dissipation power statement.

$$f_{\mathrm{t}ij}^{n+1} = \frac{\partial \Phi_{\mathrm{t}ij}^{n+1}}{\partial \gamma_{ij}^{n+1}}, \qquad \mathcal{D}_{ij}^{n+1} = -\left[\frac{\partial \Phi_{\mathrm{t}ij}^{n+1}}{\partial \gamma_{\mathrm{pl}ij}^{n+1}}\dot{\gamma}_{\mathrm{pl}ij}^{n+1} + \frac{\partial \Phi_{\mathrm{t}ij}^{n+1}}{\partial \alpha_{ij}^{n+1}}\dot{\alpha}_{ij}^{n+1}\right] \geq 0. \tag{7.9}$$

Therein, the partial derivatives denote the thermodynamic forces, Q_1 and Q_2, which are conjugated to the rates of the internal variables $\dot{\gamma}_{\mathsf{pl}ij}$ and $\dot{\alpha}_{ij}$.

$$Q_1 = -\frac{\partial \Phi_{\mathsf{t}ij}^{n+1}}{\partial \gamma_{\mathsf{pl}ij}^{n+1}} = E_{\mathsf{t}ij}\gamma_{\mathsf{el}ij}^{n+1} \quad \text{and} \quad Q_2 = -\frac{\partial \Phi_{\mathsf{t}ij}^{n+1}}{\partial \alpha_{ij}^{n+1}} = -h_{ij}\alpha_{ij}^{n+1} \tag{7.10}$$

We introduce a yield function of COULOMB type which includes the previous derived thermodynamical forces,

$$Y_{ij}^{n+1} = |Q_1| + Q_2 \leq c. \tag{7.11}$$

Therein, we demand the sum of the thermodynamical forces to be less than or equal to a predefined constant c. The constant is set to $c = f_{\mathsf{n}ij}^{n+1}\tan(\rho)$, with ρ being the internal friction angle. Solving the classical optimization problem, i.e., satisfying the principle of maximum dissipation, compare for example SIMO & HUGHES [129], yields the evolution equations for the internal variables,

$$\dot{\gamma}_{\mathsf{pl}ij}^{n+1} = \lambda E_{\mathsf{t}ij}\operatorname{sgn}\left(\gamma_{\mathsf{el}ij}^{n+1}\right) \quad \text{and} \quad \dot{\alpha}_{ij}^{n+1} = \lambda. \tag{7.12}$$

This result as well as the definition of the thermodynamic forces yields an explicit expression for the discrete inter-particle dissipation power,

$$\mathcal{D}_{ij}^{n+1} = \lambda f_{\mathsf{n}ij}^{n+1}\tan(\rho) \geq 0, \tag{7.13}$$

depending on the plastic multiplier λ as well as on the magnitude of the current normal contact force. To obtain the incremental potential, we insert the discrete inter-particle dissipation power in the CLAUSIUS-PLANCK inequality and integrate the result with respect to time.

$$W_{\mathsf{t}ij}^{n+1}\left(\gamma_{ij}^{n+1}, \Delta\lambda_{ij}\right) = \Phi_{\mathsf{t}ij}^{n+1} - \Phi_{\mathsf{t}ij}^{n} + \Delta\lambda_{ij} f_{\mathsf{n}ij}^{n+1}\tan(\rho). \tag{7.14}$$

Finding the reduced incremental potential relates to a minimization problem with respect to the incremental plastic multiplier:

$$\widehat{W}_{\mathsf{t}ij}^{n+1} = \inf_{\Delta\lambda_{ij}}\left(W_{\mathsf{t}ij}^{n+1}\left(\gamma_{ij}^{n+1}, \Delta\lambda_{ij}\right)\right). \tag{7.15}$$

The solution of the minimization problem usually involves a NEWTON-type iteration scheme, however, based on the nature of the here assumed energy storage function, the incremental plastic multiplier is calculated directly:

$$\Delta\lambda_{ij} = -\frac{f_{ij}^{n+1}\tan(\rho) - Y_{ij}^{n+1}}{E_{\mathsf{t}ij} + h_{ij}}. \tag{7.16}$$

The update procedures for the plastic share of the inter-particle slip, as well as for the internal hardening variable result to:

$$\gamma_{\mathsf{pl}ij}^{n+1} = \gamma_{\mathsf{pl}ij}^{n} + \Delta\lambda_{ij}\mathsf{sgn}\left(f_{\mathsf{t}ij}\left(\gamma_{ij}^{n+1}, \gamma_{\mathsf{pl}ij}^{n}\right)\right) \quad \alpha_{ij}^{n+1} = \alpha_{ij}^{n} + \Delta\lambda_{ij}. \tag{7.17}$$

In the event of contact breaking, γ_{ij}^{n+1} and $\gamma_{\mathsf{pl}ij}^{n+1}$ are set to zero.

Remark 7.1 (Update procedure) Let us remark that the derived update procedure equals a standard procedure known from computational plasticity, the so-called return map algorithm. Based on the linearity of the present elastic and the plastic part of the tangential contact model, the return map algorithm consists of an elastic trial step and a possible plastic corrector step. ■

In accordance to the normal contact, one is able to define an incremental potential for a single grain as well as for the overall aggregate.

$$\widehat{W}_{\mathsf{t}i}^{n+1} = \sum_{\substack{j\in\mathscr{P}\\ j\neq i}} \widehat{W}_{\mathsf{t}ij}^{n+1} \quad \text{and} \quad \widehat{W}_{\mathsf{t}}^{n+1} = \frac{1}{2}\sum_{i\in\mathscr{P}}\sum_{\substack{j\in\mathscr{P}\\ j\neq i}} \widehat{W}_{\mathsf{t}ij}^{n+1}. \tag{7.18}$$

7.2.3. Contact tangential force

The frictional tangential contact forces generate by taking the negative derivative of the reduced incremental potential, given in (7.15), with respect to the current particle positions,

$$\boldsymbol{f}_{\mathsf{t}ij}^{n+1} = -\frac{\partial \widehat{W}_{\mathsf{t}ij}^{n+1}}{\partial \boldsymbol{x}_i^{n+1}} = -E_{\mathsf{t}ij}\gamma_{\mathsf{el}ij}^{n+1}\mathscr{H}\left(\varepsilon_{ij}^{n+1}\right)\frac{\left\|\boldsymbol{l}_{ij}^{n}\right\|}{\left\|\boldsymbol{l}_{ij}^{n+1}\right\|}\left[\boldsymbol{t}_{ij}^{n}\cdot\boldsymbol{t}_{ij}^{n+1}\right]\boldsymbol{t}_{ij}^{n+1}. \tag{7.19}$$

In contrast to the contact normal force, compare (4.8), the derivative of the kinematic variable with respect to the current particle position introduces a type of scaling factor,

$$c_{\mathsf{t}ij}^{n+1} = \frac{\left\|\boldsymbol{l}_{ij}^{n}\right\|}{\left\|\boldsymbol{l}_{ij}^{n+1}\right\|}\boldsymbol{t}_{ij}^{n}\cdot\boldsymbol{t}_{ij}^{n+1}, \tag{7.20}$$

whereby the factor itself relates to the possible change of the contact direction. Based on the orientation of the tangential contact force as well as on its origin, couples act on the individual particles. These couples result by taking the negative derivative of the incremental potential function; at this point with respect to the individual current

particle rotation,

$$m_{\mathsf{t}ij}^{n+1} = -\frac{\partial \widehat{W}_{\mathsf{t}ij}^{n+1}}{\partial \theta_i^{n+1}} = -E_{\mathsf{t}ij}\gamma_{\mathsf{el}ij}^{n+1}\mathscr{H}\left(\varepsilon_{ij}^{n+1}\right) r_i. \tag{7.21}$$

As an equilibrium requirement, one would demand the total particle forces as well as the particle couples to vanish, i.e.:

$$\boldsymbol{f}_i^{n+1} = \sum_{\substack{j\in\mathscr{P}\\ j\neq i}} \left[\boldsymbol{f}_{\mathsf{n}ij}^{n+1} + \boldsymbol{f}_{\mathsf{t}ij}^{n+1}.\right] = \boldsymbol{0} \quad \text{and} \quad m_i^{n+1} = \sum_{\substack{j\in\mathscr{P}\\ j\neq i}} m_{ij}^{n+1} = 0. \tag{7.22}$$

Carefully observe that the derived couples do not fit the obtained tangential forces, i.e., $m_{\mathsf{t}ij}^{n+1}\boldsymbol{e}_3 \neq r_i / \left[r_i + r_j\right] \boldsymbol{l}_{ij}^{n+1} \times \boldsymbol{f}_{\mathsf{t}ij}^{n+1}$. Hence, the use of the derived quantities leads an unbalanced global torque, while individual particles are well balanced. Remedy is found by an algorithmic modification of the particle couples. Therefore, the individual couples are scaled by (7.20).

$$m_{\mathsf{algo}\,\mathsf{t}ij}^{n+1} = \frac{\left|\left|\boldsymbol{l}_{ij}^{n}\right|\right|}{\left|\left|\boldsymbol{l}_{ij}^{n+1}\right|\right|} \boldsymbol{t}_{ij}^{n} \bullet \boldsymbol{t}_{ij}^{n+1} m_{\mathsf{t}ij}^{n+1}. \tag{7.23}$$

This modification satisfies the balance of the local as well as global torque. Now, equilibrium requires:

$$\boldsymbol{f}_i^{n+1} = \sum_{\substack{j\in\mathscr{P}\\ j\neq i}} \left[\boldsymbol{f}_{\mathsf{n}ij}^{n+1} + \boldsymbol{f}_{\mathsf{t}ij}^{n+1}.\right] = \boldsymbol{0} \quad \text{and} \quad m_{\mathsf{algo}\,i}^{n+1} = \sum_{\substack{j\in\mathscr{P}\\ j\neq i}} m_{\mathsf{algo}\,ij}^{n+1} = 0. \tag{7.24}$$

For completeness, we present a flow chart which allows for illustrative insight of the numerical procedure. Comparing the computational effort between the normal and the tangential forces, one finds a significant increase under the assumption of friction.

Remark 7.2 (Tangential contact force) Based on the incremental nature of the derived approach, quantities concerning the current as well as the last converged load step contribute to the tangential contact force. Letting the load step size tend towards zero, i.e., $n \to n+1$, the expression of the tangential contact force, given in (7.19) as well as the algorithmically modified couples in (7.23) yield,

$$\boldsymbol{f}_{\mathsf{t}ij}^{n+1} = -E_{\mathsf{t}ij}\gamma_{\mathsf{el}ij}^{n+1}\mathscr{H}\left(\varepsilon_{ij}^{n+1}\right) \boldsymbol{t}_{ij}^{n+1} \quad \text{and} \quad m_{\mathsf{algo}\,\mathsf{t}ij}^{n+1} = m_{\mathsf{t}ij}^{n+1}. \tag{7.25}$$

Observe that the direction of the tangential contact force given in (7.19) and (7.25) do align. The major difference is found in the absence of the introduced scaling factor for the tangential forces as well as related couples. ■

1. compute:

$$\boldsymbol{l}_{ij}^{n+1} = \boldsymbol{x}_j^{n+1} - \boldsymbol{x}_i^{n+1}, \quad \varepsilon_{ij}^{n+1} = r_i + r_i - \left|\left|\boldsymbol{l}_{ij}^{n+1}\right|\right|$$

2. IF $\varepsilon_{ij}^{n+1} > 0$ THEN

set:

$$\gamma_{\mathrm{pl}ij}^{n+1} = \gamma_{\mathrm{pl}ij}^{n}, \quad \alpha_{ij}^{n+1} = \alpha_{ij}^{n}$$

compute:

$$f_{\mathrm{n}ij}^{n+1} = E_{\mathrm{n}ij}\varepsilon_{ij}^{n+1}, \quad \boldsymbol{n}_{ij}^{n+1} = \frac{\boldsymbol{l}_{ij}^{n+1}}{\left|\left|\boldsymbol{l}_{ij}^{n+1}\right|\right|}, \quad \boldsymbol{l}_{ij}^{n} = \boldsymbol{x}_j^{n} - \boldsymbol{x}_i^{n},$$

$$\boldsymbol{t}_{ij}^{n+1} = \boldsymbol{\Omega} \bullet \boldsymbol{n}_{ij}^{n+1}, \quad \boldsymbol{t}_{ij}^{n} = \frac{\boldsymbol{\Omega} \bullet \boldsymbol{l}_{ij}^{n}}{\left|\left|\boldsymbol{l}_{ij}^{n}\right|\right|}$$

$$\gamma_{ij}^{n+1} = \gamma_{ij}^{n} + \left[\left[\theta_i^{n+1} - \theta_i^{n}\right] r_i + \left[\theta_j^{n+1} - \theta_j^{n}\right] r_j\right] \frac{\left|\left|\boldsymbol{l}_{ij}^{n+1}\right|\right|}{r_i + r_j} - \left|\left|\boldsymbol{l}_{ij}^{n}\right|\right| \boldsymbol{t}_{ij}^{n} \bullet \boldsymbol{n}_{ij}^{n+1}$$

$$f_{\mathrm{t}ij}^{n+1} = E_{\mathrm{t}ij}\left[\gamma_{ij}^{n+1} - \gamma_{\mathrm{pl}ij}^{n+1}\right]$$

$$Y_{ij}^{n+1} = |f_{\mathrm{t}ij}^{n+1}| - h_{ij}\alpha_{ij}^{n+1}$$

IF $Y_{ij}^{n+1} \geq f_{\mathrm{n}ij}^{n+1}\tan(\rho)$ THEN

compute:

$$\Delta\lambda_{ij} = -\frac{f_{\mathrm{n}ij}^{n+1}\tan(\rho) - Y_{ij}^{n+1}}{E_{\mathrm{t}ij} + h_{ij}}$$

$$\gamma_{\mathrm{pl}ij}^{n+1} = \gamma_{\mathrm{pl}ij}^{n+1} + \Delta\lambda_{ij}\mathrm{sgn}\left(f_{\mathrm{t}ij}^{n+1}\right), \quad \alpha_{\mathrm{pl}ij}^{n+1} = \alpha_{\mathrm{pl}ij}^{n+1} + \Delta\lambda_{ij}$$

$$f_{\mathrm{t}ij}^{n+1} = E_{\mathrm{t}ij}\left[\gamma_{ij}^{n+1} - \gamma_{\mathrm{pl}ij}^{n+1}\right]$$

END IF

compute:

$$\boldsymbol{f}_{ij}^{n+1} = \left(\boldsymbol{f}_{\mathrm{n}ij}^{n+1} + \boldsymbol{f}_{\mathrm{t}ij}^{n+1}, m_{\mathrm{algo\ t}ij}^{n+1}\right)^T$$

ELSE

set:

$$\gamma_{ij}^{n+1} = 0, \quad \gamma_{\mathrm{p}ij}^{n+1} = 0, \quad \alpha_{ij}^{n+1} = \alpha_{ij}^{n}$$

END IF

Table 7.1.: Pseudocode to calculate the generalized contact force.

Remark 7.3 (Microscopic boundary conditions) In relation to the used continuum formulation, we do not enhance the previously described displacement boundary conditions by rotational constraints. Thus, we allow all particles of the rve to rotate freely.■

Remark 7.4 (Calculation of the macroscopic stress) Due to the equivalence of the overall derivation process with respect to the macroscopic stress measure, we provide the reader with the related result of the CAUCHY stress.

$$\overline{\sigma} = -\frac{1}{v_{\mathsf{rve}}} \sum_{i \in \mathscr{P}} \boldsymbol{f}_i^{n+1} \otimes \boldsymbol{x}_i^{n+1} \tag{7.26}$$

■

7.3. Representative numerical examples

Using the proposed extension, we perform numerical examples to demonstrate the macroscopic effect of inter-particle friction. Similar as in Chapter 5, we consider three different loading scenarios. At first we observe uni-axial compression. Afterwards we focus on simple shear. The last example consists of applying cyclic loading. All examples are solely performed for the assumption of TAYLOR. Selecting this boundary condition allows to concentrate on the macroscopic impact of microscopic friction, while influences from microscopic topology changes stay unconsidered. As rves we select the set containing 150 primary particles. The normal as well as the tangential contact stiffness are set to $E_{\mathsf{n}} = E_{\mathsf{t}} = E = 1\text{E+}03$, while the relative convergence threshold for the particle couples is selected to 1E−08.

7.3.1. Macroscopic investigations - uni-axial compression

The performed uni-axial compression tests equal the deformation scenarios in Chapter 5. At this point we focus on the macroscopic influence of different microscopic friction angles. Therefore, we perform 4 calculations with different microscopic friction angles between 0° and 30°. The obtained stress results are presented in Figure 7.2. The left side of Figure 7.2 refers to the horizontal compression, while the right side shows results in regards to the vertical compression. The top row of Figure 7.2 depicts the horizontal as well as vertical components of the macroscopic CAUCHY stress. We identify the horizontal components of the macroscopic CAUCHY stress by solid lines. Vertical components of the macroscopic CAUCHY stress are denoted by dashed lines. Similar to the observations of frictionless particles, the switched direction of loading yields similar macroscopic results. Overall, we find the depicted results satisfactory. For a friction angle equal to zero, the obtained results equal to the frictionless observations. The increase of the microscopic friction angle yields a stiffness increase in the direction of loading. Orthogonal to the direction of loading, the increase of the microscopic friction angle enforces a decrease in stress. This behavior, i.e., the widening

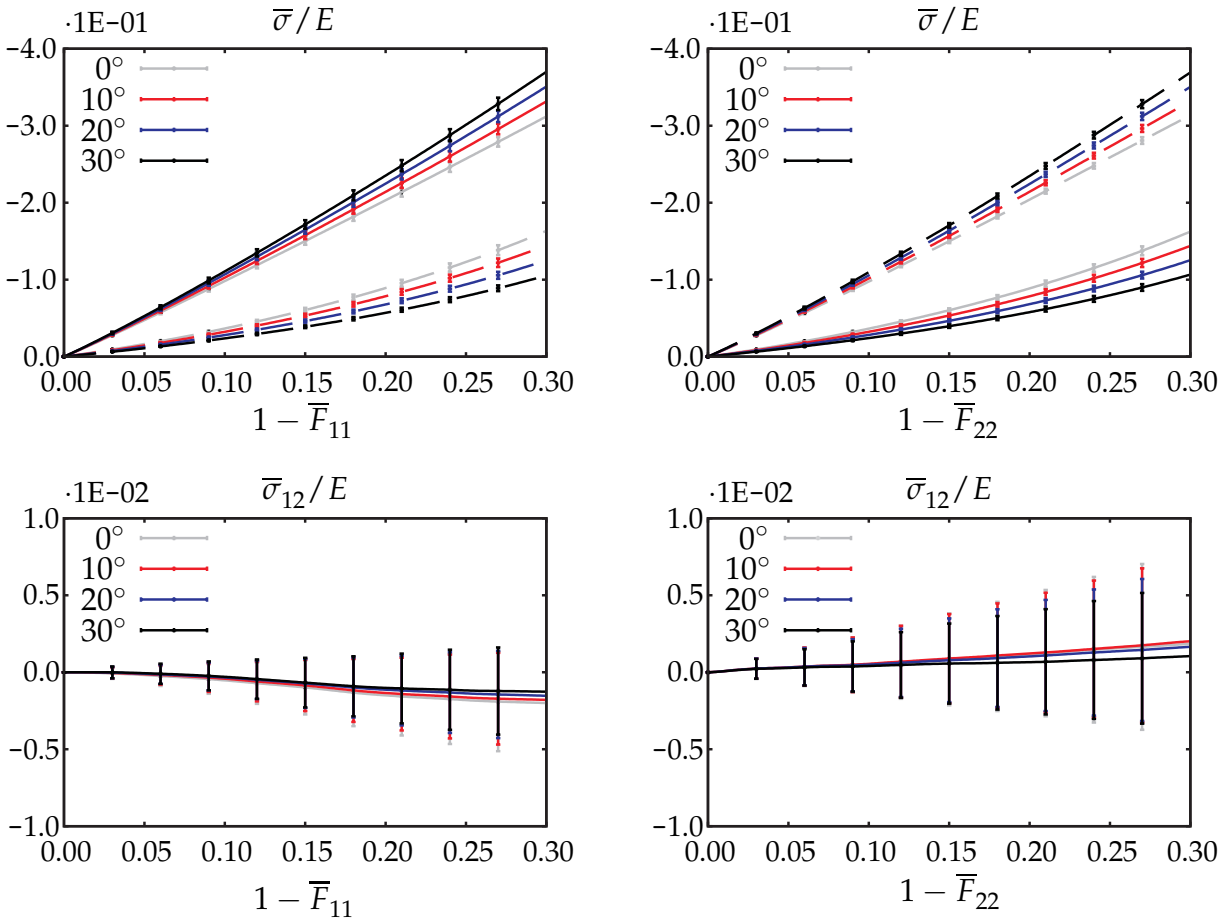

Figure 7.2.: Macroscopic influence of the microscopic friction angle under uni-axial compression: Assumption of TAYLOR. Error bars show the standard deviation. All curves and error bars are scaled by the normal contact stiffness. *Left column*: Horizontal compression. *Right column*: Vertical compression. *Top row*: Macroscopic CAUCHY stress. Solid lines denote the stress components in horizontal direction, while dashed lines refer to the vertical stress components. *Bottom row*: Shear component of the macroscopic CAUCHY stress.

between the two curves, explained by the micro mechanics of frictional contacts. In detail, the direction as well as the magnitude of the normal contact force stay equivalent for all variations of the microscopic friction angle. Hence, the tangential contact direction does not change either. However, the magnitude of the tangential contact force differs depending on the angle of inter-particle friction. This phenomena allows for the rise of loading directed forces, while orthogonal to the direction of loading a decrease in force is imposed. The apparent linear behavior between the individual results relates to the formulation of the inter-particle friction and is strongly connected to the behavior of the tangent function. The related shear components of the macroscopic CAUCHY stress are located in the bottom row of Figure 7.2. These plots do not allow for a general statement in regards to the macroscopic influence of the microscopic friction angle. Nevertheless, similar to the frictionless results, one observes a tendency of the stress components to a value of zero as well as an enlargement of the error bars for

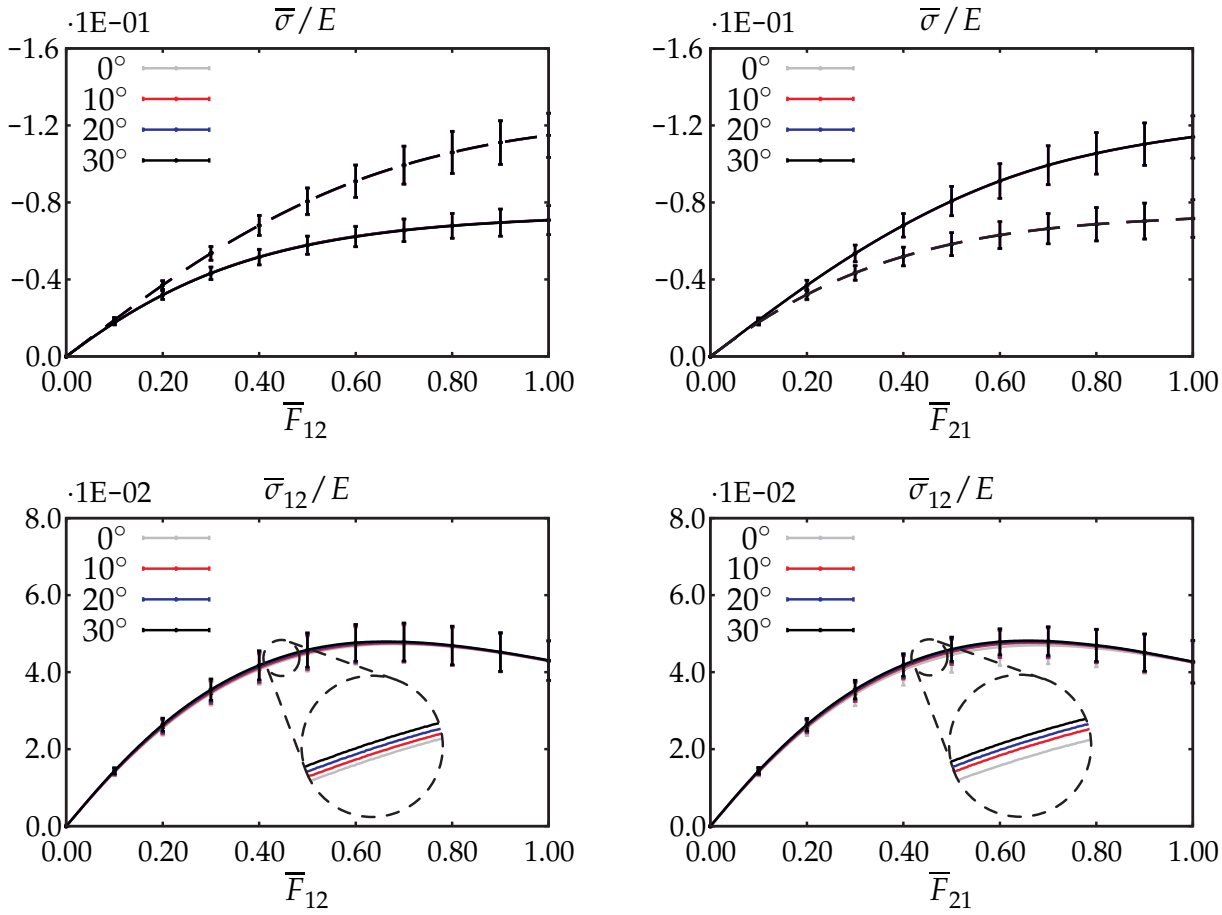

Figure 7.3.: Macroscopic influence of the microscopic friction angle under simple shear: Assumption of TAYLOR. Error bars show the standard deviation. All curves and error bars are scaled by the normal contact stiffness. *Left column*: Horizontal compression. *Right column*: Vertical compression. *Top row*: Macroscopic CAUCHY stress. Solid lines denote the stress components in horizontal direction, while dashed lines refer to the vertical stress components. *Bottom row*: Shear component of the macroscopic CAUCHY stress.

increasing deformation.

7.3.2. Macroscopic investigations - simple shear

The detailed description of the overall simple shear deformation process is detailed in the example section of Chapter 5. As in the previous example, we observe the deformation in the horizontal as well as in the vertical direction. Against the background of the presented theory, our investigations focus on the macroscopic impact of the inter-particle friction angle. For this purpose, identical to Subsection 7.3.1, we plot the components of the macroscopic CAUCHY stress. Overall, we find identical behaviors for the switched directions of loading. The horizontal as well as vertical components of the macroscopic CAUCHY stress shows a remarkable equivalence. No influences in regards to the variation of the inter-particle friction angle are noticed. In particular,

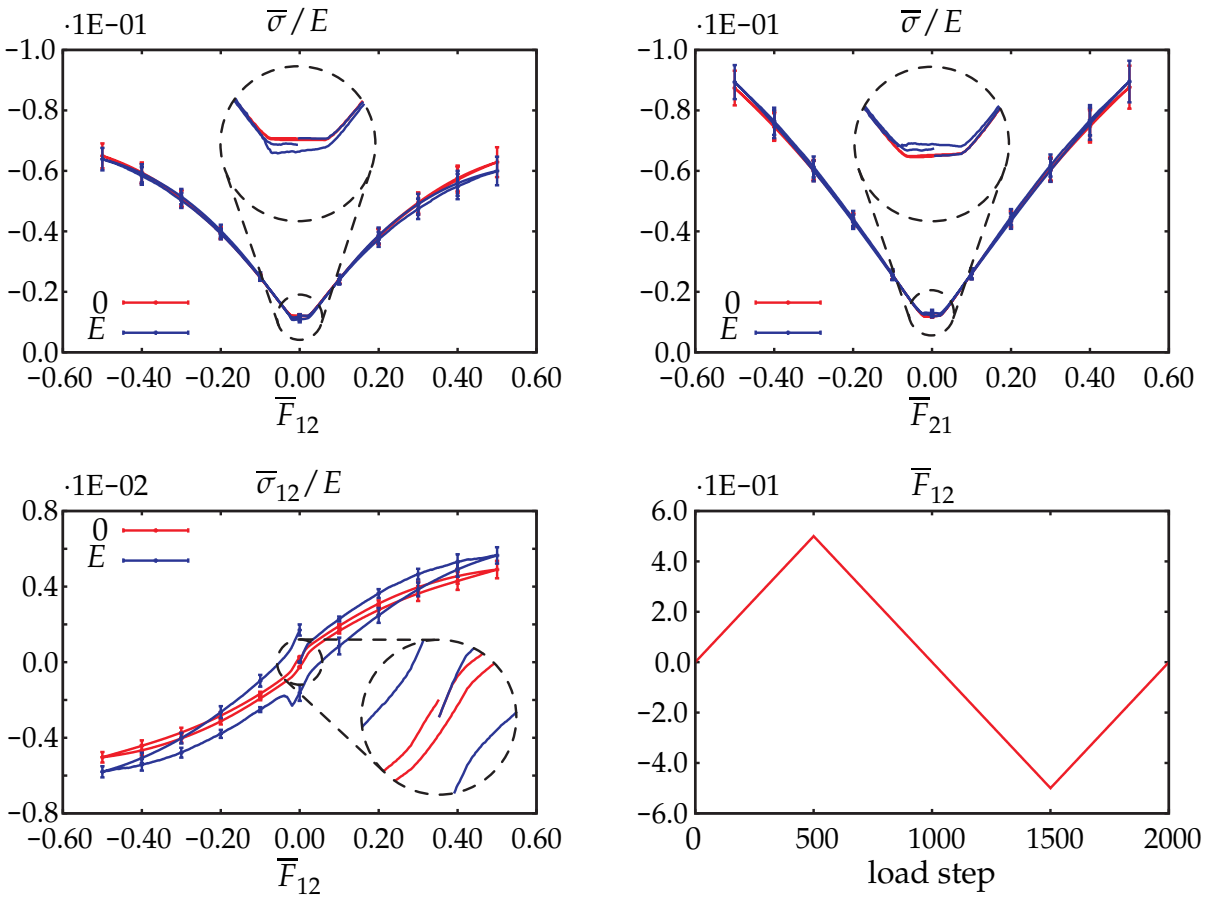

Figure 7.4.: Macroscopic influence of the microscopic hardening modulus under cyclic loading: Assumption of TAYLOR. Error bars show the standard deviation. All stress related curves and error bars are scaled by the normal contact stiffness. *Top left*: Horizontal component of the macroscopic CAUCHY stress. *Top right*: Vertical component of the macroscopic CAUCHY stress. *Bottom left*: Shear component of the macroscopic CAUCHY stress. *Bottom right*: Prescribed behavior of the shear component of the macroscopic deformation gradient.

we find all plots to deliver almost identical values which are congruent with the frictionless results. The coarse scale behavior of the shear components of the macroscopic CAUCHY stress show a nearly identical output. Further, on the fine scale based, investigations reveal a manner which relates to the observations under uni-axial loading, i.e., we detect minor increase for an increase of the inter-particle friction angle.

7.3.3. Macroscopic investigations - cyclic loading

Next, we investigate on the macroscopic impact of the inter-particle hardening modulus. Therefore, we select a cyclic loading deformation scenario. We compute the response for $h_{ij} = h = 0$ as well as $h_{ij} = h = E$, keeping the inter-particle friction angle to 30°. Based on the discussed results, we restrict this study to horizontal deformation. Further details in regards to the deformation process are given in Subsection 5.4.3. Here we solely provide the reader with a plot of the significant change

of the shear component of the macroscopic deformation gradient, compare Figure 7.4 (bottom right). The results of the macroscopic CAUCHY stress are depicted in the remaining graphs of Figure 7.4. The top row, presenting the horizontal (left) as well as vertical (right) component of the macroscopic CAUCHY stress, show almost identical behaviors for both selections of the microscopic hardening variable. A zoom in on the fine scale of the plotted graph allows for further observations. For the horizontal as well as vertical stress component a history dependent behavior is noticed. The horizontal component shows a decreasing tendency, while the vertical component depicts an increasing behavior. However, both observations are considered to be small in comparison to topological based history effects. The shear components of the macroscopic CAUCHY stress allow to identify significant differences between the different hardening moduli. We observe a distinct hysteresis for $h = E$, while for $h = 0$ a rather flat hysteresis curve is noticed. In contrast to the cyclic loading of frictionless particles, the overall results show a macroscopic history dependence which solely relates to microscopic dissipation processes of the proposed inter-particle friction.

8. Closure

8.1. Discussion and conclusion

The present manuscript covers the computational homogenization of granular media. Presented are concepts to generate appropriate rves, to define general as well as microscopic boundary condition specific macroscopic quantities and to incorporate volume averaged grains-scale constitutive laws in macroscopic continuum formulations. We focus on smooth as well as frictional inter-particle contact. Topological and frictional based microscopic dissipation is discussed and linked to the macroscopic level. The essential contributions of this work are discussed in the following:

- **rve generation**:
  The generation of geometrically periodic random rves is of general interest for various different applications of granular media. Motivated by the LUBACHEVSKY-STILLINGER algorithm, developed in the context of computational chemistry, we discuss a strategy to generate periodic microstructures with the ultimate goal of incorporating them as rves on the integration point level in an overall finite element analysis. The rves generated by the LUBACHEVSKY-STILLINGER algorithm show a number of distinguishing features that seem highly attractive in particular for applications in geomechanical areas: They are geometrically periodic, heterogeneous, densely packed full sets, which essentially reflect user-defined grain size distribution patterns. Technically speaking, the underlying algorithm is embedded in a serial event-driven scheme starting with a random spatial distribution of particles of size zero. The particle size increases systematically as time evolves whereby each particle has to be assigned a characteristic growth rate. These individual particle growth rates can be extracted through a one-to-one mapping from prescribed grain size distributions, which essentially govern the random heterogeneity of the microstructure. Accordingly, basically any given sieve curve can be accounted for naturally and the generation of monodisperse as well as polydisperse packings of various degrees of heterogeneity is straightforward. Unless the final packing density is prescribed externally, for example when generating a particular concrete microstructure with a given aggregate volume fraction, the algorithm was shown to produce remarkably large packing densities. Compared with natural findings, the obtained three dimensional outcomes reflect realistic packing densities. Due to the underlying algorithmic simplicity, the present algorithm is believed to provide a stable and efficient tool to generate random geometrically periodic microstructures that will be extremely useful in different areas of computational physics, geomechanics, concrete design, material modeling and homogenization.

- **soft particle contact method**:
  In contrast to the classical dem, the proposed soft particle contact method is based on the existence of an inter-particle contact potential. Forces between the individual grains are exclusively transferred at contact points, allowing the used potential to rely on the inter-particle overlap between contacting particles. The restriction to dry matter leaves possible attraction between the obstacles unconsidered. We select a one-sided harmonic potential, describing a quadratic relation between the obtained energy and the inter-particle overlap. Inter-particle contact forces naturally derive of the proposed contact potential. Using the generated rves, we apply different boundary conditions by means of the macroscopic deformation gradient. Technically speaking, we utilize the macroscopic deformation gradient to prescribe microscopic particle positions. The selection of these grains determines the used boundary conditions. We consider the assumption of TAYLOR, the restricted TAYLOR boundary condition, as well as periodic boundary conditions. As proper solution procedure of the DIRICHLET based boundary value problem, we suggest a dynamic relaxation based solution algorithm. Uniaxial compression as well as simple shear examples are selected to deliver deeper insight. The obtained results are rated and discussed by investigating their force network, contact density as well as force density function plots. Under the assumption of TAYLOR we obtain predictable results which may be regarded as homogeneous mappings of the individual outsets. The contact density functions regarding the restricted TAYLOR assumption uncover a well balanced contact network. However, based on the prescribed boundary particle set, the related force flux is strongly distorted by influences from inter boundary contacts. In contrast to both TAYLOR-based boundary conditions, the results concerning periodic boundary conditions return rather neutral and well balanced answers.

- **discrete homogenization**:
  For homogenization purposes, we define a macroscopic constitutive potential of the overall microscopic granular assembly. Thereby, the macroscopic potential is related to the volume average of the discrete summation over all relevant inter-particle contact potentials. Therefrom, the general macroscopic PIOLA stress is derived, which itself defines as a volume average over microscopic discrete quantities. For comparative reasons we as well investigate on the definition of the general macroscopic PIOLA stress by means of a virtual work relation between the two scales. Both expressions of the general macroscopic PIOLA stress are identical. With the general macroscopic PIOLA stress at hand, we define microscopic boundary specific macroscopic stress measures. Exclusively considering the possible event of periodic particle flux under periodic boundary conditions, we outline a strategy to retain the symmetry of the macroscopic CAUCHY stress by means of periodic boundary enhancements. We decide to study the macroscopic impact of different microscopic boundary conditions by systematic error bar analysis. Thereby, we concentrate on the obtained macroscopic potential energy density as well as on the components of the macroscopic CAUCHY stress. As before, we select basic deformation scenarios to perform this research. It turns

out that the solutions converges for the assumption of TAYLOR as well as for the periodic boundary conditions. Thus, the selected numbers of grains seem to be a reasonable choice for the performed two dimensional simulations. In the case of the restricted TAYLOR assumption we do not observe convergence to a meaningful value. Taking the microscopic observations into account, the noticed macroscopic phenomena strongly relates to the dominating influence of the inter boundary contacts. All macroscopic results reveal non-linear answers which, considering the linear force overlap relation on the grain-scale level, must exclusively rely on contact network and topology changes. Furthermore, we find topology based history effects under cyclic loading for the restricted TAYLOR as well as periodic boundary conditions.

- **fem-dem coupling**:
  The computational simulation of granular assemblies is a rather challenging and cumbersome task since granular materials are discrete in nature but yet consist of millions of particles which are expensive to trace individually. Following recent trends, we apply a multiscale simulation approach that captures individual contact forces on the microscopic scale and applies the concept of a representative volume element to characterize stresses on the macroscopic scale. Computationally speaking, we combine dem on the microscopic scale with a fem on the macroscopic scale. To bridge the gap between the individual scales, we locally attach a representative volume element and apply the discussed boundary conditions. We then solve the particle contact problem based on the dem. Based on these preliminary studies, we then elaborate the overall finite element solution procedure. Existing multiscale models similar to the one we suggest have typically applied somewhat cumbersome solution techniques to solve the non-linear finite element equations on the macroscopic scale. Instead of following the literature, we suggest to embed the overall solution in a classical NEWTON-RAPHSON solution procedure. Accordingly, we illustrate the consistent linearization of the governing equations on the material point level lending itself to the algorithmic tangent operator which basically ensures quadratic convergence of the suggested solution scheme. Apart from the fact that each particle contact not only contributes to the overall stress but also to the overall tangent operator, the proposed algorithm is highly efficient. It displays the characteristic properties of the classical NEWTON-RAPHSON scheme and we were able to show its quadratic convergence for a typical finite element benchmark problem. Nevertheless, we would like to point out that for a problem that is discrete in nature and essentially based on a continuous formation, removal and re-formation of inter-particle contacts, the overall solution is, of course, non-smooth.

Finally, we would like to point out that although the presented algorithm has been proven highly effective and algorithmically efficient, it is far from being general enough to capture all characteristic effects in granular media. Nevertheless, the presented results point to new ways of handling the complicated nature of granular materials and give rise as well as opportunities to perform additional breakthrough research in the area of computational homogenization of confined granular matter.

8.2. Future work

The presented concepts with respect to the computational homogenization of particulate matter allow for the extension in multiple areas of research. In principle, this manuscript is taken as a basis, whereby extensions are applied by means of interfaces. Thus, solely considering first-order homogenization of particulate matter, the presented concepts and algorithms permit a strait forward extension. We outline specific possibilities of enhancement, keeping the order of importance unconsidered. Basically, extensions are divided into two main topics which are combinable. The first topic concerns the enhancement or complete replacement of the particle method. Thereby, the overall homogenization scheme stays unaltered. The second expansion concentrates on the possibility of applying enhanced homogenization concepts. This issue does not touch the general concept of microscopic computations. Next to the replacement by different modeling techniques, a main topic on the grain-scale level is the extension with respect to the spatial dimension. The obtained two dimensional outcomes show qualitative similarities to experimental results, e.g., the dilatancy behavior. It is known that this phenomena strongly depends on the volume density as well as on the shape of the individual grains. From the rve generation, we recognize that three dimensional rves provide a more realistic volume density. Thus, to allow for a qualitative comparison and study, the need for an overall three dimensional model is absolutely essential. This encloses an elaboration of the grain shapes to, e.g., super ellipsoidal or three dimensional polygonal particle. Different grain shapes in two or three dimension will yield different results with respect to topological and frictional based dissipation. The implementation of different particle inter-action in the context of multi-physics enables the extensions to other research fields. Especially interesting are chemical or electro-magnetical phenomenas. Turing away from dry matter, i.e., allowing small portions of liquid or even full saturation, cays, multiphase or glue-bonded materials might be covered. With respect to the homogenization process, there is great interest in allowing the failure on the macroscopic level, introduced by microscopic changes. Such considerations require the application of higher-order homogenization techniques.

A. Tensor operations and derivatives

The used mathematical notation includes: Standard symbols that represent scalar quantities, e.g., $a, b, c, \ldots$ or $\alpha, \beta, \gamma, \ldots$. Lower case bold symbols that define first order tensors, e.g., $\boldsymbol{a}, \boldsymbol{b}, \boldsymbol{c}, \ldots$. Upper case bold letters that represent second order tensors, e.g., $\boldsymbol{A}, \boldsymbol{B}, \boldsymbol{C}, \ldots$. Fourth order tensors that are denoted by special letters, e.g., $\mathbb{A}, \mathbb{B}, \mathbb{C}, \ldots$. Additional tensor quantities which do not match the introduced notation are defined upon their appearance. Appendix A.1 allows the reader to familiarize with the used tensor operation symbols. In Appendix A.2, the interested reader is confronted with frequently used tensor derivatives. The last part of this Appendix, see A.3, focuses on the required non-trivial derivative of the individual microscopic fluctuations with respect to the macroscopic deformations gradient tensor.

A.1. Tensor operations

A basic overview of employed tensor operations is given in this part of the appendix. Particularly, we introduce single and double contractions as well as standard and special dyadic products.

single contraction						
	a	$=$	$\boldsymbol{b} \cdot \boldsymbol{c}$	a	$=$	$b_\alpha c_\alpha$
	$\boldsymbol{a}$	$=$	$\boldsymbol{B} \cdot \boldsymbol{c}$	a_α	$=$	$B_{\alpha\beta} c_\beta$
	$\boldsymbol{A}$	$=$	$\boldsymbol{B} \cdot \boldsymbol{C}$	$A_{\alpha\beta}$	$=$	$B_{\alpha\gamma} C_{\gamma\beta}$
double contraction						
	a	$=$	$\boldsymbol{B} : \boldsymbol{C}$	a	$=$	$B_{\alpha\beta} C_{\alpha\beta}$
	$\boldsymbol{A}$	$=$	$\mathbb{B} : \boldsymbol{C}$	$A_{\alpha\beta}$	$=$	$B_{\alpha\beta\gamma\delta} C_{\gamma\delta}$
dyadic product						
	$\boldsymbol{A}$	$=$	$\boldsymbol{b} \otimes \boldsymbol{c}$	$A_{\alpha\beta}$	$=$	$b_\alpha c_\beta$
	$\mathbb{A}$	$=$	$\boldsymbol{B} \otimes \boldsymbol{C}$	$A_{\alpha\beta\gamma\delta}$	$=$	$B_{\alpha\beta} C_{\gamma\delta}$
special dyadic product						
	$\mathbb{A}$	$=$	$\boldsymbol{B} \overline{\otimes} \boldsymbol{C}$	$A_{\alpha\beta\gamma\delta}$	$=$	$B_{\alpha\gamma} C_{\beta\delta}$
	$\mathbb{A}$	$=$	$\boldsymbol{B} \underline{\otimes} \boldsymbol{C}$	$A_{\alpha\beta\gamma\delta}$	$=$	$B_{\alpha\delta} C_{\beta\gamma}$

A.2. Frequently used tensor derivatives

This part of the appendix provides the reader with frequently used tensor derivatives. To not overly stress the topic of tensor derivation, only specific results are presented. The actual derivation procedure is not discussed, instead, the interested

reader is referred to the common continuum mechanics literature, see for example HOLZAPFEL [60] or WRIGGERS [160].

A.2.1. Derivatives with respect to the microscopic branch vector

Derivative of the length of the microscopic branch vector:

$$\frac{\partial \left|\left| \boldsymbol{l}_{ij} \right|\right|}{\partial \boldsymbol{l}_{ij}} = \boldsymbol{n}_{ij} \tag{A.1}$$

Derivative of the microscopic particle overlap:

$$\frac{\partial \varepsilon_{ij}}{\partial \boldsymbol{l}_{ij}} = -\frac{\partial \left|\left| \boldsymbol{l}_{ij} \right|\right|}{\partial \boldsymbol{l}_{ij}} = -\boldsymbol{n}_{ij} \tag{A.2}$$

A.2.2. Derivatives with respect to the macroscopic deformation gradient

Derivative of the microscopic branch vector:

$$\frac{\partial \boldsymbol{l}_{ij}}{\partial \overline{\boldsymbol{F}}} = \boldsymbol{1} \otimes \left[\boldsymbol{L}_{ij} + \boldsymbol{\Xi}_j - \boldsymbol{\Xi}_i \right] \tag{A.3}$$

Derivative of the length of the microscopic branch vector:

$$\frac{\partial \left|\left| \boldsymbol{l}_{ij} \right|\right|}{\partial \overline{\boldsymbol{F}}} = \frac{\partial \left|\left| \boldsymbol{l}_{ij} \right|\right|}{\partial \boldsymbol{l}_{ij}} \cdot \frac{\partial \boldsymbol{l}_{ij}}{\partial \overline{\boldsymbol{F}}} = \boldsymbol{n}_{ij} \otimes \left[\boldsymbol{L}_{ij} + \boldsymbol{\Xi}_j - \boldsymbol{\Xi}_i \right] \tag{A.4}$$

Derivative of the microscopic contact unit normal:

$$\frac{\partial \boldsymbol{n}_{ij}}{\partial \overline{\boldsymbol{F}}} = \frac{\partial \dfrac{\boldsymbol{l}_{ij}}{\left|\left| \boldsymbol{l}_{ij} \right|\right|}}{\partial \overline{\boldsymbol{F}}} = \frac{1}{\left|\left| \boldsymbol{l}_{ij} \right|\right|} \left[\boldsymbol{1} - \boldsymbol{n}_{ij} \otimes \boldsymbol{n}_{ij} \right] \otimes \left[\boldsymbol{L}_{ij} + \boldsymbol{\Xi}_j - \boldsymbol{\Xi}_i \right] \tag{A.5}$$

A.2.3. Derivatives with respect to the microscopic material fluctuation

Derivative of the microscopic branch vector:

$$\frac{\partial \boldsymbol{l}_{ij}}{\partial \boldsymbol{\Xi}_i} = -\overline{\boldsymbol{F}} \qquad \frac{\partial \boldsymbol{l}_{ij}}{\partial \boldsymbol{\Xi}_j} = \overline{\boldsymbol{F}} \tag{A.6}$$

Derivative of the length of the microscopic branch vector:

$$\frac{\partial \left|\left| \boldsymbol{l}_{ij} \right|\right|}{\partial \boldsymbol{\Xi}_i} = -\boldsymbol{n}_{ij} \bullet \overline{\boldsymbol{F}} \qquad \frac{\partial \left|\left| \boldsymbol{l}_{ij} \right|\right|}{\partial \boldsymbol{\Xi}_j} = \boldsymbol{n}_{ij} \bullet \overline{\boldsymbol{F}} \tag{A.7}$$

Derivative of the microscopic unit contact normal:

$$\frac{\partial \boldsymbol{n}_{ij}}{\partial \boldsymbol{\Xi}_i} = \frac{1}{\left|\left| \boldsymbol{l}_{ij} \right|\right|} \left[\boldsymbol{n}_{ij} \otimes \boldsymbol{n}_{ij} - \boldsymbol{1} \right] \bullet \overline{\boldsymbol{F}} \qquad \frac{\partial \boldsymbol{n}_{ij}}{\partial \boldsymbol{\Xi}_j} = \frac{1}{\left|\left| \boldsymbol{l}_{ij} \right|\right|} \left[\boldsymbol{1} - \boldsymbol{n}_{ij} \otimes \boldsymbol{n}_{ij} \right] \bullet \overline{\boldsymbol{F}} \tag{A.8}$$

A.3. The non-trivial derivative

The presumption of individual microscopic particle fluctuations introduces a non-trivial derivative, see GRYTZ & MESCHKE [49],KOUZNETSOVA, GEERS & BREKELMANS [69], MIEHE [89, 90] and MIEHE ET AL. [95, 96] for the continuous case. More precisely, the non-trivial derivative is identified as the derivative of the particle fluctuations with respect to the macroscopic deformation gradient. An explicit expression of the individual particle fluctuations is unknown, however, we assume that the fluctuations themselves strongly depend on the structural arrangement of the grains. Forming the desired derivative, we follow a way which was proposed in the context of molecular dynamics by TADMOR ET AL. [135]. In particular, at a state of equilibrium, we variate the microscopic internal forces with respect to the macroscopic deformation gradient,

$$\frac{\mathsf{d}}{\mathsf{d}\overline{\boldsymbol{F}}} \left[\frac{\partial \Phi_{\mathsf{n}}}{\partial \boldsymbol{\Xi}_n} \right] \equiv \boldsymbol{0}, \quad \text{with} \quad n \in \mathscr{F}, \tag{A.9}$$

whereby $\mathscr{F}$ refers to a subset of $\mathscr{P}$, i.e., $\mathscr{F} \subseteq \mathscr{P}$, solely including particles which include a fluctuational displacement share. An equivalent procedure is employed in the continuous case, i.e., the sensitivity of the individual fluctuations with respect to the macroscopic deformation gradient is obtained by linearizing the equation of static equilibrium, see for example MIEHE [90] and MIEHE ET AL. [95, 96]. Straightforward derivation, including the use of the chain rule, results in a formulation including the desired expression of the non-trivial derivative,

$$\frac{\partial^2 \Phi_{\mathsf{n}}}{\partial \boldsymbol{\Xi}_n \otimes \partial \overline{\boldsymbol{F}}} + \sum_{m \in \mathscr{F}} \frac{\partial^2 \Phi_{\mathsf{n}}}{\partial \boldsymbol{\Xi}_n \otimes \partial \boldsymbol{\Xi}_m} \bullet \frac{\partial \boldsymbol{\Xi}_m}{\partial \overline{\boldsymbol{F}}} = \boldsymbol{0}. \tag{A.10}$$

To extract the desired non-trivial derivative, located in the summation on the right side of (A.10), we introduce the non-standard tensors $\boldsymbol{\mathcal{G}}$ and $\boldsymbol{\mathcal{H}}$. Both tensors belong to the

vector space $\mathbb{R}^{2\cdot\#_{\mathscr{F}}\times 2\times 2\times 2}$. In particular, both tensors can be thought of as a collection,

$$\boldsymbol{\mathcal{G}} = \left[\frac{\partial^2 \Phi_{\mathsf{n}}}{\partial \boldsymbol{\Xi}_1 \otimes \partial \overline{\boldsymbol{F}}}, \ldots, \frac{\partial^2 \Phi_{\mathsf{n}}}{\partial \boldsymbol{\Xi}_{\#_{\mathscr{F}}} \otimes \partial \overline{\boldsymbol{F}}}\right]^t, \qquad \boldsymbol{\mathcal{H}} = \left[\frac{\partial \boldsymbol{\Xi}_1}{\partial \overline{\boldsymbol{F}}}, \ldots, \frac{\partial \boldsymbol{\Xi}_{\#_{\mathscr{F}}}}{\partial \overline{\boldsymbol{F}}}\right]^t. \tag{A.11}$$

The collection of the second partial derivative of the volume average of the microscopic potential function with respect to the microscopic particle fluctuations yields a modified microscopic aggregate matrix, denoted by $\widetilde{\boldsymbol{K}}$. The entries of $\widetilde{\boldsymbol{K}}$ compute to $\widetilde{\boldsymbol{k}}_{ij} = \overline{\boldsymbol{F}}^t \cdot \boldsymbol{k}_{ij} \cdot \overline{\boldsymbol{F}}$, with $\boldsymbol{k}_{ij}$ defined in (4.12). Using the introduced non-standard tensors, we can rewrite (A.10).

$$\boldsymbol{\mathcal{G}} + \widetilde{\boldsymbol{K}} \cdot \boldsymbol{\mathcal{H}} = \boldsymbol{0}. \tag{A.12}$$

With $\widetilde{\boldsymbol{K}}$ being positive definite, i.e., $\det\left(\widetilde{\boldsymbol{K}}\right) > 0$, we solve for the non-standard tensor $\boldsymbol{\mathcal{H}}$ and obtain a definition for the non-trivial tensor derivative,

$$\frac{\partial \boldsymbol{\Xi}_m}{\partial \overline{\boldsymbol{F}}} = -\overline{\boldsymbol{F}}^{-1} \cdot \sum_{n \in \mathscr{F}} \left[\boldsymbol{K}^{-1}\right]_{nm} \cdot \overline{\boldsymbol{F}}^{-t} \cdot \frac{\partial^2 \Phi_{\mathsf{n}}}{\partial \boldsymbol{\Xi}_n \otimes \partial \overline{\boldsymbol{F}}}. \tag{A.13}$$

Therein, $\left[\boldsymbol{K}^{-1}\right]_{nm}$ denotes a two by two entry of the inverted microscopic stiffness matrix. Relating the last term to the individual inter-particle contact potentials, the sensitivity of the individual microscopic fluctuations with respect to the macroscopic deformation gradient reads:

$$\frac{\partial \boldsymbol{\Xi}_m}{\partial \overline{\boldsymbol{F}}} = -\overline{\boldsymbol{F}}^{-1} \cdot \sum_{n \in \mathscr{F}} \left[\boldsymbol{K}^{-1}\right]_{nm} \cdot \overline{\boldsymbol{F}}^{-t} \cdot \sum_{\substack{l \in \mathscr{P} \\ l \neq n}} \frac{\partial^2 \Phi_{\mathsf{n}ln}}{\partial \boldsymbol{\Xi}_n \otimes \partial \overline{\boldsymbol{F}}}. \tag{A.14}$$

Bibliography

[1] *DIN Deutsches Institut für Normung e.V.. DIN 1045-2 Tragwerke aus Beton, Stahlbeton und Spannbeton, Teil 2: Beton – Festlegung, Eigenschaften, Herstellung und Konformität, Anwendungsregeln zu DIN EN 206-1*. Beuth Verlag GmbH, 10772 Berlin, 2001.

[2] BAGI, K. A quasi-static numerical model for micro-level analysis of granular assemblies. *Mechanics of Materials 16* (1993), 101 – 110.

[3] BAGI, K. Microstructural stress tensor of granular assemblies with volume forces. *ASME Journal of Applied Mechanics 66* (1999), 934 – 936.

[4] BAGI, K. From order to chaos: The mechanical behaviour of regular and irregular assemblies. In *Bagi, K. (ed), Proc. QuaD-PM'03 Workshop, Budapest, Hungary* (2003), pp. 33–42.

[5] BAGI, K. An algorithm to generate random dense arrangements for discrete element simulations of granular assemblies. *Granular Matter 7* (2005), 31 – 43.

[6] BARAM, R. M. *Polydisperse Granular Packings and Bearings*. PhD thesis, Institute für Computeranwendungen 1, Universität Stuttgart, 2005.

[7] BARDET, J. P., AND PROUBET, J. Adaptive dynamic relaxation for statics of granular media. *Computers and Structures 39*, 3/4 (1991), 221 – 229.

[8] BELYTSCHKO, T., LIU, W. K., AND MORAN, B. *Nonlinear Finite Elements for Continua and Structures*. Wiley-VCH, 2000.

[9] BERNAL, J. D. *The geometry of the structure of liquids*. Liquids: Structure, Properties, Solid Interactions : 25. Elsevier, New York, 1965, p. 25.

[10] BETKE, U., AND GRITZMANN, P. Über L. Fejes Tóths Wurstvermutung in kleinen Dimensionen. *Acta Mathematica Hungarica 43* (1984), 299 – 307.

[11] BETTEN, J. *Kontinuumsmechanik*. Springer, 2001.

[12] BONET, J., AND WOOD, R. D. *Nonlinear Continuum Mechanics for Finite Element Analysis*. Cambridge University Press, 1997.

[13] BORJA, R. I., AND WREN, J. R. Micromechanics of granular media part I: Generation of overall constitutive equation for assemblies of circular disks. *Computer Methods in Applied Mechanics and Engineering 127* (1995), 13–36.

[14] BORN, M. *Dynamik der Kristallgitter*. Teubner, 1915.

[15] BREWSTER, D. On the law of the partial polarization of light by reflexion. *Philosophical Transactions of the Royal Society of London 2* (1830), 387 – 389.

[16] CAMBOU, B., DUBUJET, P., AND NOUGUIER-LEHON, C. Anistropy in granular materials at different scales. *Mechanics of Materials 36* (2004), 1185 – 1194.

[17] CAUCHY, A. L. De la pression ou tension dans un système de points matériels. *Exercises De Mathématiques* (1828), 253–277.

[18] CAUCHY, A. L. Sur l'équilibre et le mouvement d'un système de points matériels sollicités par des forces d'attraction ou de répulsion mutuelle. *Exercises De Mathématiques* (1828), 227–252.

[19] CHANG, C. S., AND MISRA, A. Computer simulation and modelling of mechanical properties of particulates. *Computers and Geotechnics 7* (1989), 269 – 287.

[20] CHANG, C. S., AND MISRA, A. Application of uniform strain theory to heterogeneous granular solids. *ASCE Journal of Engineering Mechanics 116* (1990), 2310 – 2329.

[21] CHRISTOFFERSEN, J., MEHRABADI, M. M., AND NEMAT-NASSER, S. A micromechanical description of granular material behavior. *ASME Journal of Applied Mechanics 48* (1981), 339 – 344.

[22] COMI, C., AND PEREGO, U. A unified approach for variationally consistent finite elements in elastoplasticity. *Computer Methods in Applied Mechanics and Engineering 121* (1995), 323 – 344.

[23] COSTANZO, F., GRAY, G. L., AND ANDIA, P. C. On the definitions of effective stress and deformation gradient for use in MD: Hill's macro-homogeneity and virial theorem. *International Journal of Engineering Science 43* (2005), 533 – 555.

[24] COULOMB, C. A. Essai sur une application des régles des maximis et minimis áquelques problémes dé statique relatifs á l'architecture. *Academie Royale des Sciences, Mémoires de Mathématique et de Physique, présentés á l'Academie Royale des Sciences, par divers savants, et lus dans les Assemblées 7* (1776), 342 – 382.

[25] COUSINS, C. S. G. Inner elasticity. *Journal of Physics C: Solid State Physics 11*, 4867–4879 (1978).

[26] COUSINS, C. S. G. General expressions for inner elastic constants. *Journal of Physics C: Solid State Physics 12* (1979), 1601–1607.

[27] CUNDALL, P. A., AND STRACK, O. D. L. The distinct element method as a tool for research in granular media. Tech. rep., Report to the National Science Foundation Concerning NSF Grant ENG76-20711, PART I, 1978.

[28] CUNDALL, P. A., AND STRACK, O. D. L. A discrete numerical model for granular assemblies. *Géotechnique 29*, 1 (1979), 47–65.

[29] CUNDALL, P. A., AND STRACK, O. D. L. The distinct element method as a tool for research in granular media. Tech. rep., Report to the National Science Foundation Concerning NSF Grant ENG76-20711, PART II, 1979.

[30] D'ADDETTA, G., RAMM, E., DIEBELS, S., AND EHLERS, W. A particle center based homogenization strategy for granular assemblies. *Engineering Computations 21*, 2/3/4 (2004), 360–383.

[31] DANTU, P. Contribution a l'etude mecanique et geometrique des milieux pulverulents. In *Proceedings of the 4th Intl. Conf. on soils Mechanics and Fundations Engineering, London* (1957), Butterworths Scientic Publications, pp. 144 – 148.

[32] DE JONG, G. D. J., AND VERRUIJT, A. Etude photo-élastique d'un empilement de disques. *Cahiers du group Francais de Rheologie 2* (1969), 73 – 86.

[33] DETTMAR, J. P. *Static and Dynamic Homogenization Analyses of Discrete Granular and Atomistic Systems on Different Time and Length Scales*. PhD thesis, Institut für Mechanik (Bauswesen) , Universität Stuttgart, 2006.

[34] DONEV, A., CISSE, I., SACHS, D., VARIANO, E. A., STILLINGER, F. H., CONNELLY, R., TORQUATO, S., AND CHAIKIN, P. M. Improving the density of jammed disordered packings using ellipsoids. *Science 303* (2004), 990 – 993.

[35] DONEV, A., TORQUATO, S., STILLINGER, F. H., AND CONNELLY, R. Jamming in hard sphere and disk packings. *Journal of Applied Physics 95*, 3 (2004), 989 – 999.

[36] DONEV, A., TORQUATO, S., STILLINGER, F. H., AND CONNELLY, R. A linear programming algorithm to test for jamming in hard-sphere packings. *Journal of Computational Physics 197* (2004), 139 – 166.

[37] DRESCHER, A., AND DE JOSSELIN DE JONG, G. Photoelastic verification of a mechanical model for the flow of a granular material. *Journal of the Mechanics and Physics of Solids 20* (1972), 337 – 351.

[38] DRUCKER, D. C., GIBSON, R. E., AND HENKEL, D. J. Soil mechanics and work-hardening. *Transactions, ASCE 122* (1957), 338 – 346.

[39] DURAN, J. *Sands, Powders, and Grains*. Springer, 1999.

[40] EHLERS, W., DIEBELS, S., AND MICHELITSCH, T. *Microscopic modelling of granular materials taking into account particle rotations*. Continuous and Discontinuous Modelling of Cohesive Frictional Materials, Lecture Notes in Physics 586. Springer-Verlag, Berlin, Germany, 2001, pp. 259–274.

[41] EHLERS, W., RAMM, E., DIEBELS, S., AND D'ADDETTA, G. A. From particle ensembles to cosserat continua: homogenization of contact forces towards stresses and couple stresses. *International Journal of Solids and Structures 40*, 24 (2003), 6681–6702.

[42] EVANS, L. C. *Partial Differential Equations*. American Mathematical Society, 2002.

[43] FENG, Y. T. On the dynamic nature of the conjugate gradient method. *Journal of Computational Physics 211* (2006), 91 – 98.

[44] FISHER, N. I. Smoothing a sample of circular data. *Journal of Structural Geology 11* (1989), 775 – 778.

[45] FU, X., ELLIOTT, J. A., BENTHAM, A. C., HANCOCK, B. C., AND CAMERON, R. E. Application ofx-ray microtomography and image processing to the investigation of a compactedgranular system. *Particle and Particle Systems Characterization 23* (2006), 229 – 236.

[46] GITMAN, I. M., GITMAN, M. B., AND ASKES, H. Quantification of stochastically stable representative volumes for random heterogeneous materials. *Archive of Applied Mechanics 75* (2006), 79 – 92.

[47] GOLDSMITH, W. *Impact, The Theory and Physical Behaviour of Colliding Solids*. Dover, Mineola, New York, 2001.

[48] GOODMAN, M. A., AND COWIN, S. C. A continuum theory for granular materials. *Archive for Rational Mechanics and Analysis 44* (1972), 249 – 266.

[49] GRYTZ, R., AND MESCHKE, G. Consistent micro-macro transitions at large objective strains in curvilinear convective coordinates. *International Journal for numerical Methods in Engineering* (2007), in press.

[50] GUDEHUS, G. Elastoplastische Stoffgleichungen für trockenen Sand. *Ingenieur-Archiv 42* (1973), 151 – 169.

[51] GURTIN, M. E. *An Introduction to Continuum Mechanics*. Academic Press, 1981.

[52] HALES, T. C. Sphere packings I. *Discrete and Computational Geometry 17* (1997), 1 – 51.

[53] HALES, T. C. Sphere packings II. *Discrete and Computational Geometry 18* (1997), 135 – 149.

[54] HALES, T. C. An overview of the kepler conjecture, 1998.

[55] HALES, T. C. Sphere packings III, 2002.

[56] HALES, T. C. Sphere packings IV, 2002.

[57] HALES, T. C. The kepler conjecture, 2007.

[58] HILL, R. Elastic properties of reinforced solids: Some theoretical principles. *Journal of the Mechanics and Physics of Solids 11* (1963), 357 – 372.

[59] HIRSCHBERGER, C. B. *A Treatise on Micromorphic Continua. Theory, Homogenization, Computation*. PhD thesis, University of Kaiserslautern, 2008.

[60] HOLZAPFEL, G. A. *Nonlinear Solid Mechanics*. Wiley, 2001.

[61] HRENNIKOFF, A. Solution of problems of elasticity by the framework method. *ASME Journal of Applied Mechanics 8* (1941), 169–175.

[62] JENKIN, C. F. The pressure exerted by granular material: An application of the principles of dilatancy. *Proceedings of the Royal Society of London. Series A 131*, 816 (1931), 53 – 89.

[63] JOHNSON, S., AND WILLIAMS, J. Contact resolution for an ellipsoid approximation for discrete element modeling. *Engineering computations 21* (2004), 215 – 234.

[64] KANEKO, K., TERADA, K., KYOYA, T., AND KISHINO, Y. Global-local analysis of granular media in quasi-static equilibrium. *International Journal of Solids and Structures 40* (2003), 4043–4069.

[65] KANIT, T., FOREST, S., GALLIET, I., MOUNOURY, V., AND JEULIN, D. Determination of the size of the representative volume element for random composites: statistical and numerical approach. *International Journal of Solids and Structures 40* (2003), 3647 – 3679.

[66] KANSAL, A. R., TORQUATO, S., AND STILLINGER, F. H. Computer generation of dense polydisperse sphere packings. *Journal of Chemical Physics 117*, 18 (2002), 8212 – 8218.

[67] KISHINO, Y. Disc model analysis of granular media. In *Micromechanics of Granular Materials* (1988), M. Satake and J. Jenkins, Eds., Elsevier, pp. 143–152.

[68] KOUZNETSOVA, V., BREKELMANS, W. A. M., AND BAAIJENS, F. P. T. An approach to micro-macro modeling of heterogeneous materials. *Computational Mechanics 27*, 1 (2004), 37–48.

[69] KOUZNETSOVA, V., GEERS, M. G. D., AND BREKELMANS, W. A. M. Multi-scale constitutive modelling of heterogeneous materials with a gradient-enhanced computational homogenization scheme. *International Journal for Numerical Methods in Engineering 54*, 8 (2002), 1235–1260.

[70] KOUZNETSOVA, V. G. *Computational homogenization for the multi-scale analysis of multi-phase materials*. PhD thesis, Technical University of Eindhoven, 2002.

[71] LARSSON, F., AND RUNESSON, K. RVE computations with error control and adaptivity: the power of duality. *Computational Mechanics 39* (2007), 647–661.

[72] LÄTZEL, M., LUDING, S., AND HERRMANN, H. J. *From discontinuous models towards a continuum description*. Continuous and Discontinuous Modelling of Cohesive Frictional Materials, Lecture Notes in Physics 586. Springer-Verlag, Berlin, Germany, 2001, pp. 215–230.

[73] LILIE, C. *Dreidimensionales Diskrete Elemente Modell für Superellipsoide*. PhD thesis, Institut für Baumechanik und Numerische Mechanik, Gottfried Wilhelm Leibniz Universität, Hannover, 2007.

[74] LUBACHEVSKY, B. D. How to simulate billiards and similar systems? *Journal of Computational Physics 94* (1991), 255 – 283.

[75] LUBACHEVSKY, B. D., AND STILLINGER, F. H. Geometric properties of random disk packings. *Journal of Statistical Physics 60* (1990), 561 – 583.

[76] LUBACHEVSKY, B. D., STILLINGER, F. H., AND PINSON, E. N. Disks vs. spheres:Contrasting properties of random packings. *Journal of Statistical Physics 64* (1991), 501 – 524.

[77] LUDING, S. Cohesive, frictional powders: contact models for tension. *Granular Matter* (2008), (in press).

[78] MALVERN, L. E. *Introduction to the Mechanics of a Continuous Medium*. Prentice Hall, 1969.

[79] MARTIN, J. W. Many-body forces in metals and the brugger elastic constants. *Journal of Physics C: Solid State Physics 8* (1975), 2837–2857.

[80] MARTIN, J. W. Many-body forces in solids : Elastic constants of diamond-type crystals. *Journal of Physics C: Solid State Physics 8* (1975), 2869–2888.

[81] MARTIN, J. W. Many-body forces in solids and the Brugger elastic constants : II. Inner elastic constants. *Journal of Physics C: Solid State Physics 8* (1975), 2858–2868.

[82] MEIER, H. A., E.KUHL, AND STEINMANN, P. Towards confined granular multiscale methods. In *ECCOMAS Thematic Conference, Modelling of Heterogeneous Materials with Applications in Construction and Biomedical Engineering.* (2007), M. Jirásek, Z. Bittnar, and H. Mang, Eds., pp. 172 – 173.

[83] MEIER, H. A., KUHL, E., AND STEINMANN, P. Failure of granular materials at different scales - microscale approach. In *Proceedings in Applied Mathematics and Mechanics* (2006), WILEY-VCH Verlag GmbH & Co. KGaA, Weinheim, pp. 399–400.

[84] MEIER, H. A., KUHL, E., AND STEINMANN, P. A note on the generation of periodic granular microstructures based on grain size distributions. *International Journal for Numerical and Analytical Methods in Geomechanics 32*, 5 (2008), 509–522.

[85] MEIER, H. A., SCHLEMMER, M., WAGNER, C., KERREN, A., HAGEN, H., KUHL, E., AND STEINMANN, P. Visualization of particle interactions in granular media. *IEEE Transactions on Visualization and Computer Graphics 14* (2008), 1110–1125.

[86] MEIER, H. A., STEINMANN, P., AND E.KUHL. On discrete modeling and visualization of granular media. In *Proceedings of the first workshop of DFG's International Research Training Group "Visualization of Large and Unstructured Data Sets - Applications in Geospatial Planning, Modeling, and Engineering"* (2006), H. Hagen, A. Kerren, and P. Dannenmann, Eds., pp. 165 – 175.

[87] MEIER, H. A., STEINMANN, P., AND E.KUHL. Towards completness, a multiscale approach of confined particulate systems. In *Proceedings of the second workshop of DFG's International Research Training Group "Visualization of Large and Unstructured Data Sets - Applications in Geospatial Planning, Modeling, and Engineering"* (2007), H. Hagen, M. Hering-Bertram, and C. Garth, Eds., pp. 103 – 114.

[88] MEIER, H. A., STEINMANN, P., AND E.KUHL. Towards multiscale computation of confined granular media - contact forces, stresses and tangent operators -. *Technische Mechanik 28* (2008), 32 – 42.

[89] MIEHE, C. Strain-driven homogenization of inelastic microstructures and composites based on an incremental variational formulation. *International Journal for Numerical Methods in Engineering 55*, 11 (2002), 1285–1322.

[90] MIEHE, C. Computational micro-to-macro transitions for discretized micro-structures of heterogeneous materials at finite strains based on the minimization of averaged incremental energy. *Computer Methods in Applied Mechanics and Engineering 192*, 5-6 (2003), 559–591.

[91] MIEHE, C., AND DETTMAR, J. A framework for micro - macro transitions in periodic particle aggregates of granular materials. *Computer Methods in Applied Mechanics and Engineering 193* (2004), 225–256.

[92] MIEHE, C., AND KOCH, A. Computational micro-to-macro transitions of discretized microstructures undergoing small strains. *Archive of Applied Mechanics (Ingenieur Archiv) 72*, 4-5 (2002), 300–317.

[93] MIEHE, C., SCHOTTE, J., AND LAMBRECHT, M. Homogenization of inelastic solid materials at finite strains based on incremental minimization principles. application to the

texture analysis of polycrystals. *Journal of the Mechanics and Physics of Solids 50*, 10 (2002), 2123–2167.

[94] MIEHE, C., SCHRÖDER, J., AND BAYREUTHER, C. On the homogenization analysis of composite materials based on discretized fluctuations on the micro-structure. *Acta Mechanica 155*, 1-2 (2002), 1–16.

[95] MIEHE, C., SCHRÖDER, J., AND BECKER, M. Computational homogenization analysis in finite elasticity: material and structural instabilities on the micro- and macro-scales of periodic composites and their interaction. *Computer Methods in Applied Mechanics and Engineering 191*, 44 (2002), 4971–5005.

[96] MIEHE, C., SCHRÖDER, J., AND SCHOTTE, J. Computational homogenization analysis in finite plasticity simulation of texture development in polycrystalline materials. *Computer Methods in Applied Mechanics and Engineering 171*, 3-4 (1999), 387–418.

[97] MINDLIN, D. Compliance of elastic bodies in contact. *ASME Journal of Applied Mechanics 16*, 3 (1949), 259 – 268.

[98] MISRA, A., AND CHANG, C. S. Effective elastic moduli of heterogeneous granular solids. *International Jounral of Solids and Structures 30* (1990), 2547 – 2566.

[99] MUNJIZA, A. *The combined finite-discrete element method*. Wiley, 2004.

[100] MUNJIZA, A., OWEN, D. R. J., AND CROOK, A. J. L. An $M\left(M^{-1}K\right)^m$ proportional damping in explicit integartion of dynamic structural systems. *International Journal for Numerical Methods in Engineering 41* (1998), 1277 – 1296.

[101] NEMAT-NASSER, S. Averaging theorems in finite deformation plasticity. *Mechanics of Materials 31* (1999), 493–523.

[102] NIGHTINGALE, F. *Notes on Matters Affecting the Health, Efficiency, and Hospital Administration of the British Army*. London: Harrison & Sons., 1858.

[103] NOVA, R. Soil models as a basis for modelling the behaviour of geophysical materials. *Acta Mechanica 64* (1986), 31 – 44.

[104] OAKLEY, D. R., AND KNIGHT JR, N. F. Adaptive dynamic relaxation algorithm for non-linear hyperelastic structures, Part I Formulation. *Computer Methods in Applied Mechanics and Engineering 126* (1995), 67 – 89.

[105] OAKLEY, D. R., AND KNIGHT JR, N. F. Adaptive dynamic relaxation algorithm for non-linear hyperelastic structures, Part II Single - processor implementation. *Computer Methods in Applied Mechanics and Engineering 126* (1995), 91 – 109.

[106] OAKLEY, D. R., AND KNIGHT JR, N. F. Adaptive dynamic relaxation algorithm for non-linear hyperelastic structures, Part III Parallel implementation. *Computer Methods in Applied Mechanics and Engineering 126* (1995), 111 – 129.

[107] OAKLEY, D. R., AND KNIGHT JR, N. F. Non-linear structural response using adaptive dynamic relaxation on a massively parallel-processing system. *International Journal for Numerical Methods in Engineering 39* (1996), 235 – 259.

[108] ODA, M., AND KONISHI, J. Microscopic deformation mechanism of granular material in simple shear. *Japanese Society of Soil Mechanics and Foundation Engineering 14*, 4 (1974), 25 – 38.

[109] OGDEN, R. W. *Non-Linear Elastic Deformations*. Dover Publications, 2004.

[110] ORTIZ, M., AND PANDOLFI, A. A variational Cam-clay theory of plasticity. *Computer Methods in Applied Mechanics and Engineering 193* (2004), 2645 – 2666.

[111] ORTIZ, M., AND STAINIER, L. The variational formulation of viscoplastic constitutive updates. *Computer Methods in Applied Mechanics and Engineering 171* (1999), 419 – 444.

[112] OTTER, J. R. H. Dynamic relaxation compared with other iterative finite difference methods. *Nuclear Engineering and Design 3* (1966), 183 – 185.

[113] PAN, L., METZGER, D., AND NIEWCZAS, M. The meshless dynamic relaxation techniques for simulating atomic structures of materials. In *Computational Mechanics: Developments and Applications* (2002), N. Badie, Ed., ASME PVP Vol. 441, pp. 15–26.

[114] PAPADRAKAKIS, M. A method for the automatic evaluation of the dynamic relaxation parameters. *Computer Methods in Applied Mechanics and Engineering 25* (1981), 35 – 48.

[115] PODIO-GUIDUGLI, P. *A Primer in Elasticity*. Kluwer Academic Publishers, 2004.

[116] POULIQUEN, O., BELZONS, M., AND NICOLAS, M. Fluctuating particle motion during shear induced granular compaction. *Physical Review Letters 91* (2003), 014301.

[117] RETTIG, G. Beschreibung granularer Medien im Rahmen einer Kontinuumstheorie. *Zeitschrift für Angewandte Mathematik und Mechanik 64* (1984), 517 – 527.

[118] REYNOLDS, O. On the dilatancy of media composed of rigid particles in contact, with experimental illustrations. *Philosophical Magazine 20* (1885), 469 – 481.

[119] REYNOLDS, O. Experiments showing dilatancy, a property of granular material, possibly connected with gravitation. *Journal and Proceedings of the Royal Institute, Great Britain 11* (1886), 354 – 362.

[120] RICHARD, P., NICODEMI, M., DELANNAY, R., RIBIÉRE, P., AND BIDEAU, D. Slow relaxation and compaction of granular systems. *Nature 4* (2005), 121 – 128.

[121] RICHARD, P., PHILIPPE, P., BARBE, F., BOURLÈS, S., THIBAULT, X., AND BIDEAU, D. Analysis by x-ray microtomography of a granular packing undergoing compaction. *Physical Review E 68* (2003), 020301.

[122] RICHARDSON, L. F. The approximate arithmetical solution by finite differences of physical problems involving differential equations, with an application to the stresses in a masonry dam. *Philosophical transactions of the Royal society of London. Series A 210* (1910), 307 – 357.

[123] ROSCOE, K. H., SCHOFIELD, A. H., AND WROTH, C. P. On the yielding of soils. *Geotechniqué 8* (1958), 22 – 53.

[124] ROTHENBURG, L., AND SELVADURAI, A. P. S. A micro-mechanical definition of the cauchy stress tensor for particulate media. In *Proceedings of the International Symposium on the Mechanical Behavior of Structured Media, Ottawa, Canada* (1981), pp. 469 – 486.

[125] ROWE, P. W. The stress-dilatancy relation for static equilibrium of an assembly of particles in contact. *Proceedings of the Royal Society of London. Series A 269*, 1339 (1962), 500 – 527.

[126] SAUVÉ, R. G., AND METZGER, D. A hybrid explicit solution technique for quasi-static transients. In *Computer Technology: Applications and Methodology* (1996), G. M. Hulbert, Ed., ASME PVP Vol 326, pp. 151–157.

[127] SCHNEEBELI, G. Une analogie mécanique pour les terres sans cohésion. *Comptes Rendus de l'Academie des Sciences Paris 243* (1956), 125 – 126.

[128] SCHRÖDER, J. Homogenisierungsmethoden der nichtlinearen kontinuumsmechanik unter beachtung von stabilitätsproblemen. Habilitation, Bericht Nr.: I-7 des Instituts für Mechanik (Bauwesen) Lehrstuhl I, Universität Stuttgart, 2000.

[129] SIMO, J. C., AND HUGHES, T. J. R. *Computational Inelasticity*. Springer-Verlag, 2000.

[130] SOKOLOV, V. N., AND O'BRIEN, N. R. A fabric classification of argillaceous rocks, sediments, soils. *Applied Clay Science 5* (1990), 353 – 360.

[131] SPENCER, A. J. M. *Continuum Mechanics*. Dover Publications, 2004.

[132] STROEVEN, M., ASKES, H., AND SLUYS, L. J. Numerical determination of representative volumes for granular materials. *Computational Methods for Applied Mechanics and Engineering 193* (2004), 3221 – 3238.

[133] STRONGE, W. J. *Impact Mechanics*. Cambridge University Press, 2000.

[134] SUNYK, R. *On Aspects of Mixed Continuum-Atomistic Material Modelling*. PhD thesis, University of Kaiserslautern, 2004.

[135] TADMOR, E. B., SMITH, G. S., BERNSTEIN, N., AND KAXIRAS, E. Mixed finite element and atomistic formulation for complex crystals. *Physical Review B 59*, 1 (1999), 235 – 245.

[136] TANG, Z., ZHAO, H., LI, G., AND ALURU, N. R. Finite-temperature quasicontinuum method for multiscale analysis of silicon nanostructures. *Physical Review B 74* (2006), 064110–1 – 064110–16.

[137] TAYLOR, G. I. Plastic strain in metals. *Journal Institute of Metals 62* (1938), 307–324.

[138] TEMIZER, I., AND ZOHDI, T. I. A numerical method for homogenization in non-linear elasticity. *Computational Mechanics 40* (2007), 281 – 298.

[139] TORQUATO, S., AND STILLINGER, F. H. Multiplicity of generation, selection, and classification procedures for jammed hard-particle packings. *Journal of Physical Chemistry 105* (2001), 11849 – 11853.

[140] TORQUATO, S., TRUSKETT, T. M., AND DEBENEDETTI, P. G. Is random close packing of spheres well defined? *Physical Review Letters 84*, 10 (2000), 2064 – 2067.

[141] TÓTH, L. F. Research problems. *Periodica Mathematica Hungarica 6*, 2 (1975), 197 – 199.

[142] TURNER, M. J., CLOUGH, R. W., MARTIN, H. C., AND TOPP, L. J. Stiffness and deflection analysis of complex structures. *Journal of the Aeronautical Sciences 23*, 9 (1956), 805 – 823.

[143] UNDERWOOD, P. Dynamic relaxation. In *Computational Methods for Transient Analysis* (1983), T. Belytschko and T. Hughes, Eds., Elsevier, pp. 245–265.

[144] VOIGT, W. *Lehrbuch der Kristallphysik*. Teubner, Leibzig, 1910.

[145] ŘEŘICHA, P. Optimum load time history for non-linear analysis using dynamic relaxation. *International Journal for Numerical Methods in Engineering 23* (1986), 2313 – 2324.

[146] VU-QUOC, L., AND ZHANG, X. An accurate and efficient tangential force-displacement model for elastic frictional contact in particle-flow simulations. *Mechanics of Materials 31* (1999), 235 – 269.

[147] VU-QUOC, L., AND ZHANG, X. An elastoplastic contact force-displacement model in the normal direction: displacement-driven version. *Proceedings of the Royal Society A 455* (1999), 4013 – 4044.

[148] VU-QUOC, L., ZHANG, X., AND LESBURG, L. Anormal force-displacement model for contacting spheres accounting for plastic deformation: Force-driven formulation. *Journal of Applied Mechanics 67* (2000), 363 – 371.

[149] VU-QUOC, L., ZHANG, X., AND WALTON, O. R. A 3-d discrete-element method for dry granular flows of ellipsoidal particles. *Mechanics of Materials 31* (2000), 483 – 528.

[150] WAKABAYASHI, T. Photoelastic method for determination of stress in powdered mass. In *Proceedings of the 7th Japenese National Conference on Applied Mechanics*, (1957), pp. 153 – 158.

[151] WALTON, O. R. Numerical simulation of inclined chute flows of monodisperse inelastic, frictional spheres. *Mechanics of Materials 16* (1993), 239 – 247.

[152] WALTON, O. R., AND BRAUN, R. L. Viscosity granular-temperature and stress calculations for shearing assemblies of inelastic frictional disks. *Journal of Rheology 30* (1986), 949 – 980.

[153] WEBER, J. Recherches concernant les contraintes intergranulaires dans les milieux pulvérulents. *Bulletin de liaison des Ponts et Chaussées 20* (1966), 1 – 20.

[154] WELLMANN, C., LILLIE, C., AND WRIGGERS, P. Homogenization of granular material modeled by a three-dimensional discrete element method. *Computers and Geotechnics* (2007), in press.

[155] WELLS, N. A. Are there better alternatives to standard rose diagrams? *Journal of Sedimentary Research 70* (2000), 37 – 46.

[156] WICHTMANN, T. *Explicit accumulation model for non-cohesive soils under cyclic loading*. PhD thesis, Schriftreihe des Institutes für Grundbau und Bodenmechanik der Ruhr-Universität Bochum, Heft 38, 2005.

[157] WILLNER, K. *Kontinuums- und Kontaktmechanik*. Springer, 2003.

[158] WILSON, E. L. The static condensation algorithm. *International Journal for Numerical Methods in Engineering 8* (1974), 198 – 203.

[159] WREN, J. R., AND BORJA, R. I. Micromechanics of granular media part II: Overall tangential moduli and localization model for periodic assemblies of circular disks. *Computer Methods in Applied Mechanics and Engineering 141* (1997), 221–246.

[160] WRIGGERS, P. *Nichtlineare Finite-Element-Methoden*. Springer-Verlag, 2001.

[161] ZIENKIEWICZ, O. C., AND PANDE, G. N. Time-dependent multilaminate model of rocks - a numerical study of deformation and failure rock masses. *International Journal for Numerical and Analytical Methods in Geomechanics 1* (1977), 219–247.

[162] ZIENKIEWICZ, O. C., AND TAYLOR, R. L. *The Finite Element Method for Solid and Structural Mechanics*. Butterworth-Heinemann, 2005.

[163] ZOHDI, T. I. Homogenization methods and multiscale modeling: linear problems. Encyclopedia of Computational Mechanics. E. Stein, R. de Borst and T. Hughes Editors, 2004.

[164] ZOHDI, T. I. Charge-induced clustering in multifield particulate flow. *International Journal for Numerical Methods in Engineering 62* (2005), 870 – 898.

[165] ZOHDI, T. I. Modeling and direct simulation of near-field granular flows. *International Journal of Solids and Structures 42*, 2 (2005), 539 – 564.

[166] ZOHDI, T. I., FEUCHT, M., GROSS, D., AND WRIGGERS, P. A description of macroscopic damage via microstructural relaxation. *The International Journal of Numerical Methods in Engineering 43* (1998), 493 – 507.

[167] ZOHDI, T. I., AND POWELL, D. Multiscale construction and large-scale simulation of structural fabric undergoing ballistic impact. *Computer Methods in Applied Mechanics and Engineering 193* (2006), 94 – 109.

[168] ZOHDI, T. I., AND WRIGGERS, P. On the sensitivity of homogenized material responses at infinitesimal and finite strains. *Communications in Numerical Methods in Engineering 16*, 9 (2000), 657–670.

[169] ZOHDI, T. I., AND WRIGGERS, P. Computational micro-macro material testing. *Archives of Computational Methods in Engineering 8* (2001), 131 – 228.

[170] ZOHDI, T. I., AND WRIGGERS, P. *Introduction to computational micromechanics*. Springer-Verlag, 2005.

List of Figures

2.1. Homogenization concept 6

3.1. Hard particle contact. 13
3.2. Concept of periodicity, the periodic boundary box. 16
3.3. Evolution process of a two dimensional monodisperse rve. 17
3.4. Evolution process of a three dimensional monodisperse rve. 19
3.5. Grain size distribution: quartz sand. 20
3.6. Evolution process of a two dimensional polydisperse rve. 22
3.7. Evolution of the time step size. 23
3.8. Evolution process of a three dimensional polydisperse rve. 24
3.9. Grain size distribution: Concrete aggregate. 25
3.10. Evolution process of a two dimensional polydisperse rve. 26
3.11. Evolution process of a three dimensional polydisperse rve. 27
3.12. Final rves, including 1000 primary particles. 29

4.1. Inter-particle contact. 34
4.2. One-sided harmonic potential. 35
4.3. Inter-particle contact force. 36
4.4. Comparison of different microscopic boundary conditions: Continuous case. . . 40
4.5. Comparison of different microscopic boundary conditions: Discrete case. . . . 41
4.6. Particle reaction forces: Assumption of TAYLOR. 42
4.7. Particle reaction forces: Restricted TAYLOR boundary condition. 43
4.8. Definition of the boundary particle sets. 45
4.9. Particle reaction forces: Periodic boundary conditions. 46
4.10. Jammed state of individual grains. 48
4.11. Jammed state of individual grains: Triple angle criterion. 49
4.12. Undeformed rve. 54
4.13. Algorithmic results: Uni-axial compression. 55
4.14. Investigation on large displacements under periodic boundary conditions. . . . 55
4.15. Motion of the individual grains by trace lines: Uni-axial compression. 56
4.16. Uni-axial compression: TAYLOR assumption. 58
4.17. Uni-axial compression: Restricted TAYLOR assumption. 59
4.18. Uni-axial compression: Periodic boundary conditions. 60
4.19. Motion of the individual grains by trace lines: Simple shear deformation. . . . 61
4.20. Simple shear deformation: TAYLOR assumption. 62
4.21. Simple shear deformation: Restricted TAYLOR assumption. 63
4.22. Simple shear deformation: Periodic boundary conditions. 64

5.1. Volume of an geometric periodic rve. 69
5.2. Absolute values: Shear components of the macroscopic CAUCHY stress. 75
5.3. Boundary reformulation under periodic boundary conditions. 76

5.4. Macroscopic quantities, uni-axial compression: Assumption of TAYLOR. 78
5.5. Macroscopic quantities, uni-axial compression: Restricted TAYLOR b.c.. 79
5.6. Macroscopic quantities, uni-axial compression: Periodic boundary condition. . . 80
5.7. Comparison of mean values of macroscopic quantities: Horizontal compression. 81
5.8. Macroscopic quantities, simple shear: Assumption of TAYLOR. 83
5.9. Macroscopic quantities, simple shear: Restricted TAYLOR b.c.. 84
5.10. Macroscopic quantities, simple shear: Periodic b.c.. 85
5.11. Comparison of mean values of macroscopic quantities: Horizontal simple shear. 86
5.12. Macroscopic quantities under cyclic loading: Rest. TAYLOR and periodic b.c.. . . 88

6.1. Rectangular block example. 96
6.2. Comparison of macroscopic results for different side pressures. 98
6.3. Basic examples of REYNOLDS' dilatancy principle 100
6.4. Bi-axial compression test. 101
6.5. Comparison of macroscopic quantities in response to different microscopic b.c.. 103
6.6. Deformed bi-axial specimen depicting VON MISES stress. 103
6.7. Zoom in on selected micro structures. 104
6.8. Undeformed mesh of the slope stability problem. 105
6.9. Deformed mesh of the slope stability problem, showing the VON MISES stress. . 106

7.1. Tangential contact 108
7.2. Macroscopic influence of the microscopic friction angle: Uni-axial compression. 116
7.3. Macroscopic influence of the microscopic friction angle: Simple shear. 117
7.4. Macroscopic influence of the microscopic hardening modulus: Cyclic loading. . 118

List of Tables

3.1. Pseudocode of the packing algorithm. 15
3.2. Input parameter: Quartz sand example. 21
3.3. Input parameter: Concrete aggregate example. 25

4.1. Pseudocode for microscopic computations (restricted TAYLOR). 44
4.2. Pseudocode for microscopic computations (periodic boundary conditions). . . . 47
4.3. Iterative algorithm to find rattlers. 50
4.4. Pseudocode for the microscopic dynamic relaxation procedure (rest. TAYLOR). . 52

5.1. Input parameters: 150, 300 and 600 primary particles. 77

6.1. Convergence behavior, rectangular block, TAYLOR assumption. 97
6.2. Convergence behavior, rectangular block, restricted TAYLOR assumption. . . . 97
6.3. Convergence behavior, rectangular block, periodic boundary conditions. . . . 97
6.4. Convergence behavior, bi-axial compression, TAYLOR assumption. 102
6.5. Convergence behavior, bi-axial compression, restricted TAYLOR assumption. . . 102
6.6. Physical parameters of the slope stability problem. 105
6.7. Convergence behavior, slope stability test, TAYLOR assumption. 105

7.1. Pseudocode to calculate the generalized contact force. 114

Curriculum Vitae

Name	Holger Andreas Meier
Nationality	German
Date of Birth	April 15th, 1977
Place of Birth	Essen
1983 - 1987	Grundschule in der Vöde, Bochum
1987 - 1996	Goethe Gymnasium, Bochum
1997 - 2004	Study of Civil Engineering, Ruhr-Universität, Bochum
since 2005	Research Associate, University of Kaiserslautern Department of Mechanical and Process Engineering Chair of Applied Mechanics (Prof. Dr.-Ing. P. Steinmann)